DISS. ETH NO. 25045

Technologies for Cellular-Resolution Connectomics

A thesis submitted to attain the degree of

DOCTOR OF SCIENCES of ETH ZURICH

(Dr. sc. ETH Zurich)

Presented by

THOMAS TEMPLIER

Diplôme d'ingénieur, Ecole Supérieure d'Electricité
Dipl.-Ing. Univ., Technical University Munich

born on 12.11.1987

citizen of

France

accepted on the recommendation of

Prof. Richard H.R. Hahnloser
Prof. Mehmet Fatih Yanik

2018

Abstract

Cellular-resolution connectomics is a field of neuroscience that aims to decipher how neurons in the brain are wired together at the resolution of single synaptic connections. The current only existing approach for systematic mapping of all neuronal wires and their connections in a small chunk of brain tissue is volumetric electron microscopy. The extraction of these tiny chunks from their surrounding tissue however severs the connections between observable neuronal components (neurites, somas) and the larger neuronal circuit they are part of, preventing a circuit-level understanding of the observed components. The correlative array tomography (CAT) technique mitigates this limitation by labeling neurons in circuits of interest with neuroanatomical tracers that can then be observed with light microscopy and merged into the electron microscopy imagery.

In this thesis I extended the library of tracers suitable for CAT and developed a pipeline for the automated acquisition and assembly of correlative light and electron microscopy imagery from collected ultrathin sections of labeled brain tissue. A major long-standing obstacle that I faced was the ability to collect many ultrathin sections reliably from a piece of brain in order to provide a volumetric dimension to the CAT technique. Towards that goal I invented the following method: plasticized tissue blocks can be augmented with a block of resin containing superparamagnetic nanoparticles. It ensues that freely-floating ultrathin sections cut from such augmented blocks can be remotely actuated at a water surface with a magnetic field and agglomerated. Subsequently the water is slowly removed to let the sections sink onto a previously immersed collecting substrate such as a piece of silicon wafer.

The high packing density of the sections collected on substrate allowed me to then make the following pioneering discovery: collected sections can be submitted to repeated cycles of electron microscopy and broad ion beam milling, yielding a final electron microscopy imagery with a significantly improved axial resolution.

Overall, by solving the longstanding obstacle of reliable section collection on flat substrates for CAT, the hybrid magnetic section collection method combined with repeated cycles of broad ion beam milling and electron microscopy imaging is opening a new technological avenue in volume correlative light and electron microscopy for biology. In particular, the hybrid magnetic collection and BIB milling paves the way for volumetric correlative light and isotropic multi-beam electron microscopy on large-area tissue sections and in unprecedentedly large volumes.

Résumé

La connectomique à résolution cellulaire est un domaine des neurosciences qui aspire à révéler comment les neurones du cerveau sont câblés entre eux, et ceci à une résolution synaptique. La seule approche existante pour la cartographie systématique de tous les câbles neuronaux et leurs connections dans un petit cube de cerveau est la microscopie électronique volumétrique. L'extraction de ces minuscules cubes de leur tissu environnant cependant coupe les connections entre les éléments observables dans le cube (neurites, corps cellulaires) et le circuit neuronal plus large dont ils font partie, empêchant ainsi une compréhension des éléments observés d'un point de vue relatant aux circuits neuronaux. La technique *Correlative Array Tomograhy* (CAT) atténue cette limitation en marquant les neurones d'un circuit donné avec des traceurs neuronaux qui peuvent ensuite être observés avec de la microscopie à fluorescence et superimposée dans l'imagerie acquise au microscope électronique.

Dans cette thèse nous avons étendu le catalogue de traceurs compatibles avec la methode de CAT et développé une pipeline pour l'acquisition et l'assemblage d'imagerie de microscopie corrélative optique et électronique provenant de sections ultrafines de tissu neuronal marqué avec des traceurs. Un obstacle majeur auquel nous avons fait face était notre aptitude à collecter de manière fiable des sections ultrafines provenant d'un bout de tissu de cerveau afin de conférer une dimension volumétrique à la technique de CAT. A cette fin, l'invention suivante a été réalisée: les blocs de tissu plastifiés peuvent être augmentés avec un bloc de résine contenant des nanoparticules superparamagnétiques. Il s'ensuit que les sections coupées flottant sur une surface d'eau peuvent être aggrégées en un point avec un champ magnétique avant de finalement retirer lentement l'eau afin que les sections se déposent au fond sur une plaque de collection tel qu'un bout de plaquette de silicium.

La haute densité spatiale avec laquelle les sections sont collectées nous a permis de realiser une seconde découverte: les sections collectées peuvent être soumises à des cycles répétés de microscopie électronique et de gravure à l'aide d'un faisceau ionique large, offrant ainsi une résolution axiale améliorée de manière significante pour l'imagerie à microscopie électronique.

En résolvant le problème de la collection de sections sur des substrats plats pour la méthode CAT, la méthode hybride de collection magnétique combinée avec des cycles répétés de microscopie électronique et de gravure à faisceau ionique non focalisé ouvre une nouvelle voie pour la microscopie volumétrique corrélative en biologie. En particulier, la méthode hybride proposée nous rapproche d'un système pour microscopie volumétrique corrélative à lumiere et à microscopie électronique isotropique et multi-faisceau sur des sections à large surface.

Acknowledgements

I thank the members of the Institute of Neuroinformatics and its founders for the stimulating environment. I thank M. F. Yanik for corefereeing this thesis.

I thank my parents and my brothers Nicolas and Simon.

I thank my friend Nicolas Broguière for insightful scientific conversations pleasantly interspersed with jazz manouche practice.

I thank colleagues with whom I discussed or from whom I heard inspiring talks.

I thank my friends from tennis and Jazz Manouche who unknowingly contributed to this work.

Foreword

Chapter 1, serving as an introduction to this thesis, is a book chapter currently in press that provides an overview of the correlative array tomography method and serves as an introduction to the use of correlative light and electron microscopy for cellular-resolution connectomics.

Chapter 2 describes an invention to collect hundreds of consecutive ultrathin sections from a plasticized sample directly onto silicon wafer substrates. The chapter demonstrates its use in the context of cellular-resolution connectomics in the songbird brain with correlative light and electron microscopy.

Chapter 3 proposes a novel technology for correlative light and electron microscopy by combining magnetic collection of mechanically cut ultrathin sections with cycles of broad ion beam milling and electron microscopy imaging.

Chapter 4 introduces eye-tracking technology as a means to record decisions made by humans at unprecedentedly high speed while they navigate volumetric electron microscopy imagery.

Note: The unified page numbering of this thesis is placed centered at the bottom of the pages.

Chapter 1

Correlative Array Tomography

Correlative Array Tomography

Thomas Templier, Richard H. R. Hahnloser

Institute of Neuroinformatics, University of Zurich and ETH Zurich
Neuroscience Center Zurich, ZNZ
{templier, rich}@ini.ethz.ch

Abstract

Array tomography (AT) is a sample preparation and imaging method that provides excellent optical and physical access to biological tissues over extended length scales and potentially across their whole depth. It comprises embedding a sample in resins, sectioning it, and collecting hundreds of consecutive ultrathin sections, followed by one or more cycles of immunohistochemical staining and fluorescent light microscopic (LM) imaging. Since the introduction of AT in 2007, efforts have been made towards extending AT to correlative light and electron microscopy (EM) approaches suitable for volumetric ultrastructural neural circuit reconstruction. In such correlative array tomography (CAT) techniques, samples must be optimally prepared to preserve antigenicity of proteins and dyes of interest and to yield good EM ultrastructure quality. We review several CAT protocols and describe ours in which LM imagery of ultrathin sections resolves different neuron types previously labeled by *in-vivo* injection of neuroanatomical tracers. EM imagery of the same sections resolves cellular compartments and synapses of interest in their ultrastructural context. In combination, these imaging modalities unambiguously provide information about neuronal connectivity.

Abbreviations:

ABC: avidin-biotin complex
AT: array tomography
CAT: correlative array tomography
BDA: biotinylated dextran amine
DAB: diaminobenzidin
EM: electron microscope/microscopy
IHC: immunohistochemistry
LM: light microscope/microscopy
FA: formaldehyde
RA: nucleus Robustus of the Arcopallium

Contents

I. Introduction

A. Array tomography and its tradeoffs

The understanding of structure-function relationships in biological tissues necessitates the visualization of both proteins and their three-dimensional physical context. Several microscopy imaging techniques can visualize either the former or the latter. However, the quest for a single technique that can readily capture both remains open. Array tomography (AT), introduced in 2007 (1) is an approach to resolve conflicting requirements for the simultaneous volumetric ultrastructural observation of biological samples with the resolution of electron microscopy together with the analysis of antigens by the means of fluorescent light microscopy (LM). In the following, we review diverse AT protocols and discuss their strengths and weaknesses.

It is well known that the preservation of both antigenicity and ultrastructure are two largely incompatible aims of current tissue preparation protocols (2–8). This incompatibility prevents the simultaneous observation of both molecular and physical architectures. To address this issue, three main array tomography sample preparation methods have been introduced. The original approach aimed to visualize the molecular composition of brain tissues (1,9–13), it employed a sample preparation protocol tuned for antigenicity preservation (e.g., no glutaraldehyde fixation, no heavy metal staining, bench embedding, and resin infiltration), at the expense of the loss of ultrastructure quality. A first variation of this original protocol has been recently introduced by the same laboratory (14) to provide a better ultrastructure quality while maintaining a comparable LM quality. That improved protocol relies mainly on freeze substitution and the absence of Osmium tetroxide staining. The second variation to the original AT sample preparation, correlative array tomography (CAT), which we detail in this chapter, aims at tissue ultrastructure preservation necessary for assessment of neural connectivity, at the expense of prohibiting access to the endogenous molecular architecture (15,16). CAT makes use of the fixative agent glutaraldehyde and requires heavy metal staining for ultrastructural contrast. CAT offers several advantages over many EM-only techniques, namely convenient volumetric data acquisition, easy simultaneous handling, staining and storage of hundreds of sections, and, most importantly, suitability for imaging by correlative light and electron microscopy procedures.

B. Volumetric electron microscopic imaging: to handle, stain, and store hundreds of ultrathin sections

A key component of AT relies on the production of arrays of ultrathin sections from resin-embedded biological samples. Ultrathin serial sectioning substantially increases the resolution along the depth axis from an optical resolution of at best about 700 nm (1) to the physical sectioning resolution in the 30-200 nm range. Subsequent sample collection provides the ability to create libraries of sectioned samples that can be processed at any time (17) (note however that LM imaging should be performed shortly after staining, see supplementary information in (18)). For high-resolution EM imaging, a microscope operator has the choice of either acquiring complete (imaging of all sections) or partial datasets from a portion of the sectioned tissue and return to specific areas for more detailed analysis at a later date. Image acquisition can be performed with advanced sample navigation tools (19,20).

Collection of a large number of thin sections by ultramicrotomy and their mounting on a single rigid physical substrate provides a convenient means for thin section handling, loading in light or scanning electron microscopes (SEMs), and sample storage, compared for example with dexterous manual handling of fragile grids required in transmission electron microscopy (TEM). As we describe in detail in Section IIB, AT on a rigid substrate allows for on-section immunohistochemistry, which is achieved by depositing the labeling solution on the flat substrate. In this way, all sections can be simultaneously stained, avoiding the need both for EM grid staining machines used in TEM (21) and for time-consuming and error-prone manual handling and loading of TEM grids (22–24). Rigid substrates usually fit through the airlock opening of SEMs (large substrates of up to 10 cm x 10 cm can also be readily loaded via the chamber door), allowing simple loading of dozens up to potentially thousands of serial sections at a time.

By contrast, non-AT approaches to volumetric imaging such as focused ion beam (FIB)(25) and serial block face (SBF)(26) scanning electron microscopy (SEM) both irreversibly and systematically destroy the tissue after imaging (destructive techniques), forcing the experimenter to either take the risk of missing regions of interest or to image the entire exposed area, the latter of which slows down the acquisition process and introduces challenges around post processing and evaluation of very large datasets.

C. Correlative light and electron microscopy

The need for correlative light and electron microscopy lies in the intrinsic properties of biological tissues, namely the intricate relationship between the molecular and physical architectures. In neuroscience, the gold standard imaging technique for analysis of morphology and connectivity of neural tissue at the level of single synapses and organelles is undoubtedly electron microscopy (7,27). Nevertheless, the last decade has seen a significant increase in the number of correlative microscopy studies in biology (28–31). Mainly two combinations of light and electron microscopy imaging modalities have been explored: 1) confocal light microscopy and subsequent focused ion beam SEM (32,33); 2) two-photon microscopy followed by either serial block face SEM (26), TEM (34), or FIB-SEM (35). Compared to AT, all these methods suffer from the inability to combine the two modalities on the exact same sample and at the same stage of the processing pipeline. This inability entails that additional efforts are required to achieve the desired correlation of LM-EM modalities. These alternative methods not only necessitate extremely careful sample handling and preparation in order to conserve regions of interest for subsequent EM imaging, but they also lead to difficult computer vision problems arising from the much smaller spatial resolution of LM versus EM imagery.

We report here only on AT approaches based on wide field fluorescence microscopy. In principle, the arrays of sections collected on a rigid support could also be imaged with new generation sub-diffraction light microscopes such as STED (36) or STORM (37), the latter of which achieve an impressive volumetric resolution of 28 nm x 28 nm x 40 nm (37).

D. Workflow

The CAT workflow presented in this chapter is sketched in Figure 1; all steps are described and discussed throughout the core of this chapter.

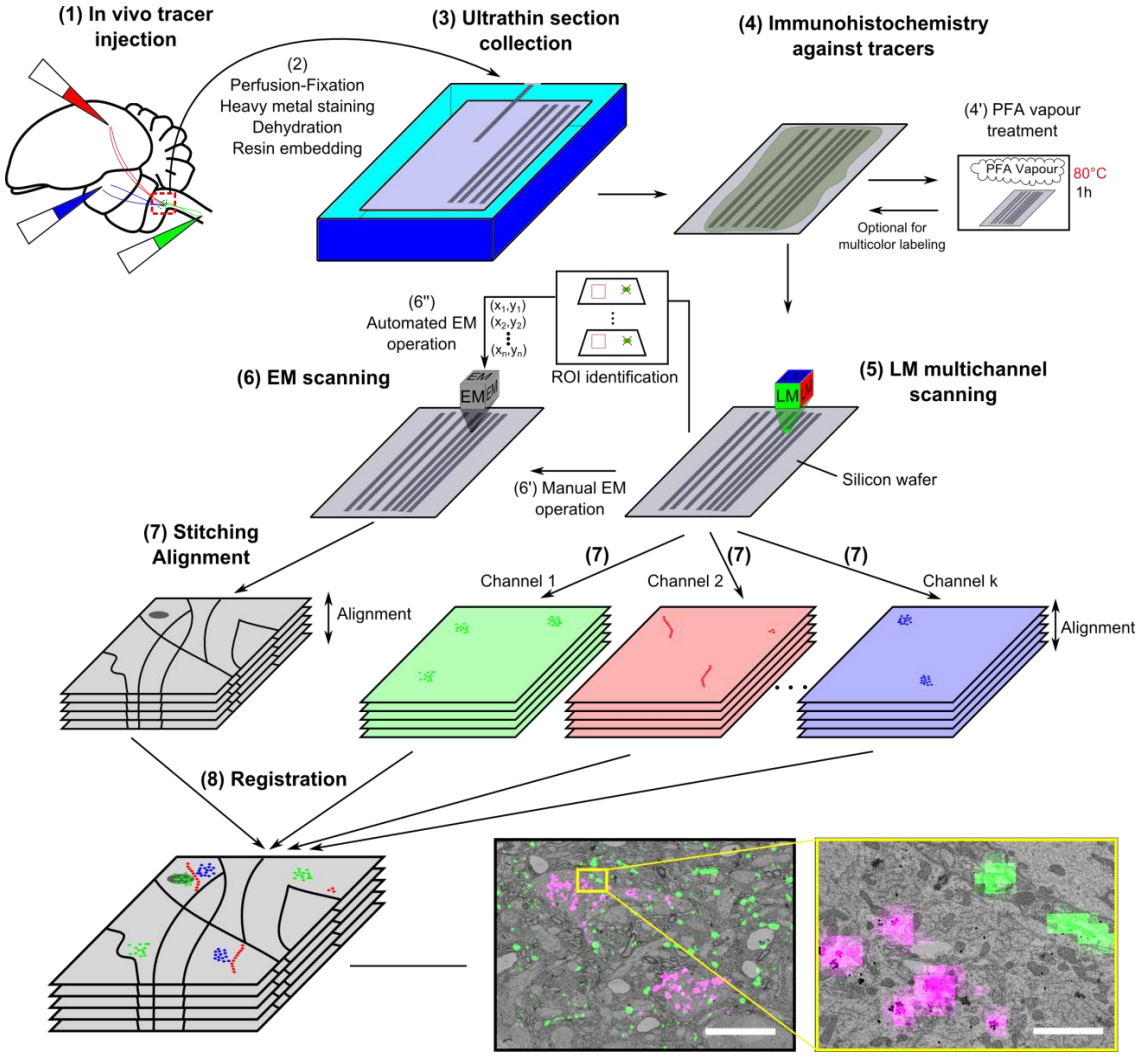

Figure 1. **Workflow of correlative array tomography (CAT) for identification of neuron types in their ultrastructural context.** (1) In vivo injection of neuroanatomical tracers to label structures of interest. (2) The animal is perfused with fixative for optimal fixation. The brain is dissected out, cut manually or with a vibratome to extract a region of interest. This region is subsequently stained with heavy metals, dehydrated, infiltrated with epoxy resin and cured at 52°C. (3) Sectioning of ultrathin sections of the resin-hardened sample and collection on a flat conductive silicon wafer. (4) Immunohistochemistry is performed on the silicon wafer by placing drops of staining solution on the substrate. (4') Optional treatment with formaldehyde vapor to destroy free remaining binding sites of secondary antibodies, this treatment allows the staining of different antigens with two different antibodies stemming from the same species. (5) The silicon wafer is cover slipped and scanned in a wide-field fluorescent microscope. (6) The wafer is subsequently scanned in the EM. The locations to scan in the EM are either defined manually by the EM operator (6') or calculated from the location of objects of interest, identified in the LM (6''). (7) Images acquired in the LM and the EM are then automatically stitched and aligned using custom software, resulting in several aligned volumetric image stacks. (8) The EM and LM datasets are automatically aligned using custom software. White scale bars bottom left and bottom right: 15 µm and 2 µm.

II. CAT sample preparation protocols

The sample preparation protocol should be carefully chosen depending on the goal of the experiment. We describe here the protocol optimized for circuit tracing developed in our laboratory, and briefly review the one optimized for proteometric analysis, as originally introduced with AT in 2007. The differences in these protocols reflect the well-known compromise between ultrastructure and antigenicity preservation (5,6,38–40).

A. Fixation and embedding

Fixation, dehydration and resin embedding are necessary steps in order to visualize biological tissue in electron microscopes. In the following, we summarize the key differences between CAT protocols for circuit tracing (15,16) and for proteometric analysis (1,9).

1. CAT sample preparation for circuit tracing

The sample preparation protocol optimized for correlative circuit tracing developed in our laboratory contains two different heavy metals (1% Osmium tetroxide and 1% Uranyl acetate) to ensure strong staining of membranes (see (15) for detailed protocol).
Similarly to published protocols that yield good ultrastructure quality and that to some extent enable postembedding IHC (41–43), fixation in our protocol is performed with 4% formaldehyde (FA) and 0.075% glutaraldehyde (GA) diluted in 0.1 M phosphate buffer at pH 7.4. This protocol yields good ultrastructure but destroys antigenicity of endogenous proteins. Namely, none of the following endogenous molecules could be visualized using immunohistochemistry in our laboratory: acetylcholine, parvalbumin, synapsin, and PSD-95 (data not shown); similar findings are reported in (14). The Looger laboratory has recently developed endogenous tags that survive to some extent mild EM embedding protocols (44,45). It is not known though whether these tags would also survive harsher protocols optimized for connectomics (46–48).

Fortunately, we found that some exogenous molecules such as biotin and some fluorophores carried by neuroanatomical tracers conserve their antigenicity and even their fluorescence in some cases after embedding for electron microscopy (see Table 1).

2. AT sample preparation for proteometric analysis

AT has been introduced in 2007 for high-dimensional proteometric analysis using fluorescence microscopy. The original AT sample preparation has been tuned to maximize antigenicity at the expense of good ultrastructure. In this paragraph, we detail the steps of AT sample preparation together with explanations. The choice of the fixative mixture has a crucial impact on the ultrastructure quality and antigenicity preservation of endogenous molecules.

As described in complete details in (1), the brain is first fixed in 4% formaldehyde only, without any glutaraldehyde. It is thought that glutaraldehyde fixation is harsh and leads to alteration of the 3D conformation of relatively large molecules, whereas it can retain small molecules such as metabolites (23). Some antigens (GABA, glutamate, PIP2) were visualized (1) only when glutaraldehyde was added to the fixative solution. The effects of fixation on the ability of an antibody to bind to its target are complex, and we refer the reader to the following publications (49–51) for further reading.
Osmium (with proteolytic activity) is omitted in AT, because it heavily alters the three dimensional conformation of many endogenous proteins, thus making them inaccessible to IHC (14). Osmium is, however, an excellent staining agent for electron microscopy (46–48). Uranyl acetate is also omitted even though it is considered less harsh than osmium tetroxide in terms of alteration of three-dimensional conformation (14,52–54).

Also, in the original AT study, the tissue dehydration prior to resin infiltration was pursued only up to 95%. The resin LR White was preferred over other resins because it preserves antigenicity (8,42); LR White polymerizes at a temperature of 50°C. Epon would probably have led to optimal sectioning quality; however, Epon is a hydrophobic resin that tends to react more with biological molecules (55). Synapse counts reported with this AT protocol are consistent with synapse densities obtained with stereological methods using electron microscopy. Many antibodies against endogenous proteins have been successfully used, including well-known synaptic proteins such as Synapsin, Synaptophysin, VGluT1, VGluT2, PSD-95, NMDAR, GAD, and Gephyrin (1,9).

3. Other variations of CAT sample preparation protocols

We review in this section several recent studies that have introduced variations to the original AT sample preparation protocol. The variations reflect the tight compromise in sample preparation to achieve both preservation of antigenicity and ultrastructure.

Stemming from the laboratory that originally developed AT, the study (14) reports about “Conjugate Array Tomography”, an AT variation that better preserves ultrastructure while maintaining good antigenicity of endogenous molecules. This feat is mainly due to the following modifications: perfusion fixation is done with 2% FA, 2% Glutaraldehyde at pH 6.8, uranyl acetate staining is done at -90 °C with a high concentration of 2-4%, infiltration with the Lowicryl resin HM20 is done at -45°C and polymerization is performed with UV radiation at room temperature.

In (56), thalamocortical input onto layer 5 pyramidal neurons in mouse were investigated. Authors used genetic lines and viral vectors to express endogenous fluorescent proteins in pre- and post-synaptic neurons of interest. In order to validate the location of putative synapses identified with AT, the authors correlated LM imagery with EM imagery. To this end, they developed a protocol that provided enough ultrastructural contrast for synapse identification, while antigenicity of endogenous proteins was retained. Their sample preparation protocol includes 0.2% of glutaraldehyde in the perfusion fixation solution, 0.001% osmium tetroxide staining, and a low temperature (-20 °C) infiltration and polymerization of the hydrophilic resin LR White.

In a large collaborative effort, new fluorescent probes have been designed (45) that can be targeted with IHC after perfusion fixation with 4% formaldehyde and 0.2% glutaraldehyde, staining with 1% osmium tetroxide, and freeze substitution embedding with the HM20 resin. It remains to be tested whether these new probes can be processed using protocols aimed at ultrastructure preservation (46–48).

B. Section cutting and collection

We briefly review several AT-compatible techniques for the collection of ultrathin sections of resin-embedded tissue. These can be classified based on the type of substrate on which the sections are collected: flat conductive substrate or conductive flexible tape.

1. Flat conductive substrate

There exist several flat conductive substrates for correlative microscopy, including indium tin oxide coated (ITO) glass (e.g., coverslips or LM slides) and silicon wafers (Ted Pella, #16015 Type P <100> or #21610-6). We found that the latter substrate presents several advantages (15,16,57): 1) Silicon wafers are naturally conductive and they do not require any chemical pretreatment ([1]an acid sulfuric and perhydrol pretreatment can be performed to permanently hydrophilize the substrate (57), however, we prefer to hydrophilize temporarily with a simple glow discharge treatment because we later make use of the hydrophobicity for staining). We have observed that samples collected on silicon wafers can be imaged with a high current /probe in SEMs (3 nA) without charging problem, whereas such high currents are unusable with samples collected on ITO slides because of charge buildup at the surface of the substrate. 2) Collected sections are visible to the naked eye and can be imaged using bright-field reflection microscopes. 3) Silicon wafers are easily cleavable with a diamond scriber into rectangles of any shape (for silicon wafers with a <100> crystal orientation). 4) The hydrophobicity of silicon wafers allows straightforward immunohistochemical (IHC) staining, because drops of solution stay in place, which substantially reduces the amount of solution (and cost) needed for staining. In the example of Figure 2, we used only 150 µl of solution for IHC during each staining step to label approximately 600 sections, representing a ratio of 0.25 µl/section. 5) Silicon wafers reflect light, therefore the fluorescence signal emitted in the direction of the substrate is reflected towards the objective, yielding a stronger signal than ITO glass for example. Finally, 6) silicon wafers are nearly perfectly flat and thus are suitable for new-generation multibeam FEGSEM because all beams can simultaneously be in focus, whereas samples collected on tape might exhibit stronger height variations.
In the next paragraphs we focus on techniques for section collection.

a. Ribbon pick-up by wafer retraction

To acquire volumetric tissue information it is important to reliably cut and collect large numbers of consecutive ultrathin sections from the same sample, for example using so-called “histo-Jumbo” diamond knifes provided by Diatome (58). These diamond knives are operated over a large water boat in which

entire microscope slides can be immersed. The approach proposed initially in (58) and enhanced in (9) is to obliquely insert a flat substrate into the water boat of a diamond knife, so that the front part is immersed and the back part remains dry above the water. Thereafter, ribbons of consecutive sections are produced (see (59) for details), detached from the knife edge, and moved to the substrate with an eye lash. When the beginning of the ribbon reaches the non-immersed part of the substrate, it adheres to it and anchors the whole chain of sections. The substrate is then slowly retracted out of the water, which can be done manually using forceps, or with a custom substrate holder such as the one introduced in (57), or the more elaborate one in (60).

b. Ribbon pick-up by water removal

Instead of partly immersing the silicon wafer (substrate) at an oblique angle to the surface, we prefer to immerse it entirely prior to cutting. During and after the cutting process, the series of ribbons can be moved on the water surface using eye lashes. The water is then slowly removed with a custom-made flexible syringe to deposit the sections on the silicon wafer. As soon as the surface is dry enough to prevent the sections from flowing off the wafer, the substrate is carefully removed and placed on a heating plate at 45°C for 10 to 30 minutes to uniformly dry the sections without creating folds. To avoid damaging the sections, care should be taken that the knife edge remains dry during the few minutes needed to remove the water (the sections could get stuck on the edge).

We believe that collecting sections on a silicon wafer is ideal for staining and imaging of large numbers of consecutive sections, as shown in Figure 2, in which a wafer is shown that carries more than 550 consecutive sections (2 sections missing). The density of sections on the wafer can be high because ribbons can be moved very close to each other.

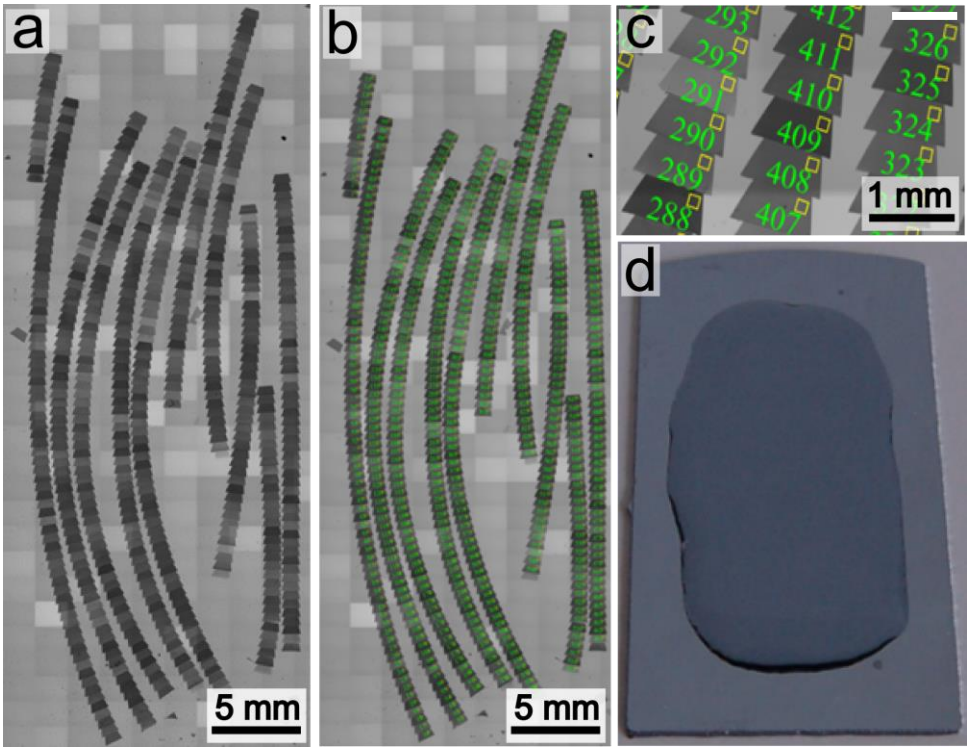

Figure 2. **589 consecutive[1] (2 sections missing) ultrathin sections collected on a single silicon wafer.** a) Brightfield mosaic of the wafer surface. The sections are clearly visible as dark regions. b) All sections have been segmented with custom software. The algorithm detects the section borders first and then identifies section corners. c) Magnified region of b) showing three ribbons of ultrathin sections. The yellow frames have been automatically inserted on all subsequent sections after manual definition of a region of interest within the first section, demonstrating automated access to corresponding subregions d) Solution placed on a silicon wafer. The hydrophobicity of the substrate allows the liquid to stay in place.

2. Flexible tape

A method for automated section collection is the ATUM (Automated Tape collection Ultra Microtome) developed by K. Hayworth and colleagues (17). The ATUM consists of a conveyer belt that loads a flexible tape into the boat of a conventional diamond knife. Sections are produced with a conventional ultramicrotome, they are collected on the tape and subsequently stored in a reel. An operator can then unroll the tape, cut parts of appropriate lengths (about 1 section per 1 mm) and glue the ribbon parts onto a carbon adhesive tape which itself is glued onto a silicon wafer. Each silicon wafer holds approximately 200 sections that can be imaged in a normal SEM with a back-scattered electron detector. Most tapes come with the drawback of being strongly autofluorescent, thus preventing their use in light microscopy. A possible solution for correlative microscopy is to collect sections on a ribbon made of thin glass (personal communication Richard Schalek, Lichtman's laboratory).

C. Post-embedding on-section immunohistochemistry

1. Neuroanatomical tracers retaining fluorescence and/or antigenicity

The CAT approach in (15,16) aims at preserving antigenicity not of endogenous proteins, e.g. synaptic proteins, but of exogenous compounds, e.g., fluorophores of neuroanatomical tracers. We have identified a set of exogenous neuroanatomical tracers (listed in Table 1) whose antigenicity and sometimes whose fluorescence survive the harsh embedding protocol. So far we successfully used four tracers in anterograde labeling experiments (biotinylated dextran amine (BDA), Texas Red, Fluorescein, and Dextran 488), and four tracers in retrograde labeling experiments (Texas Red, Fluorescein, Dextran 488, and Lucifer Yellow). We performed tracer localization in ultrathin embedded sections using conventional on-section immunohistochemical staining (61,62) that is composed of the following steps: short etching, blocking, primary antibody labeling, washing, secondary antibody labeling, and final washing (see (15) for details).

Carrier	Hapten	Antigenicity	Fluorescence	Product number (Life Technologies)	Antibody Species	Product number
Dextran	BDA	+	-	D-1956	Mouse Streptavidin	Jackson Immu. : 200-002-211 Life Tech.: S-11223
Dextran	488	+	-	D-22910	Rabbit Rat	Life Tech.: A-11094 Biotem: custom
Dextran	Texas Red	+	+	D-3328	Rabbit Goat	Life Tech.: A-6399 Vector Labs: SP-0602
Dextran	Fluorescein	+	+	D-1820	Rabbit	Life Tech.: A-889
Dextran	Lucifer Yellow	+	-	D-1825	Rabbit	Life Tech.: A-5750
Dextran	647	-	-	D-22914	Mouse Guinea Pig	Abcam: ab52060 Biotem: custom
Dextran	Tetramethyl-rhodamine	-	-	D-1817	Rabbit	Life Tech.: A-6397

Table 1. Neuroanatomical tracers tested for antigenicity preservation in our embedding protocol. - = no survival, + = some survival.

For example, we have found that the antigenicity of Dextran-647 does not survive the embedding at all. We tried two different commercial antibodies and a custom-made antibody that all successfully stained

Alexa647 in fixed wet sections but did not give any positive signal in post-embedding IHC. In contrast, the fluorescence of the two fluorophores Texas Red and Fluorescein is preserved after embedding (as shown in Figure 3). However, the signal is very weak, and comparing native fluorescence with the signal after IHC shows that most of the fluorophores lost their fluorescence but retained their antigenicity.

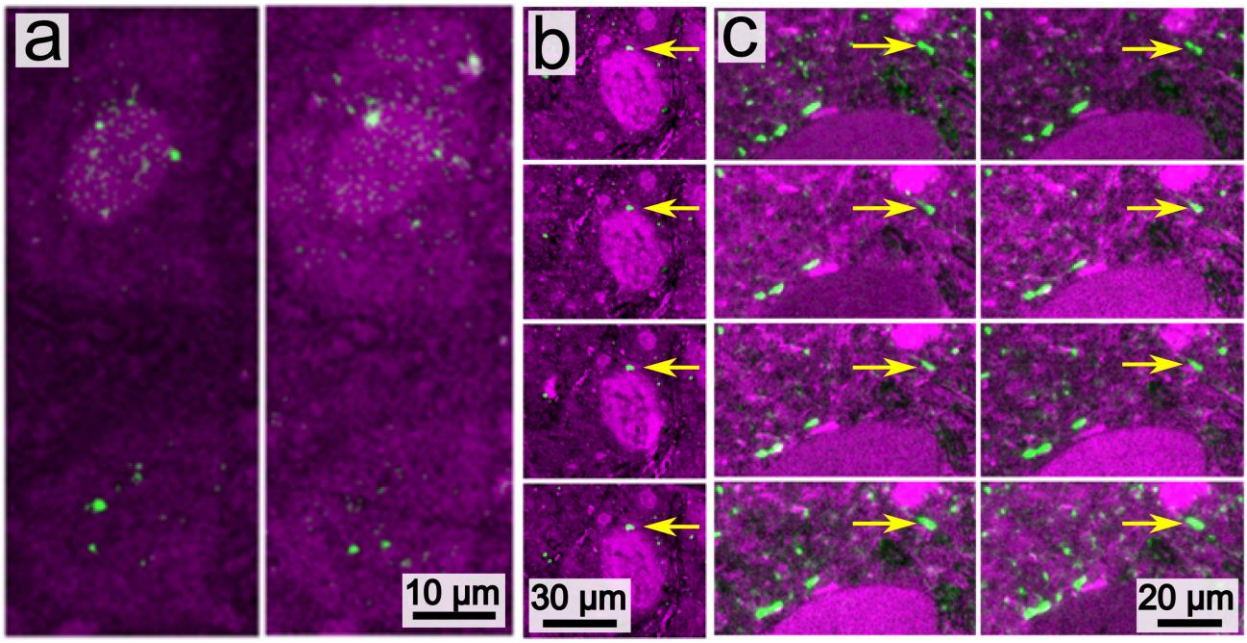

Figure 3. **Post-embedding antigenicity and/or fluorescence preservation of several neuroanatomical tracers.** (a) Two consecutive sections showing the survival of fluorescence of Fluorescein (green) in two adjacent retrogradely labeled neurons. (b) Four consecutive sections showing the survival of Fluorescein antigenicity in anterogradely labeled axons. The yellow arrows point to an axon that can be clearly followed over the consecutive sections. (c) 8 consecutive sections showing antigenicity survival of the fluorophore Alexa 488 in anterogradely labeled axons. The arrows indicate an axon that can be clearly followed over consecutive sections.

We have found that the anterograde tracer biotinylated dextran amine (BDA) exhibits excellent post-embedding antigenicity. We recommend using BDA with IHC rather than with avidin-biotin complexes (ABCs) for ultrastructure studies, for the following reasons: 1) In IHC there is no limitation of sample size beyond the limitation set by the penetration depth of reagents during the embedding protocol. In contrast, the ABC technique requires sections thinner than 60-70 µm to allow the reagents to penetrate wet section. 2) BDA antigens can be labeled either with fluorophores, electron dense gold particles, or both. Note that the labeling of BDA with black diaminobenzidin (DAB) deposit used in the ABC method often obstructs visualization of fine ultrastructural details, whereas immunogold staining is easily adjustable (gold particle size, antibody concentration, incubation duration, and silver enhancement duration) to visualize also surrounding structures of labeled cells. 3) IHC localizes BDA antigens accurately and does not co-label adjacent structures, as can be the case with the ABC method. 4) Using IHC, the

tissue can be immediately processed for embedding after microtomy, whereas the ABC procedure necessitates approximately half a day, which may compromise ultrastructure quality in EM.

2. Post-embedding multicolor imaging

Here we discuss various strategies for simultaneous visualization of different neuroanatomical tracers. The main obstacle towards achieving multicolor imaging is the fact that most commercially available antibodies against fluorophores are raised in the same species and are based on the same isotype (rabbit IgG, see Table 1), limiting IHC to only one primary antibody.

a. Custom antibodies

The first option that we have investigated is the elaboration of custom antibodies raised in other species than rabbit. The first question arising when producing antibodies is the choice between monoclonal and polyclonal antibodies. Polyclonal antibodies might in theory be less sensitive to 3D conformation alteration of their antigen as they recognize many antigenic epitopes, increasing the probability of recognizing an unmodified epitope. The development of polyclonal antibodies is usually faster, cheaper and more likely to succeed, compared with the development of monoclonal antibodies. A monoclonal antibody tends to be more sensitive to epitope alterations undergone during EM embedding. In our case, we have successfully used both monoclonal and polyclonal antibodies to target fluorophores and biotin. It should be noted that our targets (fluorophores and biotin) are so small that they probably exhibit a single epitope, similarly to digitonin or polysaccharides, e.g., chitin. It implies that monoclonal antibodies might work for our targets against which a polyclonal antibody has proven successful.

Custom antibodies were produced by the company Biotem (Apprieu, France) within roughly 4 months. We produced polyclonal antibodies raised in three rats against the fluorophore AlexaFluor 488. Given the small size (600 Da) and the known lack of immunogenicity of AlexaFluor 488, we decided to attach it to a keyhole limpet hemocyanin (KLH) protein to trigger an immune reaction with the result that the produced antibodies recognized specifically the target Alexa Fluor 488 but not the other fluorophores listed in Table 1. This custom antibody allowed us to increase the number of simultaneously usable fluorescent channels from 3 to 4 (Rabbit/Lucifer Yellow, Mouse/BDA, Goat/Texas Red and additionally Rat/488) in same-section multilabeling experiments.

b. Direct immunohistochemistry

Another strategy to achieve multicolor imaging is to use direct immunohistochemistry, that is, to use labeled primary antibodies. Such an approach allows simultaneous use of primary antibodies raised in the same species. However, direct labeling is achieved at the expense of labeling sensitivity, because available antigens at the surface of the ultrathin section are sparse. Moreover, the conjugation of primary antibodies with fluorophores might be laborious, prone to errors, and might alter the antibody binding properties. These drawbacks led us to not investigate this option.
We note, however, that we satisfactorily used fluorophore-labeled Streptavidin to label biotin. The relatively high sensitivity we achieved is probably due to the affinity of (strept)avidin to biotin, which is very high compared with affinities of classic antibodies. Streptavidin is also convenient because it is

readily commercially available with almost any fluorescent or electron-dense tag (fluorophore, gold, fluoronanogold), though gold-streptavidin has the downside of being a poor detection system (personal communication, B. Humbel).

3. Markers for post-embedding on-section immunohistochemistry

Many markers have been used in the past decades for visualization of antigens on ultrathin sections. Some are visible in the electron microscope, some in the fluorescence microscope, and some in both. We review in this section markers of interest for AT.

The most broadly used markers for on-section labeling were originally colloidal gold particles (63) coupled to either Immunoglobulin G (IgG) or protein A. Gold particles of different sizes can be used to distinguish various antigens (64) and are often silver enhanced to augment their visibility in the electron microscope.

Fluorescent markers used for on-section post-embedding labeling allow the visualization of antigens in conventional bright field (1,15,31,61,65) and new generation superresolution fluorescence microscopes. They provide a high versatility by allowing multichannel fluorescence imaging. Bright field microscopes provide a maximum resolution of 200 nm and superresolution microscopes a resolution down to 20 nm (66). The scanning speed we achieved with a modern motorized bright-field fluorescence microscope (Zeiss Axioobserver Z2) is about 30 s / 30 x 30 μm^2 with 4 fluorescence channels (1 s exposure time each) and a bright-field illumination channel.

Attempts to visualize antigens in both LM and EM lead to the development of dual markers such as fluoronanogold (67) and fluorophore-coupled colloidal gold. These markers consist of an immunoglobulin, decorated with both fluorophores and gold particles. We have successfully used colloidal gold Alexa 488 IgG (Life technologies, A-31561) as shown in Figures 6 and 7. A simple technique for antigen labelling in both LM and EM is sequential labeling with a fluorophore followed by gold particles (see (62) for interesting diverse variants). It should be noted that the close proximity of gold particles and fluorochromes can lead to a decrease in fluorescence (68). In this technique, the incubation time of the secondary antibody is split into two phases: the first one contains gold-labeled IgGs and the second one contains fluorophore-labeled IgGs. The binding affinity of gold-decorated IgGs tends to be smaller than that of fluorophore-decorated IgGs, therefore the gold labeling step takes place first and is usually longer (we obtained good results with 1 h gold followed by 30 min fluorophore labeling).

Quantum dots are relatively recent markers that have been introduced for their use in biology in (69) and popularized in (29,70). We have used quantum dots coupled to secondary antibodies for on-section immunolabeling and found that the labeling is satisfactory, as also reported in (71). That is, the relative brightness (as assessed by measuring signal intensity with constant imaging settings including exposure times) of quantum dots compared with classic fluorophores in our application is approximately the same as in (71). The main advantage of quantum dots for multilabeling experiments is their narrow emission spectrum along with a constant broad excitation spectrum. Appropriate emission filters (but not excitation filters) are required to visualize them.
It has been shown (72) that quantum dots are visible as electron dense aggregates in electron

micrographs. However, we did not succeed in obtaining a satisfactory signal, even after silver enhancement of variable duration. This limitation might come from the relatively strong background signal of our samples, which is not present in (72).

Cathodoluminescent materials exhibit the property of sending photons when hit by electrons. They are excellent candidate markers for CAT because the multidimensional fluorescence signals can be collected simultaneously with the EM signal inside the imaging chamber of a single microscope. Efforts are being undertaken to produce small, spectrally well separated cathodoluminescent probes that can be used as tags in conventional immunohistochemistry (73,74).

It is worth mentioning the existence of new dual markers called plasmonic fluorophores. They consist of gold nanoparticles and fluorophores being brought into one single construct. The electron dense compound has a rod shape, providing the interesting property of being distinguishable from gold particles in electron micrographs. However, we have not obtained any positive signal with anti-rabbit antibodies decorated with these markers.

Finally, we note that singlet oxygen generators (2) represent a powerful alternative method for visualizing endogenous proteins in the EM by generating singlet oxygen that catalyzes a polymerization reaction of diaminobenzidine into an electron dense product. However, currently we are not aware of successful extensions of the singlet oxygen method which yield high membrane contrast in the EM (but see (75) for the identification of molecularly defined synapse types).

D. Data acquisition

In this section, we detail imaging procedures for the two modalities. LM imaging consists of acquiring first a low-resolution overview and then of scanning all regions of interest at high resolution. EM imaging is performed on regions of interest identified in LM imagery.

1. LM

The first step in acquiring imaging data for correlative array tomography is to scan the samples in a light microscope (e.g. Axio Observer, Zeiss). This order is preferred because the electron beam readily quenches fluorescence (62). Moreover, prior LM scanning can greatly ease the EM operation afterwards, as shown later in this chapter.

First, we acquire a low resolution mosaic overview of the complete piece of wafer (typically with a 5x air objective) in the bright-field channel. This step takes only a few minutes for a wafer such as in Figure 2. We subsequently stitch the image tiles with the plugin “Grid/CollectionStitching” (76) available in Fiji. We wrote custom scripts for automating the recognition of ultrathin sections and for extraction of their locations, using only minimal user input for proper ribbon numbering. The result is shown in Figure 2 b,c, where the section numbers are overlaid with the sections. This section numbering provides the list of

coordinates of all sections on the wafer. At this point, we can manually define a region of interest (ROI) in one of the sections and automatically compute the corresponding ROIs on all other sections (yellow frames in Figure 2.b,c). These ROIs can be read by the light microscope software and are subsequently scanned automatically (in the example of the wafer in Figure 2, it would take a long time to manually define more than 550 regions to be scanned).

For high-resolution light-microscopic imaging, Fluoromount DAPI mounting medium (Life Techologies, S36939) is applied to the wafer, which is then covered with a 0.17 mm cover glass. Each ROI is scanned in the prescribed list of fluorescence channels, giving rise to a multi-dimensional mosaic that we stitch together using the tools freely available from the Smith laboratory ([1]http://smithlabsoftware.googlecode.com) and custom software scripts. We then align imagery from consecutive sections using the contrast-enhanced DAPI channel that provides ultrastructural details at low resolution (see Fig 4). This alignment is achieved with the TrakEM2 SIFT alignment algorithm "elastic mosaic alignment" (77), resulting in an aligned multidimensional image stack in which each stack section corresponds to one physical section.

2. EM

After LM imaging, the coverslip is removed, the wafer is washed during 2x10 minutes in double distilled water, and the sections undergo a silver enhancement treatment for 15 minutes (Nanoprobes, HQ Silver). Then, the wafer is washed again, treated with 1% uranyl acetate, followed by Reynold's lead citrate, and mounted on a 100 mm pin mount (Ted Pella, #16111) with carbon sticks (Ted Pella, #16084-3).
We used the secondary electron detector (Merlin, Zeiss) for fast navigation and for manual positioning of the electron beam on the large wafer. We acquired images at high magnification using the backscattered electron detector with a dwell time of 10 µs and at a resolution of 5 nm/pixel. Although we have not investigated thoroughly every possible parameter combination, we found the following parameters to be satisfactory: 2 keV acceleration voltage, 2 nA probe current, 1 keV energy threshold for the backscattered electron filter, and about 3.5 mm working distance.

a. Targeted EM imaging

The growing need for volumetric EM imaging necessitates image acquisition from large numbers of consecutive sections. Neuronal processes can be contained in thousands or tens of thousands of ultrathin sections because they exhibit cross-section areas that vary between a few dozens of nanometers up to a few dozens of micrometers (27), and because their length can grow up to the millimeter range. Such numbers call for automated electron microscope operation, as demonstrated in (78,79) for TEM and in (19) for SEM imaging.

A volume of 200 x 200 x 200 μm^3 necessitates scanning of 4000 consecutive 50-nm thick sections. To manually assign 4000 locations in the electron microscope would be extremely time consuming, therefore we wrote custom scripts that implement the following semi-automatic imaging workflow: 1) Define reference points in the LM coordinate system, which are also visible in the EM (corners of

sections, glass scribe markings on wafer). 2) A human operator either a) defines a reference region within one single ultrathin section (Fig 2,c yellow frame) or b) scrolls through the aligned multidimensional LM stack and selects a region of interest in each consecutive section. 3) The operator locates in the EM the reference points previously defined in the LM. 4) The custom script generates the locations and imaging parameters that are read by the EM scanning software (Atlas 4, Fibics Inc.).

We have worked so far with a simple manual identification in step 2) b), however, we seek to provide automated methods to extract objects of interest from the LM volumetric data. Thus, we foresee that the entire LM and EM image acquisition processes could be automated, after manual initialization.

3. Registration of LM and EM imagery

We combine the high versatility of LM with high resolution EM by overlay of LM and EM imagery. We have written custom scripts to allow automated registration in TrakEM2 of low resolution LM pictures and high resolution EM micrographs. Figure 4a gives an overview of the process, which is based on a few steps. **(1)** The stitched EM high-resolution image is down-sampled and contrast enhanced, Figure 4a, using the local contrast enhancement implemented in Fiji (80). **(2)** The DAPI channel of the low-resolution LM image is up-sampled and contrast enhanced. The contrasted LM and EM pictures are astonishingly similar. **(3)** The landmark-based registration algorithm implemented in TrakEM2 is applied (77) ([1]found under “Elastic registration Mosaic”). This algorithm computes an affine transformation that maps the DAPI channel to the down-sampled EM picture. **(4)** All fluorescence channels are then affine transformed according to the calculated transformation. The resulting registered DAPI and EM images are shown in Figure 4b and c. **(5)** Finally, the low resolution fluorescence channel pictures are up-sampled and overlaid with the original high resolution EM picture, Figure 4a.

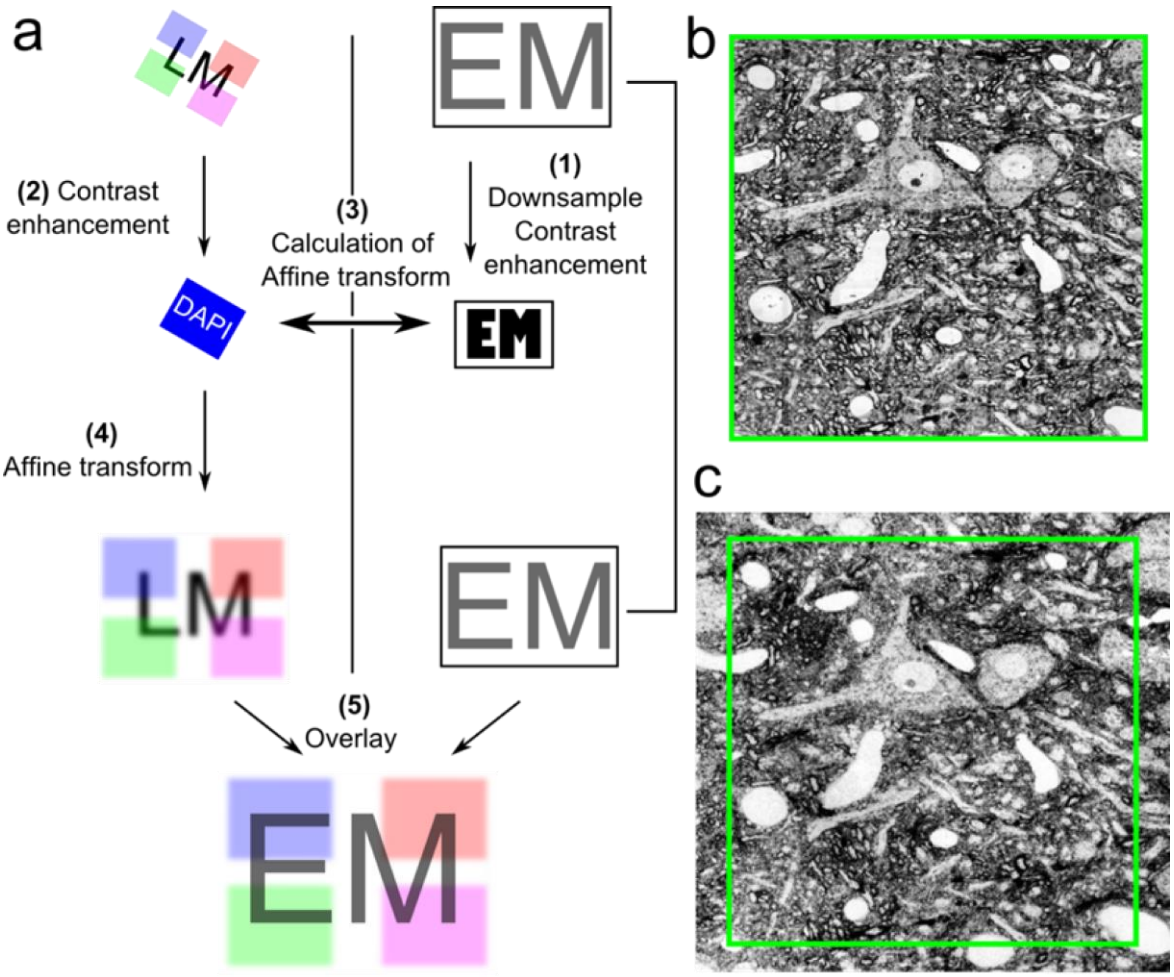

Figure 4. **Registration of low-resolution LM images to high-resolution EM micrographs.** (a) workflow of the registration procedure. The different steps are described in detail in the text. (b) Down-sampled and contrast-enhanced electron micrograph. (c) Up-sampled and contrast enhanced DAPI channel. The green frames in b and c highlight the same sample region as identified after the affine transformation.

To assess the accuracy of the registration, we labelled discrete structures (BDA-filled axons) on-section using immunohistochemical staining with fluoro-colloidal gold. The dual marker is visible both in the LM and in the EM and serves as a ground truth for the registration. In one ultrathin section, we manually selected 64 labels distributed over the entire section (in a regular 6 x 6 grid spanning a 350 x 350 μm^2 area, 2 labels per grid unit if available) and manually marked their positions in the LM and EM images. An example is provided in Figure 5. We then computed the registration error as the distance between the centers of mass of the two manually labeled regions. The root-mean square (RMS) error was 0.53 µm and the largest error was only 1.06 µm. This RMS error corresponds to the size of approximately 1.5 LM pixels (LM imaging has been performed with a 20x air objective, providing 0.32 µm/pixel). Our method is thus very accurate. Such high accuracy of the LM-EM registration allows us to easily navigate the sections and identify corresponding structures across the two modalities. However, some neuronal processes exhibit

much smaller dimensions than the maximum RMS error reported. Therefore, if the object is not dually labeled in the two modalities and that neighboring structures exhibit similar shapes, then the assignment of the LM label to its corresponding EM micrograph position cannot be unambiguously done within a single section. Reliable assignment would require the analysis of a sufficient number of consecutive sections in order to distinguish between the labeled process and neighboring similar ones. However, we never encountered an ambiguous case, we were always able to identify a dually labelled antigen of interest. We therefore conclude that our registration procedure is highly satisfactory.

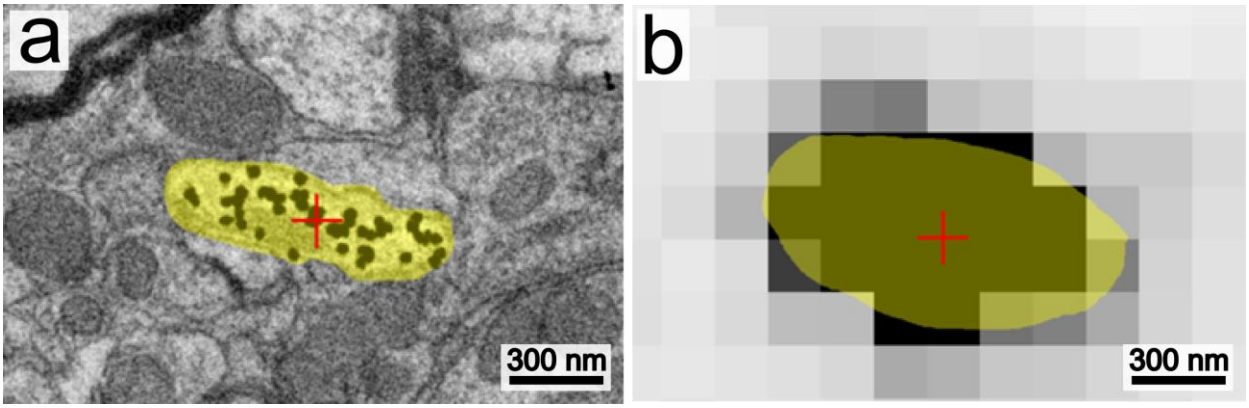

Figure 5. **Electron (a) and fluorescent light (b) micrographs showing a BDA-labeled axon marked by dual silver enhanced colloidal gold-Alexa 488.** The yellow regions have been manually drawn on the electron dense and fluorescent labels. The red crosses are the centers of mass of the yellow regions and have been used for the estimation of registration error. Scale bars 300 nm.

4. Integrated LM/EM

Note that another promising approach for correlative microscopy is to incorporate a high-numerical aperture light microscope into the SEM, Figure 6, (81,82), or to acquire cathodoluminescent signals within a SEM chamber stemming from new generation dual markers such as nanodiamonds excited by the electron beam (73). The registration step could be omitted thanks to direct acquisition of LM data inside the EM. However, as long as the LM acquisition time is much smaller than the EM acquisition time and as long as the tissue exhibits sufficient contrast in LM and EM imagery for automated accurate registration, we feel there is almost no inconvenience to first imaging the specimen in the LM and subsequently in the EM.

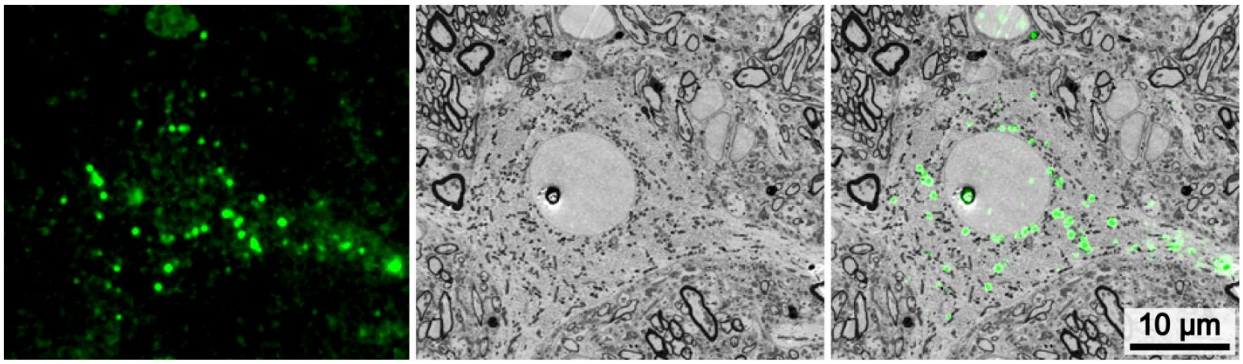

Figure 6. Simultaneous LM and EM imaging with an integrated LM/EM (samples imaged at Delmic BV, Delft, Netherlands with an integrated SECOM platform (LM 100x oil objective) and Quanta 250 FEG (FEI Company, Eindhoven)). Left: LM; Middle: EM; Right: LM/EM merge. Shown are motoneurons in the hypoglossal nucleus labeled during postembedding IHC with rabbit anti Alexa 488 and Alexa 546 anti rabbit. The tracer Alexa 488 was retrogradely transported from the syrinx of a zebra finch into hypoglossal motoneurons.

III. Application: Identification of projection neuron type in ultrastructural context

In the last part of this chapter we present an application that demonstrates the power of CAT applied to the analysis of brain circuits. Our animal model is the zebra finch, a songbird whose brain contains a set of discrete and interconnected brain nuclei dedicated to song production and learning. We injected BDA in a motor cortical region, the nucleus Robustus of the Arcopallium (RA) in order to anterogradely label descending axon terminals innervating motoneurons of the syringeal muscles, the muscles of the vocal organ. We also injected fluorescent tracers *in vivo* into different syringeal muscles, leading to retrograde labeling of motoneurons.

Figure 7 shows light and electron micrographs of two consecutive ultrathin sections taken from the termination site of labeled cortical axons. The secondary antibody used for labeling BDA on ultrathin sections was decorated with the dual marker Colloidal Gold-Alexa 488 (Life Technologies, A31561) and colloidal gold was enhanced with silver (Nanoprobes, HQ Silver).
As can be seen in the light micrographs of Fig. 7a,d, green signal (Alexa 488) present in one section is also present in the consecutive section. Note that the conventional processing of BDA-labeled axons with the ABC procedure produces electron-dense deposits within single neuronal processes. These deposits are visible consistently in every consecutive section (83,84). However, it is not known whether this consistent staining is due to the continuous presence of tracer molecules in every section, or due to the ABC reaction spreading and filling gaps in tracer-free portions of the neuronal processes. To resolve this question, the data in Fig. 7 (see also Fig. 8) suggest that tracer molecules are present in significant amount on every consecutive section. The density of gold particles in labeled structures is 8.2 d/µm^2, compared to 0.2 d/µm2 in non-labeled structures, demonstrating that post-embedding visualization of BDA by means of on-section immunohistochemistry is as sensitive as the conventional pre-embedding ABC procedure.

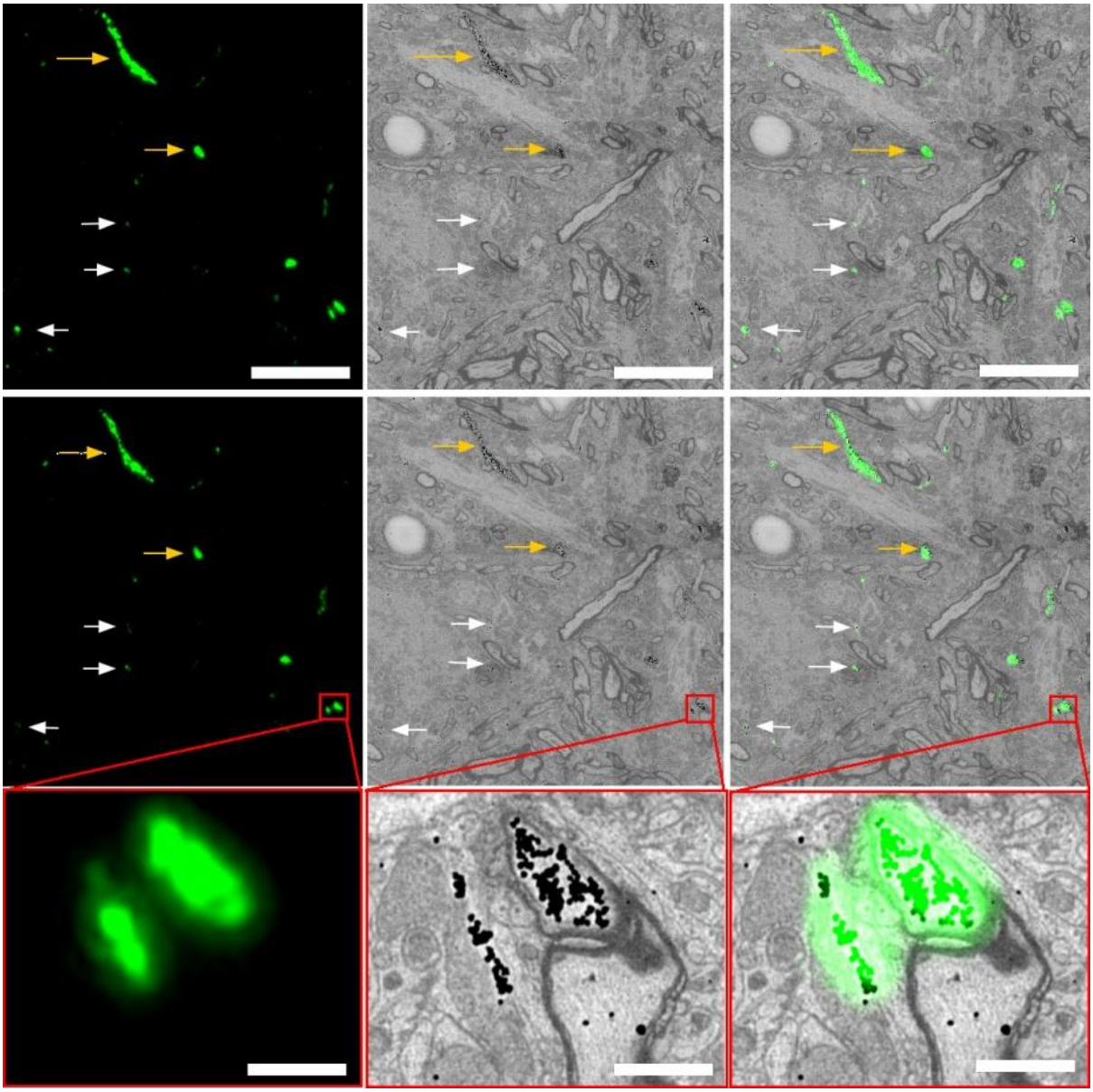

Figure 7. **Light (left), electron (middle) and overlay (right) images of labeled axon terminals in the hypoglossal nucleus originating from the cortical-like motor area RA.** Immunogold markers are indicated by arrows in the electron micrographs. (a,b) Low resolution overview of two consecutive 50 nm thick ultrathin sections. Consecutive sections serve as control for assessing the reliability of the fluorescence signal: The left parts in a and b are almost identical (arrows). Many labeled axons (arrows) are present and even very small ones are clearly visible (white arrows). (c) Higher magnification view of the region delineated by red in b, showing a labeled unmyelinated and a labeled myelinated axon. The two close axons are clearly distinguishable in the LM channel. The density of electron dense dots inside labeled axons is 8.2 d/μm^2, whereas it is 0.2 d/μm^2 in non-labeled areas. Single dots have an average diameter of 34 nm. Scale bars in a, b: 10 µm, in c: 1 µm.

Figure 8 shows light and electron micrographs of the hypoglossal (motor) nucleus containing motoneurons and descending cortical axons. Which muscle does a given cell body innervate? Thanks to the injection of different tracers into different muscles, we can retrieve the identity of the innervated cell body by overlaying the LM and EM pictures of this same region, Fig. 8b. In this Figure, the magenta label identifies Texas Red tracer molecules that had been injected in vivo into the Ventralis Syringealis (VS) vocal muscle. The retrograde tracer is present in cell bodies (cyan arrows in Fig. 8a), proximal dendrites (yellow arrows in Fig. 8a), and in some distal dendrites, as shown in Fig 8c. The green label localizes descending cortical axons as depicted in Figure 7. The overlay of the two modalities not only provides the identity of the structures, but it offers also a convenient way to browse the dataset. Namely, in TrakEM2 (85), a software optimized for the visualization of large image datasets, a user can quickly navigate and zoom into ROIs identified in LM imagery, thus greatly speeding up the analysis of the EM imagery.

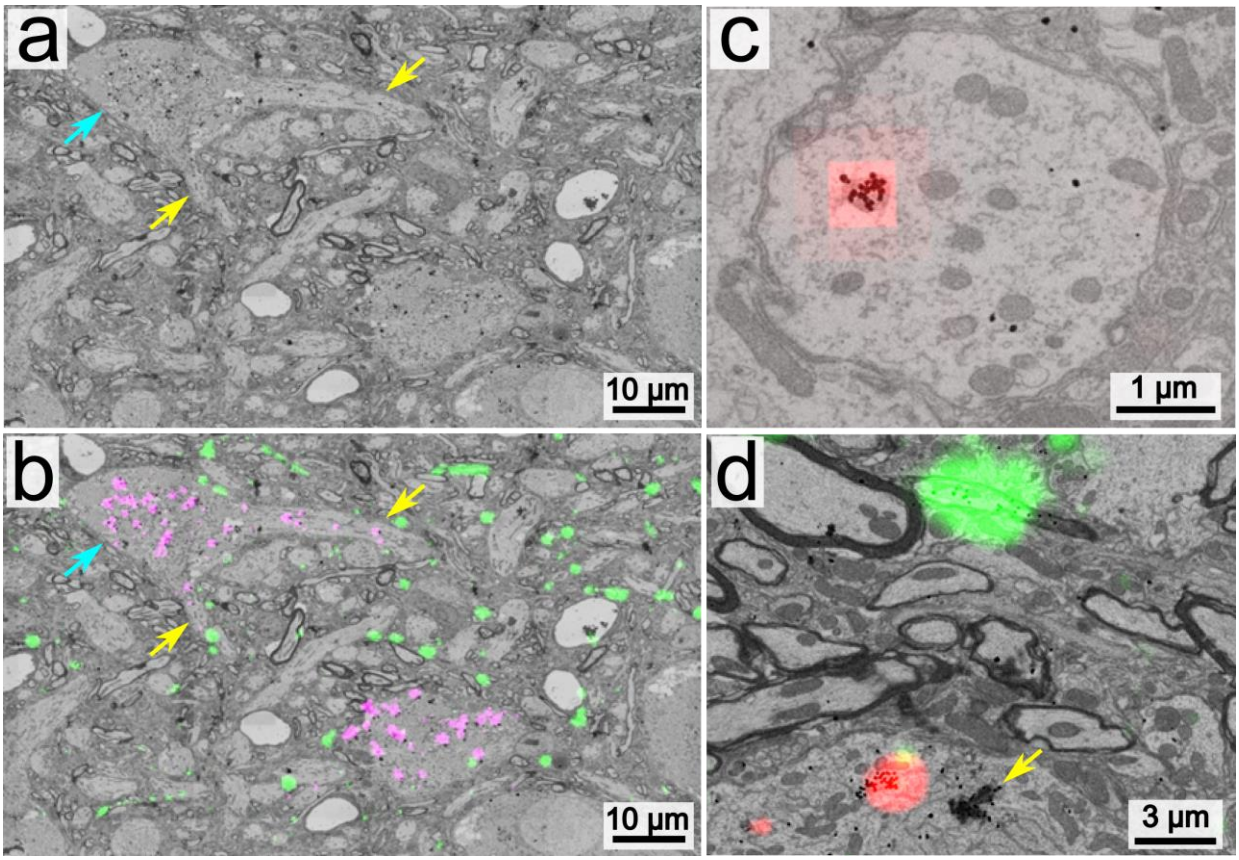

Figure 8. **Multicolor array tomography.** (a) Large EM field of view of part of the avian vocal motor nucleus (hypoglossal nucleus). Part of a cell body is visible on the top left, with two dendritic processes extruding from it (marked with yellow arrows). (b) Overlay of EM and LM imagery. The magenta label indicates presence of Texas Red molecules, and the green label indicates presence of biotin molecules. (c) A motoneuron dendrite containing a lysosome filled with Texas red molecules, as revealed by IHC. Sequential gold labeling followed by fluorophore labeling reveals label simultaneously visible in the EM (black, electron-dense dots) and in the LM (red, fluorescent signal). The LM channel was acquired with an objective with lower resolution than usual, yielding pixelated signal and accentuating the discrepancy

between LM and EM resolution). (d) ROI showing the close apposition of labeled structures. A cortical axon is labeled in green (BDA) and a motoneuron soma is labeled in red (Texas Red). Both axons and motoneurons are also labeled with gold (black dots). The yellow arrow shows an artifact of silver enhancement.

Conclusion

In this chapter we have introduced correlative array tomography (CAT), a correlative light and electron microscopy technique. We hope to have convincingly demonstrated that CAT enhances the observation of ultrastructural details in EM imagery by harnessing the power of multidimensional light microscopy. CAT is driven by our desire of attaining biological understanding by relating structure to function. We have detailed the sample preparation and visualization procedures required for CAT. Currently, CAT works well with chemical fluorophores but not yet with fluorescent proteins or endogenous proteins. To be able to clearly visualize endogenous molecules in their ultrastructural context including high membrane contrast would constitute an immense breakthrough for biological structure-function studies.

Acknowledgements

We thank Bruno Humbel and Roland Fleck for helpful comments on this chapter.
This work was supported by the Swiss National Science Foundation (grant 31003A_127024) and by the European Research Council under the European Community's Seventh Framework Programme (FP7/2007-2013 / ERC Grant AdG 268911). The authors acknowledge support from the Scientific Center for Optical and Electron Microscopy ScopeM of the Swiss Federal Institute of Technology ETHZ.

References

1. Micheva KD, Smith SJ. Array tomography: a new tool for imaging the molecular architecture and ultrastructure of neural circuits. Neuron [Internet]. 2007 Jul;55(1):25–36. Available from: http://dx.doi.org/10.1016/j.neuron.2007.06.014
2. Shu X, Lev-Ram V, Deerinck TJ, Qi Y, Ramko EB, Davidson MW, et al. A genetically encoded tag for correlated light and electron microscopy of intact cells, tissues, and organisms. PLoS Biol [Internet]. 2011 Apr;9(4):e1001041. Available from: http://dx.doi.org/10.1371/journal.pbio.1001041
3. Rostaing P, Weimer RM, Jorgensen EM, Triller A, Bessereau J-L. Preservation of Immunoreactivity and Fine Structure of Adult C. elegans Tissues Using High-pressure Freezing. J Histochem Cytochem [Internet]. 2004;52(1):1–12. Available from: http://jhc.sagepub.com/content/52/1/1.abstract
4. Grabenbauer M, Geerts WJC, Fernadez-Rodriguez J, Hoenger A, Koster AJ, Nilsson T. Correlative microscopy and electron tomography of GFP through photooxidation. Nat Meth [Internet]. 2005 Nov;2(11):857–62. Available from: http://dx.doi.org/10.1038/nmeth806
5. Fiserova J, Goldberg M. Immunoelectron Microscopy of Cryofixed Freeze-Substituted Saccharomyces cerevisiae. In: Schwartzbach SD, Osafune T, editors. Immunoelectron

Microscopy [Internet]. Humana Press; 2010. p. 191–204. Available from: http://dx.doi.org/10.1007/978-1-60761-783-9_15

6. Salio C, Lossi L, Merighi A. Combined Light and Electron Microscopic Visualization of Neuropeptides and Their Receptors in Central Neurons. In: Merighi A, editor. Neuropeptides [Internet]. Humana Press; 2011. p. 57–71. Available from: http://dx.doi.org/10.1007/978-1-61779-310-3_3
7. Morgan JL, Lichtman JW. Why not connectomics? Nat Meth [Internet]. Nature Publishing Group, a division of Macmillan Publishers Limited. All Rights Reserved.; 2013 Jun;10(6):494–500. Available from: http://dx.doi.org/10.1038/nmeth.2480
8. Newman GR, Jasani B, Williams ED. A simple post-embedding system for the rapid demonstration of tissue antigens under the electron microscope. Histochem J [Internet]. Kluwer Academic Publishers; 1983;15(6):543–55. Available from: http://dx.doi.org/10.1007/BF01954145
9. Micheva KD, Busse B, Weiler NC, O'Rourke N, Smith SJ. Single-synapse analysis of a diverse synapse population: proteomic imaging methods and markers. Neuron [Internet]. 2010 Nov;68(4):639–53. Available from: http://dx.doi.org/10.1016/j.neuron.2010.09.024
10. Busse B, Smith S. Automated Analysis of a Diverse Synapse Population. PLoS Comput Biol [Internet]. Public Library of Science; 2013;9(3):e1002976. Available from: http://dx.doi.org/10.1371/journal.pcbi.1002976
11. Kopeikina KJ, Carlson GA, Pitstick R, Ludvigson AE, Peters A, Luebke JI, et al. Tau Accumulation Causes Mitochondrial Distribution Deficits in Neurons in a Mouse Model of Tauopathy and in Human Alzheimer's Disease Brain. Am J Pathol [Internet]. 2011 Oct;179(4):2071–82. Available from: http://www.sciencedirect.com/science/article/pii/S0002944011006559
12. Allen NJ, Bennett ML, Foo LC, Wang GX, Chakraborty C, Smith SJ, et al. Astrocyte glypicans 4 and 6 promote formation of excitatory synapses via GluA1 AMPA receptors. Nature [Internet]. Nature Publishing Group, a division of Macmillan Publishers Limited. All Rights Reserved.; 2012 Jun;486(7403):410–4. Available from: http://dx.doi.org/10.1038/nature11059
13. Micheva KD, Bruchez MP. The gain in brain: novel imaging techniques and multiplexed proteomic imaging of brain tissue ultrastructure. Curr Opin Neurobiol [Internet]. 2012 Feb;22(1):94–100. Available from: http://dx.doi.org/10.1016/j.conb.2011.08.004
14. Collman XF, Buchanan J, Phend KD, Micheva KD, Weinberg RJ, Smith SJ. Mapping Synapses by Conjugate Light-Electron Array Tomography. 2015;35(14):5792–807.
15. Oberti D, Kirschmann MA, Hahnloser R. Correlative microscopy of densely labeled projection neurons using neural tracers. Front Neuroanat. 2010;4(0).
16. Oberti D, Kirschmann MA, Hahnloser RHR. Projection neuron circuits resolved using correlative array tomography. Front Neurosci [Internet]. 2011;5(0). Available from: http://www.frontiersin.org/Journal/Abstract.aspx?f=55&name=neuroscience&ART_DOI=10.3389/fnins.2011.00050
17. Hayworth KJ, Kasthuri N, Schalek R, Lichtman JW. Automating the Collection of Ultrathin Serial Sections for Large Volume TEM Reconstructions. Microsc Microanal

[Internet]. 2006;12(Supplement S02):86–7. Available from: http://dx.doi.org/10.1017/S1431927606066268

18. Micheva KD, Busse B, Weiler NC, O'Rourke N, Smith SJ. Single-synapse analysis of a diverse synapse population: proteomic imaging methods and markers. Neuron [Internet]. Elsevier Inc.; 2010 Nov 18 [cited 2013 Nov 11];68(4):639–53. Available from: http://www.pubmedcentral.nih.gov/articlerender.fcgi?artid=2995697&tool=pmcentrez&rendertype=abstract

19. Terasaki M, Shemesh T, Kasthuri N, Klemm RW, Schalek R, Hayworth KJ, et al. Stacked Endoplasmic Reticulum Sheets Are Connected by Helicoidal Membrane Motifs. Cell [Internet]. 2013;154(2):285–96. Available from: http://www.sciencedirect.com/science/article/pii/S0092867413007708

20. Hayworth KJ, Morgan JL, Schalek R, Berger DR, Hildebrand DGC, Lichtman JW. Imaging ATUM ultrathin section libraries with WaferMapper: a multi-scale approach to EM reconstruction of neural circuits. Front Neural Circuits [Internet]. 2014 Jan [cited 2014 Aug 31];8(June):68. Available from: http://www.pubmedcentral.nih.gov/articlerender.fcgi?artid=4073626&tool=pmcentrez&rendertype=abstract

21. Van Damme D, Coutuer S, De Rycke R, Bouget F-Y, Inz D, Geelen D. Somatic Cytokinesis and Pollen Maturation in Arabidopsis Depend on TPLATE, Which Has Domains Similar to Coat Proteins. Plant Cell Online [Internet]. 2006;18(12):3502–18. Available from: http://www.plantcell.org/content/18/12/3502.abstract

22. Anderson JR, Jones BW, Yang J-H, Shaw M V, Watt CB, Koshevoy P, et al. A computational framework for ultrastructural mapping of neural circuitry. PLoS Biol [Internet]. 2009 Mar;7(3):e1000074. Available from: http://dx.doi.org/10.1371/journal.pbio.1000074

23. Anderson JR, Jones BW, Watt CB, Shaw M V, Yang J-H, Demill D, et al. Exploring the retinal connectome. Mol Vis [Internet]. Emory University; 2011;17(41):355–79. Available from: http://www.pubmedcentral.nih.gov/articlerender.fcgi?artid=3036568&tool=pmcentrez&rendertype=abstract

24. Cardona A, Saalfeld S, Preibisch S, Schmid B, Cheng A, Pulokas J, et al. An integrated micro- and macroarchitectural analysis of the Drosophila brain by computer-assisted serial section electron microscopy. PLoS Biol [Internet]. 2010;8(10). Available from: http://dx.doi.org/10.1371/journal.pbio.1000502

25. Knott G, Marchman H, Wall D, Lich B. Serial Section Scanning Electron Microscopy of Adult Brain Tissue Using Focused Ion Beam Milling. J Neurosci [Internet]. 2008;28(12):2959–64. Available from: http://www.jneurosci.org/content/28/12/2959.short

26. Briggman KL, Helmstaedter M, Denk W. Wiring specificity in the direction-selectivity circuit of the retina. Nature [Internet]. Nature Publishing Group, a division of Macmillan Publishers Limited. All Rights Reserved.; 2011 Mar;471(7337):183–8. Available from: http://dx.doi.org/10.1038/nature09818

27. Helmstaedter M. Cellular-resolution connectomics: challenges of dense neural circuit reconstruction. Nat Meth [Internet]. Nature Publishing Group, a division of Macmillan

Publishers Limited. All Rights Reserved.; 2013 Jun;10(6):501–7. Available from: http://dx.doi.org/10.1038/nmeth.2476

28. Brown E, Mantell J, Carter D, Tilly G, Verkade P. Studying intracellular transport using high-pressure freezing and Correlative Light Electron Microscopy. Semin Cell Dev Biol [Internet]. 2009;20(8):910–9. Available from: http://www.sciencedirect.com/science/article/pii/S1084952109001530

29. Giepmans BNG, Deerinck TJ, Smarr BL, Jones YZ, Ellisman MH. Correlated light and electron microscopic imaging of multiple endogenous proteins using Quantum dots. Nat Methods [Internet]. 2005 Oct;2(10):743–9. Available from: http://dx.doi.org/10.1038/nmeth791

30. MCDONALD KL. A review of high-pressure freezing preparation techniques for correlative light and electron microscopy of the same cells and tissues. J Microsc [Internet]. Blackwell Publishing Ltd; 2009;235(3):273–81. Available from: http://dx.doi.org/10.1111/j.1365-2818.2009.03218.x

31. Watanabe S, Punge A, Hollopeter G, Willig KI, Hobson RJ, Davis MW, et al. Protein localization in electron micrographs using fluorescence nanoscopy. Nat Methods [Internet]. 2011 Jan;8(1):80–4. Available from: http://dx.doi.org/10.1038/nmeth.1537

32. Sonomura T, Furuta T, Nakatani I, Yamamoto Y, Unzai T, Matsuda W, et al. Correlative Analysis of Immunoreactivity in Confocal Laser-Scanning Microscopy and Scanning Electron Microscopy with Focused Ion Beam Milling. Front Neural Circuits [Internet]. 2013;7(26). Available from: http://www.frontiersin.org/neural_circuits/10.3389/fncir.2013.00026/abstract

33. Canty AJ, Huang L, Jackson JS, Little GE, Knott G, Maco B, et al. In-vivo single neuron axotomy triggers axon regeneration to restore synaptic density in specific cortical circuits. Nat Commun [Internet]. Nature Publishing Group, a division of Macmillan Publishers Limited. All Rights Reserved.; 2013 Jun;4:- – . Available from: http://dx.doi.org/10.1038/ncomms3038

34. Bock DD, Lee W-CA, Kerlin AM, Andermann ML, Hood G, Wetzel AW, et al. Network anatomy and in vivo physiology of visual cortical neurons. Nature [Internet]. 2011 Mar;471(7337):177–82. Available from: http://dx.doi.org/10.1038/nature09802

35. Maco B, Holtmaat A, Cantoni M, Kreshuk A, Straehle CN, Hamprecht FA, et al. Correlative <italic>In Vivo</italic> 2 Photon and Focused Ion Beam Scanning Electron Microscopy of Cortical Neurons. PLoS One [Internet]. Public Library of Science; 2013;8(2):e57405. Available from: http://dx.doi.org/10.1371/journal.pone.0057405

36. Punge A, Rizzoli SO, Jahn R, Wildanger JD, Meyer L, Schönle A, et al. 3D reconstruction of high-resolution STED microscope images. Microsc Res Tech [Internet]. Wiley Subscription Services, Inc., A Wiley Company; 2008;71(9):644–50. Available from: http://dx.doi.org/10.1002/jemt.20602

37. Nanguneri S, Flottmann B, Horstmann H, Heilemann M, Kuner T. Three-dimensional, tomographic super-resolution fluorescence imaging of serially sectioned thick samples. PLoS One [Internet]. 2012;7(5):e38098. Available from: http://dx.doi.org/10.1371/journal.pone.0038098

38. Muehlfeld C, Richter J. High-pressure freezing and freeze substitution of rat myocardium for immunogold labeling of connexin 43. Anat Rec Part A Discov Mol Cell Evol Biol [Internet]. Wiley Subscription Services, Inc., A Wiley Company; 2006;288A(10):1059–67. Available from: http://dx.doi.org/10.1002/ar.a.20380

39. Ghrebi SS, Owen GR, Brunette DM. Triton X-100 Pretreatment of LR-white Thin Sections Improves Immunofluorescence Specificity and Intensity. Microsc Res Tech [Internet]. Wiley Subscription Services, Inc., A Wiley Company; 2007;70(7):555–62. Available from: http://dx.doi.org/10.1002/jemt.20422

40. Stierhof Y-D, Kasmi F El. Strategies to improve the antigenicity, ultrastructure preservation and visibility of trafficking compartments in Arabidopsis tissue. Eur J Cell Biol [Internet]. 2010;89(2–3):285–97. Available from: http://www.sciencedirect.com/science/article/pii/S0171933509003677

41. Heck WL, Slusarczyk A, Basaraba AM, Schweitzer L. Subcellular localization of GABA receptors in the central nervous system using post-embedding immunohistochemistry. Brain Res Brain Res Protoc [Internet]. 2002 Jun;9(3):173–80. Available from: http://www.ncbi.nlm.nih.gov/pubmed/12113777

42. Luby-Phelps K, Ning G, Fogerty J, Besharse JC. Visualization of Identified GFP-expressing Cells by Light and Electron Microscopy. J Histochem Cytochem [Internet]. 2003;51(3):271–4. Available from: http://jhc.sagepub.com/content/51/3/271.abstract

43. Kraehenbuhl JP andJD J. Localization of intracellular antigens using immunoelectron microscopy. Electron Microsc Cytochem. 1973;181192.

44. Paez-Segala MG, Sun MG, Shtengel G, Viswanathan S, Baird M a, Macklin JJ, et al. Fixation-resistant photoactivatable fluorescent proteins for CLEM. Nat Methods [Internet]. 2015 Jan 12;(November 2014). Available from: http://www.nature.com/doifinder/10.1038/nmeth.3225

45. Viswanathan S, Williams ME, Bloss EB, Stasevich TJ, Speer CM, Nern A, et al. High-performance probes for light and electron microscopy. Nat Methods [Internet]. 2015;(April). Available from: http://www.nature.com/doifinder/10.1038/nmeth.3365

46. Mikula S, Denk W. High-resolution whole-brain staining for electron microscopic circuit reconstruction. Nat Methods [Internet]. 2015;(April). Available from: http://www.nature.com/doifinder/10.1038/nmeth.3361

47. Hua Y, Laserstein P, Helmstaedter M. Large-volume en-bloc staining for electron microscopy-based connectomics. Nat Commun [Internet]. Nature Publishing Group; 2015;6:7923. Available from: http://www.nature.com/doifinder/10.1038/ncomms8923

48. Tapia JC, Kasthuri N, Hayworth KJ, Schalek R, Lichtman JW, Smith SJ, et al. High-contrast en bloc staining of neuronal tissue for field emission scanning electron microscopy. Nat Protoc [Internet]. Nature Publishing Group, a division of Macmillan Publishers Limited. All Rights Reserved.; 2012 Feb;7(2):193–206. Available from: http://dx.doi.org/10.1038/nprot.2011.439

49. Hayat MA. Glutaraldehyde: role in electron microscopy. Micron Microsc Acta. 1986;17:115–35.

50. Glauert, AM and Lewis P. Biological Specimen Preparation for Transmission Electron

Microscopy [Internet]. Princeton University Press. 1999. 316 p. Available from: http://press.princeton.edu/titles/6666.html

51. Skepper JN, Powell JM. Ultrastructural immunochemistry. Cold Spring Harb Protoc. 2008;3:1–6.

52. Phend KD, Rustioni a, Weinberg RJ. An osmium-free method of epon embedment that preserves both ultrastructure and antigenicity for post-embedding immunocytochemistry. J Histochem Cytochem. 1995;43:283–92.

53. Terzakis J a. Uranyl acetate, a stain and a fixative. J Ultrastruct Res. 1968;22:168–84.

54. Berryman M a, Rodewald RD. An enhanced method for post-embedding immunocytochemical staining which preserves cell membranes. J Histochem Cytochem. 1990;38:159–70.

55. Hayat MA. Immunogold-silver staining: principles, methods, and applications. CRC Press; 1995.

56. Fetter RD, Myers EW, Chklovskii DB, Svoboda K, Harris TD, Isaac JTR, et al. Thalamocortical input onto layer 5 pyramidal neurons measured using quantitative large-scale array tomography. 2013;7(November):1–16.

57. Horstmann H, Kaerber C, Saetzler K, Aydin D, Kuner T. Serial Section Scanning Electron Microscopy (S(3)EM) on Silicon Wafers for Ultra-Structural Volume Imaging of Cells and Tissues. PLoS One [Internet]. 2012;7(4):e35172. Available from: http://dx.doi.org/10.1371/journal.pone.0035172

58. Blumer MJF, Gahleitner P, Narzt T, Handl C, Ruthensteiner B. Ribbons of semithin sections: an advanced method with a new type of diamond knife. J Neurosci Methods. 2002 Oct;120(1):11–6.

59. Micheva KD, O'Rourke N, Busse B, Smith SJ. Array tomography: production of arrays. Cold Spring Harb Protoc. 2010 Nov;2010(11):pdb.prot5524.

60. Spomer W, Hofmann A, Wacker I, Ness L, Brey P, Schroder RR, et al. Advanced substrate holder and multi-axis manipulation tool for ultramicrotomy. Microsc Microanal [Internet]. 2015;21(Supplement S3):1277–8. Available from: http://journals.cambridge.org/article_S1431927615007175

61. Schwarz H, Humbel B. Correlative Light and Electron Microscopy Using Immunolabeled Resin Sections. In: Kuo J, editor. Electron Microscopy [Internet]. Humana Press; 2007. p. 229–56. Available from: http://dx.doi.org/10.1007/978-1-59745-294-6_12

62. Fabig G, Kretschmar S, Weiche S, Eberle D, Ader M, Kurth T. Chapter 5 - Labeling of Ultrathin Resin Sections for Correlative Light and Electron Microscopy. In: Müller-Reichert T, Verkade P, editors. Correlative Light and Electron MIcroscopy [Internet]. Academic Press; 2012. p. 75–93. Available from: http://www.sciencedirect.com/science/article/pii/B9780124160262000054

63. Robenek H. Colloidal gold: Principles, methods, and applications vols. I and II (vol. III in preparation) Edited by M. A. Hayat Academic Press, Inc., New York, 1989 ISBN 0–12–333927–8, Vol. I, 536 pages ISBN 0–12–333928–6, Vol. II, 484 pages. Scanning [Internet]. Wiley Periodicals, Inc.; 1990;12(4):244. Available from: http://dx.doi.org/10.1002/sca.4950120410

64. Wang BL, Larsson LI. Simultaneous demonstration of multiple antigens by indirect immunofluorescence or immunogold staining. Novel light and electron microscopical double and triple staining method employing primary antibodies from the same species. Histochemistry. 1985;83(1):47–56.

65. Schwarz H. Immunolabeling of ultrathin sections for fluorescence and electron microscopy. Electron Microsc. 1994;Vol. 3:255256.

66. Huang B, Bates M, Zhuang X. Super-resolution fluorescence microscopy. Annu Rev Biochem. 2009;78:993–1016.

67. Takizawa T, Suzuki K, Robinson JM. Correlative Microscopy Using FluoroNanogold on Ultrathin Cryosections: Proof of Principle. J Histochem Cytochem [Internet]. 1998;46(10):1097–102. Available from: http://jhc.sagepub.com/content/46/10/1097.abstract

68. Humbel BM, De Jong MDM, Müller WH, Verkleij AJ. Pre-embedding immunolabeling for electron microscopy: An evaluation of permeabilization methods and markers. Microsc Res Tech. 1998;42:43–58.

69. Chan WCW, Nie S. Quantum Dot Bioconjugates for Ultrasensitive Nonisotopic Detection. Science (80-) [Internet]. 1998;281(5385):2016–8. Available from: http://www.sciencemag.org/content/281/5385/2016.abstract

70. Michalet X, Pinaud FF, Bentolila LA, Tsay JM, Doose S, Li JJ, et al. Quantum Dots for Live Cells, in Vivo Imaging, and Diagnostics. Science (80-) [Internet]. 2005;307(5709):538–44. Available from: http://www.sciencemag.org/content/307/5709/538.abstract

71. Nisman R, Dellaire G, Ren Y, Li R, Bazett-Jones DP. Application of quantum dots as probes for correlative fluorescence, conventional, and energy-filtered transmission electron microscopy. J Histochem Cytochem. 2004 Jan;52(1):13–8.

72. Dahan M, Laevi S, Luccardini C, Rostaing P, Riveau B, Triller A. Diffusion dynamics of glycine receptors revealed by single-quantum dot tracking. Science (80-) [Internet]. 2003 Oct;302(5644):442–5. Available from: http://dx.doi.org/10.1126/science.1088525

73. Glenn DR, Zhang H, Kasthuri N, Schalek R, Lo PK, Trifonov AS, et al. Correlative light and electron microscopy using cathodoluminescence from nanoparticles with distinguishable colours. Sci Rep [Internet]. 2012;2:865. Available from: http://dx.doi.org/10.1038/srep00865

74. Zhang H, Aharonovich I, Glenn DR, Schalek R, Magyar AP, Lichtman JW, et al. Silicon-vacancy color centers in nanodiamonds: Cathodoluminescence imaging markers in the near infrared. Small. 2014;10:1908–13.

75. Atasoy D, Betley JN, Li W-P, Su HH, Sertel SM, Scheffer LK, et al. A genetically specified connectomics approach applied to long-range feeding regulatory circuits. Nat Neurosci [Internet]. 2014;17:1830–9. Available from: http://www.ncbi.nlm.nih.gov/pubmed/25362474

76. Preibisch S, Saalfeld S, Tomancak P. Globally optimal stitching of tiled 3D microscopic image acquisitions. Bioinformatics [Internet]. 2009;25(11):1463–5. Available from: http://bioinformatics.oxfordjournals.org/content/25/11/1463.abstract

77. Saalfeld S, Fetter R, Cardona A, Tomancak P. Elastic volume reconstruction from series of ultra-thin microscopy sections. Nat Meth [Internet]. Nature Publishing Group, a division of Macmillan Publishers Limited. All Rights Reserved.; 2012 Jul;9(7):717–20. Available from: http://dx.doi.org/10.1038/nmeth.2072

78. Potter CS, Chu H, Frey B, Green C, Kisseberth N, Madden TJ, et al. Leginon: a system for fully automated acquisition of 1000 electron micrographs a day. Ultramicroscopy [Internet]. 1999;77(3–4):153–61. Available from: http://www.sciencedirect.com/science/article/pii/S0304399199000431

79. Suloway C, Pulokas J, Fellmann D, Cheng A, Guerra F, Quispe J, et al. Automated molecular microscopy: the new Leginon system. J Struct Biol [Internet]. 2005 Jul;151(1):41–60. Available from: http://dx.doi.org/10.1016/j.jsb.2005.03.010

80. Zuiderveld K. Graphics gems IV. In: Heckbert PS, editor. San Diego, CA, USA: Academic Press Professional, Inc.; 1994. p. 474–85. Available from: http://dl.acm.org/citation.cfm?id=180895.180940

81. Liv N, Zonnevylle AC, Narvaez AC, Effting APJ, Voorneveld PW, Lucas MS, et al. Simultaneous Correlative Scanning Electron and High-NA Fluorescence Microscopy. PLoS One [Internet]. 2013;8(2):e55707. Available from: http://dx.doi.org/10.1371/journal.pone.0055707

82. ZONNEVYLLE AC, VAN TOL RFC, LIV N, NARVAEZ AC, EFFTING APJ, KRUIT P, et al. Integration of a high-NA light microscope in a scanning electron microscope. J Microsc [Internet]. 2013;n/a – n/a. Available from: http://dx.doi.org/10.1111/jmi.12071

83. da Costa NM, Martin KAC. Selective targeting of the dendrites of corticothalamic cells by thalamic afferents in area 17 of the cat. J Neurosci [Internet]. 2009 Nov;29(44):13919–28. Available from: http://dx.doi.org/10.1523/JNEUROSCI.2785-09.2009

84. Lang S, Drouvelis P, Tafaj E, Bastian P, Sakmann B. Fast extraction of neuron morphologies from large-scale SBFSEM image stacks. J Comput Neurosci [Internet]. 2011 Nov;31(3):533–45. Available from: http://dx.doi.org/10.1007/s10827-011-0316-1

85. Cardona A, Saalfeld S, Schindelin J, Arganda-Carreras I, Preibisch S, Longair M, et al. TrakEM2 Software for Neural Circuit Reconstruction. PLoS One [Internet]. Public Library of Science; 2012;7(6):e38011. Available from: http://dx.doi.org/10.1371/journal.pone.0038011

Chapter 2

MagC: Magnetic Augmentation and Collection of Ultrathin Sections for Volumetric Correlative Light and Electron Microscopy

MagC

Magnetic Augmentation and Collection of Ultrathin Sections for Volumetric Correlative Light and Electron Microscopy

Thomas Templier

Institute of Neuroinformatics
Neuroscience Center Zurich
University of Zurich and ETH Zurich

thomas.templier2@gmail.com

I. Abstract

We upgrade Array Tomography with a method for collecting hundreds of consecutive ultrathin sections from a resin-embedded sample directly onto flat substrates at high packing density. Resin-embedded tissue samples are augmented with resin containing magnetic and fluorescent particles. Magnetic particles allow damage-free remote magnetic actuation, dense agglomeration and deposition of freely floating sections onto a substrate previously immersed in the large bath of a diamond knife. Post-collection retrieval of the serial section order is achieved with electron microscopy or with light microscopy of the fluorescent particles. We show volumetric correlative light and electron microscopy imagery of brain tissue suitable for cellular-resolution connectomic analysis. We predict that our section collection technique will have wide-ranging applications in volumetric ultrastructural research such as cellular-resolution connectomics and volumetric correlative light and electron microscopy.

II. Introduction

Cellular-resolution connectomics, a field of neuroscience, is the current driver for the development of sample sectioning [1]–[3] and volume electron microscopy (EM) [4]–[13] technologies. The field seeks to acquire larger volumes of brain tissue, at higher throughput, with increased isotropicity and with the ability to correlate EM imagery with fluorescent light (LM) or cathodoluminescent microscopy.

We briefly review the existing sample preparation and imaging technologies, focusing particularly on the correlative aspect before introducing our technique, which will be particularly well suited for volumetric correlative imaging.

A. FIBSEM and SBFSEM

The focused ion beam scanning EM (FIBSEM) and serial block face scanning EM (SBFSEM) technologies offer volumetric EM imaging of small samples (up to ~100 µm x 100 µm x 100 µm) with high isotropicity (z-resolution down to a few nanometers) and relatively large samples (up to ~500 µm x 500 µm x 500 µm) with good isotropicity (z-resolution down to ~15-20 nm [14]–[16]), respectively. None of them allows a direct post-embedding correlation with fluorescent LM, that is, there exists to our knowledge no integrated FIBSEM or SBFSEM microscope with a high numerical aperture (NA) fluorescent LM. On a same sample, LM-EM correlation can only be obtained with pre-embedding LM [10], [11], [17]–[22], for example, by correlating 2-photon microscopy fluorescent imagery with volumetric EM [10], [11], [23]. As the tissue undergoes major morphological and chemical changes between the pre-embedding state and the final volumetric EM imagery (heavy-metal staining, dehydration, resin infiltration, resin curing), non-negligible effort is needed to register precisely the two imageries into a same coordinate system [6], [16], [21], [23], [24].

B. Tape-collected sections

Non-destructive serial physical sectioning combined with the ATUM tape collection system has produced several large volumetric EM datasets ([3], [4], [7], [25]. It could in theory also provide the collected sections in a setting compatible with correlated light and electron microscopy (CLEM), nevertheless there has been no such report to date to our knowledge. How could post-embedding immunohistochemistry (IHC) be performed on tape-collected sections ?

1. IHC in a reel-to-reel fashion

A reel-to-reel staining device such as the one introduced by Own et al. [26], [27] could be used to sequentially stain sections directly on tape. However typical incubation times are at least one hour each for primary and secondary antibody staining. It is therefore not clear to us how it would be possible to stain in a rapid manner for example 1000 consecutive sections from a single roll of tape with such a device. Moreover, decay of staining happens within few hours as reported by Micheva et al. ([28], fig. S3) which gives an additional time constraint.

Subsequent imaging performed also in a reel-to-reel manner could probably be done only with low-NA non-immersion objectives, because cover-slipping the sections one by one in the reel would be a difficult process to automate.

2. IHC on tape cut and glued on wafer

IHC could be performed after the tape has been cut into smaller chunks and glued onto a silicon wafer. For incubation steps with non-expensive liquids (blocking solution, buffer washing, water washing) the whole wafer could be immersed entirely into a given liquid. For antibody incubation steps, the staining liquid could be deposited in drops one by one on each section, with typically about 200 sections per wafer. Alternatively, the section could be turned with sections facing down and placed in a dish containing a relatively small volume of staining liquid. To avoid physical contact of the sections with the bottom of the dish, four small spacers could be placed at the periphery of the dish and would not touch sections. Subsequent imaging, as with the reel-to-reel setting mentioned above, would probably be performed only with low-NA non-immersion objectives because cover-slipping such sections would probably be an error-prone and difficult process.

C. TEM

Non-destructive serial physical sectioning combined with section collection onto transmission electron microscopy (TEM) grids has allowed researchers to enhance the raw EM imagery by chemically treating the collected sections, typically with immunostaining [29]–[32]. Only after 1998 have such immuno-EM approaches been used with fluorescent light microscopy [33], by using fluorophores to tag structures of interest instead of electron-dense particles. In immuno-TEM, grids are handled manually one by one or manually arrayed onto glass slides [30], exposed to droplets of staining reagents, and imaged with LM or EM. The manual section collection and subsequent staining and imaging are error-prone and tedious procedures when performed on many dozens of grids.

Although some automation has emerged for the handling of TEM grids for TEM imaging [6], there has been no report so far of automated immunostaining of hundreds of sections collected on TEM grids. Shahidi et al. [34] built a tray to ease the handling of TEM grids and enable simultaneous immonustaining of several grids, however the procedure still requires very careful manipulation of TEM grids by an expert.

A recent extension of the tape-collection technique with a tape incrusted with TEM grids enables TEM imaging of tape-collected sections. The reel-to-reel staining device introduced by Own et al. would be a good candidate for reel-to-reel immunostaining of sections, nevertheless the same limitations apply as mentioned earlier for reel-to-reel staining of tape-collected sections.

D. Non-destructive sectioning and collection

Non-destructive serial physical sectioning with collection onto flat substrates such as glass substrates [35]–[43] or silicon wafer substrates [44]–[47] is probably the sample preparation of choice to enable post-embedding immunostaining with subsequent correlative fluorescent light and electron microscopy.

Typically, ultrathin sections are cut with a sharp diamond knife, float on the water surface of an adjacent bath and are collected by withdrawal of a previously obliquely semi-immersed substrate [45]–[49] or withdrawal of the water [50]. For fluorescent LM, immunostaining is simultaneously performed on all sections by easily depositing drops of staining reagents or by using passive microfluidic pumping in small channels [51]. Subsequently, sections are imaged with transmission (transparent substrate) or reflection (opaque or transparent substrate) fluorescent LM with multiple spectral channels. In either case, sections can be mounted with mounting medium and cover-slipped to enable LM imaging with high-NA high-magnification immersion objectives. Finally, EM imaging can be performed on the exact same sections in the same state as during LM imaging and directly correlated with the LM imagery [36], [40], [47].

Collecting sections directly onto silicon wafer substrates presents several advantages. High current probes can be used during SEM imaging without producing any charging, as opposed to imaging with coated glass substrates. Collected sections are well visible by eye on silicon wafers whereas sections are barely visible and hard to locate on transparent glass substrates. Silicon wafers are easily cleavable to any rectangular size for convenient handling and are also more robust than thin coverslips.

E. Outline

From this short review we see that the collection of ultrathin sections directly onto flat substrates such as silicon wafers offers an optimal platform to perform post-embedding immunostainings and subsequent correlated light and electron microscopy imaging.

In the present manuscript we present a novel way to collect hundreds of ultrathin sections directly onto silicon wafers using remote magnetic actuation. We introduce a method to retrieve the sectioning order lost during section collection. Finally we show CLEM imagery of zebra finch brain tissue suitable for cellular-resolution connectomic analysis.

III. Materials and Methods

Data sets 1 and 2 are defined in section IV.D

A. Brain tissue preparation

1. Tracer injection

Zebra finches were anesthetized with isofluorane and placed in a stereotaxic device. Fluorescent tracers were bilaterally injected (0.5-1 µL) into different areas using stereotaxic coordinates which are summarized in Table 1 (relative to Lambda).

	RA	AreaX	Avalanche
Head angle (degrees)	65	45	45
Pipette angle (degrees)	45	-20	0
Anterior-Posterior (mm)	3	6.45*	1.8
Media-Lateral (mm)	2.45	1.55	2
Dorso-Ventral (mm)	1.3	2.95	1.05

*with a 0 degree pipette angle

Table 1 Coordinates of nuclei targeted with tracer injections

2. Tissue processing

Three to five days after tracer injection, the animals were sacrificed by perfusion fixation with fixative concentrations of 2% formaldehyde and 2.5% glutaraldehyde in buffer with 0.1M cacodylate, 2mM calcium chloride (referred to as cacodylate buffer). The brain was extracted and slices of 150 µm thickness were cut with a vibratome (Thermoscientific, #Microm HM650V) in cold cacodylate buffer. Portions of the slices containing the nucleus HVC were dissected out with a surgical scalpel and processed similarly as in the protocols described by Deerinck et al. [52] and Tapia et al. [53]. The sections were washed with cacodylate buffer, stained with heavy metals (2% osmium tetroxide reduced with 1.5% potassium ferrocyanide, washed, 1% thiocarbohydrazide, washed, 2% osmium tetroxide, washed, 1% uranyl acetate at 4C overnight, washed, 0.6% lead aspartate, washed), dehydrated with increasing ethanol concentrations (50%, 70%, 80%, 90%, 95%, 100%, 100%), infiltrated in epoxy Durcupan resin (10g component A/M, 10g B, 0.3g C, 0.2g D), and finally cured in an oven at 52 C for 48 hours.

B. Fluomagnetic resin

Magnetic resin was prepared as described by Puig et al. [54] with 8% weight concentration of iron oxide superparamagnetic nanoparticles (CAN Hamburg, Germany, #SMB-0-038) in epoxy resin (Diglycidylether of Bisphenol A, #D3415 Sigma Aldrich). In addition, fluorescent particles (Cospheric, mean diameter 2 μm, #FMG, #FMR, 0.2% and 1% weight concentration in data sets 1 and 2, respectively) and coumarin dye (SigmaAldrich, #257370, 7-Amino-4-methylcoumarin, 0.5% weight concentration) were added to the resin mixture prior to mixing. The resin mixture was poured between a glass slide (bottom) and a piece of aclar sheet (top), both coated with mould separating agent (#62407445, Glorex, [55]). A PDMS spacer of about 600 μm thickness surrounded the resin and a small weight was put on top of the aclar sheet for flattening . The resin was cured for 6 hours at 70C.

C. Magnetic augmentation of a block of interest

Resin-embedded samples of interest (SOI) were cured between a glass slide and a piece of aclar sheet (Ted Pella, #10501-25), both coated with mould separating agent [55]. After extraction of the SOI from the sandwiching substrates, it was glued onto a plastic stab (Peep material, 5 mm diameter, 13 mm height) or a block of polymerized epoxy with instant superglue. Magnetic augmentation was performed by gluing a polymerized piece of fluomagnetic resin with Durcupan epoxy (same formulation as used for brain tissue with the four A/M, B, C, and D components) and by trimming with a razor blade and finally with a diamond knife trimmer (Diatome, #Trim20). The step-by-step procedure is described with illustrations in the Results section.

D. Section collection procedure

1. Equipment

The equipment described in this paragraph is shown in Figure 1. A diamond knife was mounted on a custom-built large bath of dimensions 55 x 44 mm with a clearance angle of 35 degrees (this prototype then became the product #Ultra ATS, Diatome). A hole was drilled at the bottom of the bath to plug a tube to control the water level. A ionizer (Leica, #EM Crion) was placed about 2 to 8 cm away from the diamond edge and turned on at maximal power during sectioning. A heating pad was glued to the bottom of the bath in order to warm it and its content for faster water evaporation at the wafer surface after water withdrawal.

A 50 mL syringe was filled with double distilled water and placed in a syringe pump (KDScientific, #210) which was controlled with a custom script.

A 3-axis motorized actuator (Thorlabs, #LTS150/M, #PT1/M-Z8) carried an aluminum plate with a goniometer (Thorlabs, #GN2/M) screwed at its extremity, facing down. A cylindric Neodimium magnet (Supermagnete, cylindrical, 15 mm diameter, 8 mm height) was magnetically anchored to a steel plate screwed to the goniometer. The orientation of the magnet was adjusted with the goniometer in order to make its bottom surface parallel to the water level.

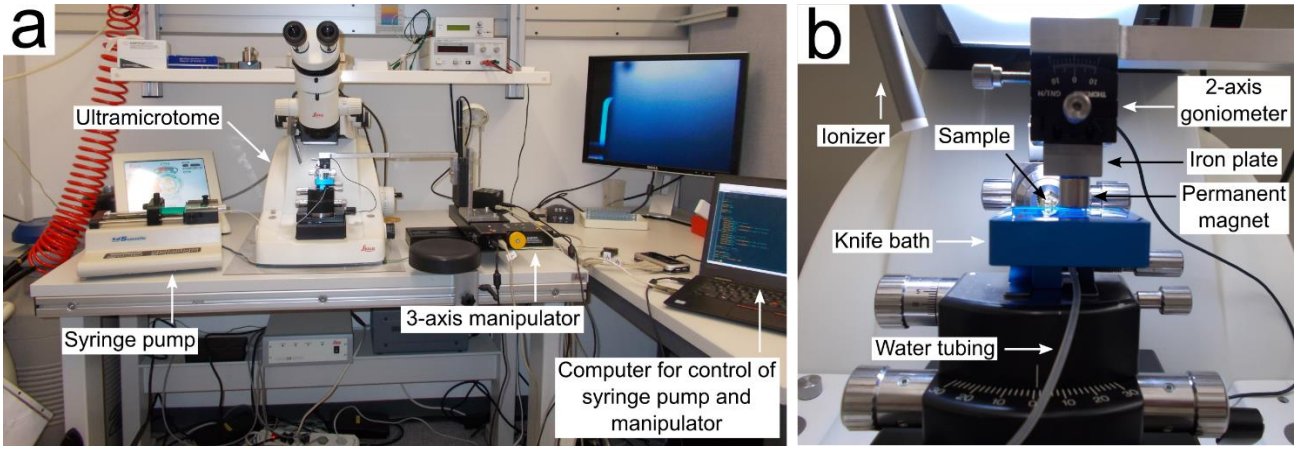

*Figure 1 Section collection setup. **a**. Overview of the ultramicrotomy setup. **b**. Close-up of the equipment around the sample.*

2. Procedure

a. Sectioning

A silicon wafer (2, 3, or 4 inches diameter) or a cleaved piece of silicon wafer was treated with an oxygen plasma for 1 min with a coating current of 25 mA (Emitech, #K100X) to make its surface hydrophilic. The substrate was inserted at the bottom of the trough of the custom large diamond knife. Three stacked coverslips were placed asymmetrically below the collecting substrate in order to tilt it to the left or right to approximately 2 degrees. This tilt ensured that the location on the wafer where the water evaporated last was not located at the center of the wafer where the sections were collected, because the dirt accumulated at the water surface during sectioning otherwise tends to accumulate at a central location when the substrate is not tilted relative to water level.

The block was mounted in an ultramicrotomy block holder on an ultramicrotome (Leica UC6) and a few sections were cut with the custom large knife to ensure proper alignment of the diamond with the block prior to the sectioning session. A cutting window was set at the ultramicrotome. Typical parameters used were 50 nm thickness and 0.4 mm/s cutting speed. Note that an air-tight enclosure would have been beneficial to produce sections of homogenous thicknesses [56] however at the time of the experiment we did not have such an enclosure. The ionizer was turned on, and automated sectioning was started.

b. Collection

After sectioning, the magnet was lowered approximately to 1mm above the water surface. A few sections (about a dozen when collecting 500 sections) that might have stuck to the walls of the bath are manually detached with a fine eyelash mounted on a tooth pick. With custom scripts, the magnet scanned at constant speed of about 1 mm/s the surface of the bath to drag the sections to a central place. The magnet typically described a snake path. After manual inspection ensuring that no section remained outside of the magnetic collection area under the magnet, the water was slowly removed (5 mL/min) and the magnet was accordingly simultaneously lowered to maintain the 1 mm air gap between the water surface and the magnet. Shortly before the water level went below the substrate level, the heating pad was turned on to warm the bath and its water to about 40 degrees to speed up evaporation of the remaining water on the substrate. As soon as the substrate was dry, it was placed on a hot plate at 50C for 30 minutes.

E. Wafer mapping

1. Imaging

The wafers were imaged in mosaics at low resolution (5x objective) with widefield reflection brightfield and fluorescent light microscopy (dapi, red, green) using a Zeiss Z1 microscope. The fluorescent beads were visible in the red and green channels but were not subsequently used. Tiles were stitched with the Fiji stitching plugin [57] on the brightfield channel.

A semi-automated pipeline was run with a custom Fiji script with the following steps.

2. Section segmentation

First, the user is prompted to describe a template section in the mosaic overview of the wafer (using TrakEM2) by clicking on the 4 corners of the tissue portion and the 4 corners of the magnetic portion of the chosen section. Using the WEKA segmentation plugin in Fiji [58] the user is then prompted to train a classifier by drawing manually small lines inside and outside of a few sections in the DAPI channel imagery (this imagery shows the magnetic portion of the sections that contain the Coumarine dye visible in the DAPI channel, depicted in blue in **Figure 4**). The script then determines the location and orientation of the sections with a template matching search using the DAPI channel. Finally, two graphical user interfaces allow the experimenter to adjust if needed the precise location of the found sections and to manually input sections that have been missed in the automated search.

3. Landmarks and tissue center

During the semi-automated wafer mapping, the user is also prompted to define landmarks on the wafer: we used 4 corners of four sections in the wafer overview, typically located at the left, top, right and bottom of the sections.
The user is also prompted to define a center in the tissue part of a template section which determines the center of the imagery that will later be acquired with the LM and EM at high resolution. For this the user clicks on four corners of the tissue part then on the center.

4. Output of wafer mapping

The final output of the wafer mapping process was then:
- the four corners of the tissue part of each section
- the four corners of the magnetic part of each section
- four landmarks for section coordinate mapping in the stages of light and electron microscopes
- a location in the tissue part of a section to determine the center of subsequent high resolution LM and EM imaging

F. Fluorescent imaging for section order retrieval

The silicon wafer was installed in the holder of an inverted LM microscope (Nikon Ti Eclipse, 20x, 0.7 NA). Using a python script controlling the microscope through Micromanager [59], [60], landmarks defined earlier were mapped to generate a rigid transform between the coordinates of the low resolution wafer overview imagery and the coordinates of the wafer in the microscope stage. The mapping consisted in driving manually the x-y stage to the first two landmarks and clicking a button. The

custom software then conveniently placed the stage at the calculated locations of the remaining landmarks for the user to adjust the exact location.

After manual calibration of the hardware autofocus (Nikon, #PerfectFocusSystem), fluorescent LM acquisition was performed automatically with the same script controlling the microscope through Micromanager. Depending on the cross-sectional area of the fluomagnetic resin, a single field of view or a mosaic of field of views can be acquired each section. A single field of view was used for the data of the manuscript. Hardware autofocus was performed at each field of view. The channels used were standard green and red for fluorescent beads, "DAPI" for visualization of the Coumarin dye for section segmentation and optionally brightfield for mosaic stitching when several fields of view are acquired.

G. Section order retrieval

Section order retrieval (SOR) was performed using EM imagery of the heavy metal stained brain tissue sections and with the fluorescent beads contained in the appended fluomagnetic composite resin.

1. SOR with EM imagery

Automated SOR with EM imagery was integrated into our custom data assembly pipeline. A dissimilarity measure was computed as follows for all pairs of sections. A complete EM section was made of a mosaic of EM tiles: 3x3 and 2x2 tiles for data sets 1 and 2, respectively. For a given pair of EM sections, a dissimilarity was computed for each pair of mosaic tiles (the tile with coordinates (1,2) in the mosaic is compared to the corresponding tile with coordinates (1,2) in the other mosaic, because the mosaics have the same orientation relative to the sections and therefore the single tiles correspond to the same region of the section), and averaged across the tiles to yield the complete dissimilarity between two EM sections. The dissimilarity of two tiles was calculated as follows: an affine transform matching was sought between the pair of images, using the SIFT matching algorithms implemented in Fiji. If no affine transform was found, then the pair of tiles was given an arbitrary high dissimilarity. If a transform was found, then it was used to align the two tiles and a normalized cross-correlation was computed in a central box of 2000 x 2000 pixels. The value *(2 – correlation)* was used as the dissimilarity value between the two tiles.

When averaging the dissimilarities across tiles for a given pair of EM sections, the non-matching tiles were excluded if there were some other tiles that were matching. This makes the dissimilarity value more robust to artefacts that may have prevented a match to be found in one of the tiles.

The set of pairwise dissimilarity values between pairs of sections was then interpreted as a set of pairwise distances between the nodes of a graph so that the problem of retrieving the serial order in which the sections were cut was reformulated into an open traveling salesman problem (TSP) [61], [62] that we solved using the Concorde library [63].

2. SOR with fluorescent beads imagery

Section order retrieval based on LM imagery of the fluorescent beads was performed automatically with a set of jython scripts for the Fiji software that performed the following operations. If the imagery was acquired in a mosaic fashion, then stitching of the mosaic was computed for each section using the brightfield channel [57] and propagated to the other channels using TrakEM2 [64].
After preprocessing ("Normalize local contrast" Fiji plugin, thresholding), the center location of the

beads was extracted (Maxima Finder) for each fluorescent channel. The locations of the beads from the two fluorescent channels were merged into a single final channel.

We computed a dissimilarity value for every pair of sections. For each pair of bead center sets, descriptor matching was performed (using descriptor-based bead alignment available in Fiji [65]). If no geometric match was found for a given pair of sections, then the dissimilarity value was set to a fixed large number. If a geometric match was found, then a matching affine transform was computed and applied to the first bead set, thus bringing the pair of bead sets into a same coordinate system.

In this common coordinate system, the bead centers contained outside a central bounding box were excluded from further calculations to avoid considering beads that are present in one section but not in the other one due to a limited field of view and due to the different orientations of the section. The pair of remaining bead sets was then matched again with the descriptor-based tool. For each match, that is each pair of two matching beads, the absolute difference of the diameters of the matching beads was computed. The dissimilarity of two sections was then defined as the sum of these diameter differences across all matching beads.

Similarly as for the SOR with EM imagery, a traveling salesman problem was formulated using the dissimilarities as distances between nodes of a graph, and the problem was solved with the Concorde solver.

H. Post-embedding immunohistochemistry

We deposited and exchanged staining solutions manually with graduated pipettes on the sections collected on flat substrate. All steps were performed at room temperature. The blocking solution was: 1% Baurion BSA-c, 0.05% Tween [40] in TBS pH 7.4. The detailed procedure was:

1.Blocking -- blocking solution -- 2x 10 min
2.Primary antibody incubation -- 1:50 in blocking solution -- 1.5h
3.Washing -- TBS -- 4x5min
4.Secondary antibody -- 1:100 in blocking solution -- 1 h
5.Washing -- TBS -- 2x5min
6.Washing -- dH2O -- 2x5min
7.Drying with hand dust blower (Bergeon #30540)
8.Air drying – 5 min
Proceed to fluorescent imaging within the next hours to avoid decay of staining as reported by Micheva et al. [28] (Figure Sup. S3).

I. Fluorescent imaging of labeled tissue
    1. Wafer mounting

Drops of mounting medium (Molecular Probes, #S36937) were deposited on the sections and were subsequently coverslipped with standard microscope slides of appropriate size to cover the area of collected sections. The coverslip was maintained in place with a pair of small magnets (one below the wafer, one above the coverslip).

2. Landmark mapping

The silicon wafer substrate was placed in the holder of an inverted microscope. Landmarks were mapped with our custom software in two steps: first with a 20x dry objective, then with a high magnification 63x immersion objective. The reason for this two-step procedure is that the use of an inverted microscope prevented intuitive manual navigation to find the initial first two landmarks, which would have been a difficult task using solely a high magnification objective. Therefore after successful mapping with the 20x non-immersion objective, immersion liquid was added onto the coverslip and the holder was put back in the same position. The script then guided the user through all landmarks who only had to adjust precisely with the high magnification objective the suggested landmark locations from the low magnification objective mapping. As with the bead imaging earlier, an affine transform was computed to transform the coordinates from the wafer overview imagery to the microscope stage coordinates.

3. Imaging

We defined all imaging parameters in our custom python software: fluorescent channels, exposure times, z-offset per channel, imaging grid (e.g. 3x2 mosaic). Multichannel mosaics were automatically imaged for all sections with hardware autofocus activated at each field of view.

4. Wafer unmounting

After LM imaging, the pair of small magnets was gently removed before removing the cover slip while taking care that the immersion oil was not coming in contact with the wafer. The wafer was immersed three times for 5 minutes each in a small dish of double distilled water to wash away the mounting medium. The wafer was finally dried at room temperature with a hand blower.

J. Post-staining

Heavy metal post-staining was performed by exposing sections on wafer to a few drops of 2% aqueous uranyl acetate, then to a few drops of Reynold's lead citrate (lead 4.4% weight concentration), both for 90 seconds. Between the two stains and after the second stain, the entire piece of wafer was immersed consecutively in 3 small petri dishes of double distilled water for 30 seconds each. After the second washing, the wafer was dried with a manual air blower.

K. EM imaging

The wafers were mounted on standard EM stubs (Tedpella, #16111, #16144) with double-sided carbon tape (Tedpella, #16084-1, #16084-2) and inserted into a scanning electron microscope (Zeiss, Merlin). The sample was cleaned for 10 minutes with an in-chamber air plasma (Evactron, Zephyr model 25 plasma cleaner) to minimize carbon contamination during imaging with an inlens detector.

As with LM imaging, the four previously defined landmarks were mapped on the wafer with the 3-axis stage of the EM to provide the x-y coordinates (z-axis remained fixed), angle and working distance of each section. The scanning angle of the beam was rotated according to the section angle so that each section was acquired with the same orientation.

Mosaics of 3x3 (data set 1) and 2x2 (data set 2) tiles were acquired for each section. An antofocus-autostigmation-autofocus sequence was performed at the center of each mosaic. To avoid performing

that sequence on a low-contrast area such as a large cell body or a blood vessel, a subregion was selected around the center of the mosaic that contained enough contrast as determined by looking at the intensity of the neighborhood imagery after applying an edge filter. The main EM imaging parameters were: 2 keV incident energy, 800 pA current probe, 3.5 mm working distance, 750 ns and 6000 ns dwell time for data sets 1 and 2, respectively.

L. Pipeline for correlative LM-EM data assembly

A set of python and jython scripts was written to enable the entirely automated assembly of aligned and registered correlative imagery starting from the raw data produced by the light and electron microscopes.

1. LM assembly

The brightfield channel of the LM imagery was used for the stitching, alignment and registration operations. All tiles of the brightfield channel were first preprocessed with a local contrast normalization ("Normalize local contrast" plugin available in Fiji) with blocks of 100 pixel x 100 pixel (or small variations thereof). The mosaics of each section were stitched using the least square stitching implemented in the TrakEM2 plugin of Fiji [66]. The stitching was then propagated to all fluorescent channels.

2. EM assembly

The top 20 rows of pixels were discarded from each acquired EM tile (solution recommended by Zeiss) because the API control of the Zeiss scan generator did not allow the beam to settle correctly at the beginning of tiles. All acquired EM tiles were preprocessed with a local contrast normalization with blocks of 500 x 500 pixel ("Normalize local contrast" plugin available in Fiji). The following operations were then performed in the Fiji framework with TrakEM2: downsampling of all individual tiles, mosaic stitching of downsampled tiles with the Fiji stitching plugin followed by elastic stitching [67] of the full resolution tiles. The full resolution elastically stitched mosaics were downsampled to perform a first rigid alignment ("Register Virtual Stacks" Fiji plugin). The computed rigid transforms were then upscaled and applied to the full resolution tiles in TrakEM2 to yield an elastically-montaged and rigid-aligned volume. Finally, elastic alignment [67] was performed in TrakEM2.

3. LM-EM registration

The stitched mosaics of the brightfield channel were preprocessed with local contrast enhancement and Gaussian blurring. The EM counterpart mosaics were downsampled to exhibit roughly the same pixel size as the LM imagery and further preprocessed with local contrast enhancement. The LM brightfield and EM imageries then exhibited a similar appearance so that corresponding SIFT features [68] could be computed across the two modalities. Moving least squares transforms [69] were computed based on these matching SIFT features using Fiji. The transforms were then upsampled and applied to all fluorescent channels of the LM imagery in the TrakEM2 plugin to yield a volumetric correlative LM-EM stack.

4. Visualization

a. Export from TrakEM2 to Render

The EM imagery assembled in TrakEM2 along with all transforms (affine, elastic and moving least squares) was converted into a Render project[1] [6] with custom scripts and the TrakEM2 converter script of the Render project.

Similarly, TrakEM2 projects were created for each LM channel that contained stitching and moving least square transforms. These TrakEM2 projects were converted to separate Render projects.

b. Export from Render to Neuroglancer

The imagery of the EM and LM Render projects was rendered to files using a custom script and the Render script for mipmap creation (render_catmaid_boxes). With a custom script, these mipmaps were then used to create chunks at different resolutions in the "precomputed format" of Neuroglancer[2].

c. Online visualization

The chunks were uploaded to an online cloud storage service (Google storage) and an instance of the Neuroglancer software hosted online (neurodataviz from the MICrONS project) was used to visualize the data. The EM imagery and each fluorescent LM channel were added into a neuroglancer session as separate data sources.

d. Extraction of LM-EM imagery to disk

After online visualization with the neuroglancer viewer, stacks of correlative imagery were fetched using the cloud-volume library[3] from Seung's laboratory.

M. Software

The complete software pipeline for MagC is available on github[4].

[1] https://github.com/saalfeldlab/render
[2] https://github.com/google/neuroglancer
[3] https://github.com/seung-lab/cloud-volume
[4] https://github.com/templiert/MagC

IV. Results

A. Magnetic augmentation

1. Section collection principles

a. Imposed constraints

We initially set the goal of collecting many hundreds of consecutive ultrathin sections directly onto silicon wafer substrates with a high packing density to allow for convenient post-embedding immunostaining followed by correlative light and scanning electron microscopy imaging. A first constraint we imposed was to minimize the number of interruptions of the sectioning process [4], [7] to prevent large section thickness inhomogeneities after restarts. A second constraint we imposed was to perform the procedure within a hermetic box (hence no experimenter in immediate vicinity) to prevent air drifts and temperature variations contributing to thickness inhomogeneity across consecutive sections [56].

b. Ribbons and their limitations

The standard approach to collecting sections on a flat substrate is taking advantage of the fact that consecutively cut sections tend to form relatively long and tight ribbons that constitute a single physical object floating on the water surface [45], [47], [49], [56], [70]. One or several ribbons can be manually manipulated with an eyelash at the water surface of the bath and subsequently anchored to a flat substrate by withdrawing the water, or moving obliquely the substrate outside the water [45], [49].

In a first implementation published elsewhere [50] we used an eyelash mounted on a 3-axis motorized manipulator that we remotely controlled with a joystick to actuate freely floating ribbons of sections in the water bath of a diamond knife. The water was then slowly withdrawn to let packed ribbons land onto a previously immersed piece of silicon wafer. However, these experiments required however intense manual monitoring to ensure that ribbons remained packed and well oriented throughout the procedure. A major caveat that we could not control was the random curvature exhibited by ribbons of consecutive sections. Successive ribbons consecutively produced from a same block appeared successively straight, bent to the left, or the right, then bent in the opposite direction, and so on in an apparently random manner that we could not explain. We assumed that for given steady cutting conditions (alignment of block relative to the diamond edge unchanged, knife damage negligible over few dozens of sections, ionizer present to remove charging), the plasticized block of biological tissue itself was responsible for different curvatures of the ribbons. The various ribbon shapes rendered the manual task of maintaining order among the floating ribbons tedious, and the automation of this task would have been a challenge. Periodically detaching ribbons from the knife edge was also an inconvenient operation. The conclusions we drew were that ribbons are difficult to work with and periodic ribbon detachment is a non-trivial problem that presents a risk to damage sections.

c. Giving up on ribbons

We kept the idea of producing many sections at the water surface and to subsequently withdraw the water to let them land onto a previously immersed substrate. As a first novel idea, we questioned whether producing long ribbons of sections was necessary. These ribbons have two advantages. First,

the serial order of the sections is conserved in the physical arrangement of the sections. For example, when we collected a handful of long consecutive ribbons, the experimenter had to keep track of the serial order of the few ribbons while they were floating to later retrieve the serial order of all sections. Second, many sections bind together to form a single physical object for simultaneous actuation.

We reasoned that dealing instead with unordered freely-floating sections would give the opportunity to use different methods for simultaneous actuation of many sections, and that the serial order could be monitored with cameras following sections at the water surface during the collection procedure, or that the order could be laser-etched on the side of the block or later retrieved using microscopy imagery of the sections.

Our new goal was then to produce many disordered sections on the water surface, then concentrate them at high packing density, and finally withdraw the water to let the sections land onto a previously immersed flat substrate such as a piece of silicon wafer.

d. Stay away from walls

Walls are necessary to contain the water onto which the sections are floating. We observed that when a freely-floating section is in the vicinity of the edge of a wall, water withdrawal creates a meniscus at the edge in which the section gets stuck. Eventually the section will stick to the vertical wall edge and is considered lost. Using hydrophobic (PDMS) or hydrophilic (plasma-treated anodized aluminum) walls did not help. We also observed that following physical contact to a wall edge, freely-floating sections tend to remain stuck to it. This phenomenon increases the likelihood that randomly floating sections would finally get trapped in edge menisci and are considered lost.

This wall effect already excluded the simple approach consisting in immersing prior to sectioning a substrate with the same dimensions as the water bath, hoping so that water withdrawal would let all sections land on the substrate. Instead, a non-negligible number of sections would stick to the walls.

e. Vertical pin barriers

Next we asked: is it possible to create a barrier that would contain floating sections without creating a meniscus ? We thought that a wall made of small diameter vertical bars would satisfy these properties. We 3d-printed a rectangular frame to be placed on the frame of a large custom diamond knife. Our workshop drilled 250 µm diameter holes along the frame with 1 mm spacing between each hole. In each hole a metallic pin (10 mm height, 200 µm diameter) was inserted vertically and was prevented to fall through by a small extrusion made of glue at its top. This pin arrangement ensured that each pin would be in contact with an immersed substrate in the collecting bath so that no section would escape until complete water withdrawal.

We observed a lack of meniscus and sections landing without damage while in close vicinity of the barriers. However, we also observed sections with small damage du to the pins as they probably stuck to a pin during landing on the substrate. Another issue was to provide a gate in front of the diamond edge that would later need to be closed after sectioning prior to water withdrawal. A last issue was to move sections away from the vicinity of the knife edge and to not let them stick to the surrounding wall at the gate. We thought that these issues would be difficult to solve.

f. Remote actuation without mechanical contact

After the attempts described above we sought a method for remote actuation of sections that would move sections away from walls and would enable their accumulation into a given location to maximize the section packing density on substrate. Experiments with water currents created by a miniature pump were not successful as it proved difficult to create currents that lead to the accumulation of sections into one location.

Instead, we thought that remote magnetic actuation of magnetized sections would ideally not only actuate sections remotely but also enable accumulation of sections into one given location using the magnetic attractive force.

We then asked: how to magnetize tissue sections ? We thought of coating a resin tissue block with paramagnetic material such as iron however we anticipated that the cutting properties of the iron would be very different from the resin-embedded tissue and would impair sectioning. We were also worried that plain iron would damage the diamond knife.

We thought of diffusing superparamagnetic nanoparticles in the tissue. Given that the minimal size of such particles is about 4 nm, simply incubating tissue sections in ferrofluid would likely not have enabled a deep and homogenous penetration of the particles into the tissue so that each ultrathin tissue section would have carried enough magnetic material for actuation. In vivo injection of superparamagnetic particles would also have been difficult with uncertain outcomes.

We then became aware of studies showing epoxy resins containing an homogenous dispersion of superparamagnetic nanoparticles [54], [71], [72] and thought of using such resin for tissue embedding. However, as for incubation ot tissue into ferrofluid mentioned earlier, we doubted that particles would penetrate homogeneously into the tissue. Instead, we thought of augmenting a polymerized tissue block with a block of polymerized magnetic resin by simply gluing them together. This approach proved successful and is described in this manuscript.

2. Magnetic augmentation: implementation
    a. Mounting helper device

The magnetic augmentation consisted in gluing additional resin blocks to a plasticized sample. A successful augmentation required to position precisely the additional blocks and to maintain their position during temperature curing. We built a device that allowed the experimenter to maintain the position of an additional block with a fine needle and to process several samples in a row with the same device. The device worked as follows:
1. The manipulator is mechanically coupled to the needle holder with a bar. The needle is placed at the desired location by moving the needle holder in the x-y plane with the manual manipulator (Narishige).
2. The linking bar between the needle holder and the manipulator is removed from the needle holder by unscrewing the screw on top of the needle holder. At that stage the location of the needle is still maintained thanks to the bottom magnet that keeps the position that has been set by the manipulator.
3. The detachable part can be removed and placed in an oven, see Figure 2, b. Another detachable unit can be used to prepare another sample.

b. Procedure

The resin-embedded sample was trimmed manually with a razor blade, Figure 2, c. A piece of fluomagnetic resin was glued to the sample with a drop of plain Durcupan epoxy resin (same formulation as used for brain tissue with the four A/M, B, C, and D components), Figure 2, d. The fluomagnetic piece was maintained in contact with the anchoring surface with a fine needle applying slight pressure towards the block during curing overnight at 55C. Figure 2,e is an overlay of a color micrograph and two fluorescent channels showing the fluorescent beads in the appended fluomagnetic resin. The new flat surface exposed by the fluomagnetic resin at the top of the block surface was trimmed (Figure 2, f) or left as is.

To enhance sectioning quality (see “Block orientation” paragraph) a “dummy” block of resin-embedded heavy metal-stained brain tissue was glued to the other side of the fluomagnetic resin with the same Durcupan resin and maintained in place with the mounting helper device during curing overnight at 55C, Figure 2,g. The dummy block was then trimmed as much as possible. The augmented block underwent a final trimming to produce peaks at the top (dummy) and optionally at the bottom of the block to facilitate the detachment of sections from their neighbors and from the diamond edge. The surface of the block was finally trimmed with a diamond trimmer (Diatome, #Trim20) mounted on an ultramicrotome. The final block ready for sectioning is shown in Figure 2,h.

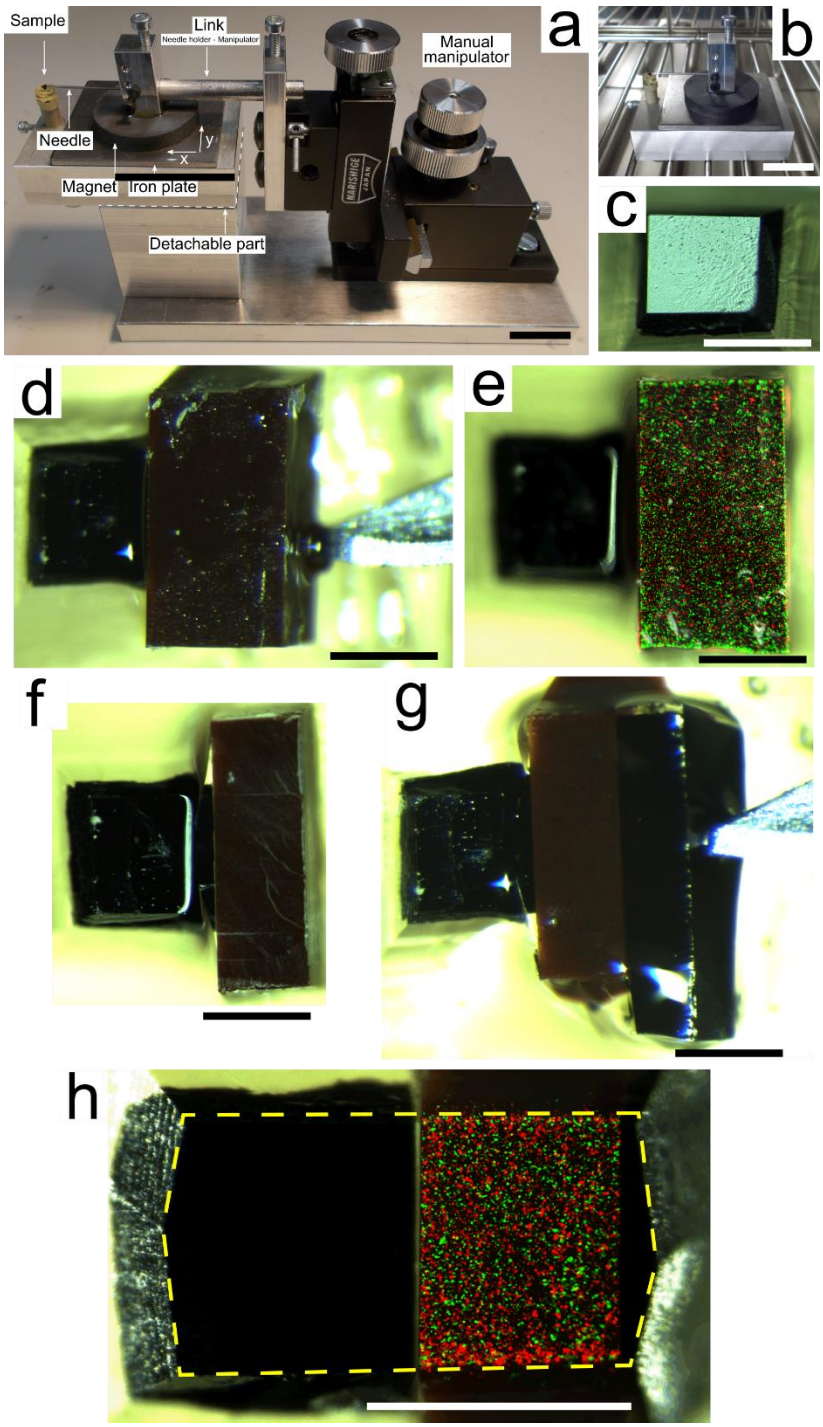

Figure 2 ***Fluomagnetic augmentation. a.****Mounting helper device.The manual manipulator allows the experimenter to precisely place the needle in contact with the block to be glued on the sample. The iron plate together with the base magnet of the needle holder maintain the position set by the manipulator.* ***b****. The detachable part is placed in an oven for temperature curing.* ***c****. The biological sample is trimmed manually with a razor blade.* ***d****. The fluomagnetic resin is glued to the sample and maintained in place with a needle.* ***e****. Overlay of color and fluorescent imagery showing the fluorescent particles contained in the fluomagnetic resin.* ***f****. The fluomagnetic resin is manually trimmed down to achieve roughly a 50/50 ratio of sample surface to fluomagnetic surface suitable for sectioning at 50 nm nominal thickness.* ***g****. An additional dummy piece of heavy metal-stained resin-embedded brain tissue is glued to the block.****h*** *After final trimming, the block presents a pointed shape (overlayed with the yellow*

dashed line) and is ready for sectioning. Note: the stronger red signal at the bottom is not due to large particle aggregates but due to out-of-focus effects. Scale bars: a,b-20 mm; c to h: 500 µm

B. Section collection

1. Section detachment

When the bottom and top edges of the block are both made of a straight line, sections tend to stick to the knife edge and also to each other resulting in chains of sections (called ribbons) that stick to the knife edge. A procedure was sought to perform some automated detachment from the knife edge or from between the sections.

a. Detachment with a fine filament

Sections can be mechanically actuated with fine filaments such as eyelashes of fine electrical wires in three ways, depicted in **Figure 3**,a. Eyelashes can either touch a section from the top and actuate it laterally while gently pressing vertically towards the section, or it can be inserted by a few millimeters into the water to push the sections from the side. Fine filaments such as stainless steel or silver wires (A-M Systems, Inc., #790600 and #785500 respectively) of diameter around 130 µm exhibit the property that their tip does not penetrate into the water surface when brought from the top, due to surface tension. Instead, the wire bends slightly and its tip floats at the water surface. The floating tip can then be used to push sections laterally. These three actuation options all presented the risk of damaging sections as the mechanical contact sometimes result in the sticking of the filament to the section. Also, the automation of the robotic control of the filaments would have been cumbersome.

b. Detachment with air currents

We experimented with small tubing, delivering pressurized gas and programmatically controlled with valves (#CPV-SC-MP, Festo). The outlet of a tube was directed towards the knife edge laterally from the left or right and blowed a puff of air after a cutting cycle. The detachment of sections from the knife was most of the time satisfactory; however, these blows let the water surface oscillate up and down very strongly and impaired the sectioning process (the ultramicrotome either needed to be stopped before cutting the next section, or the turbulent water impaired the quality of the section).

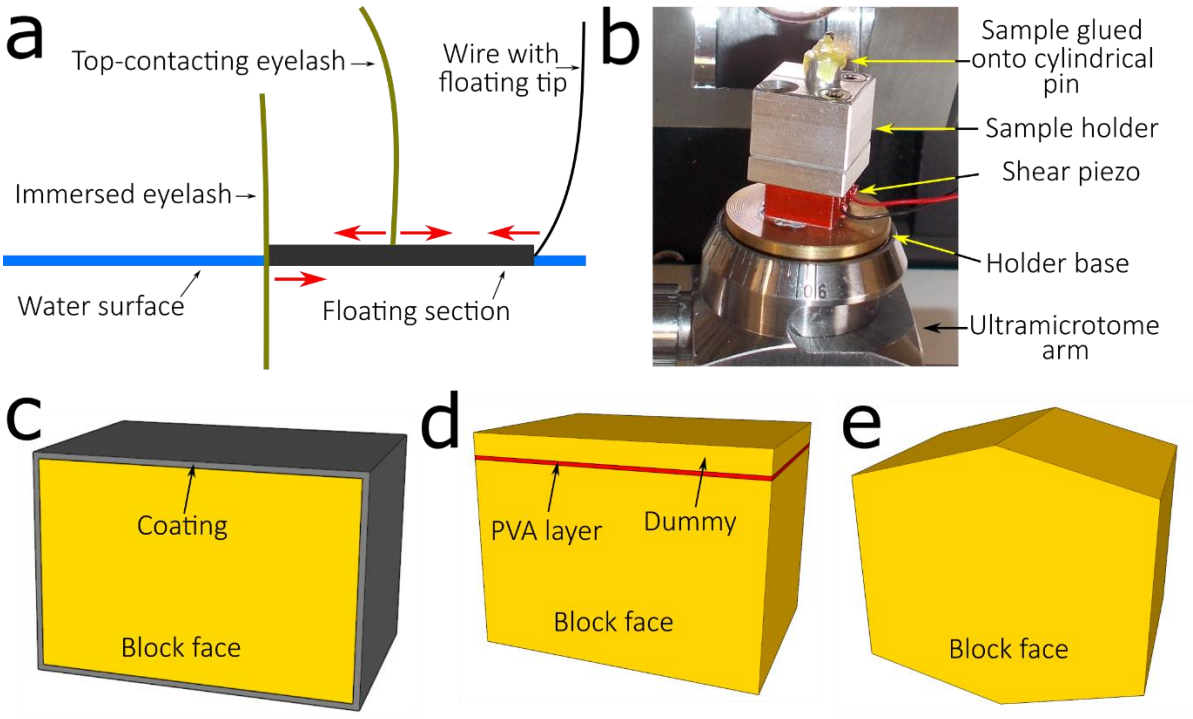

Figure 3 *Strategies for section detachment.* ***a)*** *Mechanical contact with an eyelash or a fine wire.* ***b)*** *Piezo-oscillating sample holder.* ***c)*** *Surface coating of the sample block.* ***d)*** *Layer of polyvinyl alcohol placed on top of the block of interest and protected by a dummy block.* ***e)*** *Trimmed sample block with pointed edges at the bottom and the top*

c. Detachment with surface coating on the block

We coated resin blocks with a thin layer of material with the hope that the coating carried by each section on its edges would prevent sections from sticking to the knife edge. The sole material we tried was silicon (inspired by a discussion with Adam Bleckert) and the coating thickness was varied from a few nanometers to about 150 nm (CCU-010 HV Compact Coating Unit, Safematic). A clear detachment effect could only be observed with coating thicknesses of at least about 10-20 nm, however with thicker thicknesses we noticed that the cutting quality was impaired, as it seemed that the coating was creating fine debris visible at the water surface. We thought that these debris were contaminating the knife edge. Further optimization of the coating procedure could lead to a successful detachment procedure without impairing the sectioning process.

d. Detachment through dissolution of a polyvinyl alcohol layer

Another attempt for section detachment consisted in applying a thin layer of a material at the top of the block that would dissolve with the contact of water. Aqueous polyvinyl alcohol (PVA) was chosed for its ease of preparation and application (a drop deposited with a tooth pick with fast subsequent room temperature drying, repeated 3 times), its likely innocuous effect on the knife edge and on the sections when dissolved in the water bath, and for its fast dissolution when in contact with water. Detachment was excellent as each cut section was not only detached but propulsed away from the knife edge due to the expansion of the PVA material. However, the repeated contact of the PVA at each cutting cycle with the moist diamond edge led to the gradual dissolution of the PVA directly on the block, eventually

discarding the detachment effect. To protect the PVA layer on the block, a dummy piece of tissue was glued on top of the layer which prevented its dissolution directly on the block. Nevertheless, for the method to be successful, the prepared block should never be in contact with water, which can occur when the first sections are cut. We found that this constraint substantially weakened the approach, especially for precious blocks.

e. Detachment with piezo oscillation

Lateral high frequency piezo oscillation during cutting was shown to reduce compression of sections during ultrathin sectioning [73]. It was noticed that reducing the compression with piezo oscillation significantly reduced the sticky behavior of floating sections with other sections and with the diamond edge (personal communication, H. Gnaegi). Commercially available diamond knives with lateral piezo oscillation are optimized for a given knife bath shape and size, however we were pursuing an approach in which we would use large baths that can contain many hundreds of sections. We therefore thought that using a lateral piezo oscillation of the diamond edge would not be an easy route. Instead, with guidance and support from H. Gnaegi (Diatome, Biel, Switzerland) we designed a sample holder, depicted in **Figure 3**,b that produces lateral piezo oscillation of the sample. Briefly, the holder was made of three components: a brass base that fits into the ultramicrotome arm (yellow), a shear piezo stack (orange, Physik Instrumente, #P-141.03), and an aluminum custom sample holder. Blocks were glued onto a cylindrical pin that was secured in the custom sample holder with a screw. No resonant frequency could be found automatically using the commercial controller provided by Diatome ("Ultra Sonic"). Manual searches (performed by H. Gnaegi, Diatome) led to identify a setting of 27 kHz and 15V in which compression was visually suppressed during sectioning. Although we reliably observed the sought compression removal effect with this setting, we found that detachment of sections was not systematic (with sections produced from one block being for example as sticky as without oscillation) and seemed to depend on some properties exhibited by the diverse blocks. Further investigation of the piezo-oscillation mechanism would be needed, for example monitoring the actual displacement of the shear piezo stack, to understand whether the process is working at resonant frequency or not.

f. Detachment with thin sacrificial section

We observed that when attempting to cut a section of 5 nm thickness or less, the sectioning typically failed, i.e., no section was produced. However, the subtle contact of the block with the diamond edge often led to the detachment of the section currently attached to the diamond edge. We therefore thought that periodically setting the microtome advancement to a low value such as 5 nm would lead to a periodic detachment of the last knife-attached section. Similarly, such sacrificial sections could be used every second cut section to obtain a systematic detachment of all sections. We felt nevertheless that we did not have a good control over the thickness that is actually sacrificed, and an automated programmatic control of the ultramicrotome was at the time out of reach (note that a group implemented a programmatic control of the microtome through programmatic mouse emulation[5]). We recently acquired a RS232 interface for the Leica UC7 ultramicrotome that allows such a programmatic control of the ultramicrotome, with which we will attempt in the future to implement and evaluate this sacrificial section detachment method.

[5] https://github.com/fcollman/AutoUc7

g. Detachment induced by block shape

We noticed that block shape could influence the likelihood of section detachment. Minimizing surface contact between consecutive sections could be achieved by trimming the bottom and top edges into two pointed edges, similarly as shown in the publication of Hayworth et al. [3]. Systematic detachment was observed in some blocks but not all. Nevertheless, a ionizer was always placed close to the diamond edge and created a very soft air current that was sufficient to obtain reliable detachment every at most about 5 sections. This detachment method was chosen for its ease of use and reliability.

2. Block orientation

We tested diffferent block orientations (magnetic/brain resins in left/right, bottom/top, top/bottom and oblique orientations) and found that cutting quality was best when the brain tissue was placed at the bottom and the magnetic resin at the top. However, in this configuration and with nomical cutting thicknesses below about 60 nm, we noticed that sections tended to go back slightly towards the knife edge at the end of the cutting of some sections so that the top of the cut section was covering the knife edge. This covering tended to impair the sectioning quality of the bottom of the next section. To solve this issue, we glued a dummy piece of heavy metal-stained resin-embedded brain tissue at the top of the block because in our experience such tissue provided excellent cutting quality and did not trigger the knife-covering effect described above.

3. Section cutting

During the sectioning process, one section was produced at the water surface at the rate of about 8 sections/min using a vertical sectioning speed of 0.4 mm/s in the cutting window and using the “fast” return setting of the ultramicrotome arm outside the cutting window.

We observed that sections sometimes detached easily from each other, and sometimes formed small ribbons of at most about 5 sections. These different behaviors occurred during the same sectioning session of given blocks and could not be controlled.

The ionizer, placed a few centimeters away from the knife edge, tended to create a very soft air current that gently brought sections away from the knife edge. This fortuitous feature prevented clogging of sections at the knife edge to provide a clean cutting area around the knife edge.

We observed that sections were freely floating over the whole water surface.

4. Section agglomeration

After all sections were cut, we agglomerated them into one central location at the water surface by moving a permanent magnet above the surface with an air gap of about 1-2 mm. We first manually inspected the borders of the water bath, looking for sections that looked lightly stuck to the border. We typically found about 10 such sections when cutting about 500 sections. They were gently detached manually from the border with an eyelash in order to let them freely float again.

The magnet was actuated with a 3-axis manipulator controlled by custom scripts. The magnet trajectory described first a raster snake and then was moved to the center of the bath, dragging along all floating sections. The water was then slowly removed and the heating pad below the bath was turned on when about 1-2 mm wafter depth was remaining above the wafer substrate. The magnet was slowly manually

lowered during the water withdrawal to maintain a constant air gap. The sections finally landed on the substrate and the water evaporated. **Figure 4**,a,d shows the two wafer substrates of the two data sets of this manuscript.

We observed that sections distributed around the magnet border and typically did not agglomerate in the center of the magnet (due to an attraction local maximum at the magnet border).

As can be seen in **Figure 4**, sections did not overlap, which is a crucial feature required in our approach. From all experiments conducted with this technique, we never observed overlop between sections during section collection and when landed on substrate.

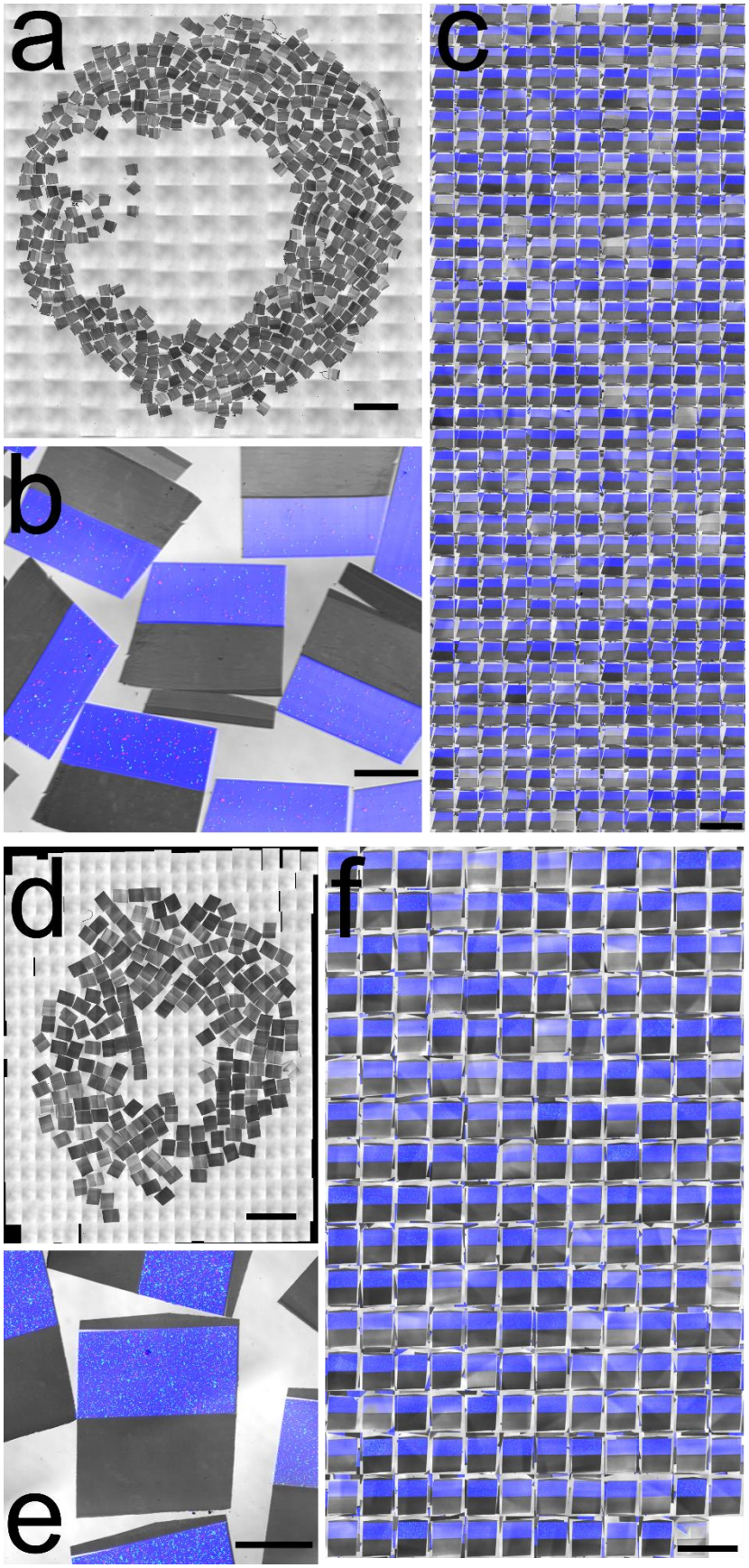
a
c
b
d
f
e

***Figure 4 Section segmentation**. **a,d**:mosaic of widefield reflection light microscopy of sections on wafer. **b,e**: Merge of four different channels: brightfield – gray color – section delineation, DAPI – blue – fluomagnetic resin, 'GFP' – green – fluorescent beads in fluomagnetic resin and 'RFP' – red – fluorescent beads in fluomagnetic resin. Note the absence of overlap between neighboring sections. **c,f**: montage of the 4-color merge of all sections on wafer. Scale bars: a-2 mm; b-200 µm; c-1 mm; d-4 mm; e-500 µm; f-2 mm*

C. Tracers and antibodies library

1. Embedding protocol

We show CLEM imagery of neuroanatomical tracers that have been injected in vivo and finally revealed with post-embedding immunohistochemistry. Unlike in earlier work of the same laboratory [36], [44], [50] we used here a standard rOTO protocol (reduced osmium, thiocarbohydrazide, osmium) with high heavy metal concentrations and complemented with uranyl acetate and lead citrate en block staining similar to the one described by Tapia et al. [53] and suitable for cellular-resolution connectomic analysis.

2. Post-embedding staining

Compared to earlier work [36], [44], [50] we skipped the etching step with sodium metaperiodate as it was significantly impairing EM imagery (same observation as in Shahidi et al. [34]). We also introduced a step of Tween treatment as in Collman et al. [40] and observed a higher qualitative labeling efficiency while retaining good EM imagery quality.

3. Library

We present CLEM imagery of the following four standard neuroanatomical tracers: Dextran Alexa Fluo 488, Dextran FITC, Dextran Texas Red, and biotinylated dextran amine (BDA). Suitable antibodies are commercially available. In order to perform simultaneous staining of several tracers in one staining round, we tested antibodies raised in different species and in addition we produced a custom antibody against Alexa Fluor 488 raised in rat in order to allow an antibody combination with one species per target antigen. The following table gives the tracer-antibody pairs with their commercial reference.

Antigen	Alexa 488 LT #D-22910	FITC LT #D-1820	Texas Red LT #D-3328	BDA LT #D-1956
Antibody species	**rabbit** (LT #A-11094) **rat** (Biotem #custom)	**mouse** **rabbit** (LT #A-889)	**goat** (VL #SP-0602)	**mouse** (JI #200-002-211)

***Table 2** Tracer-antibody library. LT: Life Technologies. VL: Vector Laboratories. JI: Jackson Immunoresearch.*

The four anatomical tracers were each injected in four different animals to ensure the presence of only one single tracer in the tissue. Tissue containing transported tracer was harvested and prepared for post-embedding staining. A few ultrathin sections (50 nm thick) from each of the four tissue blocks were collected onto 6 separate pieces of silicon wafers, yielding a total of 6 x 4 = 24 pieces of silicon wafer. The sections from a given block spanned less than 2 µm in depth as they were collected from at most 40 consecutive 50 nm-thick sections. The sections from a same block stained on different wafers therefore carried similar tissue, so that if the presence of an antigen is validated in one of the sections then it is expected that all sections collected from this block in this experiment also contain the antigen.

Each group of 6 wafers carrying tissue sections containing a given tracer were submitted separately to staining with the 6 antibodies of the library to check for cross-labeling. Figure 5 below shows expected labeling of antigens by their corresponding antibodies and no cross-talk between the antibodies.

To ensure that the same region was imaged in sections from a same block, an objective was chosen so that unambiguous signal in a section would be visible along with a corner of the section in a single field of view. Sections were manually deposited on silicon wafers without a specific orientation and wafers were not mounted according to the orientation of the sections but rather according to their rectangular shape. It resulted in the same region of different sections being imaged with different orientations. The images were therefore manually rotated to all present the same orientation with the same identifiable corner at the bottom left (easily identifiable in the brightfield channel, not shown). The truncated white parts are therefore due to the rotations of these single field of view images. Importantly, regions containing antigen were captured in sufficient extend on each image.

Due to different primary and secondary antibody efficiencies, instead of using a same threshold for all images or using a same threshold for specific groups (sections stained with the same secondary antibody, or sections carrying the same antigen, etc.), a threshold was manually chosen for each image with the goal of making the faintest signal visible to safely exclude potential weak cross-labeling.

Yellow arrows show signal in cell bodies unambiguously detected by T.T. Some images show bright points with no arrows that are non-specific labeling or debris on sections.

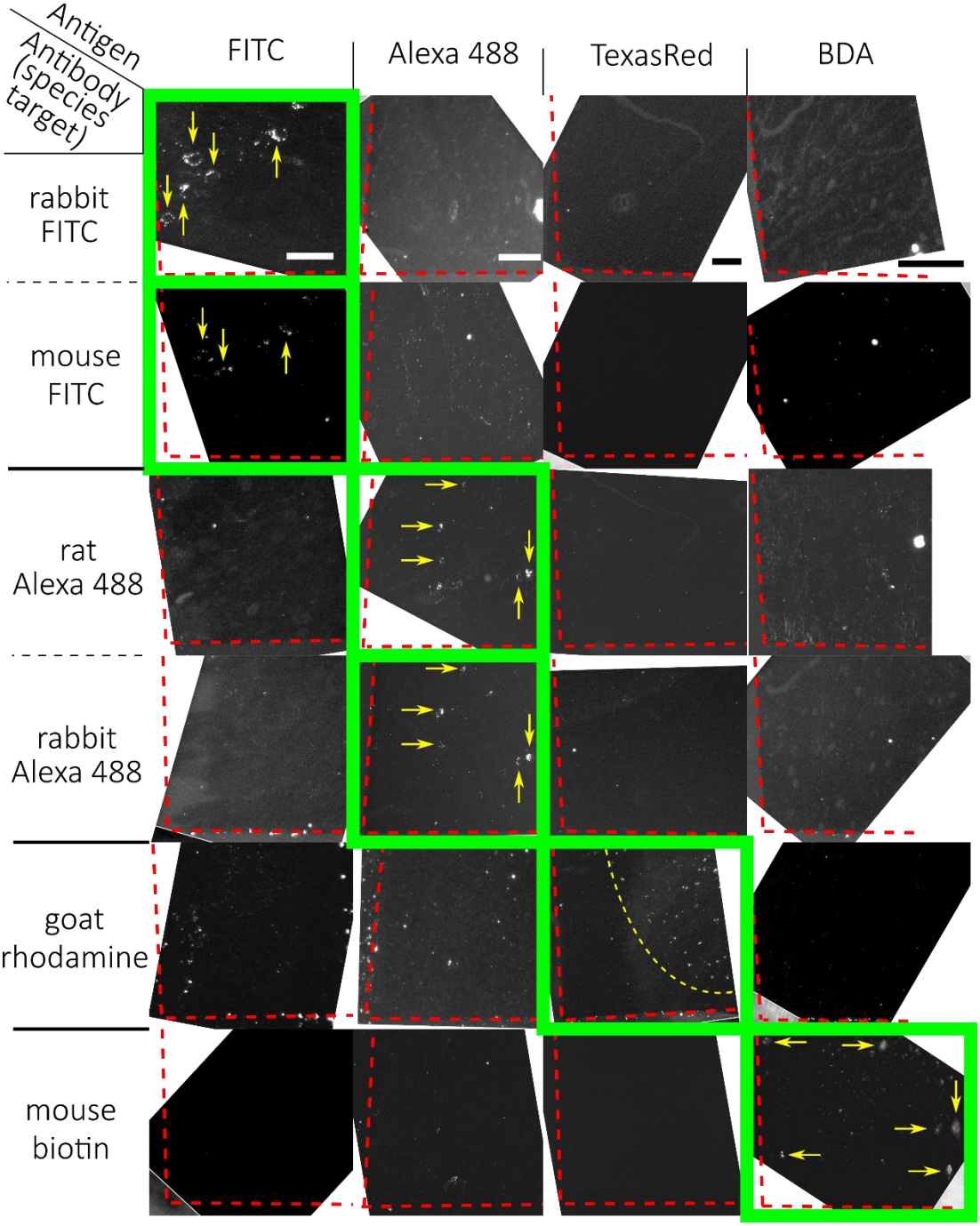

Figure 5 ***Library of tracers and their antibodies****. Each column depicts ultrathin sections from an animal that underwent an injection with a single neuroanatomical tracer. Each row corresponds to a staining performed with a single antibody. Yellow arrows show unambiguous positive staining signal in cell bodies. The red dashed lines outline the borders of the lower left corner of each section. The green frames identify images that showed specific labeling of an antigen, and are distributed as expected from the absence of cross-labeling between antibodies with different target antigens. Scale bars per column from left to right: 20,50, 50 and 50 µm.*

D. Data sets

Two tissue blocks have been sectioned, collected, stained and imaged with CLEM. The blocks stem from two different animals that underwent one or several tracer injections in vivo in different brain areas. Table 3 summarizes the characteristics of the data sets.

Data set	Section number	Anatomical region	Tracer	Injection site	Primary antibody	Secondary antibody	EM size (µm x µm)	EM Dwell time (ns)	Pixel size (nm)
1	507	HVC	alexa 488 FITC texas red	RA Area X Avalanche	rat α-488 mouse α-FITC goat α-rhodamine	488 α-rat 647 α-mouse 546 α-rhodamine	275 x 205	820	8
2	203	Dorsal RA	BDA	Caudal RA	mouse α-BDA	647 α-mouse	185 x 140	6000	8

Table 3 Characteristics of the two data sets presented in this study

Figure 6 shows slices from data set 1 acquired with brightfield fluorescent microscopy after microtomy. The nuclei Robustus of the Arcopallium and Avalanche show strong fluorescence from the tracer injections. The injection into nucleus AreaX was solely checked with a fluorescent binocular and was of good quality. No brightfield and fluorescent pictures were taken more laterally than what is presented in Figure 6 that would have shown the AreaX injection site. Nevertheless, a hint for the good quality of the injection into AreaX is the strong labeling that starts to appear laterally in the LMAN nucleus resulting from retrograde labeling from AreaX.

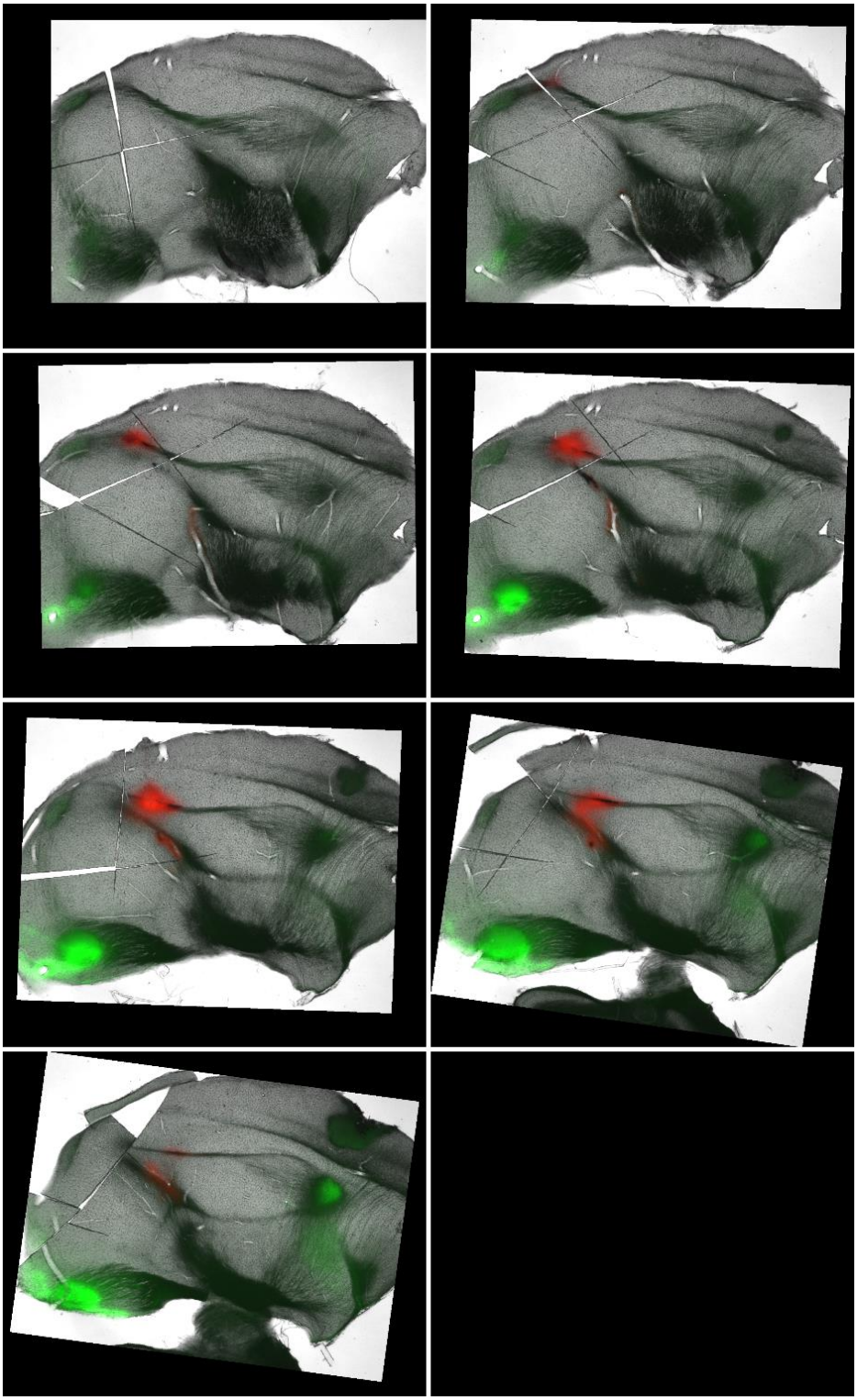

Figure 6 Microtome-sliced tissue after Injection of fluorescent tracers (data set 1). Red: tracer Texas Red targeted to nucleus Avalanche. Green: tracer Alexa 488 targeted to Nucleus Robustus of the Arcopallium (RA) and tracer FITC target to nucleus AreaX. The regions containing HVC have been separated from the slices with a surgical scalpel for further EM processing but put back in place to acquire these images (hence the visible scalpel marks in the top left of the sections).

Figure 7 shows electron micrographs of sections from the HVC data set. Panel a shows numerous sections with a high packing density on wafer, panel b shows a closer view of one section. Note the good dispersion of the magnetic nanoparticles that are virtually invisible at this magnification. Panel c shows well-dispersed superparamagnetic nanoparticles in the appended resin. Panel d shows a small contamination that can be sometimes found in the fluomagnetic resin.

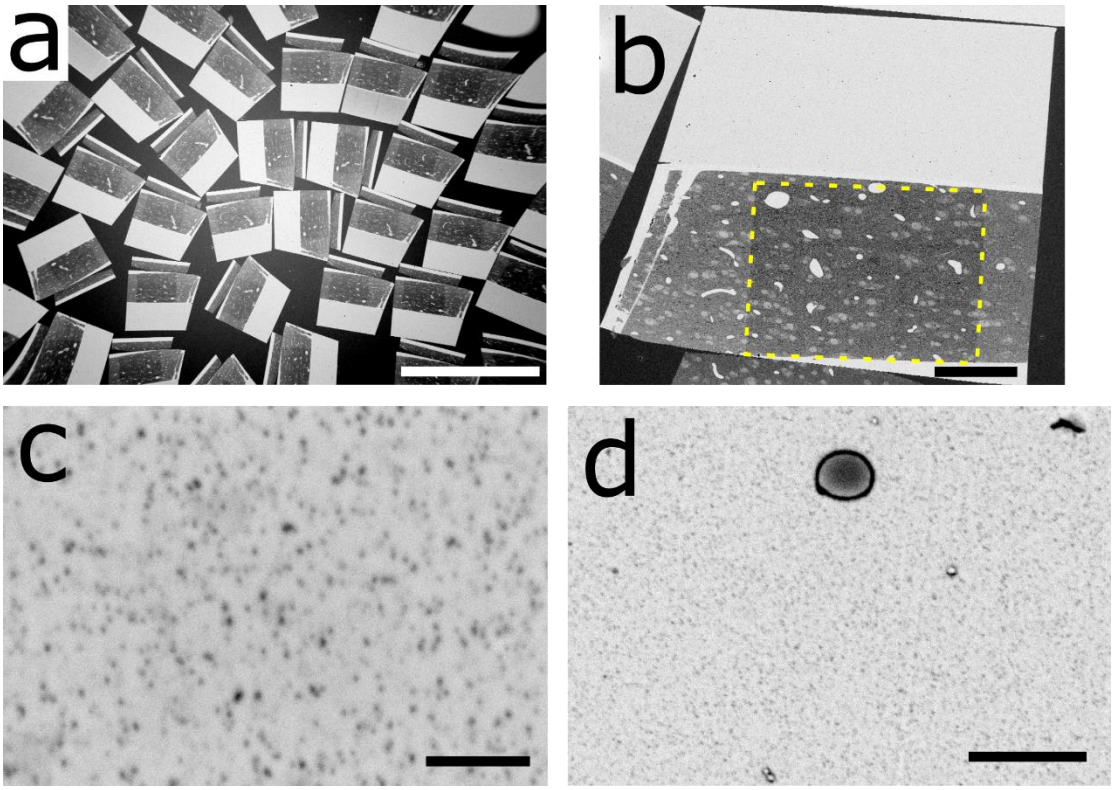

Figure 7 *Electron micrographs of the sections from the HVC data set.* ***a****: electron micrograph of numerous sections collected on wafer.* ***b****: EM of a section. The yellow dashed square highlights the region that has been imaged with the electron microscope and became darker due to the beam irradiation.* ***c****: EM of well-dispersed superparamagnetic nanoparticles in the appended resin.* ***d****: small contaminations can sometimes be found in the fluomagnetic resin. Scale bars: a-1mm, b-100 µm, c-500 nm, d-2µm*

E. Section order retrieval

We performed section order retrieval (SOR) both with electron microscopy imagery of brain tissue and with fluorescent imagery of fluorescent beads contained in the appended fluomagnetic resin. In both cases, we reformulated the SOR problem as an open traveling salesman problem by first making the simple observation that neighbor sections exhibit similar imagery while non-neighbor sections exhibit less similar imagery. Finding the original cutting order is then equivalent to finding the order that maximizes the sum of the similarities across consecutive sections. If we see sections as nodes of a graph and distances between theses nodes as the dissimilarity between the pairs of sections, then we see that the original order should correspond to the path that goes through all sections with a minimal length, which is exactly the well-known problem of the traveling salesman.

1. SOR with EM

SOR withi EM was performed as part of our CLEM data assembly pipeline. As described in the methods sections, a dissimilarity was computed for all pairs of sections using a central box in each of the mosaic tiles of each section. The initial indexing used was the one provided by the section segmentation pipeline. The dissimilarities of all pairs of data sets 1 and 2 are plotted in **Figure 8**,a and **Figure 9**,a, respectively. After solving the traveling salesman problem and reordering the dissimilarity matrix, we obtained the reordered matrices for data sets 1 and 2 in **Figure 8**,b and **Figure 9**,b, respectively. After the volumetric alignment steps of the data assembly pipeline, the order of the sections was manually checked in a volumetric stack and no flip could be noticed, that is, the computed orders were correct.

2. SOR with fluorescent beads

The weight concentration of the fluorescent beads was about 0.2% and 1% in the fluomagnetic resin used for the samples of wafer 1 and 2, respectively.

a. Metric

A metric was defined to assess the quality of the reordering process based on imagery of fluorescent beads. This metric requires the knowledge of the ground truth order, which we obtained from the SOR performed with EM imagery. We call this correct order the “EM order”.

For each section of a reordered dataset, a cost is given to the the link between the given section and the next one. The cost is equal to the difference of the indices of the sections in the ground truth order, minus one. For example, the links of the order 1-2-3-4-5-6-7-8 have the costs 0,0,0,0,0,0,0, so do the links of the 8-7-6-5-4-3-2-1 order, while the links of the order 1-2-4-5-3-8-6-7 have the costs 0,1,0,1,4,1,0. A single flip such as 1-**2**-**4**-3-5-6 has the cost 0,1,0,1,0,0. The frequency of these costs gives an estimate of how precise the reordering is.

b. Low bead concentration

With the low bead concentration used in the sample from wafer 1 the result of the reordering process was overall satisfactory, i.e., there was no major jump in the order, but it did not yield a perfect reordering. **Figure 8** c, d, and e show the results of the reordering with the similarity matrices at the three stages of the reordering process: in panel c the similarity matrix of the original order (this order was given by the section segmentation pipeline), in panel d the similarity matrix of the reordered sections with the bead order (the “bead order” refering to the order obtained with the fluorescent bead imagery), and in panel e the similarity matrix of the sections reordered with the EM order. Panel f of **Figure 8** finally gives the frequency of the costs, with 375 correct links (cost 0). Note that there is a non-negligible number of non-zero links, most of them corresponding to single flips of sections. All costs are below 4, except the highest cost which is 7 and has only one occurrence.

Nevertheless, there is no link with a cost exceeding a few dozens. Such a high cost would indicate that the reordering of a section has completely failed.

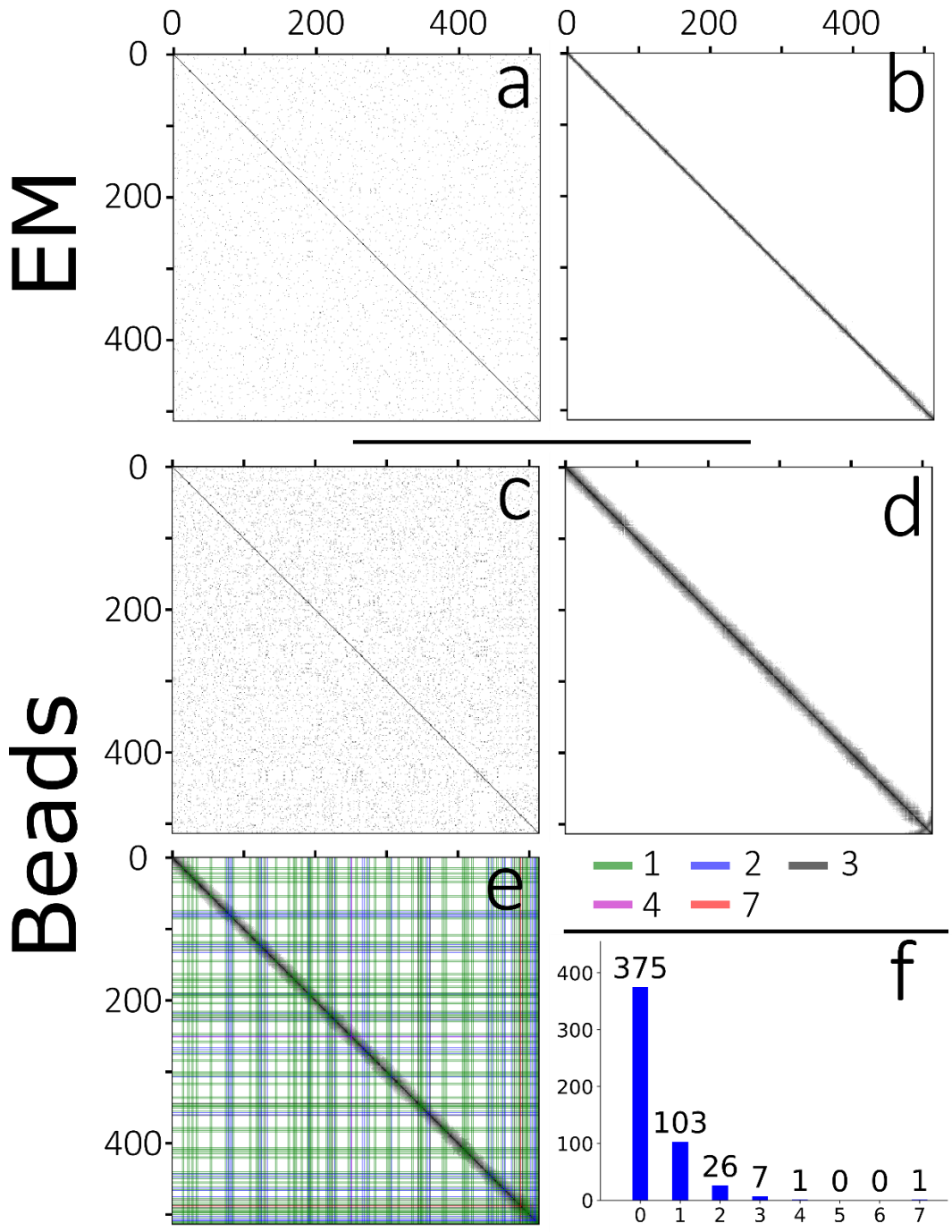

Figure 8 Section order retrieval of data set 1 (low concentration of beads). a: *matrix of pairwise similarities of unordered sections computed with EM imagery. Darker pixels depict higher similarity and white pixels depict no similarity.* ***b:*** *reordered EM matrix.* ***c****: matrix of pairwise similarities of unordered sections computed with fluorescent bead imagery. The original order is the order provided by the section segmentation pipeline.* ***d****: similarity matrix of the reordered sections. The order overall looks consistent, except slight deviations at the end of the data set (around section number 500) that can be seen in the lower left of the matrix.* ***e****: similarity matrix with the EM order. The costs of the links of the bead order are overlayed as vertical and horizontal bars of different colors. The green bars show the locations of the links that have a cost of 1, and there are 103 of them.* ***f****: the distribution of costs of the links. The largest mistake is a link with cost 7 at the end of the data set.*

c. High bead concentration

With the second data set that contained fluomagnetic resin with a higher concentration of fluorescent beads, the reordering process was excellent, leaving only a single flip of two sections at the end of the data set. The similarity matrices before reordering, after reordering with the bead order, and after reordering with the EM order are shown in **Figure 9** c, d, and e, respectively. The apparent white cross in panels d,e at section number 22 is due to a damage to the magnetic portion of the section, in turn probably due to a debris on the knife (not shown).

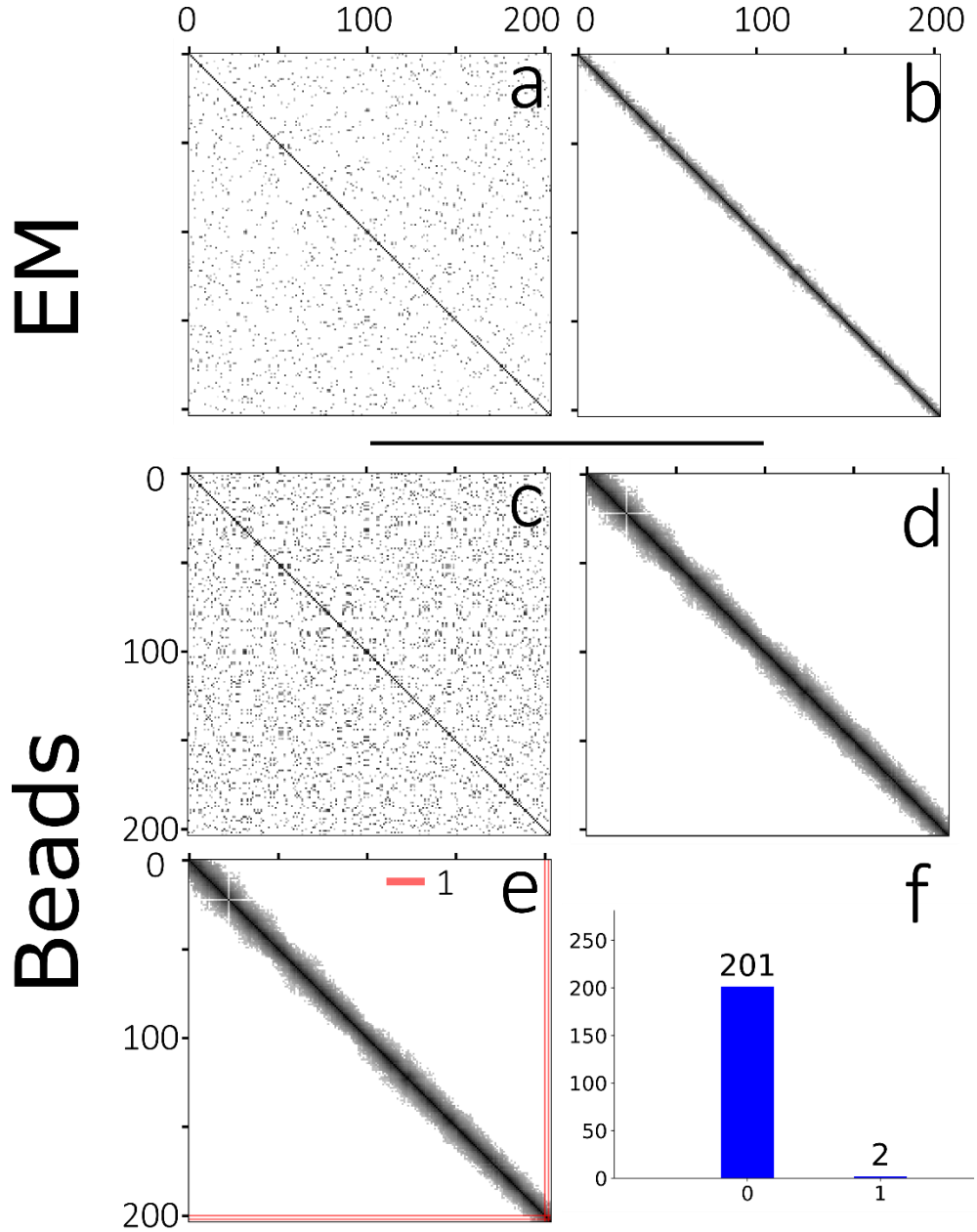

Figure 9 Section order retrieval of data set 2 (high concentration of beads). *Same captions as* ***Figure 8****.* ***e*** *Only two links have a cost of 1 (a single flip), the others have a cost of 0.*

3. Dissimilarity distributions according to neighborhood order

To characterize the accuracy of the order retrieval process we plotted in Figure 10 the distributions of dissimilarities according to the neighboring distance. These values correspond to the values of the subdiagonals in the reordered dissimilarity matrices. A high overlap between the distributions of dissimilarities of direct neighbors with the distributions of dissimilarities of second-next neighbor (2^{nd} order neighbor) indicates that the accuracy of the similarity measure is low. In that case the SOR is likely to contain flips, such as with the low concentrated beads used in sample 1, whose dissimilarity distributions are shown in Figure 10 c. In a first approximation these distributions are gaussian and a fit was computed and overlayed in the histograms of Figure 10.

A low overlap between the distributions on the contrary indicates that the SOR process was more likely to succeed. For example the distributions of first and second order neighbors barely overlap when using high-resolution EM imagery, shown in Figure 10 a,b . Note also that the distributions with the high concentrated beads in Figure 10 d are well more separated than their low concentration couterparts in Figure 10 c.

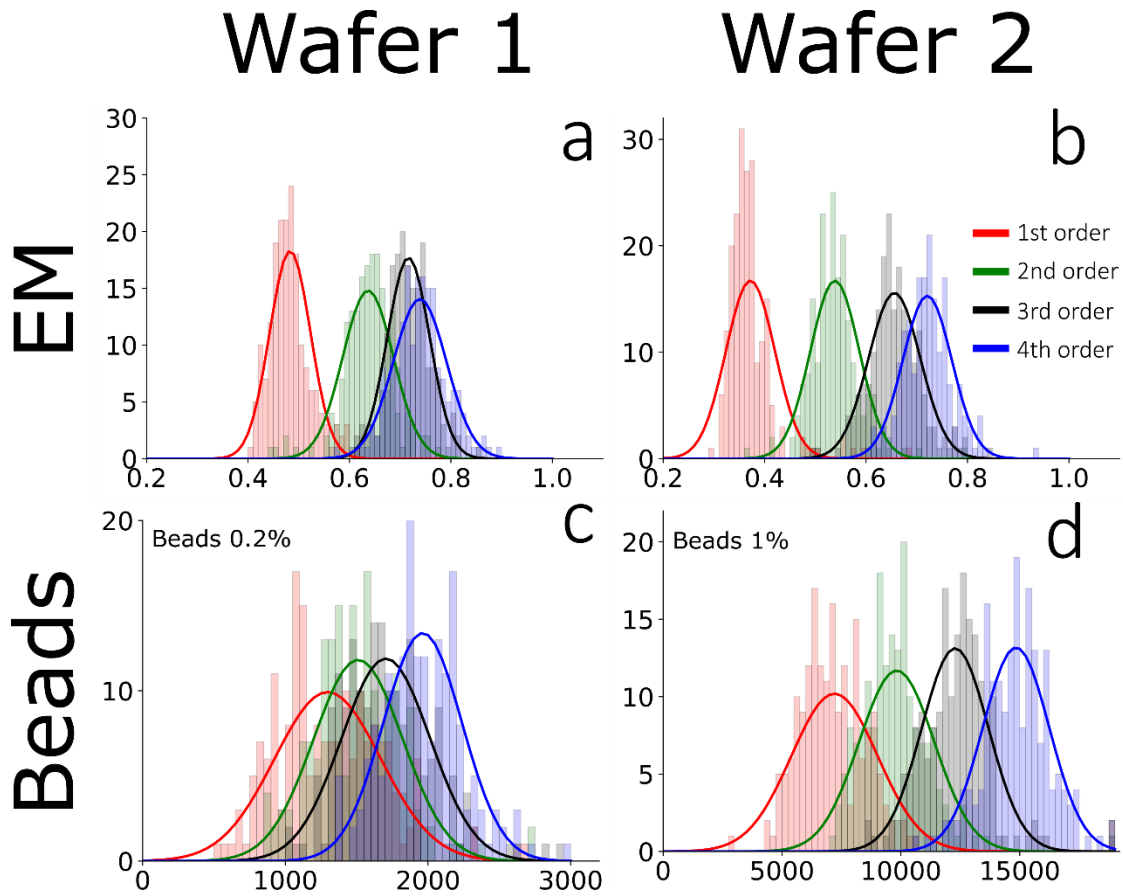

Figure 10 ***Distribution of the pairwise dissimilarities according to neighborhood distance****. The x-axis of the histograms depicts the dissimilarity values in arbitraty units for EM (cross-correlations), and in pixels for the beads (differences of bead diamters in pixels, see methods). Gaussian fits are overlayed on the histograms.* ***Left****: distribution of the dissimilarities in wafer 1.* ***Right****:*

*wafer 2. **First row**: distributions of dissimilarities computed with EM. **Second row**: distribution of dissimilarities computed with fluorescent beads.*

F. Automated LM-EM registration

We registered LM imagery to EM imagery in a fully automated manner. LM and EM imagery is acquired from the exact same tissue sections at different magnifications, therefore a simple similarity transform (rotation, scaling, no shear) would in theory be sufficient for direct cross-modality registration. Nevertheless, it is desirable to visualize correlative imagery not on the raw images directly acquired from the LM and EM microscopes, but in a stitched and aligned stack, which requires non-linear transforms for stitching and 3-dimensional alignment of consecutive sections. We took the EM channel as the reference modality to which the LM should be registered because the EM exhibits the highest resolution.

At which stage of the CLEM data assembly should the cross-modality be performed? If the registration was performed directly on the raw acquired images, then subsequent linear and non-linear transforms required for the stitching and alignment of the EM modality should also be propagated to the LM modality. Also, due to the resolution mismatch between the modalities, single LM tiles span several EM tiles, which makes the process of keeping track of cross-modality transforms cumbersome.

Instead, we chose to perform the cross-modality registration section by section from the affine-stitched LM imagery to the non-linearly stitched and elastically (non-linearly) aligned EM imagery. We did it in two steps by applying first an affine transform and then a local warping transform.

The EM sections were downsampled to the LM resolution (**Figure 11**,c) while the brightfield LM images (**Figure 11**,b) underwent a local contrasting operation ('Normalize local contrast' plugin in Fiji with blocks of 50 x 50 pixels) resulting in the image looking similar to a low-resolution EM micrograph, as shown in **Figure 11**,d.. SIFT features were computed on the images in each modality and then matched across modality according to an affine transform model with the algorithms implemented in Fiji for SIFT matching. **Figure 11**,e shows the remaining matching SIFT features across LM and EM modality in a section from data set 2. Note the high spatial density of the matching features. **Figure 11**,a shows an histogram of the number of matching SIFT features for each LM-EM pair for all sections of dataset 2. Finally, a moving least squares transform was computed with the matching SIFT features to account for small local deformations. The registration accuracy has not been quantified. Instead, when navigating manually the dataset, toggling in and out the brightfield channel on top of the EM channel provides a sense of the quality of the registration, which looks excellent.

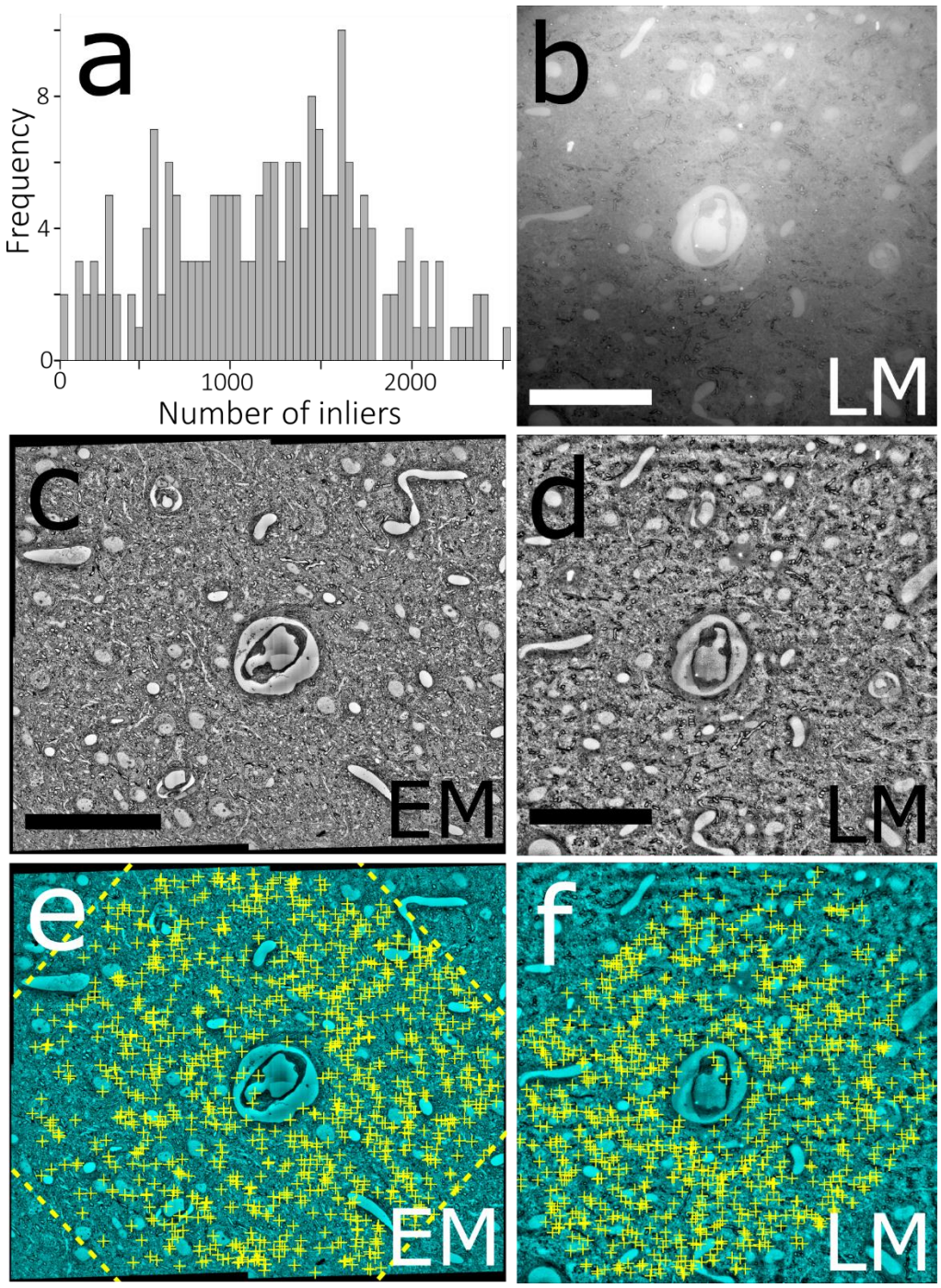

Figure 11 *Automated LM-EM registration.* ***a****: histogram of number of matching inliers found for each of the 203 LM-EM pairs of data set 2.* ***b****: a reflection brightfield light micrograph after simple thresholding.* ***c****: downscaled EM mosaic.* ***d****: same micrograph as in a after local contrast normalization. Note the high similarity with its EM counterpart micrograph in c.* ***e,f****: same micrographs as in c,d, respectively. The yellow crosses show the location of matching SIFT features between the two images. The dashed yellow lines in e show the outline of LM micrograph when affine transformed to match its EM counterpart. Scale bars: 50 µm*

G. Volumetric correlative light and electron microscopy

1. Overview

At the end of our pipeline, correlated LM-EM stacks can be conveniently visualized in an internet browser with the neurodataviz software[6] powered by neuroglancer[7]. Figure 12 below shows data set 2 visualized in an internet browser.

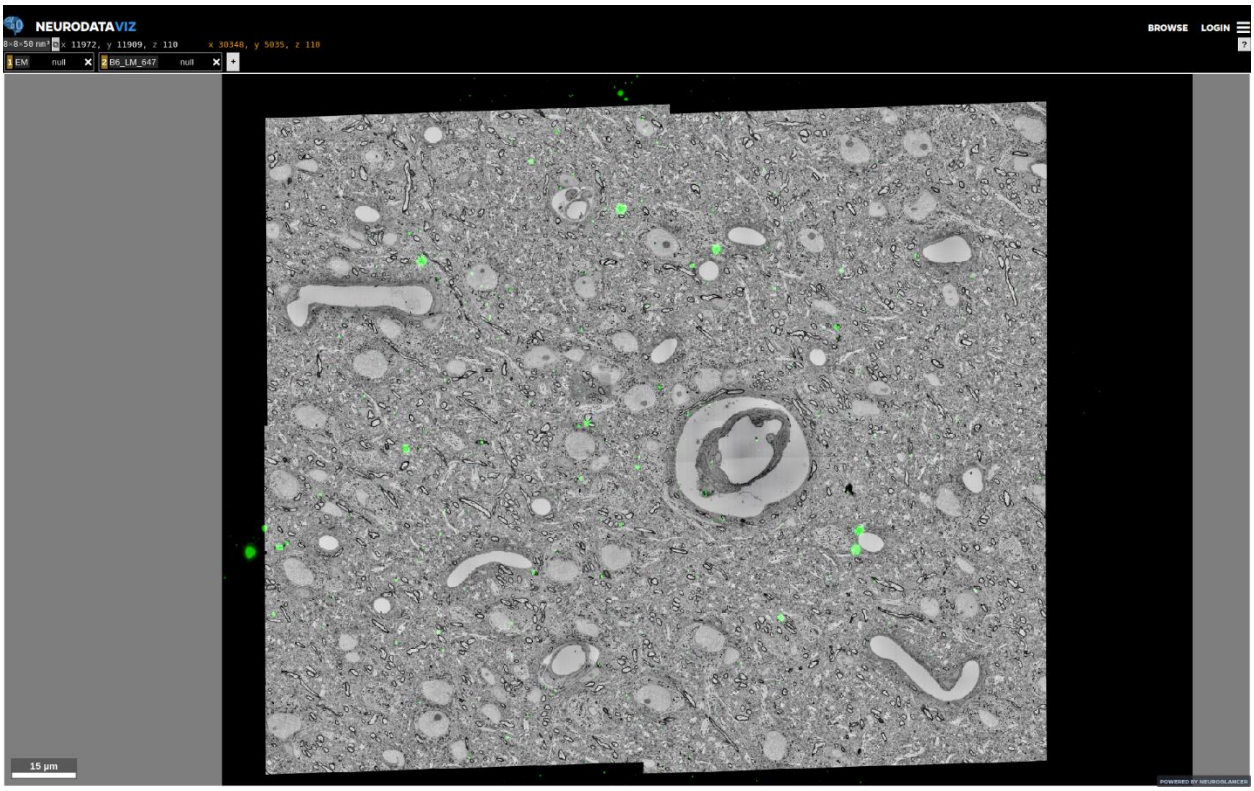

Figure 12 Visualization of CLEM data hosted online with the neurodataviz software. Scale bar 15 microns.

Figure 13 below shows the same data as above with 2 z-reslice panes and a 3-d orthogonal reslice pane.

[6] https://github.com/neurodata/ndviz
[7] https://github.com/google/neuroglancer

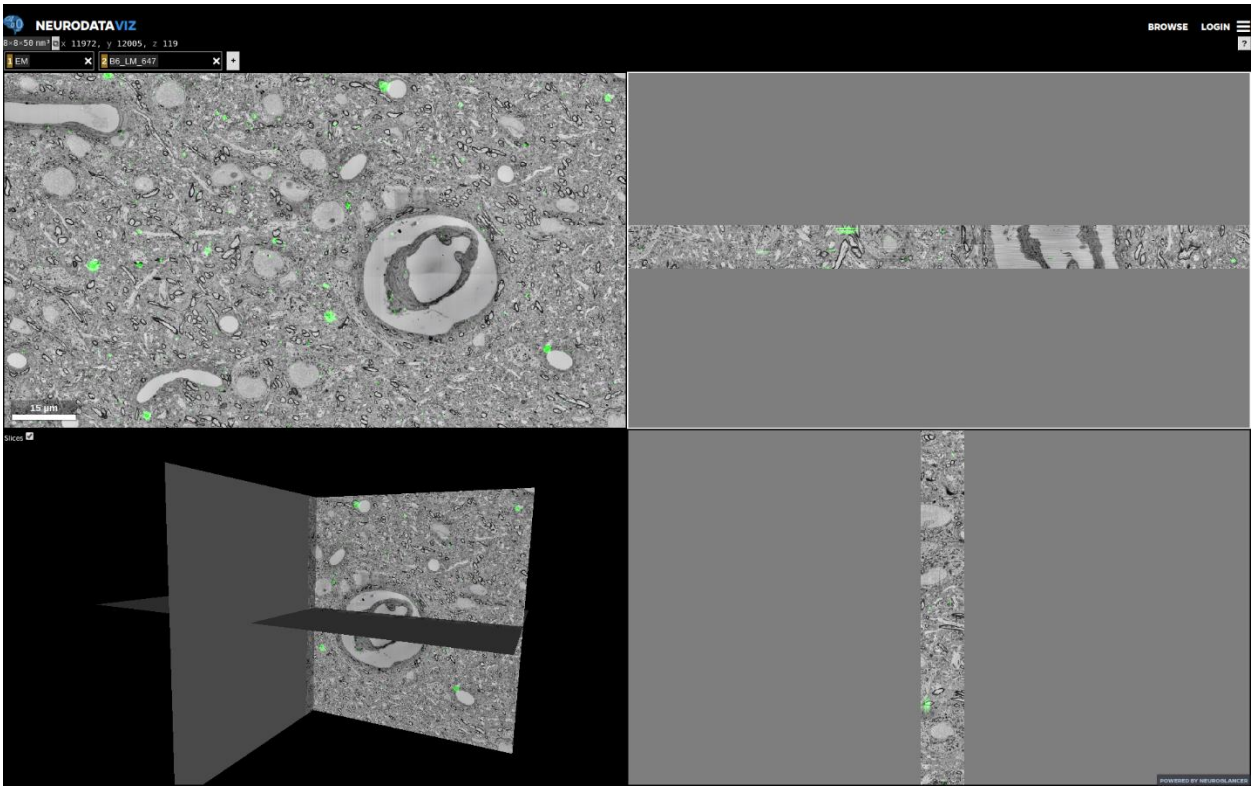

Figure 13 Visualization of CLEM data with 4 panes showing normal view, z-reliced views and 3-d rendered orthogonal views.

2. Examples of volumetric CLEM imagery

Figure 14 shows a small fiber across 48 consecutive sections. Fluorescence is present across consecutive sections in two different portions of the fiber.

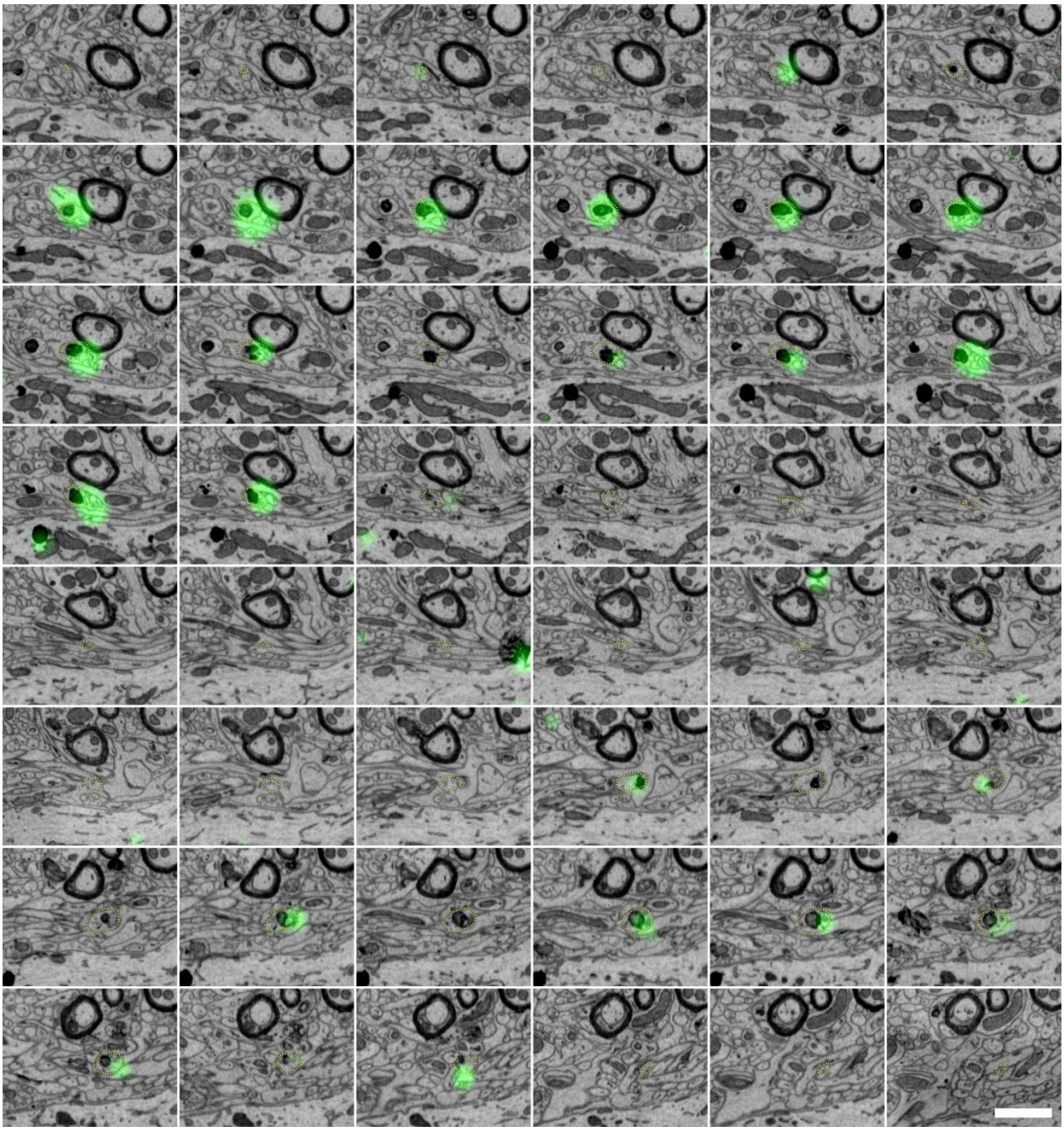

Figure 14 CLEM imagery from 48 consecutive sections showing a labeled fiber. The yellow dashed lines delineate the fiber. Scale bar 1 micron.

Figure 15 below shows a small labeled axon making a synapse *en passant*.

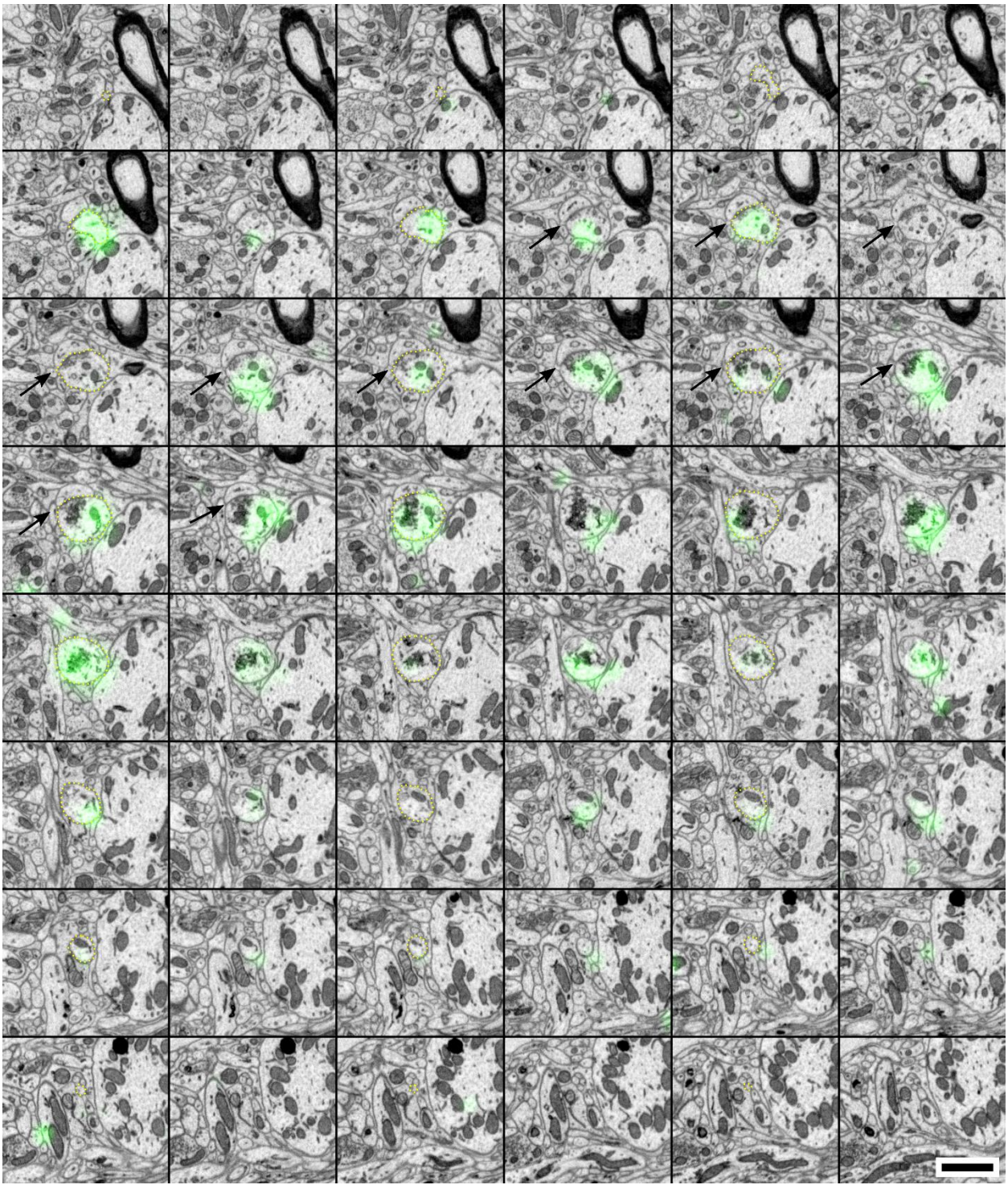

Figure 15 Labeled axon makes a synapse en passant. The axon is delineated with dashed yellow lines (every second section). Black arrows indicate the synapse. Scale bar 1 micron.

Figure 16 shows multicolor CLEM imagery taken from the volumetric data set 1.

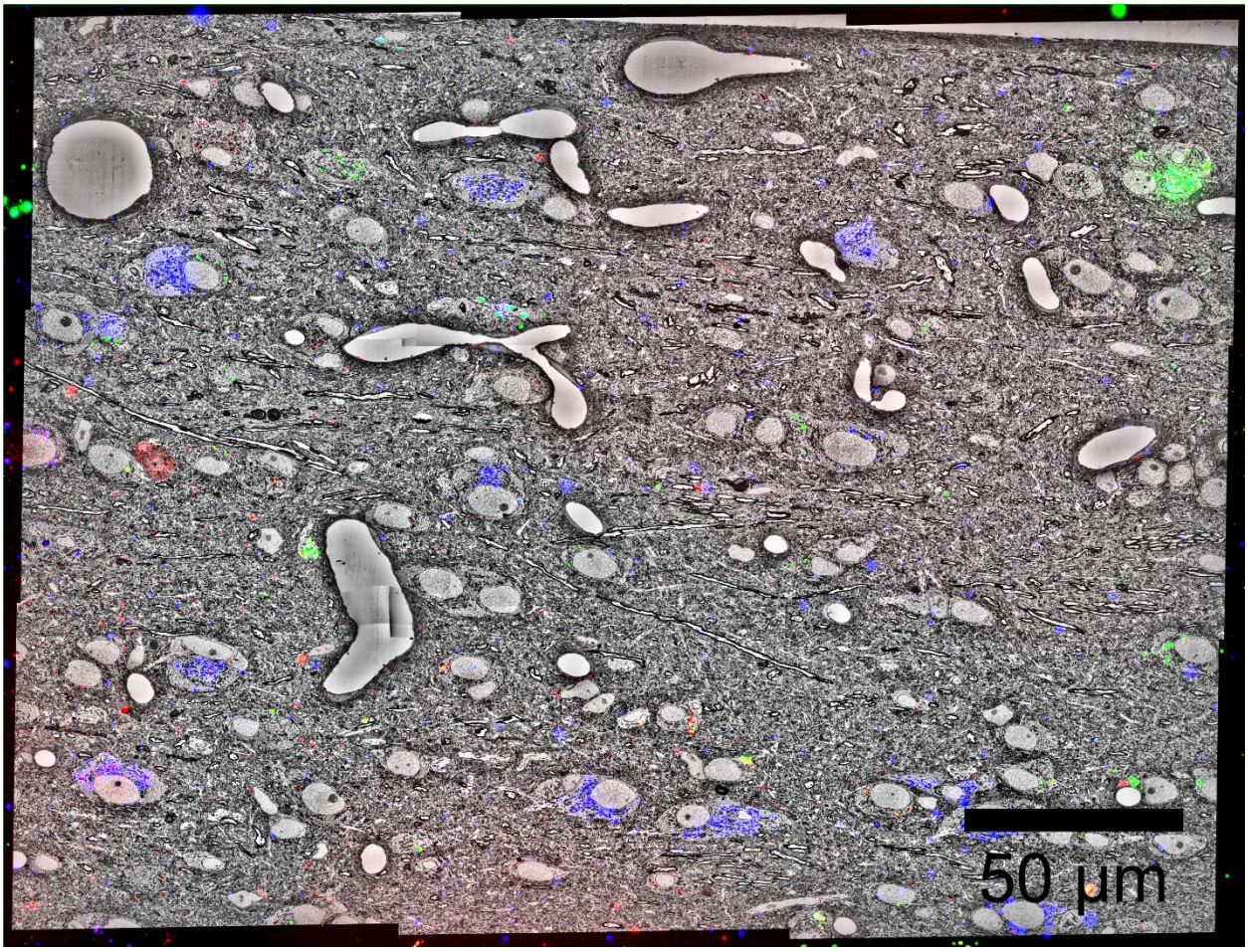

Figure 16 CLEM imagery of one section from data set 1 with 3 fluorescent channels. Green: tracer injected in RA. Red: tracer injected in Avalanche. Blue: tracer injected in Area X.

Figure 17 shows multicolor CLEM imagery of zebra finch HVC nucleus with 3 neuroanatomical tracers injected in Area X, the nucleus Robustus of the Arcopallium, and Avalanche. The two panes on the right show x and y reslices through the volume.

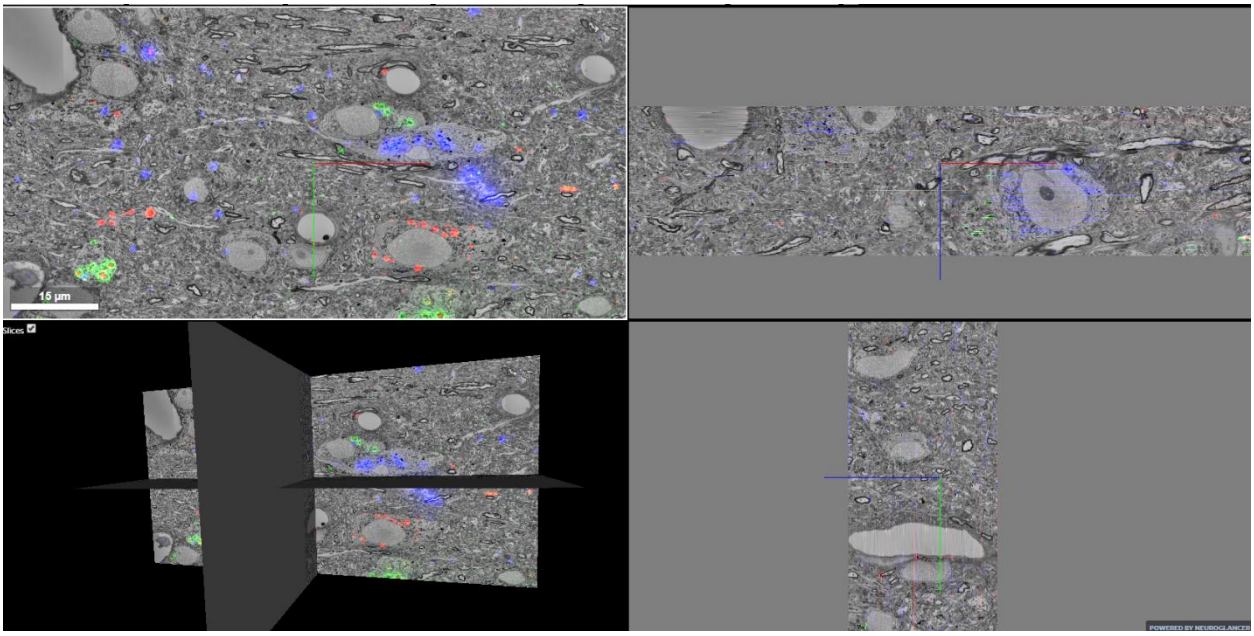

Figure 17 Multicolor CLEM of zebra finch nucleus HVC. *The two panes on the right show x and y reslices through the volume.*

V. Discussion

A. Summary

We introduced a novel technique to collect ultrathin sections of biological tissue directly onto silicon wafers. Collection on such a substrate is ideally suited for post-embedding immunohistochemistry treatment of the sections with subsequent correlative light and electron microscopy imaging. We showed an automated pipeline for data acquisition in light and electron microscopes followed by automated data assembly to finally yield a volumetric correlative stack of brain tissue.

B. A new CLEM platform

Since its introduction in 2007 by the Smith laboratory [35], volumetric postembedding correlative light and electron microscopy has been performed on manually collected ultrathin sections onto flat substrates.

Here we collected hundreds of consecutive sections of nominal thickness 50 nm directly onto silicon wafers. Silicon wafers offer both excellent fluorescent LM (no autofluorescence, easy to coverslip) and excellent EM (no charging thanks to good conductivity, very flat substrate).

The high packing density of the sections collected with MagC has allowed us to image more than 500 sections from a single piece of silicon wafer as small as about 2 cm x 2 cm. Such substrates are easy to handle, process, load into microscopes and store.

The high packing density also presented advantages to perform postembedding immunostaining. A few drops of liquids were easily and conveniently deposited at the wafer surface to simultaneously stain hundreds of sections. The packing density also enabled seamless automated light and electron microscopy imaging. After loading the small silicon wafer chip into the microscope of interest and a simple wafer coordinate calibration, automated acquisition was performed for several hours to several days without interruption.

C. More substrates

In this study we solely demonstrated the collection of ultrathin sections onto silicon wafers. Although we have not attempted it, we are confident that our MagC method should be suitable to collect as well sections on other substrates such as indium tin oxide coated microscope slides or coverslips. We believe that any substrate capable of exhibiting a hydrophilic surface during section landing would be suitable for our collection method. A high hydrophilicity enabling a smooth evaporation of the water on the substrate is necessary, as otherwise drops suddenly appear during the evaporation with uncertain outcomes as to how far might they travel on the wafer substrate, possibly exiting its surface. Also, it is common knowledge in ultramicrotomy that hydrophobic substrates tend to create small wrinkles unlike with hydrophilic substrates.

D. Collecting more sections

The two data sets presented here contained 203 and 512 consecutive ultrathin sections with a nominal thickness of 50 nm. Recent work in the field of connectomics has produced data sets with a greater number of sections, which in some cases is necessary to address questions that relate to biological processes that span a few hundred microns in all three spatial dimensions [4], [6], [7], [9]. Is our technique suited to produce data sets with many thousands of consecutive sections ?

1. Increase collection area

An important feature that we lacked during our experiment was an enclosing hermetic box around the ultramicrotome with for example an atmospheric dust particle filtering system. It would be useful for three reasons: enhance the section thickness homogeneity (as shown by Harris et al. [56]), maintain a clean environment during sectioning and collection to prevent air particles from landing on floating sections, and provide a stable atmosphere free of air currents that typically occur in laboratory rooms and which can impair the magnetic section actuation process. This third feature would have allowed us to probe the magnetic actuation system to its limit to answer what is the maximal attraction capacity of a given magnet. We currently can only claim conservatively that from our observations magnets can carry sections that occupy an area that is roughly the same size of the area of the magnet (with roughly 50 nm thick sections, 50/50 ratio of tissue to fluomagnetic resin, 8% weight magnetic particle concentration in fluomagnetic resin).

We observed that sections did not accumulate in the center of the magnets, but rather at their periphery. It is explained by border effects of magnets that exhibit local attraction maxima at their borders. Experiments with magnets of different sizes, shapes, and arrangements such as with Halbach arrays or mobile magnets would probably increase the collection area.

Increasing the ratio of fluomagnetic resin to the tissue part to for example 80/20 would increase the collection area of a given magnet. For a given section size, increasing this ratio would nevertheless reduce the size of the tissue portion.

Our standard nominal cutting thickness was 50 nm. Increasing this thickness to for example 70 nm, which is a standard in array tomography [28], [35], [39], [40], would increase the strength of the magnetic actuation for sections of a given area and would therefore increase the collection area.

It is important to note again that in order to perform these experiments that would probe the limits of our magnetic section collection, one would need to have a good enclosing system because air currents were in our experience clearly impairing the magnetic section actuation.

2. Collect several wafers

Another approach to increase the total number of collected sections would be to use similar settings as shown in this manuscript, but to simply start the collection process over once a wafer has been collected, leaving the knife alignment unchanged between consecutive runs. For example 10 wafers with 500 sections each would provide 5000 sections which represents a volume sufficiently large to tackle many biological questions. An important unsolved issue with this approach is that sectioning quality tends to be impaired when the first sections are cut during a cutting session [4], [7]. It means for example that after successful collection of 3 wafers, it could happen that the first 5 sections for wafer 4 are significantly impaired, which could break the continuity of the assembled volumetric data. Applications such as ours in connectomics in which we aim to trace fine neuronal processes over long distances would significantly suffer from such discontinuities, while other applications with more qualitative aims would probably be tolerant to such discontinuities.

E. Knife damage

A potential caveat of our method might arise from potential shortening of diamond knife lifetime due to the inclusion of nanoparticles in the sectionable resin.

The fluorescent beads are made of a proprietary polymer whose composition is unknown to us. Nevertheless, the polymer nature of the material hints at probably an innocuous effect on the lifetime of sectioning diamond knives.

The iron oxide nanoparticles might contribute to a shortening of the lifetime of the diamond knife. In our hands, 8% weight concentration of iron oxide nanoparticles did not produce any noticeable impairing effect on the sectioning quality, as demonstrated by the excellent LM and EM imagery of the sections. We successfully cut more than 500 sections in data set 1, and more than 200 in data set 2. Preliminary experiments with cutting several thousands of sections of magnetically augmented blocks did not give the experimenter the impression of significantly shortned diamond knife lifetime. Further experiments would be required to quantify the potential impairing effect of the iron oxide nanoparticles.

F. Section order retrieval

Unlike with section collection or block ablation methods that allow an easy tracking of the index of each physical section or acquired image, section order retrieval (SOR) is a crucial component of our pipeline in order to assemble volumetric imagery from the ultrathin sectioned samples. Our ultrathin sections freely float at the water surface of the collecting bath and except for short ribbons occuring from time to time during the sectioning process, the section order is not physically maintained during the collection.

We reasoned that SOR could be performed after section collection by assessing the similarity of pairs of sections using microscopy imagery. We performed SOR both with electron microscopy acquired on the heavy metal stained brain tissue sections and with fluorescent light microscopy imagery of fluorescent beads contained in the appended fluomagnetic resin. The ability to perform SOR with either modality adds versatility to our section collection approach.

1. SOR with fluorescent beads

We first showed that low concentrated fluorescent beads yielded a satisfactory SOR with only small order flips remaining, which can be manually fixed. We then showed in the second data set of this manuscript that high concentrated fluorescent beads yielded almost flip-free order retrieval (only one flip in 204 sections).

SOR with fluorescent beads presents several advantages over SOR with EM imagery:

- Simple fluorescent light microscopes are clearly more practical to use than their EM counterparts.
- The time needed to acquire fluorescent imagery of beads (about 1 hour for 500 sections) is significantly smaller than what would be needed with EM.
- SOR with EM provides the order only at the end of CLEM pipelines which unvariably first start with LM imaging and then with EM imaging. Performing SOR with EM only prevents one to perform analysis on volumetric LM data before proceeding to EM imaging.

- Some samples studied in CLEM might exhibit less contrast in EM than our brain tissue which has been strongly stained with several heavy metals. The ability to perform SOR without EM therefore does not limit our technique to samples exhibiting strong enough EM contrast for EM SOR. For example, the MagC technique would be suitable to process samples optimized for fluorescent array tomography experiments which do not exhibit strong EM contrast [39].

A SOR using fluorescent beads without any flip still remains to be demonstrated, and we mention in the following a few routes to explore to produce perfect order retrievals.

a. Increasing bead concentration

Increasing the bead concentration intuitively should lead to a more accurate assessment of similarity in pairs of sections. We observed this when increasing the fluorescent bead concentration between the two data sets presented here, resulting in a single section flip with the high bead concentration (with 203 sections). The bead concentration could be increased until it would become difficult to accurately segment separate beads.

b. Increasing the fluomagnetic area

For a given bead concentration, increasing the area of the fluomagnetic portion would enhance the similarity measure as more bead matches would be considered. Note that increasing the fluomagnetic portion of cut sections would decrease the density of tissue present on a given area of substrate.

c. Decreasing the ratio of bead size/section thickness

The beads used were polydisperse with a mean diameter of 2 µm, which is 40 times greater than the nominal thickness of the sections cut in this study. Decreasing the ratio of bead size/section thickness would increase the similarity decay across neighboring sections, which would likely spread more apart the similarity distributions across different neighbor orders. Similarly as with the increase in bead concentration, an increased bead size/section thickness ratio would also likely improve the reordering accuracy.

We did not change our nominal cutting thickness, but we tried to use smaller beads (#Fy-030, MerckMillipore, #R300, Distrilabparticles) to reduce the bead size/section thickness ratio, however they all melted during temperature curing even at low temperatures (40C).

d. Increasing imaging magnification

We imaged the beads only with a 20x, 0.7 NA objective. Using an objective with higher magnification and numerical aperture would enhance the bead segmentation by resolving close neighbors. For example, the bead imaging step could be performed during the same session as high resolution imaging of immunostained tissues with immersion objectives.

e. Better bead extraction

The simple “find maxima” plugin of Fiji could be replaced by more sophisticated algorithms that would provide better bead location and diameter estimates in cases where beads are in contact (when beads are too close, our approach with the simple “find maxima” plugin sees a single bead).

2. SOR with EM imagery

Our SOR with EM yielded flip-free reordering. Instead of performing a second round of reordering with a local optimization methods as introduced by Hanslovsky et al. [62] to resolve potential incorrect flips due to noisy similarity measures, we computed accurate similarity measures by averaging cross-correlation values across multiple fields of view.

G. Cross-modality registration

Instead of using traditional SIFT features, which are hand-crafted features, learned features could be used as well, such as learned invariant features transforms (LIFT, [74]).

Augmenting the brightfield LM imagery to make it ressemble more the EM imagery could have helped to increase the registration success rate of our automated approach [75].

H. Outlook

Our novel magnetic collection approach opens new possibilities to collect many hundreds of sections directly onto silicon wafers and suitable for large scale automaged correlative light and electron microscopy imaging. For connectomics applications, it remains to be shown that volumes spanning several hundreds of micrometers in depth can be assembled.

VI. Acknowledgements

I acknowledge that the work was conducted using infrastructure from the laboratory of R. Hahnloser. I thank Helmut Gnaegi for support in making custom diamond knives and a custom piezo holder. I thank Nicolas Broguière for suggesting Coumarin as a dye resisting to epoxy resin curing.

VII. Bibliography

[1] W. Denk and H. Horstmann, “Serial block-face scanning electron microscopy to reconstruct three-dimensional tissue nanostructure,” *PLoS Biol.*, vol. 2, no. 11, p. e329, Nov. 2004.

[2] K. L. Briggman, “Miniature serial sectioning microtome for block-face imaging,” 2015.

[3] K. J. Hayworth, J. L. Morgan, R. Schalek, D. R. Berger, D. G. C. Hildebrand, and J. W. Lichtman, “Imaging ATUM ultrathin section libraries with WaferMapper: a multi-scale approach to EM reconstruction of neural circuits,” *Front. Neural Circuits*, vol. 8, no. June, p. 68, Jan. 2014.

[4] N. Kasthuri, K. J. Hayworth, D. R. Berger, R. L. Schalek, J. A. Conchello, S. Knowles-Barley, D. Lee, A. Vázquez-Reina, V. Kaynig, T. R. Jones, M. Roberts, J. L. Morgan, J. C. Tapia, H. S. Seung, W. G. Roncal, J. T. Vogelstein, R. Burns, D. L. Sussman, C. E. Priebe, H. Pfister, and J. W. Lichtman, “Saturated Reconstruction of a Volume of Neocortex,” *Cell*, vol. 162, no. 3, pp. 648–661, 2015.

[5] K. M. Harris, J. Spacek, M. E. Bell, P. H. Parker, L. F. Lindsey, A. D. Baden, J. T. Vogelstein, and R. Burns, “A resource from 3D electron microscopy of hippocampal neuropil for user training and tool development.,” *Sci. data*, vol. 2, p. 150046, Sep. 2015.

[6] Z. Zheng, J. S. Lauritzen, E. Perlman, C. G. Robinson, D. Milkie, O. Torrens, J. Price, C. B. Fisher, N. Sharifi, L. Kmecova, I. J. Ali, B. Karsh, E. T. Trautman, J. Bogovic, P. Hanslovsky, G. S. X. E. Jefferis, M. Kazhdan, K. Khairy, R. D. Fetter, D. D. Bock, and N. Square, “A Complete Electron Microscopy Volume Of The Brain Of Adult Drosophila melanogaster,” *bioRxiv*, May 2017.

[7] D. G. C. Hildebrand, M. Cicconet, R. M. Torres, W. Choi, T. M. Quan, J. Moon, A. W. Wetzel, A. Scott Champion, B. J. Graham, O. Randlett, G. S. Plummer, R. Portugues, I. H. Bianco, S. Saalfeld, A. D. Baden, K. Lillaney, R. Burns, J. T. Vogelstein, A. F. Schier, W.-C. A. Lee, W.-K. Jeong, J. W. Lichtman, and F. Engert, “Whole-brain serial-section electron microscopy in larval zebrafish.,” *Nature*, vol. 545, no. 7654, pp. 345–349, May 2017.

[8] J. Kornfeld, S. E. Benezra, R. T. Narayanan, F. Svara, R. Egger, M. Oberlaender, W. Denk, and M. A. Long, “EM connectomics reveals axonal target variation in a sequence-generating network,” *Elife*, vol. 6, 2017.

[9] W. F. Tobin, R. I. Wilson, and W. C. A. Lee, “Wiring variations that enable and constrain neural computation in a sensory microcircuit,” *Elife*, vol. 6, 2017.

[10] D. D. Bock, W.-C. A. Lee, A. M. Kerlin, M. L. Andermann, G. Hood, A. W. Wetzel, S. Yurgenson, E. R. Soucy, H. S. Kim, and R. C. Reid, “Network anatomy and in vivo physiology of visual cortical neurons.,” *Nature*, vol. 471, no. 7337, pp. 177–182, Mar. 2011.

[11] K. L. Briggman, M. Helmstaedter, and W. Denk, “Wiring specificity in the direction-selectivity circuit of the retina.,” *Nature*, vol. 471, no. 7337, pp. 183–188, Mar. 2011.

[12] M. Helmstaedter, K. L. Briggman, S. C. Turaga, V. Jain, H. S. Seung, and W. Denk, “Connectomic reconstruction of the inner plexiform layer in the mouse retina,” *Nature*, vol. 500, no. 7461, pp. 168–174, Aug. 2013.

[13] T. Ohyama, C. M. Schneider-Mizell, R. D. Fetter, J. V. Aleman, R. Franconville, M. Rivera-Alba, B. D. Mensh, K. M. Branson, J. H. Simpson, J. W. Truman, A. Cardona, and M. Zlatic, "A multilevel multimodal circuit enhances action selection in Drosophila," *Nature*, vol. 520, no. 7549, pp. 633–9, 2015.

[14] O. Thaunat, A. G. Granja, P. Barral, A. Filby, B. Montaner, L. Collinson, N. Martinez-Martin, N. E. Harwood, A. Bruckbauer, and F. D. Batista, "Asymmetric Segregation of Polarized Antigen on B Cell Division Shapes Presentation Capacity," *Science (80-.).*, vol. 335, no. 6067, pp. 475–479, Jan. 2012.

[15] S. Dorkenwald, P. J. Schubert, M. F. Killinger, G. Urban, S. Mikula, F. Svara, and J. Kornfeld, "Automated synaptic connectivity inference for volume electron microscopy," *Nat. Methods*, vol. 14, no. 4, pp. 435–442, Apr. 2017.

[16] M. R. G. Russell, T. R. Lerner, J. J. Burden, D. O. Nkwe, A. Pelchen-Matthews, M.-C. Domart, J. Durgan, A. Weston, M. L. Jones, C. J. Peddie, R. Carzaniga, O. Florey, M. Marsh, M. G. Gutierrez, and L. M. Collinson, "3D correlative light and electron microscopy of cultured cells using serial blockface scanning electron microscopy," *J. Cell Sci.*, vol. 130, no. 1, pp. 278–291, Jan. 2017.

[17] B. Maco, A. Holtmaat, M. Cantoni, A. Kreshuk, C. N. Straehle, F. A. Hamprecht, and G. W. Knott, "Correlative In Vivo 2 Photon and Focused Ion Beam Scanning Electron Microscopy of Cortical Neurons," *PLoS One*, vol. 8, no. 2, p. e57405, 2013.

[18] a J. Canty, L. Huang, J. S. Jackson, G. E. Little, G. Knott, B. Maco, and V. De Paola, "In-vivo single neuron axotomy triggers axon regeneration to restore synaptic density in specific cortical circuits.," *Nat. Commun.*, vol. 4, no. May, p. 2038, Jun. 2013.

[19] T. Sonomura, T. Furuta, I. Nakatani, Y. Yamamoto, T. Unzai, W. Matsuda, H. Iwai, A. Yamanaka, M. Uemura, and T. Kaneko, "Correlative analysis of immunoreactivity in confocal laser-scanning microscopy and scanning electron microscopy with focused ion beam milling.," *Front. Neural Circuits*, vol. 7, no. February, p. 26, 2013.

[20] O. Urwyler, A. Izadifar, D. Dascenco, M. Petrovic, H. He, D. Ayaz, A. Kremer, S. Lippens, P. Baatsen, C. J. Guerin, and D. Schmucker, "Investigating CNS synaptogenesis at single-synapse resolution by combining reverse genetics with correlative light and electron microscopy," *Development*, vol. 142, no. 2, pp. 394–405, Jan. 2015.

[21] B. G. Kopek, G. Shtengel, J. B. Grimm, D. A. Clayton, and H. F. Hess, "Correlative Photoactivated Localization and Scanning Electron Microscopy," *PLoS One*, vol. 8, no. 10, p. e77209, Jan. 2013.

[22] P. de Boer, J. P. Hoogenboom, and B. N. G. Giepmans, "Correlated light and electron microscopy: ultrastructure lights up!," *Nat. Methods*, vol. 12, no. 6, pp. 503–513, May 2015.

[23] A. A. Wanner, C. Genoud, T. Masudi, L. Siksou, and R. W. Friedrich, "Dense EM-based reconstruction of the interglomerular projectome in the zebrafish olfactory bulb.," *Nat. Neurosci.*, vol. 19, no. 6, pp. 816–25, 2016.

[24] J. A. Bogovic, P. Hanslovsky, A. Wong, and S. Saalfeld, "Robust registration of calcium images by learned contrast synthesis," in *2016 IEEE 13th International Symposium on Biomedical Imaging (ISBI)*, 2016, pp. 1123–1126.

[25] J. L. Morgan, D. R. Berger, A. W. Wetzel, and J. W. Lichtman, "The Fuzzy Logic of Network Connectivity in Mouse Visual Thalamus," *Cell*, vol. 165, no. 1, pp. 192–206, 2016.

[26] C. S. Own, M. F. Murfitt, L. S. Own, D. Brittain, N. Costa, R. C. Reid, and G. C. David, “Reel-to-Reel Electron Microscopy : Latency-Free Continuous Imaging of Large Sample Volumes,” *Microsc. Microanal.*, vol. 21, no. 79, pp. 157–158, 2015.

[27] C. S. Own, M. F. Murfitt, L. S. Own, and J. Cushing, “Developments in Reel-to-Reel Electron Microscopy Infrastructure,” *Microsc. Microanal.*, vol. 23, no. S1, pp. 32–33, Jul. 2017.

[28] K. D. Micheva, B. Busse, N. C. Weiler, N. O’Rourke, and S. J. Smith, “Single-synapse analysis of a diverse synapse population: Proteomic imaging methods and markers,” *Neuron*, vol. 68, no. 4, pp. 639–653, Nov. 2010.

[29] W. P. Faulk and G. T. Malcolm, “Communication to the editors. An immunocolloid method for the electron microscope,” *Immunochemistry*, vol. 8, no. 11, pp. 1081–1083, Nov. 1971.

[30] J. R. Anderson, B. W. Jones, J. H. Yang, M. V. Shaw, C. B. Watt, P. Koshevoy, J. Spaltenstein, E. Jurrus, U. Kannan, R. T. Whitaker, D. Mastronarde, T. Tasdizen, and R. E. Marc, “A computational framework for ultrastructural mapping of neural circuitry,” *PLoS Biol.*, vol. 7, no. 3, pp. 0493–0512, Mar. 2009.

[31] J. R. Anderson, B. W. Jones, C. B. Watt, M. V Shaw, J. H. Yang, D. Demill, J. S. Lauritzen, Y. Lin, K. D. Rapp, D. Mastronarde, P. Koshevoy, B. Grimm, T. Tasdizen, R. Whitaker, and R. E. Marc, “Exploring the retinal connectome,” *Mol Vis*, vol. 17, no. July 2010, pp. 355–379, 2011.

[32] R. E. Marc, J. R. Anderson, B. W. Jones, C. L. Sigulinsky, and J. S. Lauritzen, “The AII amacrine cell connectome: a dense network hub,” *Front Neural Circuits*, vol. 8, no. September, p. 104, 2014.

[33] A. Pombo, M. Hollinshead, and P. R. Cook, “Bridging the resolution gap: Imaging the same transcription factories in cryosections by light and electron microscopy.,” *J. Histochem. Cytochem.*, vol. 47, no. 4, pp. 471–80, Apr. 1999.

[34] R. Shahidi, E. A. Williams, M. Conzelmann, A. Asadulina, C. Verasztó, S. Jasek, L. A. Bezares-Calderón, and G. Jékely, “A serial multiplex immunogold labeling method for identifying peptidergic neurons in connectomes,” *Elife*, vol. 4, no. DECEMBER2015, 2015.

[35] K. D. Micheva and S. J. Smith, “Array Tomography: A New Tool for Imaging the Molecular Architecture and Ultrastructure of Neural Circuits,” *Neuron*, vol. 55, no. 1, pp. 25–36, Jul. 2007.

[36] D. Oberti, M. a Kirschmann, and R. H. R. Hahnloser, “Correlative microscopy of densely labeled projection neurons using neural tracers.,” *Front. Neuroanat.*, vol. 4, no. June, p. 24, 2010.

[37] S. Nanguneri, B. Flottmann, H. Horstmann, M. Heilemann, and T. Kuner, “Three-dimensional, tomographic super-resolution fluorescence imaging of serially sectioned thick samples,” *PLoS One*, vol. 7, no. 5, p. e38098, Jan. 2012.

[38] I. Wacker and R. R. Schroeder, “Array tomography,” *J. Microsc.*, vol. 252, no. 2, pp. 93–99, Nov. 2013.

[39] Y. M. Sigal, C. M. Speer, H. P. Babcock, and X. Zhuang, “Mapping Synaptic Input Fields of Neurons with Super-Resolution Imaging,” *Cell*, vol. 163, no. 2, pp. 493–505, Oct. 2015.

[40] F. Collman, J. Buchanan, K. D. Phend, K. D. Micheva, R. J. Weinberg, and S. J. Smith, “Mapping Synapses by Conjugate Light-Electron Array Tomography,” *J. Neurosci.*, vol. 35, no. 14, pp. 5792–5807, 2015.

[41] J.-C. Rah, E. Bas, J. Colonell, Y. Mishchenko, B. Karsh, R. D. Fetter, E. W. Myers, D. B. Chklovskii, K. Svoboda, T. D. Harris, and J. T. R. Isaac, “Thalamocortical input onto layer 5 pyramidal neurons measured using quantitative large-scale array tomography.,” *Front. Neural Circuits*, vol. 7, no. November, p. 177, 2013.

[42] S. D. Gale, A. L. Person, and A. D. J. Perkel, “A novel basal ganglia pathway forms a loop linking a vocal learning circuit with its dopaminergic input,” *J. Comp. Neurol.*, vol. 508, no. 5, pp. 824–839, Jun. 2008.

[43] M. W. Linhoff, S. K. Garg, and G. Mandel, “A high-resolution imaging approach to investigate chromatin architecture in complex tissues.,” *Cell*, vol. 163, no. 1, pp. 246–55, Sep. 2015.

[44] D. Oberti, M. A. Kirschmann, and R. H. R. Hahnloser, “Projection neuron circuits resolved using correlative array tomography,” *Front. Neurosci.*, vol. 5, no. APR, 2011.

[45] H. Horstmann, C. Körber, K. Sätzler, D. Aydin, and T. Kuner, “Serial section scanning electron microscopy (S 3EM) on silicon wafers for ultra-structural volume imaging of cells and tissues,” *PLoS One*, vol. 7, no. 4, p. e35172, Jan. 2012.

[46] I. Wacker, W. Spomer, A. Hofmann, M. Thaler, S. Hillmer, U. Gengenbach, and R. R. Schröder, “Hierarchical imaging: a new concept for targeted imaging of large volumes from cells to tissues,” *BMC Cell Biol.*, vol. 17, no. 1, p. 38, 2016.

[47] T. Koike, Y. Kataoka, M. Maeda, Y. Hasebe, Y. Yamaguchi, M. Suga, A. Saito, and H. Yamada, “A Device for Ribbon Collection for Array Tomography with Scanning Electron Microscopy,” *Acta Histochem. Cytochem.*, vol. 50, no. 5, pp. 135–140, Oct. 2017.

[48] M. J. F. Blumer, P. Gahleitner, T. Narzt, C. Handl, and B. Ruthensteiner, “Ribbons of semithin sections: An advanced method with a new type of diamond knife,” *J. Neurosci. Methods*, vol. 120, no. 1, pp. 11–16, Oct. 2002.

[49] K. D. Micheva, N. O'Rourke, B. Busse, and S. J. Smith, “Array tomography: Production of arrays,” *Cold Spring Harb. Protoc.*, vol. 5, no. 11, p. pdb.prot5524, Nov. 2010.

[50] T. Templier and R. Hahnloser, “Correlative Array Tomography,” in *Biological Field Emission Gun Scanning Electron Microscopy*, 2018.

[51] F. C. Collman, Davis S., Gliko O., Keenan T. M., Parker K., Ostroff L. E., and Smith S. J., “An integrated imaging and staining platform for cubic millimeter scale array tomography,” in *Society for Neuroscience, Program No. 735.02*, 2015.

[52] T. J. Deerinck, E. a. Bushong, a. Thor, and M. H. Ellisman, “NCMIR methods for 3D EM: A new protocol for preparation of biological specimens for serial block face scanning electron microscopy,” *Microscopy*, pp. 6–8, 2010.

[53] J. C. Tapia, N. Kasthuri, K. J. Hayworth, R. Schalek, J. W. Lichtman, S. J. Smith, and J. Buchanan, “High-contrast en bloc staining of neuronal tissue for field emission scanning electron microscopy,” *Nat. Protoc.*, vol. 7, no. 2, pp. 193–206, Feb. 2012.

[54] J. Puig, C. E. Hoppe, L. A. Fasce, C. J. Pérez, Y. Piñeiro-Redondo, M. Bañobre-López, M. A. López-Quintela, J. Rivas, and R. J. J. Williams, “Superparamagnetic nanocomposites based on the dispersion of oleic acid-stabilized magnetite nanoparticles in a diglycidylether of bisphenol A-based epoxy matrix: Magnetic hyperthermia and shape memory,” *J. Phys. Chem. C*, vol. 116, no.

24, pp. 13421–13428, 2012.

[55] G. Knott, S. Rosset, and M. Cantoni, “Focussed ion beam milling and scanning electron microscopy of brain tissue.,” *J. Vis. Exp.*, no. 53, p. e2588, 2011.

[56] K. M. Harris, E. Perry, J. Bourne, M. Feinberg, L. Ostroff, and J. Hurlburt, “Uniform Serial Sectioning for Transmission Electron Microscopy,” *J. Neurosci.*, vol. 26, no. 47, pp. 12101–12103, Nov. 2006.

[57] S. Preibisch, S. Saalfeld, and P. Tomancak, “Globally optimal stitching of tiled 3D microscopic image acquisitions,” *Bioinformatics*, vol. 25, no. 11, pp. 1463–1465, 2009.

[58] I. Arganda-Carreras, M. Hiner, J. Funke, M. Ezzat, C. Rueden, P. Freydiere, E. Meijering, H. S. Seung, J. Schindelin, J.-Y. Tinevez, J. Eglinger, V. Kaynig, and A. Cardona, “Trainable_Segmentation: Release v3.1.2.” 2016.

[59] A. Edelstein, N. Amodaj, K. Hoover, R. Vale, N. Stuurman, A. Edelstein, N. Amodaj, K. Hoover, R. Vale, and N. Stuurman, “Computer Control of Microscopes Using µManager,” in *Current Protocols in Molecular Biology*, Hoboken, NJ, USA: John Wiley & Sons, Inc., 2010, p. 14.20.1-14.20.17.

[60] A. D. Edelstein, M. A. Tsuchida, N. Amodaj, H. Pinkard, R. D. Vale, and N. Stuurman, “Advanced methods of microscope control using µManager software,” *J. Biol. Methods*, vol. 1, no. 2, p. 10, Nov. 2014.

[61] T. Templier and R. H. R. Hahnloser, “Method, device and system for manipulating portions of a rigid body,” 2015.

[62] P. Hanslovsky, J. A. Bogovic, and S. Saalfeld, “Image-based correction of continuous and discontinuous non-planar axial distortion in serial section microscopy,” *Bioinformatics*, vol. 33, no. 9, p. btw794, Dec. 2016.

[63] D. Applegate, R. E. Bixby, V. Chvátal, and William J. Cook, “Concorde TSP Solver.” 2003.

[64] A. Cardona, S. Saalfeld, J. Schindelin, I. Arganda-Carreras, S. Preibisch, M. Longair, P. Tomancak, V. Hartenstein, and R. J. Douglas, “TrakEM2 software for neural circuit reconstruction,” *PLoS One*, vol. 7, no. 6, p. e38011, 2012.

[65] S. Preibisch, S. Saalfeld, T. Rohlfing, and P. Tomancak, “Bead-based mosaicing of single plane illumination microscopy images using geometric local descriptor matching,” in *Proceedings of SPIE*, 2009, vol. 7259, no. 1, p. 72592S–72592S–10.

[66] S. Saalfeld, A. Cardona, V. Hartenstein, and P. Tomančák, “CATMAID: Collaborative annotation toolkit for massive amounts of image data,” *Bioinformatics*, vol. 25, no. 15, pp. 1984–1986, 2009.

[67] S. Saalfeld, R. Fetter, A. Cardona, and P. Tomancak, “Elastic volume reconstruction from series of ultra-thin microscopy sections.,” *Nat. Methods*, vol. 9, no. 7, pp. 717–20, Jul. 2012.

[68] D. G. Lowe and D. G., “Distinctive Image Features from Scale-Invariant Keypoints,” *Int. J. Comput. Vis.*, vol. 60, no. 2, pp. 91–110, Nov. 2004.

[69] S. Schaefer, T. McPhail, and J. Warren, “Image deformation using moving least squares,” *ACM Trans. Graph.*, vol. 25, no. 3, p. 533, 2006.

[70] W. Spomer, A. Hofmann, I. Wacker, L. Ness, P. Brey, R. R. Schroder, and U. Gengenbach,

"Advanced substrate holder and multi-axis manipulation tool for ultramicrotomy," *Microsc. Microanal.*, vol. 21, no. S3, pp. 1277–1278, 2015.

[71] C. Peters, O. Ergeneman, B. J. Nelson, and C. Hierold, "Superparamagnetic swimming microrobots with adjusted magnetic anisotropy," *Proc. IEEE Int. Conf. Micro Electro Mech. Syst.*, pp. 564–567, 2013.

[72] Z. Sekhavat Pour and M. Ghaemy, "Fabrication and characterization of superparamagnetic nanocomposites based on epoxy resin and surface-modified ??-Fe2O3 by epoxide functionalization," *J. Mater. Sci.*, vol. 49, no. 12, pp. 4191–4201, Feb. 2014.

[73] Studer and Gnaegi, "Minimal compression of ultrathin sections with use of an oscillating diamond knife," *J. Microsc.*, vol. 197, no. 1, pp. 94–100, Jan. 2000.

[74] K. M. Yi, E. Trulls, V. Lepetit, and P. Fua, "LIFT: Learned Invariant Feature Transform," in *Proceedings of the {E}uropean {C}onference on {C}omputer {V}ision*, 2016.

[75] C. Ounkomol, D. A. Fernandes, S. Seshamani, M. M. Maleckar, F. Collman, and G. R. Johnson, "Three dimensional cross-modal image inference: label-free methods for subcellular structure prediction," *bioRxiv*, p. 216606, Dec. 2017.

Chapter 3

Hybrid Mechanical Sectioning and Broad Ion Beam Milling for Volumetric Correlative Light and Electron Microscopy

Contents

Hybrid Mechanical Sectioning and Broad Ion Beam Milling for Volumetric Correlative Light and Electron Microscopy

Thomas Templier[1,2]

1 Institute of Neuroinformatics, University of Zurich and ETH Zurich
2 Zurich Neuroscience Center ZNZ, Zurich, Switzerland

thomas.templier2@gmail.com

1 Abstract

Biological mechanisms operate in the three spatial dimensions and many do so at small spatial scales while extending over large volumes. An ideal structural imaging technology should allow us to visualize isotropically at nanometer resolution in large volumes the ultrastructure and protein content of biological tissues.

I introduce a new technology for biological volumetric scanning electron microscopy (EM) imaging over large cross-sectional areas, with sub-10 nm axial resolution (interspersed with ~40 nm gaps), that can be combined with postembedding immunohistochemistry (IHC) and correlated with fluorescent light microscopy (LM).

It consists in performing cycles of broad ion beam (BIB) milling and EM imaging on tissue sections that have been non-destructively mechanically cut and collected directly on silicon wafers. I show a volumetric dataset (115 μm x 85 μm x 2.4 μm) of correlative scanning EM (10 nm x 10 nm x ~6 nm interspersed every 120 nm with a ~40 nm gap) and multichannel fluorescent post-embedding LM of connectomics-grade brain tissue obtained from 20 mechanically cut sections of thickness 120 nm.

Hybrid mechanical sectioning and BIB milling combined with fluorescent LM and multi-beam scanning EM has the potential to become the new imaging technology of choice for cellular-resolution connectomics and other fields of biology.

2 Introduction

2.1 Imaging technology for cellular-resolution connectomics

Cellular-resolution connectomics is currently driving technological development for biological structural imaging with electron microscopy (EM) and is now seeking to acquire millimeter cube sized [53, 73] volumes of brain tissue at nanometric [2, 7, 26, 31, 32, 37, 42, 61, 91, 93, 95, 105] and at as isotropic as possible [83, 84, 99] resolution, possibly enhanced with immunostaining [47, 76] and possibly correlated with post-embedding fluorescent [10, 52, 59] or cathodoluminescent microscopy [20, 48, 103, 104].

There is however currently no technology offering simultaneously high-throughput, nanometric, isotropic correlative imaging of millimeter cube sized tissue volumes. I review briefly available technologies, focusing particularly on the isotropicity-volume trade-off before comparing imaging speeds and finally introducing a material-ablating technology widely spread in material science but barely used in biology.

2.2 Serial block face scanning electron microsopy

In biological serial block face scanning EM (SBFSEM) [14, 44], the smallest reported section thickness for a volumetric dataset is 10 nm over 370 consecutive sections [70], closely followed by a report of 15 nm over more than 1000 sections [88].

A finer control of the in-chamber mechanical sectioning process with a closed-loop system could lower this section thickness limit or at least increase the reliability of the process at low thicknesses such as 15 nm [6]. Note also that interspersing physical sectioning with landing multi-energy imaging combined with software deconvolution could in theory yield a clearly lower effective section thickness [3–5, 12, 65]. However, the need for signal from backscattered electrons in the landing multi-energy approach makes it likely incompatible with the high throughput scanning EM (SEM) multi-beam technology that uses secondary electrons detectors [18, 73].

2.3 Non-destructive serial physical sectioning

In non-destructive serial physical sectioning, array tomography [10, 52, 56, 59, 68, 78, 94] has produced datasets of several hundreds of consecutive sections with section thicknesses down to 50 nm. The collection of sections directly on flat substrates is indeed more difficult with lower thicknesses. With the tape conveyer belt technique called ATUM [27, 28, 37], Kasthuri et al. [37], Morgan et al. [55], and Hildebrand et al. [32] collected 2250, 10000 and ~15000 consecutive sections of mouse somatosensory cortex, mouse dLGN, and of an almost entire larval zebra fish brain, respectively, with 29, 30, and 50 nm thickness, respectively. Finally, Zheng et al. [105] produced for transmission EM 7060 sections of ~40 nm thickness of an entire Drosophila brain.

As it is the case for SBFSEM, the current lower section thickness limit of about 30 nm for volumetric non-destructive serial physical sectioning could in theory be improved by multi-energy landing deconvolution (provided that the deep signal acquired from close to the substrate is of good quality) or by performing FIBSEM on the collected physical sections to obtain isotropic imagery [94]. Note however that performing FIBSEM on individual serial sections after physical sectioning [94] is a prohibitively slow process for a large number of sections.

2.4 Serial electron tomography

Electron tomography can achieve a high z-resolution of a few nanometers. Despite a landmark contribution more than 20 years ago demonstrating the concatenation of serial electron tomograms to produce continuous volumes [79], the largest z-depth reported to my knowledge is 16 microns, resulting from the concatenation of 46 serial tomograms of thickness 300-400 nm and yielding a z-resolution of about 20 nm [58]. The limited use of serial electron tomography is likely due to the fact that the process is manual and tedious, and that the signal through the slices is impaired by the limited tilting range (see Ou et al. for recent improvements [62]). Note that new plans for automation of the serial electron tomography process are underway [24] with a 9$M grant for 3D SEM based on tomography.

2.5 Focused ion beam scanning EM

Submitting a sample block surface to cycles of focused ion beam milling and SEM imaging (FIBSEM) is currently the standard method to obtain volumetric EM imagery with typical

isotropic resolutions of 5-10 nm per pixel over hundreds of consecutively ablated sections [57].

However FIBSEM suffers from the inability to process volumes with cross-sectional areas larger than 100 μm m x 100 μm due to ion beam instability [90] and with depths greater than 100 μm due to artifacts such as "streaks and waves of thickness variation" [29]. With drastic measures and additional instrumentation, Xu et al. [99] significantly improved the reliability, speed and quality of FIBSEM and acquired a record-breaking volume of about 180 μm x 100 μm x 50 μm over 100 days with a final 8 nm isotropic resolution. In addition to these incremental improvements, [29] introduced the concept of performing parallel FIBSEM imaging on chunks of tissue subdivided from a sample with virtually lossless subdivision using a hot diamond knife. An impressive implementation of this concept has been reported [99] with the imaging of 9 consecutive chunks of Drosophila brain of dimensions 20 μm x 250 μm x 250 μm to yield a final volume of 180 μm x 250 x μm 250 μm.

2.6 Imaging speed

Parallelization is the only current method to significantly accelerate the imaging throughput given a particular sample.

In the TEMCA2 system [105] for transmission EM, cameras are parallelized in a 2x2 configuration and in combination with an automated sample loader, a net imaging speed of 50 MPixels/s was reported.

Hayworth at al. [29] and Xu et al. [99] parallelized FIBSEM microscopes to acquire different chunks partitioned from a same sample. To my knowledge, 5 FIBSEMs are operated in this parallel setting at the Janelia Research Campus Howard Hughes Medical Institute. Note that Zheng et al. [105] also parallelized their imaging with two TEMCA2 systems built on two different microscopes.

In the SEM multibeam system [18, 53, 73], up to 91 beams and detectors are parallelized to yield the highest imaging speed ever reported in electron microscopy, about 1 GPixel/s (gross speed without considering overhead such as autofocus and stage movements) [18].

2.7 Why the 'F' and the 'B' in FIB ?

The short review above shows that FIB milling is currently the sole non-mechanical tissue-ablating technology used in biology for EM imaging. As virtually every publication I have encountered about the use of FIBSEM in biology simply states that a FIB is used without justifying why specifically a F-I-B, I am taking a few lines to ask: why are we arranging ions into a **B**eam and why is the beam **F**ocused ?

If we do not arrange the ions into a beam, then we would expose our sample directly to a plasma. This plasma exposition process, called plasma etching, has been employed at industrial scales for decades in the semiconductor industry to etch with nanometer precision diverse materials such as aluminum, silicon or photoresist [17]. Why not then also plasma etch resin-embedded heavy-metal stained biological tissues ? This question was partially answered in 1984 by Linton et al. [45] who submitted resin-embedded osmicated biological tissue to plasma etching, tested three different gases (Ar^+, O_2^+, O_2), and observed selective etching phenomenons, that is, the etching was not uniform and likely not suitable for homogeneous serial ablation. I also performed such experiments with resin-embedded heavy-metal stained brain tissue (data not shown) and I similarly concluded that plasma etching is not suitable for homogeneous serial sectioning (or would need further optimization). Plasma etching of sections of resin-embedded

tissue has then been used sporadically [19, 21, 77, 81, 100, 101], mainly to enhance the quality of the SEM signal because the surface topography created by plasma etching tends to reveal more details.

2.8 Broad ion beam milling

If we do not focus the ion beam, then we are dealing with a broad ion beam (BIB). BIBs have been first introduced in 1987 (so have I) to polish telescope mirrors over large surfaces spanning many centimeters in extent [97]. Surface milling with BIBs has since then become a routine technique in material science to polish rocks, minerals, metals, polymers, polymer composites, etc. Starting from 2009 [15] it has been recognized that BIBs not only produce perfectly flat surfaces suitable for further structural characterization but also produce an ablating serial tomographic effect that can be used for volumetric imaging. It led to the first report in 2013 of an instrument allowing many cycles of BIB milling and SEM imaging without manual intervention to take the sample out of the imaging chamber [16]. It has been followed recently by a second integrated BIBSEM implementation [34]. Finally, Winiarski et al. [98] performed 35 cycles of BIB milling and SEM imaging on a small piece of an alloy of coarse-grained hard metal (tediously moving the sample back and forth between a SEM and a BIB miller) to assess the suitability of BIB as a serial sectioning technique. They convincingly showed the serial sectioning suitability of BIB milling but noted several limitations: a minimum slice thickness of about 300 nm, thickness variability between different slices, unparallel slices, surface curtaining, and local waviness of the surface.

2.9 Hybrid mechanical sectioning and BIB milling

On one hand, the sole non-mechanical beam-based ablation method (FIB-EM) provides good axial resolution but is limited to the processing of small volumes. On the other hand, mechanical diamond edge-based ablation methods can process large volumes but involve the delicate mechanical sectioning process that becomes substantially more difficult when working with small thicknesses. A combination of beam-based ablation with mechanical sectioning could combine these strengths and eliminate these weaknesses to offer volumetric imaging of large volumes with high axial resolution and reduced constraints on the mechanical sectioning process.

I hypothesized that the BIB sectioning limitations encountered by Winiarsky et al. [98] were mostly due to the hard material they processed and were amplified by the large milling depths (many micrometers) over which they were performing BIB milling.

I reasoned that sectioning over large depths ($> 100\ nm$) could be performed mechanically while final precise sectioning could be performed by BIB milling. I submitted simultaneously 20 mechanically cut serial sections to cycles of EM imaging and BIB milling, and analyzed the resulting volumetric imagery.

3 Materials and Methods

3.1 Biological tissue preparation

The tissue preparation for EM is described in Chapter 2 of this thesis. Briefly, an adult zebra finch underwent a surgery during which neuroanatomical tracers were administered to different areas of its central nervous systems. Five days later, the animal was sacrificed by perfusion

fixation with fixative concentrations of 2% formaldehyde and 2.5% glutaraldehyde. The brain was extracted and vibratome-sliced at 200 μm thickness. Portions of the slices containing the nucleus HVC were dissected out, and similarly to the protocols described by Deerinck et al. and Tapia et al. [13, 85], washed, stained with heavy metals (2% osmium tetroxide reduced with potassium ferrocyanide, 1% thiocarbohydrazide, 2% osmium tetroxide, 1% uranyl acetate, 0.6% lead aspartate) dehydrated with ethanol, infiltrated in epoxy Durcupan resin, and finally cured in an oven at 52°C.

Standard ultramicrotomy was performed to collect sections for calibration purposes on silicon wafers. Sections of the main proof of concept experiment of this manuscript were collected as follows.

3.2 Magnetic section collection

The magnetic section collection is described in detail in Chapter 2 of this thesis. Briefly, a block of resin-embedded tissue was augmented with a piece of resin containing superparamagnetic and fluorescent particles and a fluorescent dye. The augmentation was done by gluing the two blocks together with plain Durcupan resin. Sections were produced with an ultramicrotome (Leica UC6) at the surface of the large custom boat of a diamond knife (Diatome and ETH D-ITET mechanical workshop). A robotically controlled permanent magnet scanned the wafer surface with an air gap of about 1 mm to agglomerate the freely floating sections into the center of the bath, then the water was slowly removed, allowing the sections to sink onto a piece of silicon wafer that had been previously immersed in the boat. Collected sections were dried on a hot plate at 50°C for 30 minutes.

3.3 Section order retrieval

The sequential order of the sections was determined as described in Chapter 2 of this thesis. Briefly, fluorescent beads of two different spectral colors contained in the augmenting magnetic resin were imaged for each of the 20 cut sections, see Figure 1 a,b. The beads were segmented and affine transforms were computed for each pair of sections (using descriptor-based bead alignment available in Fiji [66]). A dissimilarity measure was computed for each pair of sections (number of appearing and disappearing beads in the pair of images). The set of pairwise dissimilarity measures defined a distance graph between sections for which a traveling salesman problem (TSP) was solved (Concorde solver [1]) to obtain the ordered sequence of sections that minimizes the sum of consecutive dissimilarities (note that the TSP reordering of ultrathin sections was concurrently developed unknowingly at two institutions [23, 87]). Figures 1 c and d show the unordered and reordered similarity matrices, respectively. A final set of pairwise similarity measures using cross correlation was computed on the reordered and aligned stack of bead imagery to calculate a final TSP solution that resolved one last flip and provided the final correct section reordering (later confirmed by EM), Figure 1 e.

3.4 Post-embedding immunohistochemistry

The post-embedding immunohistochemistry (IHC) procedure on collected sections is described in Chapter 2 of this thesis. Briefly, the tissue was blocked, stained with primary antibodies, washed, stained with secondary antibodies, washed, briefly dried, covered with mounting medium and finally coverslipped for fluorescent LM imaging. After LM imaging, the coverslip was removed, the mounting medium was washed away with distilled water and the sections were dried with softly blown air at room temperature.

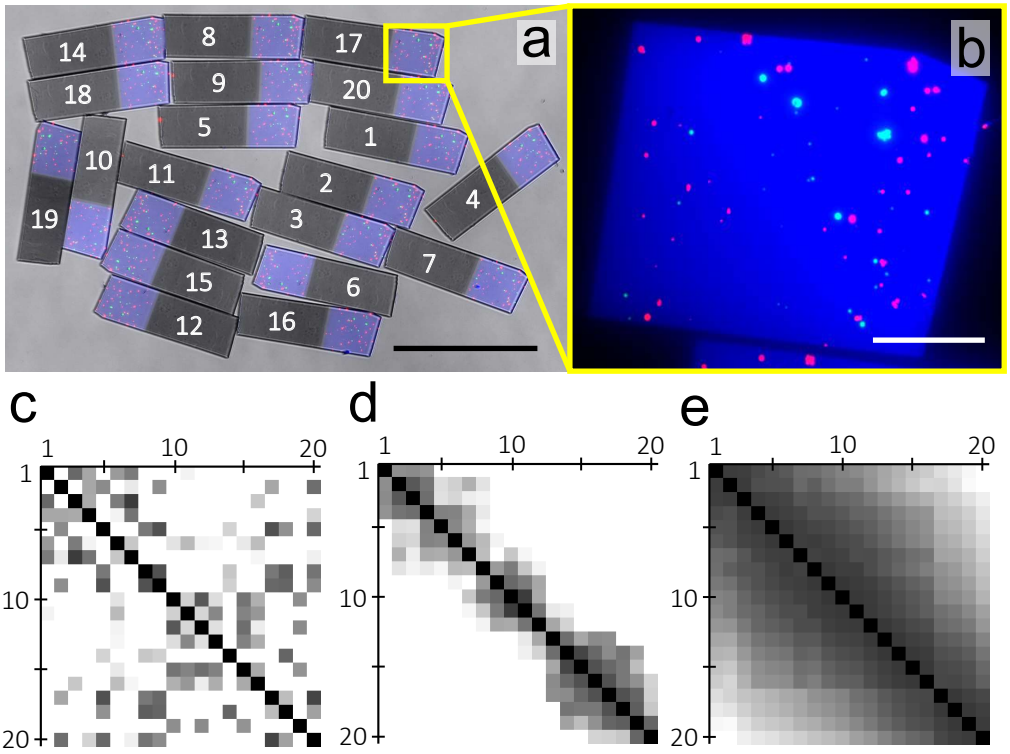

Figure 1. Post-collection section order retrieval. 20 ultrathin sections of thickness 120 nm were magnetically collected onto a piece of silicon wafer. **(a)** Merged reflection brightfield and fluorescent micrographs. The magnetic resin contains green ('GFP' channel) and red ('RFP' channel) fluorescent particles as well as a fluorescent dye visible in the DAPI channel (depicted in blue). The numbering shows the sequential cutting order of the sections and is the outcome of the order retrieval process. **(b)** Zoomed inset of (a) without the brightfield channel. **(c)** Sections had originally been given an arbitrary order. The matrix shows the pairwise similarities associated with this original order. The similarity value is the number of appearing and disappearing beads from one section to its associated pair. Darker pixels depict a higher similarity. **(d)** Similarity matrix after a first reordering using the 'appearing beads' similarity measure. **(e)** Similarity matrix after final reordering using cross correlation as a similarity measure. Darker pixels depict a cross correlation closer to 1. Scale bars: a - 400 μm, b - 50 μm

3.5 BIB milling

Silicon substrates were attached to EM mounting stubs (Agar Scientific, #G301) with double sided carbon stickers (Ted Pella, #16084-3) and mounted in a broad ion beam miller (Hitachi, IM4000) operated with these parameters: acceleration voltage 6 kV, discharge voltage 0.5-1.5 kV, gas flow 0.09 cm^3/min, continuous rotation of the substrate with 25 rotations per minute (rpm), incident angle 2 degrees (angle between beam direction and substrate surface), eccentricity 5 mm (distance between center of rotation of the substrate and the center of the beam).

3.6 Surface profilometry

Section thickness was measured by surface scanning profilometry (Bruker, Dektat XT) with a tip ball diameter of 12 μm. Typical scanning speed was 30 $\mu m/s$. To measure a section thickness, a single line scan was performed with a direction orthogonal to the section boundary. To compensate for wafer tilt and current drift over long distances the curve was linearly leveled by zeroing the average altitude of two distant regions in the wafer part of the curve. The thickness of the step was evaluated as the average altitude of a manually defined region in the section and close to the border (typically about 5 μm wide). Ambiguous cases have arisen when impurities were present at the section border, in which case the region was placed slightly further away from the section border.

3.7 Electron microscopy

Electron micrographs of the main dataset of this article were acquired with a field emission scanning electron microscope (Zeiss, Merlin) with the following parameters: dwell time 6 μs, lateral resolution 10 nm/pixel, acceleration voltage 2 keV, secondary electrons inlens detector, probe current 800 pA, working distance 3.4 mm. A mosaic of 2x2 patches of size 6144 x 4096 was acquired for each of the 20 sections after IHC and after all BIB milling sessions. One autofocus-autostigmantion-autofocus sequence was performed in the center of each section. Slight variations to these parameters probably occurred for the acquisitions of other electron micrographs of this manuscript.

Custom python scripts were used to programmatically control the microscope using the Zeiss API.

3.8 Light microscopy

Two brightfield light microscopes were used: Zeiss Z1 and Nikon Eclipse L200.

Zeiss Z1 Acquisition of the fluorescent beads (for section order retrieval) and of the immunostained tissue: 20x objective, GFP and RFP channels for the beads, GFP, RFP, Cy5 for immunostained tissue. Acquisition of wafer overview: 5x objective, reflection brightfield, DAPI, GFP and RFP channels.

Nikon Eclipse L200 Low magnification overview of the sections on wafer to reveal their interferometric colors. 5x or 10x objective, 1.4 ms exposure, episcopic illumination, Nikon Coolpix 990 Camera. Micrographs were stitched with the Fiji alignment tools [67].

3.9 Color normalization of LM

Red-Green-Blue (RGB) LM imagery acquired with the Nikon Eclipse L200 microscope was used to estimate the thickness of sections based on their color on wafer. Even if all controllable microscope parameters were held constant, fluctuations in illumination and some camera normalization occurred against which I did the following normalization. In a given micrograph, a region showing plain wafer without sections was taken as a reference from which a mean intensity in the three RGB channels was obtained. This RGB intensity was taken as reference intensity. In all micrographs used for thickness estimation, several regions covering the background were manually defined (plain wafer without section) from which the mean RGB intensity was calculated. The three RGB channels of the entire image were then multiplied by a factor so that the new mean intensity of the calibration regions was equal to the reference intensity.

3.10 Section segmentation

A LM micrograph of the 20 sections magnetically collected for the main experiment of this study was manually segmented to locate the tissue portions of each section. Four landmarks located at corners of sections were also manually defined for mapping of section locations into microscope stage coordinates. These operations were done with custom scripts using Fiji [74], and Trakem2 [9].

3.11 Assembly of the correlative data set

The automated assembly of correlative data sets from magnetically collected sections on wafers is described in details in Chapter 2 of this thesis. Briefly, custom python and jython scripts were written to perform the following operations on the ImageJ/Fiji platform [74, 75] with the TrakEM2 plugin [9] playing a central role.

Electron micrographs of each acquired 2x2 mosaic were linearly [67] then elastically [71] stitched before a linear and then elastic [71] alignments were applied.

For LM-EM registration, the brighfield LM channel was preprocessed (local contrast enhancements [106], Gaussian blurring) while corresponding EM slices were downscaled and preprocessed with the same tools. Moving least squares transforms [72] were computed from matching local features between the LM and EM imagery. These transforms were applied to all channels of the LM imagery to yield the final volumetric correlative stack.

4 Results

4.1 Qualitative tuning of BIB milling parameters

Optimal milling conditions for subsequent SEM imaging were found by varying parameters on 400 nm tissue sections as shown in Table 2. A moderate beam strength at 10 degrees incidence angle yielded tissue surfaces for which it was difficult to obtain a sharp focus, and that displayed some electron dense artefacts, typically located at plasma membranes (Figure 3 a.). With a high incidence angle of 30 degrees, the bombardment effect was clearly visible and produced uneven surfaces with craters (Figure 3 b). A low incidence angle with a low beam strength applied for longer time (10 min) showed a clear differential milling with low heavy-metal content cell bodies and dendrites exhibiting a low milling rate whereas high heavy metal content elements such as myelin and mitochondria showed a high milling rate (Figure 3 c,d). The same sections were subsequently submitted to a short milling (10 s) with the strongest beam of the device. This short milling round entirely canceled the previous strong differential milling and yielded qualitatively even sections (Figure 3 e,f). Images in Figure 3 d and f show the exact same location on the same section after long mild milling and short strong milling, respectively. Also, unlike with all the previous milling parameters tested, electron beam irradiation produced much lower carbon contamination. Finally, as milling was performed at room temperature without using a cooling device, it was unclear whether the resin-embedded tissue might have been exposed to excessive heat during milling. The same sections used in Figure 3 e,f underwent 2 minutes of milling with the strongest beam, shown in Figure 3 g, and no qualitative difference was found compared to the 10 seconds long milling, therefore excluding a possible impairing effect due to potential heat produced during prolonged beam exposition. As a conclusion to this preliminary experiment, the strongest beam (acceleration voltage 6 kV) was then used with a 2 degrees incidence angle in the rest of this study.

Table 2. Milling parameters used in Figure 3.

Figure	Incidence angle (degrees)	Duration (s)	Acceleration voltage (kV)	Discharge voltage (kV)
1.a	10	20	4	0.75
1.b	30	20	4	0.75
1.c, 1.d	2	600	1	0.75
1.e, 1.f	2	10	6	1.5
1.g	2	120	6	1.5

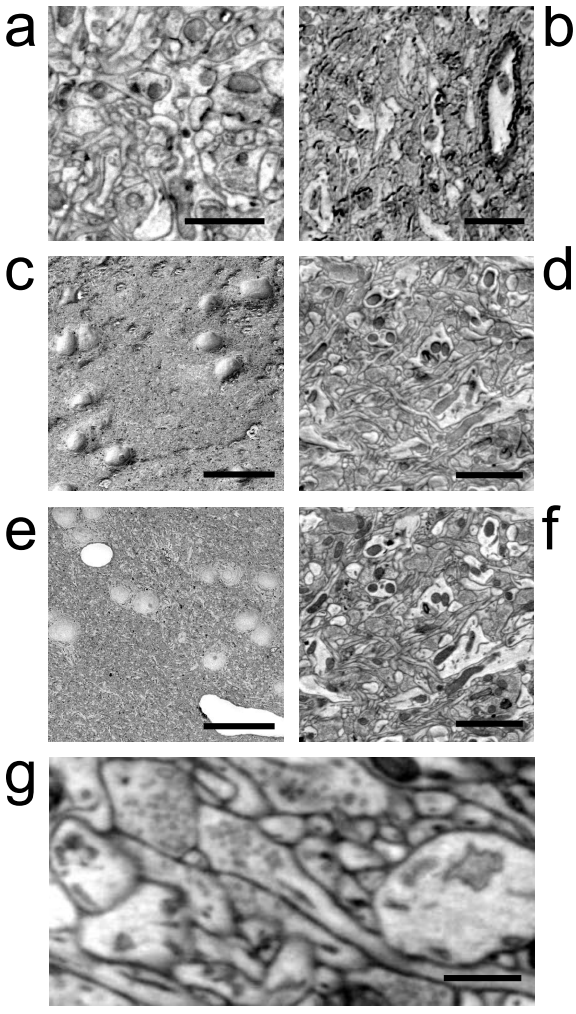

Figure 3. Effect of different milling parameters. (a) SEM micrograph after short, medium milling at medium incidence angle (see Table 2 for detailed parameters). Some electron dense artifacts are visible at plasma membranes. **(b)** After short, medium milling at large incidence angle. Note the numerous craters. **(c,d)** After long, mild milling at glancing angle. Note the different milling rates in cell bodies and dendrites compared to myelin and mitochondria. **(e,f)** After short, strong milling of the same section in (c,d) at glancing angle. No artifact is apparent, which is well demonstrated by the difference between micrographs (d) and (f) which depict the exact same location on the same section. **(g)** After 2 min of strong milling at glancing angle the surface is free of artefacts. Scale bars: a,b,d,f - 2 μm; c,e - 20 μm; g - 500 nm.

4.2 Milling spatial homogeneity and milling rate

4.2.1 Preliminary adjustments for low milling rate with high energy ions

A first milling rate estimate of about 1-2 nm/s was obtained by observing by eye the time point at which milled sections became invisible on wafer (initial thickness estimated by the ultramicrotome setting). A first milling homogeneity estimate was also obtained by observing by eye colors of sections (not shown), and it appeared that the center of the beam was roughly spanning a disk of 1-2 mm diameter.

The sample holder of the BIB miller used in this study can rotate at 25 rotations/s for homogeneous milling, nevertheless each milling session starts with a holder revolution of about 20 degrees during 3-4 seconds in order to initialize the rotary stage. Given the initial milling rate estimate, milling cycles of for example 10 nm thickness would last around 5-10 seconds, but a non-negligible inhomogeneous milling would happen during the first 3-4 seconds. A lower milling rate would decrease the influence of this short initial inhomogeneous milling for a 10 nm milling. Reducing the milling rate was achieved by reducing the discharge voltage, which regulates the amount of ions produced in the plasma but should leave their energy unchanged (controlled by the acceleration voltage). A discharge voltage of about 0.7 kV was chosen for the rest of this study, yielding a discharge current of about 80 μA.

4.2.2 Spatial homogeneity calibration

A ribbon of 39 consecutive sections (460 μm x 950 μm) of 150 nm thickness was manually collected onto a piece of silicon wafer as shown in Figure 4 a,1. The sections were submitted to five cycles of BIB milling (5, 5, 3, 3, and 3 minutes) interspersed by LM and profilometry. Figure 4 a shows LM imagery of the initial ribbon and after each of the 5 BIB milling sessions. The center of rotation of the BIB holder was located in the middle of the section intersected by the vertical dashed line spanning over Figures 4 a and b. Figure 4 b shows the milling rate (nm/min) assessed by profilometry for each of the 5 millings (a simple b-spline approximation was used to smoothen the obtained data). Note that the milling rate seems to decrease over time.

4.2.3 Section thickness estimation with LM

Ultrathin sections on wafer act as a thin film and display an interferometric color that depends on section thickness. The RGB signature of each of the sections of the ribbon used for spatial homogeneity calibration was assessed by the mean intensity value of each channel in the boxes shown in yellow in Figure 4 a,1. This set of measures provided a lookup table between RGB space and thickness. The three thickness curves (obtained with a simple b-spline interpolation from the measurements) for each color channel are shown in Figure 4 c. Note that a physically accurate fitting could have been made since the equations for interference from a film are known, it might be addressed in future studies. To determine section thickness based on LM, the measured RGB signature is matched to its euclidean nearest neighbor in the b-spline interpolated reference curve. This b-spline interpolated curve and all calibration points are plotted in 3d in Figure 4 d.

To assess the accuracy of the method, measurements from the micrographs 1, 2, 3, 4 and 6 in Figure 4 a were used to create a b-spline interpolated curve, and a standard error of 3.1 nm was obtained on the measurements from the test micrograph #5 (note that the distribution of thicknesses in micrograph #5 is roughly spanning homogeneously the thickness space). I then

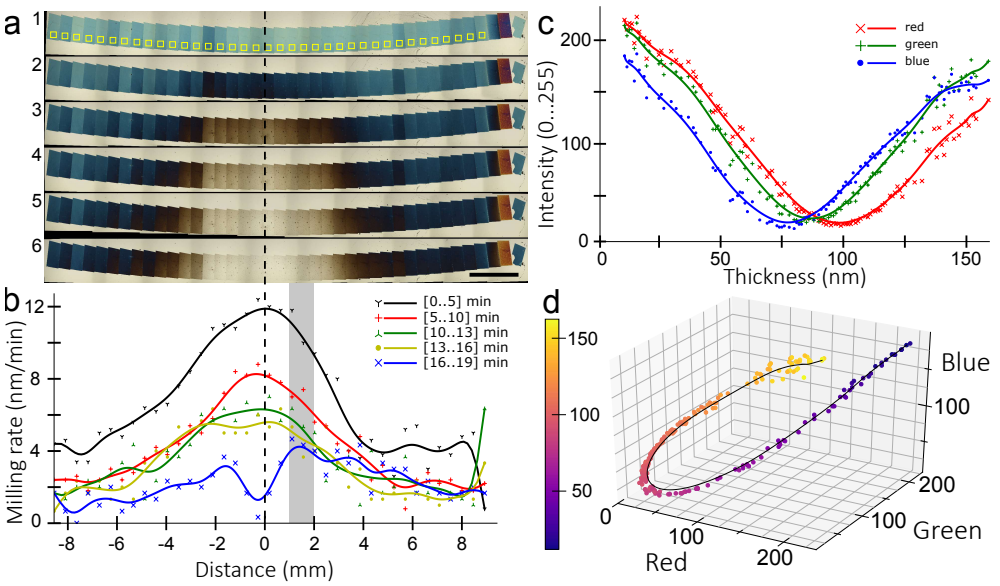

Figure 4. Milling characterization and thickness estimation from LM imagery. (a) A ribbon of 39 consecutive sections (37 used for calculations) of thickness 150 nm is shown before the first and after each milling cycle. The milling cycles lasted 5, 5, 3, 3, and 3 minutes. The center of rotation of the substrate was each time located at the center of the section (section number 19) intersected by the vertical dashed line that spans panels (a) and (b). Scale bar: 2 mm. **(b)** Milling rate observed during each milling session as a function of the distance to the center of rotation. A simple b-spline interpolation was used to smoothen the discrete data points. The gray bar indicates a region located between 1 and 2 mm apart from the center of rotation. **(c)** RGB mean intensity of small patches inside sections plotted as a function of the thickness measured by profilometry. The continuous lines show b-spline interpolations. **(d)** 3d plot of all calibration points and of the b-spline interpolation resulting from the three b-spline interpolations calculated for each color channel. The color-coding depicts the thickness

considered that all thicknesses determined by LM in this manuscript have a precision of $\pm$ 3.1 nm.

4.3 Proof of concept data set

4.3.1 Principle

Twenty consecutive sections of resin-embedded zebra finch brain tissue with 120 nm nominal thickness were collected on a piece of silicon wafer using the magnetic collection described in Chapter 2 of this thesis. Postembedding immunohistochemistry (IHC) was performed followed by multi-channel fluorescent LM imaging on each of the 20 stained sections. This fluorescent LM imaging captures the fluorophores bound at the top of the sections, i.e. at the mechanically cut surface of each section, as sketched in Figure 5 a. Cycles of EM imaging and BIB milling at glancing angle (Figure 5a, b) were then performed until the bottom of the sections was reached. For homogeneous milling over the course of multiple BIB cycles, the sample was alternatively offset at each cycle on the holder so that the axis of rotation was located either about 1.2 mm north or south from the collected sections. The locations of the two centers of rotation used are shown as black crosses in Figure 5 b. The sections were thus submitted to milling profiles spanning both from about 1 mm to 2 mm away from the center of the beam, which corresponds to the light gray area in Figure 4 b. These two profiles were localy slightly inhomogeneous, but I anticipated that milling alternatively with these two centers of rotations would finally produce a spatially homogeneous milling.

4.3.2 IHC and LM

Figure 6 shows a montage of the aligned LM imagery of the 20 sections. The three fluorescent channels and the brightfield channel have been merged. The brightfield channel has been processed with a normalization of the local contrast which makes this channel look like a low-resolution EM micrograph. This similarity was later used for automated cross-modality registration between LM and EM. Unambiguous fluorescent signal can be observed in the three

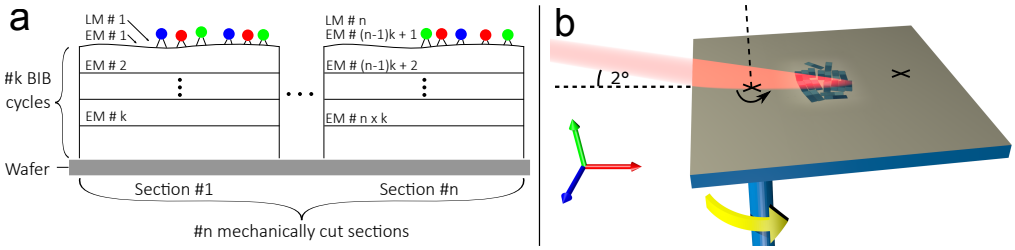

Figure 5. Principle of hybrid mechanical sectioning and BIB milling. (a) n mechanically cut sections are collected on a silicon wafer. IHC is performed by submitting the section surfaces to staining liquids followed by LM imaging of the surface of each of the collected sections. k EM imaging rounds are then performed, interspersed with $k-1$ BIB milling rounds. Overall, the process produces n LM images and nk EM images. **(b)** The BIB is shown in red. The BIB milling is performed at glancing angle and the holder rotates continuously (25 rpm with machine used in this study). For this experiment, the sample was placed in two different positions (only one depicted) so that the center of rotation of the holder was alternatively located about 1.2 mm south or north from the sections. The centers of rotation are shown with black crosses.

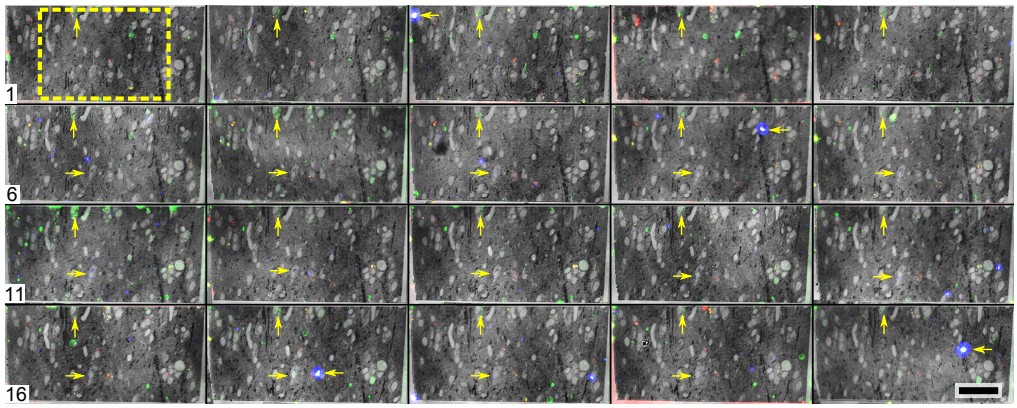

Figure 6. Montage of the merged and aligned fluorescent imagery over the 20 mechanically cut sections. Green channel Transported tracer Dextran Alexa 488 injected in the nucleus Robustus of the Arcopallium, custom rat anti-488 primary antibody, Alexa 488 anti-rat secondary antibody. **Red channel** Transported Dextran Texas Red tracer injected in nucleus Avalanche, goat anti-Texas Red, Alexa 546 anti-goat. **Blue channel** Transported Dextran FITC injected into nucleus AreaX, mouse anti-FITC, 647 anti-mouse. The **dashed square** depicts the area on section that has then been acquired with EM. **Up-pointing** and **right-pointing** arrows show consistent signal over consecutive sections in the green and blue channels, respectively. The **left-pointing** arrows point to sporadic large noise appearing in the blue channel. Scale bar: 50 μm.

fluorescent channels ('GFP', 'RFP', 'Cy5') which is present over consecutive sections. Up-pointing and right-pointing arrows show such signal in the green and blue channel, respectively. Bright signal in all three channels is typically located in cell bodies which can be recognized easily in the contrasted brightfield imagery. Some noise is present too, with some debris showing up in the blue channel being highlighted by left-pointing arrows.

4.3.3 Experimental overview of the cycles of BIB-EM

17 cycles of alternating EM and BIB milling have been performed on the 20 collected sections.

BIB milling The BIB milling durations were 40 seconds except for the first round that lasted 30 seconds to account for the higher milling rate observed in Figure 4 b when milling the fresh top of mechanically cut sections. To counter-balance the spatially non-homogeneous milling observed in Figure 4 b, the center of rotation of the BIB holder was alternatively placed at each milling cycle approximately at either of the two black crosses shown in Figure 5 a. It was thought that the spatial inhomogeneity would be canceled every two rounds of milling. Note that a milling cycle could have consisted in two sub-millings with the center of rotation located at

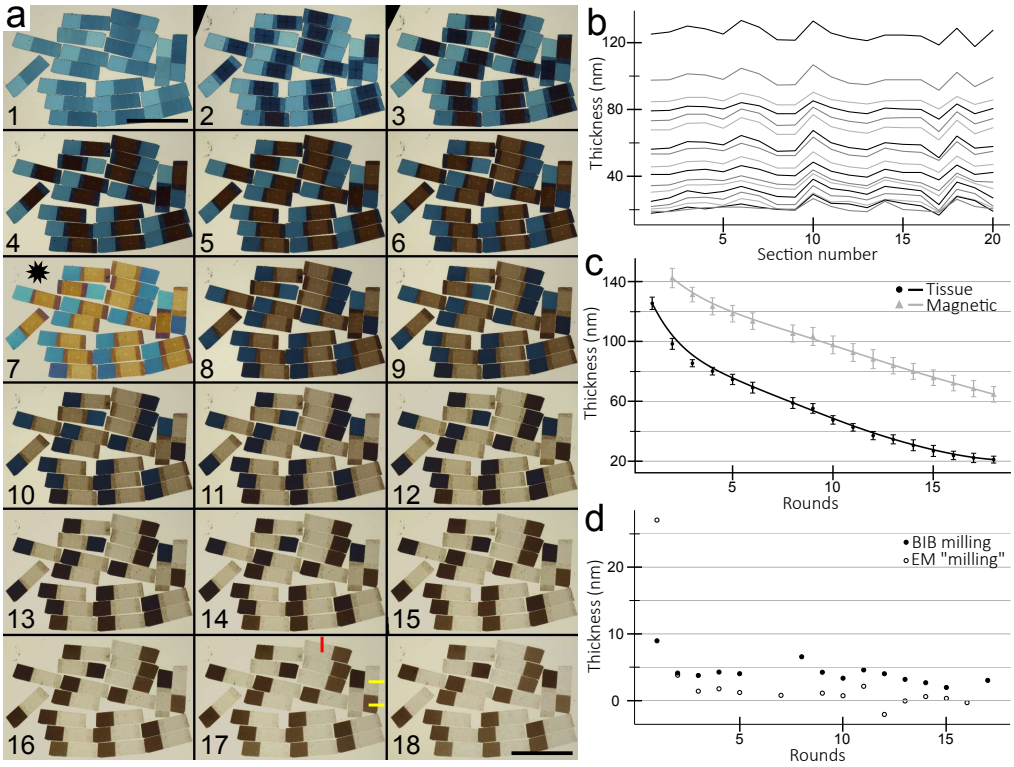

Figure 7. Section thicknesses after BIB-EM cycles (a) LM micrographs of the 20 sections after initial fluorescent LM imaging (#1) and after each EM imaging session. Micrograph #7 (indicated with a black asterisk) could not be acquired with the same microscope as for the other micrographs, resulting in a clearly different RGB signature despite background normalization. This micrograph was not used for section thickness estimations. Scale bar: 500 μm. **(b)** Estimation of the thickness of the tissue part of all sections after EM imaging using the LM micrographs in (a). Small boxes manually defined in the center of all sections (not shown) were used for the thickness estimation. **(c)** Mean and standard deviation of the thickness of both the tissue and the magnetic portion in all sections after each EM imaging session. **(d)** Thickness milled on the tissue portion of all sections as a result of each BIB milling session and each EM imaging session. LM micrographs acquired after each BIB milling (not shown) were used (a few missing due to technical reasons yielding a few missing data points on the graph). Note that 3 data points from the EM milling group are negative, which is physically unrealistic (unless some resin expansion took place). None of the graphs contains the $\pm$ 3.1 nm error calculated during calibration.

either black cross, but precisely placing the center of rotation was a tedious task therefore I chose to perform a single slightly inhomogeneous milling for each cycle. According to the curve in Figure 4 b, milling for 40 seconds at a distance of about 1.5 mm from the center should mill approximately 6 nm.

EM imaging After each BIB milling round, the wafer was placed in the imaging chamber of the EM and four landmark points were located to match previously manually defined landmarks on a reference LM micrograph. Custom scripts provided then the x-y and angle coordinates for automated acquisition of EM imagery of the 20 sections based on the segmentation of the 20 sections on the reference LM micrograph. One autofocus-autostigmation-autofocus sequence was performed at the center of each tissue section. Each EM cycle lasted for 5 hours, with approximately 15 minutes/section.

4.3.4 LM estimation of section thicknesses after BIB milling and EM imaging

Figure 7 a shows LM micrographs of the sections after initial fluorescent imaging and after each EM imaging round. Note a sharp color change of the tissue portions after the first EM cycle between micrographs #1 and #2. This apparent thickness change caused by the first EM imaging round is about 26 nm (first EM milling point in Figure 7 d). The thickness change due to EM milling then stabilizes below 3 nm in the subsequent rounds. Similarly the BIB milling rate at the first round (9 nm in 30 seconds) is greater than in subsequent rounds (about 4-5 nm in 40 seconds).

Magnetic and tissue portions of the sections exhibit clearly distinguishable colors. The color changes of the tissue and magnetic portions from micrographs #1 to #18 in Figure 7 a seem to be

similar for all sections indicating a good spatial homogeneity of the BIB milling process. It is confirmed by the graph in Figure 7 b showing conserved thickness variations over consecutive cycles. The good spatial homogeneity of the milling is also shown in Figure 7 c by the small standard deviations of the mean thickness both for the tissue and for the magnetic portions across the 20 sections.

The LM-estimated absolute values of thickness of the magnetic portions of the sections should be interpreted carefully as the calibration was performed only with parts of sections containing heavy metal stained brain tissue. The two resin regions clearly exhibit different interferometric properties. For example, the mean 140 nm thickness of the magnetic portions (Figure 7 c) is likely slightly off because mechanical sectioning cannot produce consecutive sections containing each 2 portions of thickness 120 nm and 140 nm (even though a further differential expansion of the magnetic resin after collection cannot be excluded).

Also, a different block of tissue was used for the calibration than for the proof of concept experiment. Mechanical profilometry measurements were avoided for this experiment as the physical contact of the probe with the section sometimes leaves a trace clearly visible in the EM imagery (not shown).

Nevertheless, three profilometer measures were performed on tissue portions of sections 12 and 19, depicted in red and yellow on micrograph #17, respectively. The measured thicknesses were both equal to 10 nm while the LM-estimated thicknesses were 19 nm and 20 nm respectively. A possible reason for this discrepancy is the lack of sub-15 nm sections in the calibration dataset. Also, it is known that EM irradiation affects the surface of plastic sections [11, 46] and therefore alters the interferometric readout of the thickness. The profilometric measure of the second yellow trace (the one over a magnetic portion in micrograph #17) was 49 nm while the LM estimation was 53 nm.

Figure 7 b shows that EM imaging contributes to the milling of the sections. It is not surprising in light of the literature describing irradiation damage and material removal (also called tissue shrinkage) due to EM imaging [11, 39, 44, 46, 92]. However to my surprise, even if the literature mentions stronger shrinkage phenomenons at the onset of radiation exposure, the first EM imaging cycle seems to have milled more than 25 nm away from the surface of the sections. This EM milling effect then stabilized around 2-3 nm at the following cycles.

The BIB milling remained constant at 4-6 nm per cycle according to the LM estimation. Note that as for the EM imaging, the first BIB milling seems to have removed more material than during the subsequent rounds.

4.3.5 Evaluation of the EM imagery

Assembly of the volumetric EM stack Electron microscopy imaging was performed 17 times (after the initial fluorescent imaging and after each BIB milling session) resulting in the acquisition of 17x20 physical sections $= 340$ EM mosaics. All raw fields of view (6144 x 4608 pixels) were preprocessed with the "Normalize local contrast" Fiji plugin with large block radii of 500x500 pixels. Figure 8 a and b show an overview of one of the mosaics and zoomed insets with arrows pointing to synapses, respectively.

A few mosaics of the last EM imaging round were not used for the assembly of the volumetric stack as electron dense contamination was substantially obstructing the imagery (see paragraph further below). The probable reason for electron-dense contamination appearing earlier or later through the cycles is the original slight variation in section thicknesses stemming from the mechanical sectioning process. This variation was roughly conserved throughout the cycles (see Figure 7 b) so that the bottom of some sections was likely reached earlier in the cycles.

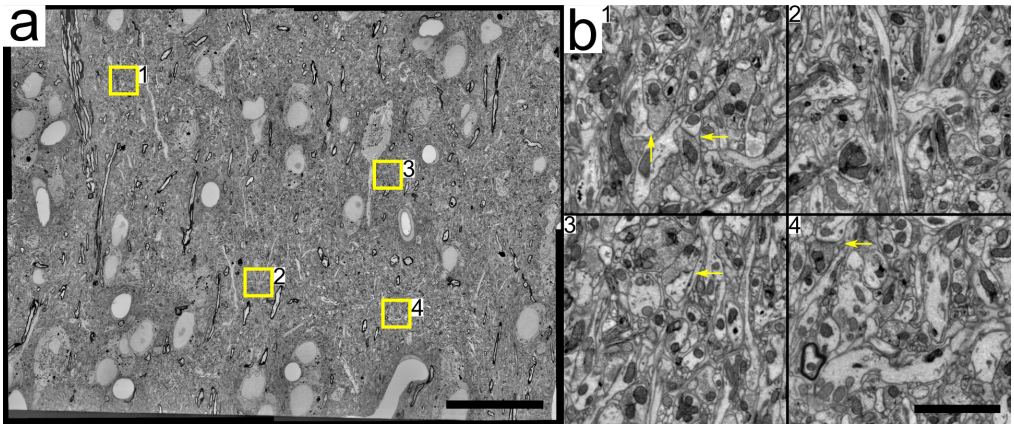

Figure 8 Overview of the EM imagery. **(a)** Electron micrograph of a complete slice of dimensions 115 μm x 85 μm. **(b)** Zoomed insets from (a). Yellow arrows point to synapses. Scale bars: a-20 μm, b-2 μm.

Thickness homogeneity and gap Figures 9 a,b, and c show three z-resliced portions of the EM volume (a z-reslice shows the stack as if viewed from the side). In each panel, the first row shows the z-reslice of the dataset when using only the top surface of the 20 consecutive sections. Large structures can be recognized such as myelinated axons, a cell body and a large dendrite. The second row is a z-reslice using 3 sections per physical section (imaging rounds 2, 8 and 15) in which detailed structures such as small neuronal fibers can be identified. There is no feeling of abrupt change across physical sections when scrolling through this stack that has an average slice thickness of 40 nm (see supplementary video S2). The third row is a z-reslice using all imaging rounds. The gap between consecutive slices is clearly visible. In the high axial resolution segments between the gaps, neuronal membranes appear very well delineated.

When scrolling through the volumetric stack containing all slices, the gap can be seen between the last slice acquired at the bottom of a section and the first slice acquired at the surface of the next consecutive physical section. The size of this gap was assessed with LM thickness estimation and with profilometry (second next paragraph).

Visualization of synapses and small fibers in z-resliced EM imagery To highlight the increase in z resolution thanks to the BIB and EM imaging cycles, Figure 10 shows 3 synapses (one per row) in the original imagery (first column), and viewed from the side with a z-reslice (last three columns). The z-resliced imagery in columns 2 and 3 is identical and contains images acquired from all BIB-EM cycles (16 or sometimes 17 cycles), while the imagery in the last column contains the imagery only from the 20 mechanically cut sections. In the second column, the presynaptic and postsynaptic partners are delineated in yellow and green, respectively, and small fibers are delineated in red. The imagery of column 2 is duplicated in column 3 to allow the reader to observe these elements without the overlays. The increase in z-resolution is unambiguously demonstrated when comparing the last two columns on the right: the synapse and small fibers are visible in the third column but cannot be observed in the last column.

Gap size estimation with LM The mechanism leading to the sharp thickness decrease observed at the first EM imaging cycle, about 26 nm (see Figure 7 b), is not yet well understood. I assume that starting from a 120 nm thick section, the first EM slice shows therefore material located at about 94 nm altitude. The mean thickness of the 20 sections after the last EM imaging cycle is estimated to be about 20 nm. The gap estimated with LM would therefore be 46 nm.

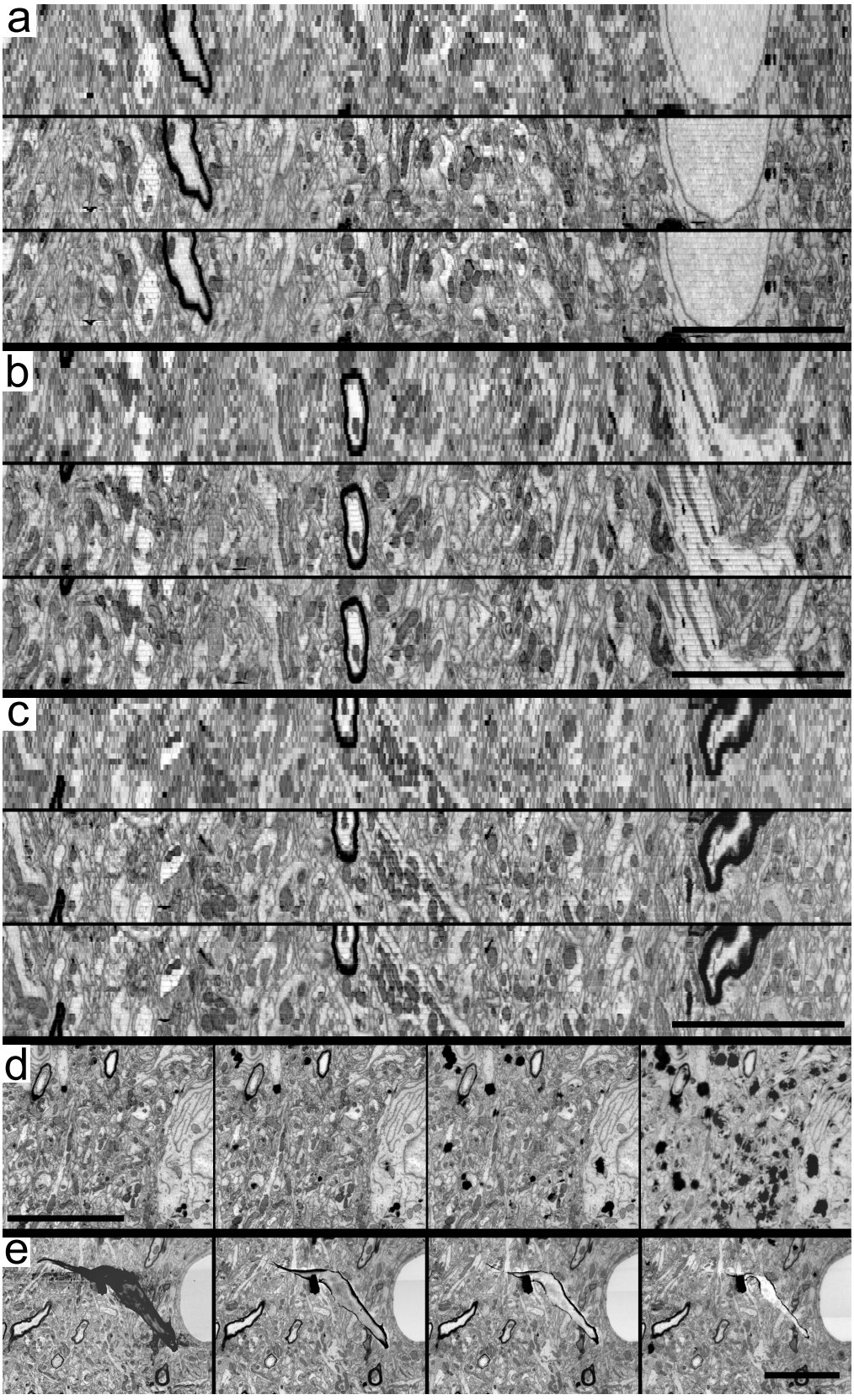
a
b
c
d
e

Figure 9. EM imagery. (a,b,c) Z-resliced imagery (without interpolation) from three regions of the proof of concept data set. The first, second and third rows of each figure show a z-reslice of EM imagery acquired from the top surface of the 20 physical sections, from imaging rounds number 2, 8 and 15 from each of the 20 sections, and from all imaging rounds (excluding sometimes the last round because of electron-dense contamination), respectively. **(d)** EM micrographs from the last 4 imaging rounds in a portion of the dataset. The last micrograph on the right was measured to be 10 nm thick by profilometry. Contamination with electron-dense spots appears preferentially on already electron-dense structures in the tissue such as lysosomes and mitochondria. **(e)** Micrographs of a debris found in the dataset imaged at rounds 1, 6, 11 and 17. Scale bars: 5 μm (only for the x-axis in panels a,b,c).

Gap size estimation with profilometry Profilometry was performed after the second last EM imaging round on two sections that were measured to be both 10 nm thick. Both mosaics from these two sections were of sufficient quality to be kept in the stack as they did not show significant obstruction from electron-dense contamination. No profilometry was performed before or after the first EM imaging cycle in order to prevent large scratches in the proof of principle stack. Taking the LM estimation of 94 nm for the first EM slice, the gap size estimate would be 36 nm.

Contrast variations The first EM slices acquired at the top of the sections look qualitatively slightly different compared to the subsequent slices acquired after several BIB millings. The controllable parameters of the microscope remained constant between cycles therefore it is a property exhibited by the tissue. Such a difference can be seen for example in the lower part of the micrographs #1 and #3 in Figure 9 e. The slices acquired after several BIB cycles (micrographs #2, #3 and #4 in Figure 9 e) give the qualitative impression of a higher sharpness (not quantified).

Apparition of electron-dense spots at the end of sections Figure 9 d shows an example of the electron-dense contamination occurring when the end bottom of the sections is imaged. The four micrographs show EM imagery of a portion of a section at the last four EM imaging cycles. The thickness of this section (section #12, see numbering in Figure 1 a) was measured with profilometry to be 10 nm after the second last round of EM imaging. Note that the signal from the tissue is clearly weaker in the last micrograph when the contamination occurs, indicating a very small thickness of the section. These black spots preferentially occur at locations that already appeared strongly electron-dense in previous micrographs, for example lysosomes and mitochondria.

Sensitivity to debris Contamination such as atmospheric dust can appear randomly during the course of experiments involving ultrathin sections. The sections were treated with care, nevertheless a few atmospheric dust particles landed on the sections and locally impaired the EM imagery, as shown in Figure 9 e. Such debris typically were present in all slices acquired from a same physical section.

4.3.6 Correlative LM-EM stack

LM imagery was automatically registered to the 3d elastically aligned EM stack by computing moving least squares transforms [72] from the LM brightfield channel to its corresponding EM counterpart. The fluorescent imaging was performed with a low magnification 20x air objective for practical reasons (instead of immersion objectives with magnification $>$ 60x), which resulted

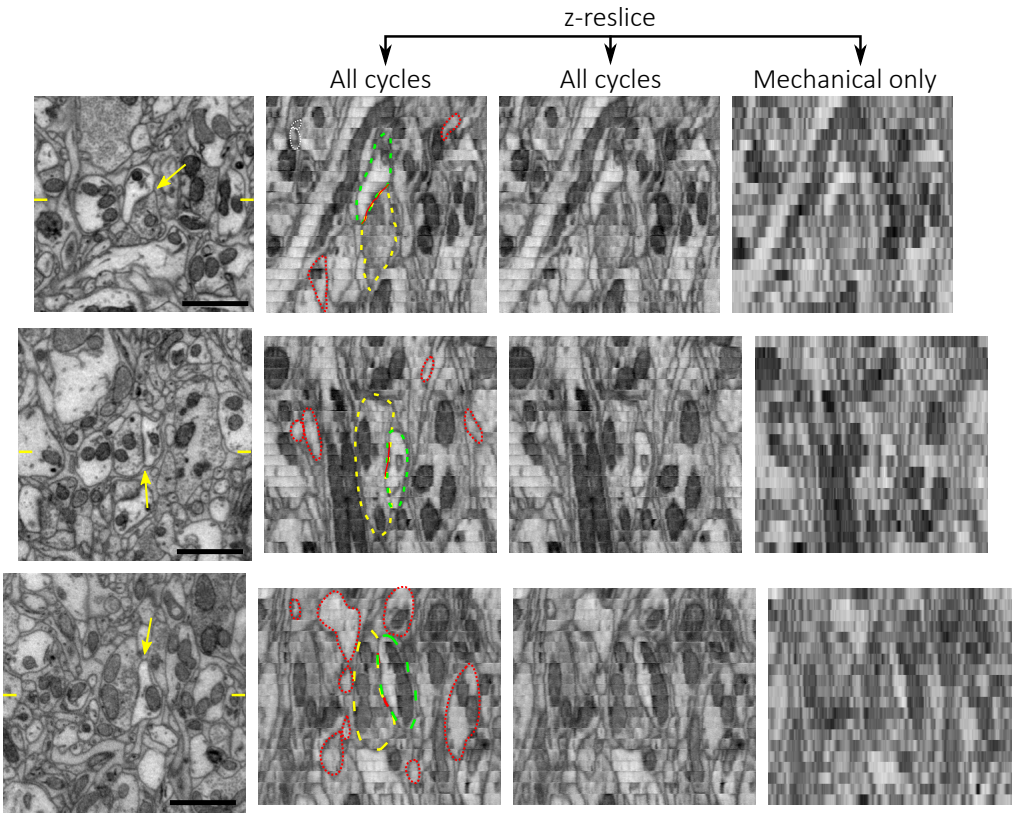

Figure 10. Normal and z-resliced EM imagery showing synapses and small neuronal fibers. Rows show different volumes from the dataset with a synapse in the center. The **first column** shows imagery stemming from the standard EM acquisition. The yellow arrows point to clearly identifiable synapses. The horizontal yellow bars indicate the position at which the z-reslice (see next columns) has been performed for columns 2,3 and 4. The **second and third columns** are identical and show the volume after a z-reslice operation (looking from the top of the image in column 1) and containing imagery from all BIB-EM cycles. In column 2, The presynaptic and postsynaptic partners are delineated in yellow and green, respectively. Small fibers are also delineated in red. **Column 4** is also a z-reslice of the volume, but here assembled only with a single image per mechanical section (20 images). The difference of resolution between columns 3 and 4 is unambiguous. Scale bars: 1 μm.

in a non-perfect alignment that required a minimal manual adjustment of a few nanometers to obtain an excellent cross-modality registration. Figure 11 b shows a montage of the correlative LM-EM imagery (2 channels shown) of the IHC-treated and unmilled top of each of the 20 physical sections. The yellow-squared micrograph of section #19 is shown in Figure 11 a.

4.4 IHC post-BIB

Can IHC be performed after BIB milling ? Two 70 nm thick sections of brain tissue were manually collected on silicon wafer. IHC was performed followed by fluorescent LM that showed unambiguous post-embedding fluorescent signal (data not shown). The sections were then washed with water, dried, and submitted to a 90 seconds milling which according to calibration in Figure 4 b should have milled about 15 nm. IHC was then performed followed by fluorescent LM imaging which showed a complete absence of post-embedding fluorescent signal (data not shown).

After washing the sections, they were then submitted for 10 minutes to wet etching with 3% aqueous sodium metaperiodate in the hope of opening access to antigens present in the tissue. It was followed by IHC and fluorescent LM, which also showed a complete absence of post-embedding fluorescent signal (data not shown).

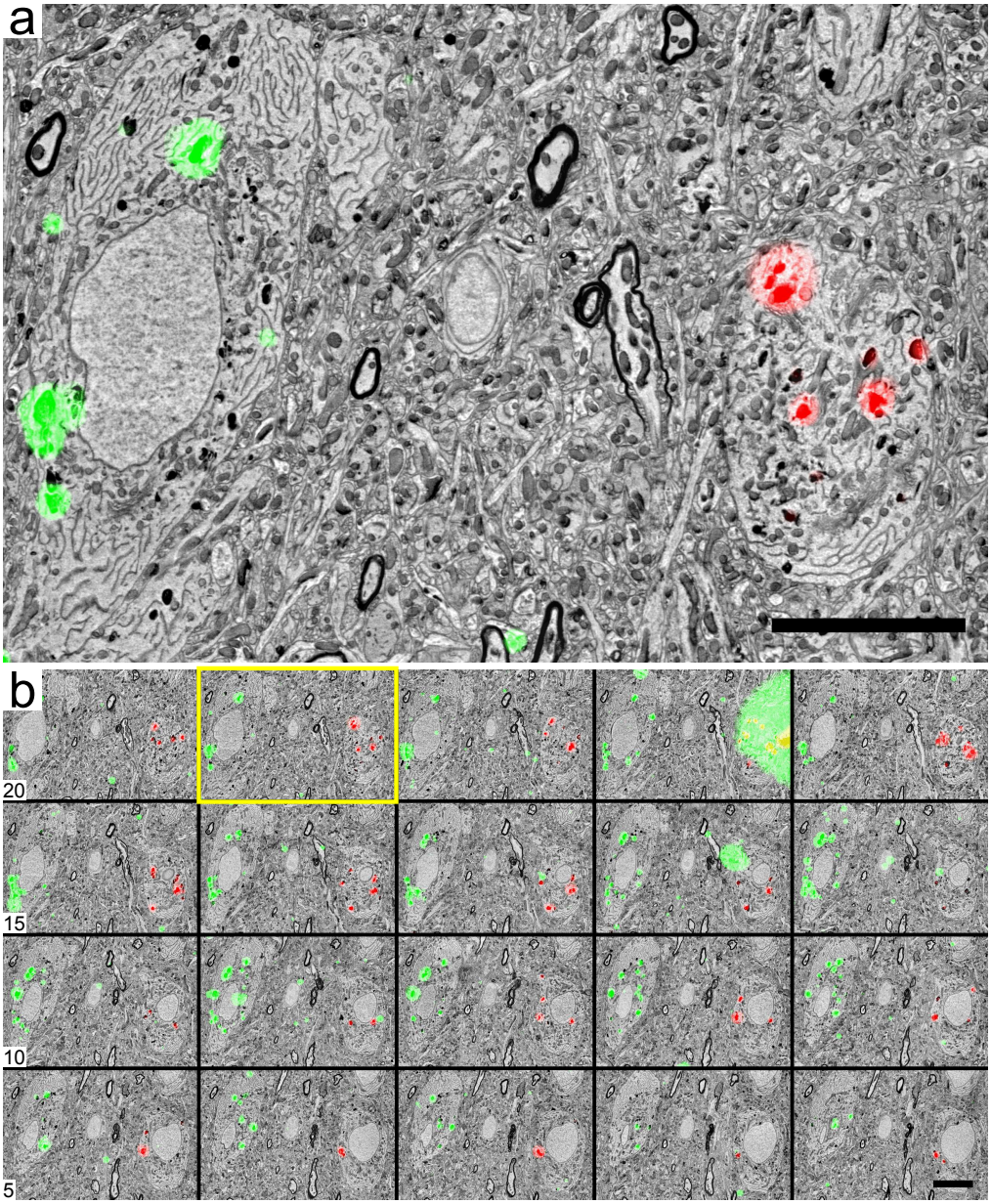

Figure 11. Correlative light and electron microscopy imagery of the IHC-treated, unmilled top of the 20 physical sections. (a) Correlative LM-EM micrograph of a portion of section #19. Green: transported FITC tracer injected in nucleus AreaX. Red: transported Texas Red tracer injected in nucleus Avalanche. **(b)** Montage of a portion of the top surface of the 20 physical sections. Scale bars: 5 μm.

5 Discussion

5.1 Summary

I demonstrated that performing cycles of alternating BIB milling and EM imaging of ultrathin sections of resin-embedded biological tissue collected on silicon wafer creates a serial tomographic effect. A relatively large area of more than 115 μm x 85 μm was easily processed on each of the sections spanning roughly 1.5 mm^2 on wafer and there is no major hurdle in sight to proceed to larger areas. Sub-10 nm axial resolution was achieved on limited segments (as indicated by thickness estimation from ligth microscopy) and interspersed with gaps of around 40 nm thickness. Inhomogeneities in the serial milling process and the gap at section boundary, further discussed below, need to be further addressed to optimize the continuity of the EM imagery across consecutive physical sections to provide isotropic sub-10nm resolution volumes.

The proof of concept dataset obtained is a correlative LM-EM dataset that includes a post-embedding IHC treatment followed by fluorescent brightfield LM imaging, which constitutes a unique advantage compared to the in-chamber imaging and ablating methods FIBSEM and SBFSEM.

Is hybrid mechanical sectioning and BIB milling new ? The existing method most similar to the concept introduced in this article was to my knowledge reported by Shimizu et al. in 2001 [77]. The authors collected 32 consecutive 1 μm thick sections on glass slides and performed a chemical treatment (toluidine blue) before first observing the sections with light microscopy. The consecutive sections were then simultaneously etched with a simple omni-directional plasma with the goal of enhancing tissue quality prior to EM imaging. Nevertheless no serial tomographic effect was observed nor anticipated.

5.2 Please mind the gap

It is unambiguously shown in Figure 9 a that sub-10 nm axial resolution was not achieved continuously at the junctions between consecutive physical sections.

These gaps across consecutive sections may not be a problem for qualitative analysis as long as the experimenter is aware of them, or when the chosen BIB milling thickness is greater than the gap size, however they would confuse automated algorithms for example for the tracing of thin neuronal wires in celluar-resolution connectomic imagery. Nevertheless, dealing with imperfect datasets is now becoming part of modern segmentation pipelines (e.g., data augmentation in [43]) and the specific problem of section unevenness and missing slices can be measured post-acquisition [23] and addressed with emerging super-resolution techniques [30, 35] or handcrafted approaches [23].

It is to my knowledge unknown how much material is lost between sections during the physical sectioning with a diamond knife. Reports of good quality in 10 nm axial resolution SBFSEM imagery [70] suggest that this loss is likely negligible. The two other contributions to this gap are phenomenons happening at the bottom and at the top of the sections during BIB milling and EM imaging.

5.2.1 Gap at the surface of the sections

It is not yet well understood what happened at the first EM imaging cycle. Thickness estimation from LM indicates that the first imaging cycle has left sections that were 26 nm less thick than before imaging. It seems to be a surprisingly strong milling effect despite EM imaging parameters that, to my knowledge, would not be considered as particularly harsh (2 keV, 800 pA current probe) and despite the known shrinkage phenomenon caused by irradiation on tissue sections [11, 39, 46]. Lowering the voltage or the current probe or both (in combination with using better detectors than I had access to), or decelerating the beam [60, 89] may reduce this milling effect. Emerging deep learning-based image restoration techniques would also help to maintain high image quality with milder imaging conditions [96].

The IHC treatment contains 0.05% of Tween which may have had an effect on the sections. In the absence of a wet etching with sodium metaperiodate, this use of Tween, inspired by [10], is crucial to obtain a LM signal of good quality from the IHC. Therefore Tween certainly affects the surface of the sections to enable successful antibody binding, and this modification may be linked to the strong EM miling observed.

The first 2-3 slices acquired at the surface of the 20 physical sections look slightly different from the slices obtained deeper after several BIB cycles (Figure 9 e) suggesting that the top surface exhibits special properties.

When comparing to FIBSEM or SBFSEM, it seems that these systems operate at a sort of steady state regime to achieve their good quality and stability. Imaging sessions typically start after some slices at the top have already been consumed.

Only a specific Durcupan resin formulation was tested in this study, which is a resin known to be well suited for FIB [40, 99] and seems to offer good resistance to impairing effects of electron beam irradiation such as tissue shrinkage [39]. Other resins remain to be tested.

The interplay between IHC treatment, EM imaging parameters and section thickness needs to be further investigated to design strategies to optimize the continuity of the imagery across consecutive physical sections. Treatments such as coatings [89] may have positive effects.

5.2.2 Gap at the bottom of the sections

Until which thickness can a section be milled to obtain imagery of good quality ? Electron-dense contamination such as shown in Figure 9 e seems to start appearing around 10-20 nm thickness. This contamination tends to appear first and to be then more pronounced at already electron-dense locations such as mitochondria and lysosomes. These spots are likely made of the heavy-metal contained in the issue, but analysis with for example energy-dispersive X-ray spectroscopy would reveal their composition.

Choosing a greater thickness for the mechanically cut sections should be a simple way to increase the thickness over which high axial resolution is ahieved by BIB milling cycles and it would reduce the frequency of the occurrence of the gaps in the volumetric imagery.

Alternatively, multi-energy landing deconvolution [3–5, 12, 65] could be performed for example when 20-30 nm of section are left on the wafer before the apparition of artifacts. This procedure would probably require back-scattered imagery, which might need some correction to fit within a volume acquired with secondary electron detectors.

5.3 Comparison to and implications for existing methods

5.3.1 Tape-collected sections

Compared to the ATUM technique [28, 32, 37, 55] that can in the best case provide long series of 30 nm thick sections [37], the proof of concept dataset presented here exhibits higher axial resolution on short segments but presents gaps that are slightly thicker than the constant 30 nm obtained with the ATUM. When compared to other datasets collected with the ATUM technique such as the whole zebra finch volume from Hildebrand et al. [32] with a mean section thickness of 60 nm, the small proof of concept data set presented here seems quite promising.

A clear advantage of the technique presented here is the ability to easily perform chemical treatments in bulk on all sections such as poststainings or here immunohistochemistry directly on the silicon wafer, followed by fluorescent reflection imaging that can typically be performed with high magnification ($>$ 60x) immersion objectives (see Chapter 2 of this thesis), although here only a 20x magnification objective was used.

Revisiting existing datasets Can sections collected on tape be submitted to cycles of BIB milling and EM imaging ? Would the tape produce debris that would contaminate the sections ? It remains to be demonstrated. If successful, it might now be possible to enhance the resolution of existing datasets. For example entire wafers from the "Kasthuri dataset" [37] containing each about 200 tape-collected sections could be milled with a BIB machine producing homogeneous milling over large surfaces. One BIB milling of 15 nm and SEM imaging could then yield a new dataset with resolution 3 nm x 3 nm x 15 nm instead of the original 3 nm x 3 nm x 29 nm. As this landmark dataset has been mined intensively with manual and automated methods [22, 36–38, 41, 43, 49, 69, 82, 86, 102] it could be interesting to evaluate the advantages offered by the higher resolution.

Similarly, Hildebrand et al. [32] points out the large thickness of the sections (60 nm) from their whole zebra fish brain dataset as a limitation for a more accurate volumetric reconstruction of neuronal processes. The authors also mention considering for this purpose to produce a new dataset with a z-resolution smaller than 30 nm. Provided that their current data set does not suffer from large breakage or improper staining, I suggest as an alternative to perform several cycles of BIB milling and SEM imaging to increase the resolution down to their desired thickness instead of producing a dataset anew.

Finally, as reel-to-reel imaging systems are emerging for tape-collected sections [54, 63, 64], a BIB milling system could be designed to mill sections directly on a reel-to-reel system, possibly inside the imaging chamber or a neighbor chamber of an electron microscope.

5.3.2 MagC: magnetic collection

The hybrid method presented here has clear benefits for the magnetic collection approach (MagC, Chapter 2 of this thesis). The high axial resolution achieved in the proof of concept dataset presented here comes from relatively thick sections with 120 nm thickness. Such thicker sections are much easier to cut and to handle than standard 50 nm sections as they are clearly less fragile. The reordering process is simplified as the similarity with distant neighbors is smaller. Importantly, thicker sections contain more magnetic material which significantly simplifies and speeds up the magnetic collection process thanks to greater attraction forces. Thicker sections will also tend to simplify the alignment of EM imagery: most of the alignment is done on consecutively milled sections, and only once in a while must imagery from two different physical sections be aligned.

An important benefit of hybrid sectioning for MagC and also in general for non-destructive serial sectioning is an additional forgiveness granted on section thickness homogeneity. It is known that stopping and restarting the ultramicrotome sectioning process has to be avoided as much as possible [25, 32] to produce continuous series of consecutive sections of homogeneous thickness [25]. The reasons are that the first sections cut after restart exhibit strong thickness variations or some sectioning cycles even do not produce a section at all, especially at nominal thicknesses around and below 30 nm [37]. Note finally that this new forgiveness granted by thicker mechanical sectioning is of considerable advantage when compared to the failure-prone processes of the tissue-destructive technologies SBFSEM and FIBSEM (although see Xu et al. [99] for industrial-grade and expensive efforts that led to safe and prolonged operation of FIBSEM at scale). The hybrid mechanical sectioning/BIB milling method therefore offers forgiveness to a very sensitive process normally prone to failure at any moment during its long execution.

Nevertheless, this new forgiveness about the inhomogeneity of the first sections comes with a reinforced unforgiveness about losing physical sections during the collection process. As these are thicker, any lost section would produce a significant gap in the volumetric imagery, which could for example be fatal in the quest of reconstructing many neuronal wires across long distances in cellular-resolution connectomics. I think however that the no-section loss unforgiveness is much less demanding than the no-restart constraint, especially when using an advanced section collection method such as the magnetic collection MagC (Chapter 2 of this thesis).

Finally, producing homogeneous milling over large areas will be needed to scale up the hybrid sectioning system combined with the on-wafer magnetic collection technique. Special rotating holders could be engineered for small BIBs such as the one used in the study, or larger machines that are current in the semiconductor industry could be used. An ideal setting would be to collect many hundreds of relatively thick sections with the MagC method, perform IHC and LM imaging, followed by cycles of BIB-EM in a multi-beam electron microscope that contains an integrated large area BIB miller. Note that skipping the use of a complex integrated BIB-SEM microscope (likely difficult to engineer in a EM multibeam setting) would still be an excellent solution, because many hundreds of sections can be processed simultaneously with a single wafer. That is, one can afford to manually transfer wafers from the EM to the BIB instruments from time to time without too much overhead.

5.3.3 Array Tomography

Manual or semi-manual section collection methods [33, 51, 80] used for array tomography could also benefit from the hybrid method with the new forgiveness, and the much easier handling of thicker sections. See ”BIB after IHC” section below.

5.3.4 Hot-knife partitioning

My hybrid method is still currently outperformed by the hot-knife partitioning approach developed by Hayworth et al. [29] about the ability to produce imagery without gaps. Further reducing the gaps shown in this manuscript would let the hybrid method catch up with the advantages of the hot-knife approach, and would in addition offer physical access to the relatively thin sections for chemical treatments and correlative microscopy. Notably, imaging operation should be incommensurably simpler with standard SEMs than with FIBSEM microscopes.

5.4 Section thickness estimation

The quality of thickness estimation using light microscopy could first be enhanced by extending the calibration set to more sections from different samples and spanning a larger range of thicknesses.

The calibrations for thicknesses smaller than 150 nm were only made on sections that had been subjected to milling, and not on umilled sections. Given that bombardment with ions or electrons affects the surface of plastic sections [11, 46] and hence probably their interferometric properties, my thickness estimation of unmilled sections was then maybe slightly less accurate than the milled ones. The mean thickness of the 20 unmilled sections of the data set (Figure 4a) was measured to be 125 nm (4c), while the microtome advancement was set at 120 nm, giving an estimation error slightly greater than the mean estimation error obtained on the test set of the calibration (containing only milled sections). This 5 nm mean error could be attributed to the change of interferometric properties of sections due to bombardment. Nevertheless, I made the gap size estimations based on the microtome nominal thickness (Leica UC6), which according to the manufacturer, is accurate well below a nanometer. A separate training set for both milled and unmilled sections would therefore only have potentially enhanced the thickness estimation of the microtome-cut, unmilled sections, for which a reliable thickness estimation was given by the microtome.

The estimation could also be enhanced by fitting calibration points to the physical model characterizing interferences in thin films instead of simply using a b-spline interpolation. A well controlled LED or laser illumination instead of a standard brightfield lamp would reduce potential illumination fluctuations between measurements. A scanning technology such as confocal microscopy with laser illumination instead of bulk imaging may also prevent artifacts in the measurements caused by the total field of view of the camera.

Atomic force microscopy has been considered and tried to perform the calibration in this study, however the instrument I had access to was rather slow and much more impractical to use compared to the profilometer. The specifications of the profilometer mention a 1 nm z-resolution (not verified) and the device seems to provide consistent results.

Interferometric measurements were also considered such as ellipsometry, but initial calibrations and fitting of models are necessary. Moreover the thin films to be measured in the ellipsometer I had access to need to cover areas larger than 1 mm^2 which was not the case for most of the sections studied (some preliminary experiments not shown). An ellipsometer with higher lateral accuracy or simply standard interferometers could be used to further measure section thickness.

Finally, image-based methods could be used to assess thickness spacing in acquired EM imagery such as the one developed by Hanslovsky et al. [23]. It requires however to have already acquired the EM imagery consistently across several slices to be able to compute an estimate. Moreover, the slight appearance variations observed between top surface slices and slices acquired after a few milling cycles is likely to bias the estimate (note though that the authors of the technique claim that it can account for some variations).

5.5 Sensitivity to contamination

As shown in Figure 9 e, atmospheric debris landing on collected sections may have a more impairing impact on the EM imagery as with standard serial non-destructive sectioning because debris would typically be present in all slices from a same physical section (note however that the debris in Figure 9 e was slowly milled away). Particular care must then be taken to avoid such contamination. It can be done by using an enclosure box around the ultramicrotome in

which only purified air is entering, and by working subsequently in a cleanroom-like environment.

An integrated BIB-SEM machine [16, 34] would also obviously significantly lower the risk of contamination by avoiding numerous transfers between the EM and the BIB milling machine. As the BIB milling process might contaminate elements in the imaging chamber, an automated transfer to a neighbor chamber might be required. Notably, I am aware of a multi-beam EM microscope being engineered to be able to intersperse imaging with plasma-based coating outside the imaging chamber in an automated fashion. This unique system seems to be close to an ideal integrated BIB-multibeam-SEM for high-throughput imaging.

5.6 BIB followed by IHC

Array tomography [52] introduced the concept of repeated cycles of simultaneous chemical treatments of many ultrathin sections collected onto a flat substrate followed by fluorescent light microscopy. Its z-resolution is limited by the physical thickness of the collected sections, typically at least 70 nm [10, 68, 78]. Performing cycles of small thickness BIB milling (e.g. 10 nm) and IHC-LM imaging would present the following advantages. First the z-resolution of the LM imagery would be much higher, e.g. 10 nm. Second, different stainings could be performed on almost exactly the same piece of tissue (only offset by a few nanometers in depth) yielding a high degree of multiplexing, that is, the ability to probe the same piece of sample repetitively with different treatments. For example, if 4 antibodies were used after each cycle of 10 nm BIB etching, 28 antibodies could be probed in a 70 nm section, the same antibody number reported in [50], but here without using any elution, which has been shown to impair the ultrastructural quality of the tissue [10]. Third, by alternatively performing IHC-LM and SEM imaging after each BIB milling, the SEM imaging would be performed on freshly milled and chemically untreated sections, and the z-resolution of both the LM and EM imagery would be twice the BIB milling depth (e.g. 20 nm) while maintaining a high degree of multiplexing (e.g., 16 antibodies in 80 nm thick sections with 4 antibodies per staining round).

On-section IHC however did not yield here any positive signal after a brief BIB milling (90 seconds, ~15-20 nm) on exact same sections in which unambiguous positive signal was obtained before the BIB milling. It can be concluded that high-energy glancing angle BIB milling, even during short periods of time, completely impairs the antigen-antibody bounding process at section surface. To my knowledge, only 3 reports mention the submission of sections of resin-embedded tissue to a plasma etching process before performing a chemical staining.

First, Squarzoni et al. [81] have for the first time performed plasma etching prior to a staining experiment (with gold-coated ribonuclease and deoxyribonuclease) and observed a reduced background with unchanged positive signal with Ar^+ and O_2 gases but no effect with a N_2 gas. Second, Goto et al. [21] performed up to 20 min argon plasma etching to expose the surface of cells embedded in LRGold resin and obtained satisfactory signal after subsequent IHC. They noted however a poor immunolabeling after a long plasma etching of 60 minutes. Third, Yahiro et al. [101] similarly found that a ”very mild” plasma treatment on micrometer thick LRWhite sections improved the quality of subsequent IHC, but that plasma treatment of ”excessive strength or extended duration” had a detrimental effect (the gas used was not mentioned).

Note that in the second reference [21], plasma etching was not performed with the purpose of improving the IHC staining, but was performed as a prerequesite step to expose tissue surrounded by resin. Note in addition that after reporting a mild improvement in IHC quality subsequent to plasma etching, the same first author 6 years later [100] instead performed etching only after IHC and not before, possibly indicating that BIB milling prior IHC may have a

negative effect.

Overall, the literature indicates that only mild plasma etching might improve IHC quality while strong plasma etching has a detrimental effect. Considering that the machine used in the present study produces a beam instead of an undirected plasma and that it is operated at maximal power, it can be hypothesized that the present treatment is very harsh and therefore prevents any antigen-antibody binding process, which agrees with the literature. Note that it cannot be excluded that the loss of signal depends on the specific sample used in this study (epoxy resin, Texas Red, Alexa 488 and FITC antigens).

Deosmication with a 10 minute treatment with 3% sodium metaperiodate did not recover the IHC signal (data not shown). It remains unknown whether IHC signal could be recovered. A deplasticizing wet treatment [8] might be tried.

5.7 IHC followed by BIB

Despite the fact that after BIB milling no IHC was obtained, BIB milling could still be used in experiments involving chemical treatment and fluorescence microscopy with subsequent SEM imaging such as correlative [59] or conjugate [10] array tomography. For example, serial 50 nm thick sections could be treated with one or several rounds of IHC (and elution) and imaged with fluorescence microscopy before undergoing a 25 nm thick BIB milling for a final SEM imaging round. The experiment would result in unaltered fluorescent imagery and high quality EM imagery acquired from freshly milled sections. The LM and EM stacks would have the same z-resolution equal to the thickness of the mechanically cut sections, e.g. 50 nm, and could be correlated as if no BIB milling had been performed because the physical slices from which signal was obtained are virtually the same, only offset on the vertical axis by the BIB milling thickness, e.g. 25 nm.

Note that employing plasma etching (but not BIB milling) as a section cleaning procedure after a chemical treatment for subsequent EM has been used sporadically in the past [19, 77]. I suggest that this principle should be updated to BIB milling (and was to some extent already used in the proof of concept data set presented here), and could for example yield correlative LM and EM imagery with not only excellent signal of endogenous proteins but also excellent EM imagery as reported by Collman et al. [10], who showed excellent LM and EM imagery, but the latter only when the sections were not submitted to IHC.

5.8 Connectomics of large brains

Projects are underway to acquire nanometric resolution volumetric EM imagery of whole large brains from species such as pygmy shrew or mouse [53]. Serial block face and tape collection [54] are the current two candidate technologies for serial ablation of material from large brain blocks. Could a sectioning approach using only BIB milling be used for whole brains ? Would an integrated BIB-multibeam electron microscope be the solution to the acquisition of nanometric volumetric EM imagery for centimeter-sized brains ? Should an hybrid approach be used combining mechanical serial block face sectioning with broad ion beam milling ? I anticipate that broad ion beam milling technology will provide the key solution to whole-brain cellular-resolution connectomics of large brains.

A Drosophila brain (500 μm x 300 μm x 300 μm) mechanically cut into 3,000 sections of thickness 100 nm would fit on a single 4 inch silicon wafer that could be submitted to 10 cycles of 10 nm BIB milling and 200Mpixels/s multibeam EM imaging lasting each 10 hours to produce in 5 days a whole Drosophila brain at resolution 8 nm x 8 nm x 10 nm. I also foresee

that BIB milling technology may be the key technology enabling whole-brain connectomics in larger species.

Alternatively, should tape collection be combined with BIB milling ? For example instead of cutting and collecting 200'000 sections of thickness 50 nm for a cubic centimeter of brain, only 20'000 sections of thickness 500 nm could be collected and then submitted to 10 cycles of EM imaging and BIB milling of thickness 50 nm.

With the magnetic collection method MagC, one 6 inch silicon wafer would contain about 100 sections of size 1 cm x 1 cm x 500 nm so that a library of about 200 wafers could contain an entire cubic centimeter of brain (a whole mouse brain for example) ready for BIB-EM imaging for cellular-resolution connectomics.

5.9 Outlook

I have demonstrated a proof of concept for hybrid mechanical sectioning and magnetic collection combined with cycles of broad ion beam milling and electron microscopy imaging. The axial resolution was not as homogeneous as currently achieved by FIBSEM or SBSFSEM but there is clear hope to fix it. The current gap of about 40 nm observed across consecutive physical sections in the EM imagery has been identified and now needs to be solved. Given that virtually no material is lost after section collection, there is also hope that we will be able to extract continuous imagery from these tissue sections using existing technologies.

I believe that magnetic collection combined with broad ion beam milling paves the way for a new avenue in volumetric electron microscopy and will eventually enable volumetric correlative light and multi-beam isotropic electron microscopy of unprecedentedly large volumes.

6 Supporting Information

6.1 S1 Video

Z-resliced electron microscopy (EM) imagery from the proof of concept correlative dataset. (accessible at https://youtu.be/CqeQlOssHeA)

Top: imagery from the top surface of the 20 physical sections of thickness 120 nm.

Middle: imagery from the EM rounds number 2, 8, and 15 from each physical section.

Bottom: imagery from all EM rounds from each physical section.

6.2 S2 Video

Flythrough in a small patch of EM imagery. (accessible at https://youtu.be/hPJojQ8qPRo)

Left: 1 image per mechanical section (120 nm nominal thickness)

Right: 3 images per mechanical section (roughly 40 nm thickness)

6.3 S3 Video

Flythrough in a small patch of EM imagery. (accessible at https://youtu.be/TsYvFOeNQN4)

Left: 1 image per mechanical section (120 nm nominal thickness)

Right: 16 (or sometimes 17) images per mechanical section

6.4 S4 Figure - Profilometer repeatability

Repeatability of the mechanical profilometry was estimated from 6 consecutive measurements on a section of about 150 nm thickness (the section was part of a ribbon cut with a nominal thickness of 150 nm) as the standard deviation of the thickness: $\sqrt{\frac{\sum(t_i-\bar{t})^2}{N-1}}$ and was equal to 0.96 nm. The thickness was calculated as the mean over the yellow range shown in Figure S1 and the six thickness measurements were: 144.58, 147.38, 146.58, 145.74, 145.73, and 145.53 nm. The measurements were aligned taking as onset the location where the curve became greater than 100 nm.

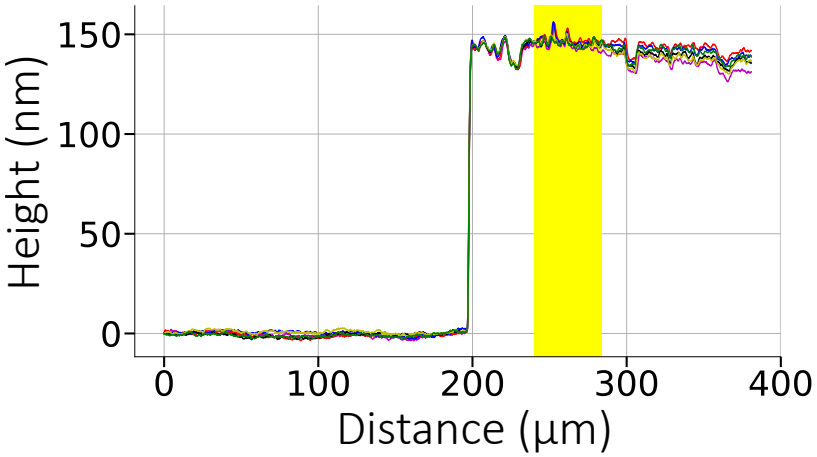

Figure S1. Repeated profilometry measurements on the same section. Six consecutive measurements were made on a section belonging to a ribbon that was cut with a 150 nm nominal thickness. The yellow rectangle shows the range over which the thickness was averaged for each trial.

Acknowledgments

I acknowledge that the work has been conducted with infrastructure support from the laboratory of Prof. Hahnloser. I thank E. Gini from the ETH cleanroom facility (FIRST) for help with the plasma etching experiment. I acknowledge support of the Scientific Center for Optical and Electron Microscopy ScopeM of the Swiss Federal Institute of Technology ETHZ.

Competing interests

The author has filed a patent application protecting the magnetic collection technique [87].

References

1. D. Applegate, R. E. Bixby, V. Chvátal, and William J. Cook. Concorde TSP Solver, 2003.
2. D. D. Bock, W.-C. A. Lee, A. M. Kerlin, M. L. Andermann, G. Hood, A. W. Wetzel, S. Yurgenson, E. R. Soucy, H. S. Kim, and R. C. Reid. Network anatomy and in vivo physiology of visual cortical neurons. *Nature*, 471(7337):177–182, 3 2011.
3. F. Boughorbel, C. S. Kooijman, B. H. Lich, and E. G. T. Bosch. SEM imaging method, 2012.
4. F. Boughorbel, X. Zhuge, P. Potocek, L. de Bruin, and B. Lich. The Future SEM Sees 3 Dimensions ... Bringing Deconvolution Techniques to the Electron Microscope. *Microsc. Mircoanal. 19 (Suppl 2)*, 19(S2):380–381, 2013.
5. F. Boughorbel, X. Zhuge, P. Potocek, and B. Lich. SEM 3D Reconstruction of Stained Bulk Samples using Landing Energy Variation and Deconvolution. *Microscopy and Microanalysis*, 18(S2):560–561, 2012.
6. K. L. Briggman. Miniature serial sectioning microtome for block-face imaging, 2015.
7. K. L. Briggman, M. Helmstaedter, and W. Denk. Wiring specificity in the direction-selectivity circuit of the retina. *Nature*, 471(7337):183–188, 3 2011.
8. S. H. Brorson. Deplasticizing or etching of epoxy sections with different concentrations of sodium ethoxide to enhance the immunogold labeling. *Micron (Oxford, England : 1993)*, 32(2):101–5, 2 2001.
9. A. Cardona, S. Saalfeld, J. Schindelin, I. Arganda-Carreras, S. Preibisch, M. Longair, P. Tomancak, V. Hartenstein, and R. J. Douglas. TrakEM2 software for neural circuit reconstruction. *PLoS ONE*, 7(6):e38011, 2012.
10. F. Collman, J. Buchanan, K. D. Phend, K. D. Micheva, R. J. Weinberg, and S. J. Smith. Mapping Synapses by Conjugate Light-Electron Array Tomography. *Journal of Neuroscience*, 35(14):5792–5807, 2015.
11. A. Cosslett. Some Applications of the Ultra-Violet and Interference Microscopes in Electron Microscopy. *Journal of the Royal Microscopical Society*, 79(3):263–271, 10 1959.

12. M. de Goede, E. Johlin, B. Sciacca, F. Boughorbel, and E. C. Garnett. 3D multi-energy deconvolution electron microscopy. *Nanoscale*, 9(2):684–689, 1 2017.

13. T. Deerinck, E. Bushong, a. Thor, and M. Ellisman. NCMIR methods for 3D EM: A new protocol for preparation of biological specimens for serial block face scanning electron microscopy. *Microscopy*, pages 6–8, 2010.

14. W. Denk and H. Horstmann. Serial block-face scanning electron microscopy to reconstruct three-dimensional tissue nanostructure. *PLoS Biology*, 2(11):e329, 11 2004.

15. G. Desbois, J. L. Urai, and P. A. Kukla. Morphology of the pore space in claystones – evidence from BIB/FIB ion beam sectioning and cryo-SEM observations. *eEarth Discussions*, 4(1):1–19, 2 2009.

16. G. Desbois, J. L. Urai, F. Perez-Willard, Z. Radi, S. Offern, I. Burkart, P. A. Kukla, and U. Wollenberg. Argon broad ion beam tomography in a cryogenic scanning electron microscope: A novel tool for the investigation of representative microstructures in sedimentary rocks containing pore fluid. *Journal of Microscopy*, 249(3):215–235, 3 2013.

17. V. M. Donnelly and A. Kornblit. Plasma etching: Yesterday, today, and tomorrow. *Journal of Vacuum Science & Technology A: Vacuum, Surfaces, and Films*, 31(5):050825, 2013.

18. A. L. Eberle, S. Mikula, R. Schalek, J. Lichtman, M. L. Knothe Tate, and D. Zeidler. High-resolution, high-throughput imaging with a multibeam scanning electron microscope. *Journal of Microscopy*, 259(2):114–120, 8 2015.

19. T. Fujiwara, D. Shimizu, K. Kon, N. Isshiki, H. Tsunokuni, and S. Aoyagi. A new method for detecting and localizing cell markers endocytosed by fibroblasts in epoxy resin semi-thin sections using scanning electron microscopy combined with energy dispersive X-ray microanalysis after ion-etching. *Journal of Electron Microscopy*, 49(4):551–558, 1 2000.

20. D. R. Glenn, H. Zhang, N. Kasthuri, R. Schalek, P. K. Lo, a. S. Trifonov, H. Park, J. W. Lichtman, and R. L. Walsworth. Correlative light and electron microscopy using cathodoluminescence from nanoparticles with distinguishable colours. *Scientific reports*, 2:865, 2012.

21. T. Goto, K. S. Wong, and D. M. Brunette. Observation of Fibronectin Distribution on the Cell Undersurface Using Immunogold Scanning Electron Microscopy. *Journal of Histochemistry & Cytochemistry*, 47(11):1487–1493, 11 1999.

22. D. Haehn, V. Kaynig, J. Tompkin, J. W. Lichtman, and H. Pfister. Guided Proofreading of Automatic Segmentations for Connectomics. *arXiv preprint arXiv:1704.00848*, 2017.

23. P. Hanslovsky, J. A. Bogovic, and S. Saalfeld. Image-based correction of continuous and discontinuous non-planar axial distortion in serial section microscopy. *Bioinformatics*, 33(9):btw794, 12 2016.

24. K. M. Harris and J. Carson. NeuroNex Technology Hub: Enhanced resolution for 3DEM analysis of synapses across brain regions and taxa. https://nsf.gov/awardsearch/showAward?AWD_ID=1707356, 2017.

25. K. M. Harris, E. Perry, J. Bourne, M. Feinberg, L. Ostroff, and J. Hurlburt. Uniform Serial Sectioning for Transmission Electron Microscopy. *Journal of Neuroscience*, 26(47):12101–12103, 11 2006.

26. K. M. Harris, J. Spacek, M. E. Bell, P. H. Parker, L. F. Lindsey, A. D. Baden, J. T. Vogelstein, and R. Burns. A resource from 3D electron microscopy of hippocampal neuropil for user training and tool development. *Scientific data*, 2:150046, 9 2015.

27. K. Hayworth, N. Kasthuri, R. Schalek, and J. Lichtman. Automating the Collection of Ultrathin Serial Sections for Large Volume TEM Reconstructions. *Microscopy and Microanalysis*, 12(S02):86–87, 2006.

28. K. J. Hayworth, J. L. Morgan, R. Schalek, D. R. Berger, D. G. C. Hildebrand, and J. W. Lichtman. Imaging ATUM ultrathin section libraries with WaferMapper: a multi-scale approach to EM reconstruction of neural circuits. *Frontiers in Neural Circuits*, 8(June):68, 1 2014.

29. K. J. Hayworth, C. S. Xu, Z. Lu, G. W. Knott, R. D. Fetter, J. C. Tapia, J. W. Lichtman, and H. F. Hess. Ultrastructurally smooth thick partitioning and volume stitching for large-scale connectomics. *Nature Methods*, 12(4):319–322, 2 2015.

30. L. Heinrich, J. A. Bogovic, and S. Saalfeld. Deep Learning for Isotropic Super-Resolution from Non-Isotropic 3D Electron Microscopy. 6 2017.

31. M. Helmstaedter. Cellular-resolution connectomics: challenges of dense neural circuit reconstruction. *Nature methods*, 10(6):501–7, 6 2013.

32. D. G. C. Hildebrand, M. Cicconet, R. M. Torres, W. Choi, T. M. Quan, J. Moon, A. W. Wetzel, A. Scott Champion, B. J. Graham, O. Randlett, G. S. Plummer, R. Portugues, I. H. Bianco, S. Saalfeld, A. D. Baden, K. Lillaney, R. Burns, J. T. Vogelstein, A. F. Schier, W.-C. A. Lee, W.-K. Jeong, J. W. Lichtman, and F. Engert. Whole-brain serial-section electron microscopy in larval zebrafish. *Nature*, 545(7654):345–349, 5 2017.

33. H. Horstmann, C. Körber, K. Sätzler, D. Aydin, and T. Kuner. Serial section scanning electron microscopy (S 3EM) on silicon wafers for ultra-structural volume imaging of cells and tissues. *PLoS ONE*, 7(4):e35172, 1 2012.

34. T. Hosman, S. Coyle, A. Abbott, M. Olvera, M. Hassel-Shearer, and J. Hunt. IPrep – Automated Serial-Section Broad-Ion-Beam Tomography. *Microscopy and Microanalysis*, 22(S3):590–591, 7 2016.

35. V. Jain. Adversarial Image Alignment and Interpolation. 6 2017.

36. M. Januszewski, J. Maitin-Shepard, P. Li, J. Kornfeld, W. Denk, and V. Jain. Flood-Filling Networks. *CoRR*, abs/1611.0, 2016.

37. N. Kasthuri, K. J. Hayworth, D. R. Berger, R. L. Schalek, J. A. Conchello, S. Knowles-Barley, D. Lee, A. Vázquez-Reina, V. Kaynig, T. R. Jones, M. Roberts, J. L. Morgan, J. C. Tapia, H. S. Seung, W. G. Roncal, J. T. Vogelstein, R. Burns, D. L. Sussman, C. E. Priebe, H. Pfister, and J. W. Lichtman. Saturated Reconstruction of a Volume of Neocortex. *Cell*, 162(3):648–661, 2015.

38. V. Kaynig, A. Vazquez-Reina, S. Knowles-Barley, M. Roberts, T. R. Jones, N. Kasthuri, E. Miller, J. Lichtman, and H. Pfister. Large-scale automatic reconstruction of neuronal processes from electron microscopy images. *Medical Image Analysis*, 22(1):77–88, 2015.

39. C. Kizilyaprak, G. Longo, J. Daraspe, and B. M. Humbel. Investigation of resins suitable for the preparation of biological sample for 3-D electron microscopy. *Journal of Structural Biology*, 189(2):135–146, 2015.

40. G. Knott, H. Marchman, D. Wall, and B. Lich. Serial Section Scanning Electron Microscopy of Adult Brain Tissue Using Focused Ion Beam Milling. *Journal of Neuroscience*, 28(12):2959–2964, 2008.

41. S. Knowles-Barley, V. Kaynig, T. R. Jones, A. Wilson, J. Morgan, D. Lee, D. Berger, N. Kasthuri, J. W. Lichtman, and H. Pfister. RhoanaNet Pipeline: Dense Automatic Neural Annotation. *arXiv preprint arXiv:1611.06973*, pages 1–13, 2016.

42. J. Kornfeld, S. E. Benezra, R. T. Narayanan, F. Svara, R. Egger, M. Oberlaender, W. Denk, and M. A. Long. EM connectomics reveals axonal target variation in a sequence-generating network. *eLife*, 6, 2017.

43. K. Lee, J. Zung, P. Li, V. Jain, and H. S. Seung. Superhuman Accuracy on the SNEMI3D Connectomics Challenge. (Nips):1–11, 5 2017.

44. S. B. Leighton. SEM images of block faces, cut by a miniature microtome within the SEM - a technical note. *Scanning electron microscopy*, (Pt 2):73–6, 1981.

45. R. W. Linton, M. E. Farmer, P. Ingram, J. R. Sommer, and J. D. Shelburne. Ultrastructural comparison of ion beam and radiofrequency plasma etching effects on biological tissue sections. *Journal of Microscopy*, 134(1):101–112, 1984.

46. P. K. Luther. Sample Shrinkage and Radiation Damage of Plastic Sections. In *Electron Tomography*, pages 17–48. Springer New York, New York, NY, 2007.

47. R. E. Marc, J. R. Anderson, B. W. Jones, C. L. Sigulinsky, and J. S. Lauritzen. The AII amacrine cell connectome: a dense network hub. *Front Neural Circuits*, 8(September):104, 2014.

48. P. Maurer, M. Prigozhin, G. Song, X. Zheng, J. Courtis, J. Trotter, J. Collins, N. Liu, S. Aloni, F. Ogletree, R. MacFarlane, T. Südhof, P. Alivisatos, J. Rao, and S. Chu. Nanoprobes for electron microscopy with bio-specificity. In *Physics of Quantum Electronics*, page 94305, 2017.

49. Y. Meirovitch, A. Matveev, H. Saribekyan, D. Budden, D. Rolnick, G. O. Dor, S. Knowles-Barley, T. R. Jones, H. Pfister, J. W. Lichtman, and N. Shavit. A Multi-Pass Approach to Large-Scale Connectomics. *CoRR*, abs/1612.0, 2016.

50. K. D. Micheva, B. Busse, N. C. Weiler, N. O'Rourke, and S. J. Smith. Single-synapse analysis of a diverse synapse population: Proteomic imaging methods and markers. *Neuron*, 68(4):639–653, 11 2010.

51. K. D. Micheva, N. O'Rourke, B. Busse, and S. J. Smith. Array tomography: Production of arrays. *Cold Spring Harbor Protocols*, 5(11):pdb.prot5524, 11 2010.

52. K. D. Micheva and S. J. Smith. Array Tomography: A New Tool for Imaging the Molecular Architecture and Ultrastructure of Neural Circuits. *Neuron*, 55(1):25–36, 7 2007.

53. S. Mikula. Progress Towards Mammalian Whole-Brain Cellular Connectomics. *Frontiers in Neuroanatomy*, 10(June):1–7, 2016.

54. S. Mikula. In-Chamber Reel-to-Reel System for Random-Access Volume Electron Microscopy. *Microscopy and Microanalysis*, 23(S1):154–155, 7 2017.

55. J. L. Morgan, D. R. Berger, A. W. Wetzel, and J. W. Lichtman. The Fuzzy Logic of Network Connectivity in Mouse Visual Thalamus. *Cell*, 165(1):192–206, 2016.

56. S. Nanguneri, B. Flottmann, H. Horstmann, M. Heilemann, and T. Kuner. Three-dimensional, tomographic super-resolution fluorescence imaging of serially sectioned thick samples. *PLoS ONE*, 7(5):e38098, 1 2012.

57. K. Narayan and S. Subramaniam. Focused ion beams in biology. *Nature Methods*, 12(11):1021–1031, 2015.

58. A. B. Noske, A. J. Costin, G. P. Morgan, and B. J. Marsh. Expedited approaches to whole cell electron tomography and organelle mark-up in situ in high-pressure frozen pancreatic islets. *Journal of Structural Biology*, 161(3):298–313, 2008.

59. D. Oberti, M. a. Kirschmann, and R. H. R. Hahnloser. Correlative microscopy of densely labeled projection neurons using neural tracers. *Frontiers in neuroanatomy*, 4(June):24, 2010.

60. K. Ohta, S. Sadayama, A. Togo, R. Higashi, R. Tanoue, and K.-i. Nakamura. Beam deceleration for block-face scanning electron microscopy of embedded biological tissue. *Micron*, 43(5):612–620, 4 2012.

61. T. Ohyama, C. M. Schneider-Mizell, R. D. Fetter, J. V. Aleman, R. Franconville, M. Rivera-Alba, B. D. Mensh, K. M. Branson, J. H. Simpson, J. W. Truman, A. Cardona, and M. Zlatic. A multilevel multimodal circuit enhances action selection in Drosophila. *Nature*, 520(7549):633–9, 2015.

62. H. D. Ou, S. Phan, T. J. Deerinck, A. Thor, M. H. Ellisman, and C. C. O'Shea. ChromEMT: Visualizing 3D chromatin structure and compaction in interphase and mitotic cells. *Science*, 357(6349), 2017.

63. C. S. Own, M. F. Murfitt, L. S. Own, D. Brittain, N. Costa, R. C. Reid, and G. C. David. Reel-to-Reel Electron Microscopy : Latency-Free Continuous Imaging of Large Sample Volumes. *Microscopy and Microanalysis*, 21(0079):157–158, 2015.

64. C. S. Own, M. F. Murfitt, L. S. Own, and J. Cushing. Developments in Reel-to-Reel Electron Microscopy Infrastructure. *Microscopy and Microanalysis*, 23(S1):32–33, 7 2017.

65. P. Potocek, F. Boughorbel, B. Lich, and M. Langhorst. Computational scanning microscopy with improved resolution, 2016.

66. S. Preibisch, S. Saalfeld, T. Rohlfing, and P. Tomancak. Bead-based mosaicing of single plane illumination microscopy images using geometric local descriptor matching. In J. P. W. Pluim and B. M. Dawant, editors, *Proceedings of SPIE*, volume 7259, pages 72592S–72592S–10. International Society for Optics and Photonics, 2 2009.

67. S. Preibisch, S. Saalfeld, and P. Tomancak. Globally optimal stitching of tiled 3D microscopic image acquisitions. *Bioinformatics*, 25(11):1463–1465, 2009.

68. J.-C. Rah, E. Bas, J. Colonell, Y. Mishchenko, B. Karsh, R. D. Fetter, E. W. Myers, D. B. Chklovskii, K. Svoboda, T. D. Harris, and J. T. R. Isaac. Thalamocortical input onto layer 5 pyramidal neurons measured using quantitative large-scale array tomography. *Frontiers in neural circuits*, 7(November):177, 2013.

69. W. G. Roncal, M. Pekala, V. Kaynig-Fittkau, D. Kleissas, J. T. Vogelstein, H. Pfister, R. Burns, R. J. Vogelstein, M. A. Chevillet, and G. D. Hager. VESICLE : Volumetric Evaluation of Synaptic Interfaces using Computer Vision at Large Scale. In Xianghua Xie Mark W. Jones and G. K. L. Tam, editors, *Proceedings of BMVC*, pages 1–13. BMVA Press, BMVA Press, 9 2015.

70. M. R. G. Russell, T. R. Lerner, J. J. Burden, D. O. Nkwe, A. Pelchen-Matthews, M.-C. Domart, J. Durgan, A. Weston, M. L. Jones, C. J. Peddie, R. Carzaniga, O. Florey, M. Marsh, M. G. Gutierrez, and L. M. Collinson. 3D correlative light and electron microscopy of cultured cells using serial blockface scanning electron microscopy. *Journal of Cell Science*, 130(1):278–291, 1 2017.

71. S. Saalfeld, R. Fetter, A. Cardona, and P. Tomancak. Elastic volume reconstruction from series of ultra-thin microscopy sections. *Nature methods*, 9(7):717–20, 7 2012.

72. S. Schaefer, T. McPhail, and J. Warren. Image deformation using moving least squares. *ACM Transactions on Graphics*, 25(3):533, 2006.

73. R. Schalek, D. Lee, N. Kasthuri, A. Peleg, T. Jones, V. Kaynig, D. Haehn, H. Pfister, D. Cox, and J. Lichtman. Imaging a 1 mm 3 Volume of Rat Cortex Using a MultiBeam SEM. In *Microscopy and Microanalysis*, volume 22, pages 582–583. Cambridge Univ Press, 2016.

74. J. Schindelin, I. Arganda-Carreras, E. Frise, V. Kaynig, M. Longair, T. Pietzsch, S. Preibisch, C. Rueden, S. Saalfeld, B. Schmid, J.-Y. Tinevez, D. J. White, V. Hartenstein, K. Eliceiri, P. Tomancak, and A. Cardona. Fiji: an open-source platform for biological-image analysis. *Nature methods*, 9(7):676–82, 2012.

75. C. A. Schneider, W. S. Rasband, and K. W. Eliceiri. NIH Image to ImageJ: 25 years of image analysis. *Nature Methods*, 9(7):671–675, 6 2012.

76. R. Shahidi, E. A. Williams, M. Conzelmann, A. Asadulina, C. Verasztó, S. Jasek, L. A. Bezares-Calderón, and G. Jékely. A serial multiplex immunogold labeling method for identifying peptidergic neurons in connectomes. *eLife*, 4(DECEMBER2015), 2015.

77. D. Shimizu, T. Fujiwara, K. Kon, N. Isshiki, and H. Tsunokuni. Three-dimensional reconstruction by scanning electron microscopy from serial epoxy resin semi-thin sections after ion-etching. *Journal of electron microscopy*, 50(1):51–5, 2001.

78. Y. Sigal, C. Speer, H. Babcock, and X. Zhuang. Mapping Synaptic Input Fields of Neurons with Super-Resolution Imaging. *Cell*, 163(2):493–505, 10 2015.

79. G. E. Soto, S. J. Young, M. E. Martone, T. J. Deerinck, S. Lamont, B. O. Carragher, K. Hama, and M. H. Ellisman. Serial section electron tomography: a method for three-dimensional reconstruction of large structures. *NeuroImage*, 1(3):230–43, 1994.

80. W. Spomer, A. Hofmann, I. Wacker, L. Ness, P. Brey, R. R. Schroder, and U. Gengenbach. Advanced substrate holder and multi-axis manipulation tool for ultramicrotomy. *Microscopy and Microanalysis*, 21(S3):1277–1278, 2015.

81. S. Squarzoni, N. Zini, F. Marinelli, and N. Maraldi. Reduction of background labeling in colloidal gold-enzyme reactions. *Histochemistry*, 94(3):297–301, 7 1990.

82. A. Suissa-peleg, D. Haehn, S. Knowles-barley, V. Kaynig, T. R. Jones, A. Wilson, R. Schalek, J. W. Lichtman, and H. Pfister. Automatic Neural Reconstruction from Petavoxel of Electron Microscopy Data. In *Microscopy and Microanalysis*, volume 22, pages 536–537. Cambridge Univ Press, 2016.

83. S.-y. Takemura, C. S. Xu, Z. Lu, P. K. Rivlin, T. Parag, D. J. Olbris, S. Plaza, T. Zhao, W. T. Katz, L. Umayam, C. Weaver, H. F. Hess, J. A. Horne, J. Nunez-Iglesias, R. Aniceto, L.-A. Chang, S. Lauchie, A. Nasca, O. Ogundeyi, C. Sigmund, S. Takemura, J. Tran, C. Langille, K. Le Lacheur, S. McLin, A. Shinomiya, D. B. Chklovskii, I. A. Meinertzhagen, and L. K. Scheffer. Synaptic circuits and their variations within different columns in the visual system of Drosophila. *Proceedings of the National Academy of Sciences*, 112(44):13711–13716, 2015.

84. S.-y. S. Takemura, Y. Aso, T. Hige, A. Wong, Z. Lu, C. S. Xu, P. K. Rivlin, H. F. Hess, T. Zhao, T. Parag, S. Berg, G. Huang, W. Katz, D. J. Olbris, S. Plaza, L. Umayam, R. Aniceto, L.-A. Chang, S. Lauchie, O. Ogundeyi, C. Ordish, A. Shinomiya, C. Sigmund, S.-y. S. Takemura, J. Tran, G. C. Turner, G. M. Rubin, and L. K. Scheffer. A connectome of a learning and memory center in the adult ¡i¿Drosophila¡/i¿ brain. *eLife*, 6:e26975, 7 2017.

85. J. C. Tapia, N. Kasthuri, K. J. Hayworth, R. Schalek, J. W. Lichtman, S. J. Smith, and J. Buchanan. High-contrast en bloc staining of neuronal tissue for field emission scanning electron microscopy. *Nature Protocols*, 7(2):193–206, 2 2012.

86. T. Templier, K. Bektas, and R. H. R. Hahnloser. Eye-Trace: Segmentation of Volumetric Microscopy Images with Eyegaze. In *Proceedings of the 2016 CHI Conference on Human Factors in Computing Systems*, pages 5812–5823, 2016.

87. T. Templier and R. H. Hahnloser. Method, device and system for manipulating portions of a rigid body, 2015.

88. O. Thaunat, A. G. Granja, P. Barral, A. Filby, B. Montaner, L. Collinson, N. Martinez-Martin, N. E. Harwood, A. Bruckbauer, and F. D. Batista. Asymmetric Segregation of Polarized Antigen on B Cell Division Shapes Presentation Capacity. *Science*, 335(6067):475–479, 1 2012.

89. B. Titze and W. Denk. Automated in-chamber specimen coating for serial block-face electron microscopy. *Journal of Microscopy*, 250(2):101–110, 5 2013.

90. B. Titze and C. Genoud. Volume scanning electron microscopy for imaging biological ultrastructure. *Biology of the Cell*, 108(11):307–323, 11 2016.

91. W. F. Tobin, R. I. Wilson, and W. C. A. Lee. Wiring variations that enable and constrain neural computation in a sensory microcircuit. *eLife*, 6, 2017.

92. J. van Marle, A. Dietrich, K. Jonges, R. Jonges, E. de Moor, A. Vink, P. Boon, and H. van Veen. Em-tomography of section collapse, a non-linear phenomenon. *Microscopy Research and Technique*, 31(4):311–316, 7 1995.

93. A. Vishwanathan, K. Daie, A. D. Ramirez, J. W. Lichtman, E. R. Aksay, and H. S. Seung. Electron Microscopic Reconstruction of Functionally Identified Cells in a Neural Integrator. *Current Biology*, 27(14):2137–2147, 2017.

94. I. Wacker and R. R. Schroeder. Array tomography. *Journal of Microscopy*, 252(2):93–99, 11 2013.

95. A. A. Wanner, C. Genoud, T. Masudi, L. Siksou, and R. W. Friedrich. Dense EM-based reconstruction of the interglomerular projectome in the zebrafish olfactory bulb. *Nature neuroscience*, 19(6):816–25, 2016.

96. M. Weigert, U. Schmidt, T. Boothe, A. M\uuml;ller, A. Dibrov, A. Jain, B. Wilhelm, D. Schmidt, C. Broaddus, S. Culley, M. Rocha-Martins, F. Segovia-Miranda, C. Norden, R. Henriques, M. Zerial, M. Solimena, J. Rink, P. Tomancak, L. Royer, F. Jug, and E. W. Myers. Content-Aware Image Restoration: Pushing the Limits of Fluorescence Microscopy. *bioRxiv*, page 236463, 12 2017.

97. S. R. Wilson and J. R. McNeil. Neutral Ion Beam Figuring Of Large Optical Surfaces, 1987.

98. B. Winiarski, A. Gholinia, K. Mingard, M. Gee, G. E. Thompson, and P. J. Withers. Broad ion beam serial section tomography. *Ultramicroscopy*, 172:52–64, 2017.

99. C. S. Xu, K. J. Hayworth, Z. Lu, P. Grob, A. M. Hassan, J. G. García-Cerdán, K. K. Niyogi, E. Nogales, R. J. Weinberg, and H. F. Hess. Enhanced FIB-SEM systems for large-volume 3D imaging. *eLife*, 6, 5 2017.

100. J. Yahiro, T. Inai, A. Tsutsui, A. Sato, T. Nagato, K. Taniguchi, E. Tsuruga, and Y. Sawa. Immunohistochemical and Immunocytochemical Localization of Amylase in Rat Parotid Glands and von Ebner's Glands by Ion Etching-Immunoscanning Electron Microscopy. *Acta histochemica et cytochemica*, 44(5):201–12, 10 2011.

101. J. Yahiro and T. Nagato. Application of ion etching to immunoscanning electron microscopy. *Microscopy Research and Technique*, 67(5):240–247, 8 2005.

102. T. Zeng, B. Wu, and S. Ji. DeepEM3D: approaching human-level performance on 3D anisotropic EM image segmentation. *Bioinformatics*, 33(16):2555–2562, 3 2017.

103. H. Zhang, I. Aharonovich, D. R. Glenn, R. Schalek, A. P. Magyar, J. W. Lichtman, E. L. Hu, and R. L. Walsworth. Silicon-vacancy color centers in nanodiamonds: Cathodoluminescence imaging markers in the near infrared. *Small*, 10(10):1908–1913, 2014.

104. H. Zhang, D. R. Glenn, R. Schalek, J. W. Lichtman, and R. L. Walsworth. Efficiency of Cathodoluminescence Emission by Nitrogen-Vacancy Color Centers in Nanodiamonds. *Small*, 13(22):1700543, 6 2017.

105. Z. Zheng, J. S. Lauritzen, E. Perlman, C. G. Robinson, D. Milkie, O. Torrens, J. Price, C. B. Fisher, N. Sharifi, L. Kmecova, I. J. Ali, B. Karsh, E. T. Trautman, J. Bogovic, P. Hanslovsky, G. S. X. E. Jefferis, M. Kazhdan, K. Khairy, R. D. Fetter, D. D. Bock, and N. Square. A Complete Electron Microscopy Volume Of The Brain Of Adult Drosophila melanogaster. *bioRxiv*, 5 2017.

106. K. Zuiderveld. Contrast Limited Adaptive Histogram Equalization. In P. S. Heckbert, editor, *Graphics Gems*, chapter Contrast L, pages 474–485. Academic Press Professional, Inc., San Diego, CA, USA, 1994.

Chapter 4

Eye-Trace: Segmentation of Volumetric Microscopy Images with Eyegaze

Eye-Trace: Segmentation of Volumetric Microscopy Images with Eyegaze

Thomas Templier, Kenan Bektas, Richard H.R. Hahnloser
Institute of Neuroinformatics
University of Zurich and ETH Zurich
Neuroscience Center Zurich, Zurich, Switzerland
{templier,rich}@ini.ethz.ch

ABSTRACT
We introduce an image annotation approach for the analysis of volumetric electron microscopic imagery of brain tissue. The core task is to identify and link tubular objects (neuronal fibers) in images taken from consecutive ultrathin sections of brain tissue. In our approach an individual 'flies' through the 3D data at a high speed and maintains eye gaze focus on a single neuronal fiber, aided by navigation with a handheld gamepad controller. The continuous foveation on a fiber of interest constitutes an intuitive means to define a trace that is seamlessly recorded with a desktop eyetracker and transformed into precise 3D coordinates of the annotated fiber (skeleton tracing). In a participant experiment we validate the approach by demonstrating a tracing accuracy of about the respective radiuses of the traced fibers with browsing speeds of up to 40 brain sections per second.

Author Keywords
Connectomics; brain mapping; array tomography; neural circuit reconstruction; segmentation; annotation; user interface design; eye tracking.

ACM Classification Keywords
H.5.2. User Interfaces: Input devices and strategies interfaces and presentation.

INTRODUCTION

Connectomics

Cellular connectomics (watch a video introduction from pioneer Jeff Lichtman [29]), a field of neuroscience that aims to decipher the organization of brain neural networks, is facing a data analysis challenge. Dozens of terabytes of high resolution volumetric electron microscopy (EM) images of brain tissue need to be analyzed in order to detect neuronal fibers and their contacts with other fibers across thousands of consecutive images (neuron tracing). Successful tracing of these fibers provides the neuron morphologies and is a prerequisite for revealing the wiring diagram of the neural network (illustrated in a short animation from the online game Eyewire [12]). Such neural circuit reconstruction is an impressively challenging and yet unsolved computer vision problem which has resisted a decade of sustained efforts in developing automated algorithms [17, 23–25, 33, 44]. All recent discoveries in the field [5, 6, 8, 22, 26, 27, 43] have extensively relied on large numbers of trained humans who annotated manually or semi-automatically these large data sets. For instance the study by Takemura et al. [43] necessitated about 15,000 person-hours of manual annotation and proofreading. In this project we explored a multimodal interaction (eyetracker and gamepad controller) approach for cellular connectomics with the aim to increase the tracing throughput of single individuals. We do so by letting users navigate through the data at high speed while continuously recording their decisions at the first easily measurable source: the eye gaze.

CHI'16, May 07-12, 2016, San Jose, CA, USA.
 ISBN 978-1-4503-3362-7/16/05…$15.00.
DOI: http://dx.doi.org/10.1145/2858036.2858578

RELATED WORK

Current Annotation Methods

Neuronal fibers are tubular objects that appear as roundish structures in high-resolution EM images taken from consecutive ultrathin sections (of 5 to 50 nm thickness) cut from a small piece of animal brain tissue (Figure 1).

Typically, skeletonization of neuronal fibers is used in purely manual methods [21, 36] and in semi-automated methods [4]. It consists of identifying fiber cross-sections with mouse clicks near their center of mass in every or in every few consecutive sections (Figure 1b). Each click can be decomposed into a) locating the fiber, b) locating the mouse cursor, c) positioning the cursor and d) clicking on the fiber. According to Fitts´s Law [14], the time required to finish the mouse based annotation operation (steps b and c) is proportional to the logarithm of the ratio of target distance to target size. Put simply, more time is required for small targets which are further away.

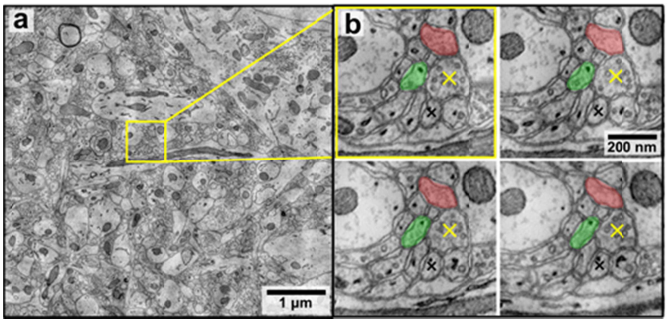

Figure 1. Electron micrographs of brain tissue. a: micrograph of a part of a section cut from a piece of mouse brain tissue. b: zoomed inset across 4 consecutive sections. Two labeled fibers are shown in red and green. The yellow and black crosses represent centers of mass of two separate fibers (skeletonization).

Also, in semi-automated methods aided by machine learning [19, 26, 27, 42], a candidate annotation that fills the inner part of each putative fiber is produced by means of computer vision algorithms (such as the green and red labels in Figure 1b). These annotations are then overlaid on the data and finally are proofread by humans.

To be able to deal with increasingly large volumes, such annotation pipelines need to be scaled up accordingly, which can be achieved by a) a better automated assessment of the locations that require manual intervention to efficiently guide proofreading, b) increasing the tracing throughput of single individuals and c) making the manual tasks easy to learn to minimize overhead from training new annotators. Both proofreading and skeletonization tasks suffer from the lack of intrinsic incentives, implying that human annotators typically must get paid or the task must be gamified [27].

Eyegaze as Input

Eye tracking consists of measuring the geometrical orientation of the eyegaze. When an individual is looking at a screen, the gaze orientation can be converted into the coordinates of the point on screen where the user is looking at.

Recently, various applications using the eye gaze as input have emerged, such as: selection of large menu items in desktop and mobile applications [28], scrolling, typing, emotion monitoring, gaze contingent visualization [3] and immersive interaction in online virtual reality environments and games. Most of these applications require a certain level of concentration known as overt attention, which occurs when an individual has the sensation of mentally focusing on a point and the measured eyegaze orientation points precisely at that same point [18].

Considering the fundamental limitations of using gaze as an input channel, Zhai et al. [45] combined gaze with mouse input by warping the pointer position to the gaze position. Their experimental study demonstrated that this system, taking advantage of Fitt´s law [14], can reduce manual effort. In an experimental study among different age groups, Murata [31] has compared the target pointing performance of participants as they use either mouse or gaze as the input modality. The results showed that with gaze input the pointing times of participants were up to 50% shorter than with mouse only. Especially for older participants with declined motor skills the target pointing with gaze was easier and simpler. Other studies with comparable setups showed that pointing with gaze is as accurate as conventional mouse pointing, and exhibits significantly shorter dwell times [13, 30, 39]. A user-centered design approach and a formative user study [41] integrated gaze as an input modality to a multi-modal environment. The findings indicate that gaze input is an intuitive modality for tasks that are in pointing nature.

To our knowledge, there is only one report of the use of eyegaze input for image analysis tasks [37]: there, a user interactively segments an object in a static (typically radiologic) image. This segmentation is achieved by feeding the eyegaze inputs to a segmentation algorithm that updates the predicted segmentation of the object of interest.

EYEGAZE FOR NEURON TRACING

In our approach, microscopy images from consecutive sections of brain tissue are displayed on a screen one after the other at a high frame rate (10 to 40 sections per second). As the sections are only a few nanometers thick, flying through them produces a pleasant impression of smooth navigation because the visible cellular structures (membranes, mitochondria, microtubuli, vesicles, myelin) evolve slowly. An observer can then perform a smooth eye pursuit and follow seamlessly these well delineated objects that they keep in their attentional spotlight. As skeletonization of neuronal tubular fibers requires a single localized label every section or every few sections, we realized that an eyegaze readout would be well suited as input to a neuron tracing system. We therefore let humans browse through the consecutive images at a constant speed and record their eyegaze with an eye tracker, infer the location on screen at which the user is foveating, and use that location as the answer to the question “Where is the cross section of the fiber currently located?”. To our knowledge, this is the first attempt of performing frame-based image annotation using eyegaze input.

EXPERIMENT

After extensive tests, a short pilot experiment with 6 participants confirmed our impression that the eyegaze tracing approach was feasible and accurate enough even by novices who are unfamiliar with the data. We therefore refined the design of the pilot experiment and conducted a within subject design experiment with the goal of answering the following main question:

Q1. What is the accuracy of tracing neuronal fibers as a function of browsing speed and fiber size?

Additionally we sought answers to the following annex questions:

q2. Can neuron tracing tasks be performed by novice untrained individuals?

q3. Does the performance improve when a user repetitively traces the same fiber?

q4. Can users maintain high accuracy while tracing long segments of fibers (1200 sections)?

Finally and more generally we also sought to know whether eyegaze based neuron tracing would potentially be accurate and reliable enough to feed data into semi-automated machine vision pipelines.

Setup

The experimental setup is shown in Figure 2. Eyegaze is measured with a desktop eyetracker (Eyetribe, 30Hz sampling rate, 0.5-1° accuracy). The navigation is controlled with a gamepad (Logitech F310) with the following functionalities: Left joystick: panning in the x-y plane; Button 1: start of browsing; Button 2: task termination. A primary display (17 inch LCD, 1280x1024, 75 Hz), presents images to the user while a secondary one, invisible to the participant, is used by the experimenter to monitor the procedure (Figure 2). The head of the user is kept with a chinrest at about 60 cm distance from the display, leading to an accuracy of the eyetracker of 40 screen-pixels. An orchestrator script (Matlab, MIJI) loads tasks consecutively by calling a custom Fiji [38] plugin for display and navigation of the image stacks. Custom scripts (python) monitored the communication with the eye tracker and the gamepad. The browsing speed reported in frames per second (fps) indicates the number of consecutive sections displayed per second.

Neuroanatomical Data

The data was generated from consecutive scanning electron micrographs of a piece of mouse neocortex brain tissue with a voxel size of 3 nm x 3 nm x 29 nm [26] downloaded from the openconnectome.org website [9] (Figure 1). Images were displayed in a Fiji canvas with a fixed magnification factor appropriately set for each task, depending on the initial size of the fiber to be traced. The magnification varied between 200% for large fibers up to 500% for small fibers. At 500% magnification, 8 image pixels correspond to 1 screen pixel. Six image stacks were extracted from the large online dataset: five stacks were of dimensions 2000 x 2000 x 300 voxels (6 µm x 6µm x 8.8 µm) and one stack, containing long fibers, was of dimensions 2000 x 2000 x 1200 voxels (6 µm x 6 µm x 35.3µm).

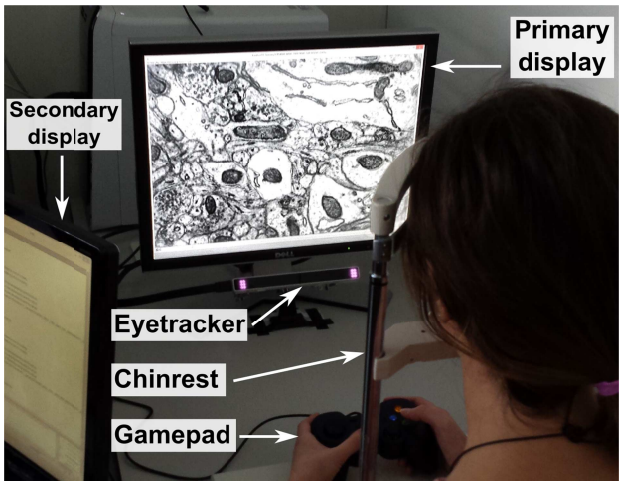

Figure 2. Experimental setup.

From these image stacks we chose 18 unique fibers to be used within the study tasks, described below. The chosen fibers did not terminate before reaching the boundary of the stack volumes. To avoid a possible bias towards more easily traceable fibers that run along the browsing axis (i.e., perpendicular to the tissue sectioning plane), we took care of selecting fibers that exhibited sharp turns.

In order to reveal the relationship between tracing speed and tracing accuracy, we classified fibers based on their diameter size. Small fibers have an average diameter of about 45 pixels (135 nm), medium fibers of 45 to 65 pixels, and large fibers of more than 65 pixels.

Participants

20 students (10 female, MSc. and PhD levels, and ages 23 to 33 years, normal or corrected-to-normal vision) participated in the experiment, provided their written consent and received a small compensation.

Procedure

Guided by the experimenter (2nd author), each participant underwent the following procedure: 1) welcoming and giving consent; 2) initial training (eye tracker calibration and 4 training tasks); 3) experiment: consecutive tracing tasks interleaved with calibrations, breaks and difficulty ratings; 4) system usability scale (SUS) rating; and 5) short debriefing.

Tasks

The experiment was divided into 129 tasks. We analyzed only the first 62 tasks, the remaining ones were designed to test further functionalities that are not reported here (branching points, complex terminations). When a task started, the initial image of a stack of sections was displayed on screen with a red cross placed in the center of the fiber that the participant had to trace. When the participant was ready, she pressed a button on the gamepad triggering the start of the browsing through the stack at a given frame rate that depends on the task. During the browsing, the participant followed the fiber of interest with

her eyes and adjusted the field of view in the x-y plane with the joystick if necessary.

The task could terminate in two ways: 1) the participant followed the fiber until the end of the stack was reached (typically after 300 sections, that is, after 15 seconds if browsing was done at 20 fps); or 2) the participant pressed the termination button before the end of the stack was reached to signify that she was not able to follow the fiber any more for whatever reason.

After the termination of a task, the participant had to briefly rate its difficulty on a Likert scale. Thereafter either the next task started five seconds later or a short thirty seconds break was given.

Experimental Design

The participants were exposed to a succession of tasks that were interleaved systematically by breaks, calibrations, or instructions.

Warmup

The first four tasks provided a short initial training and exhibited four different fibers at increasing browsing speeds of 10, 20, 30 and 40 fps. These fibers were not reused in other tasks.

Speed/Size Experiment

Tasks 5-52 constituted the **speed/size experiment** and showed small, medium and large fibers at 10, 20, 30 and 40 fps. Each of the 12 tracing conditions (4 speeds x 3 sizes) was tested 4 times, for a total of 48 tasks.

For these 48 tasks, we used a total of 12 unique fibers: 4 small, 4 medium and 4 large. All 12 fibers were 300 sections long. To prevent a task from displaying the exact same fiber as a previous task, we created four different tasks from each unique fiber by displaying the stack 1) from the first to the last section (forwards); 2) from the last to the first section (backwards); 3) forwards with a 180° rotation around the browsing axis (forward rotated); 4) backwards rotated. The 4 tasks created from a unique fiber were used across the 4 different speeds. For example, fiber number 7 has been traced in the following conditions: (10fps, backwards), (20 fps, forwards rotated), (30 fps, forwards) and (40 fps, backwards rotated).

The 48 tasks were first randomized, then we reordered two tasks to number 5 and 10 for the task repetition experiment described below. This order was the same for all participants.

Repetition Experiments

The two groups of tasks {53,54,55,56} and {58,59,60,61} constituted the **fiber repetition experiment** and displayed 4 times consecutively at 20 fps the same medium and small fiber, respectively.

Task 53 (small fiber, 20 fps) was equivalent to task 5, and task 58 (medium fiber, 20 fps) was equivalent to task 10. The two pairs of identical tasks {5,53} and {10,58} constituted the **task repetition experiment** to assess improvement of the participants between the start and the end of the approximately 1 hour long experiment.

Long Fiber Experiment

Task 57 and 62, that we named **long fiber experiment,** displayed at 20 fps a medium and a small fiber, respectively, that were 1200 sections long.

Calibration

A nine-point eye tracking calibration was performed before the initial training tasks, and before tasks 1, 25 and 49. Calibrations were repeated until an accuracy measure given by the Eyetribe server (v.0.9.49) smaller than 0.4 was achieved. This calibration criterion is slightly more conservative than the "Excellent calibration" criterion implemented in the Eyetribe user interface.

Measures

Completeness

We assessed **completeness** of a tracing task by dividing the number of correctly foveated sections by the total number of sections spanned by the fiber. A section is considered correctly annotated if the participant has not pressed the termination button beforehand. For example if the participant presses the button during section 200 in a task displaying a 300 sections long fiber, then the task completeness is 0.66 (200/300).

Tracing accuracy

Each fiber was skeleton traced by an experienced neuroscientist (1st author) by clicking in each section k $(k = 1, \dots, K)$ on the apparent center f_k of the fiber (in image pixel coordinates). The trace $(f_1, \dots, f_K)$ was defined as the ground truth trace of the fiber. The tracing **accuracy** of a task, expressed in pixels, is defined as the root-mean-square-error (RMSE) $\frac{1}{n}\sqrt{\sum_{k=1}^{n}(f_k - e_k)^2}$ of the gaze positions e_k across all sections, where e_k is the raw unfiltered gaze coordinate fetched from the eye tracker while section k is displayed, and n is the number of validly traced sections (validly traced sections are sections during which the participant was reportedly tracing, that is, he had not pressed the termination button). We computed a **collaborative trace** of a given fiber by averaging gaze coordinates over validly traced portions of fibers across participants. Intuitively, the collaborative trace is the mean trace, which represents the consensus from the crowd. The **collaborative accuracy** is the accuracy of the collaborative trace. We computed a **smoothed bias-corrected trace** by first subtracting from e_k the bias $b = \frac{1}{n}\sum_{k=1}^{n}(e_k - f_k)$ followed by applying two median filters separately on the x and y coordinates, where the respective medians are computed over 10 consecutive sections. The resulting accuracy of the smoothed bias-corrected trace was $\frac{1}{n}\sqrt{\sum_{k=1}^{n}(f_k - M(e_k - b))^2}$, where M represents the two median filters. In our hands, our desktop eye tracker was

sufficiently precise but sometimes introduced some offset. To compensate for such accuracy offsets, we made the bias correction. The median smoothing was computed to improve the precision.

For 40 fps tracing, given that eyegaze sampling is only done at 30 Hz, there was no foveation point measurement for one fourth of the sections. We chose to not interpolate and to discard these sections for RMSE calculation.

Subjective Difficulty Rating

The fiber difficulty was measured with a Single Ease Question (SEQ). After each task, participants were asked to immediately rate the difficulty they encountered in tracing that particular fiber on a Likert scale from 1 (very easy) to 5 (very difficult).

System Usability

The system usability was assessed with a standard system usability scale (SUS) [7] immediately after the end of the experiment.

RESULTS

Speed/Size Experiment

The heat maps in Figures 3 and 4 depict in detail the accuracy and completeness of all participants for the 48 tasks of the speed/size experiment. As can be seen in these heatmaps, the accuracy values roughly oscillate between 20 and 50 pixels and the task completeness is most often 100%. These data illustrate the validation of the eyegaze tracing approach by showing that the error is about the same as the extent of the fibers while the participants rarely lost track during tracing, except for small fibers at speeds 20 fps and higher.

The accuracy tended to decrease with higher flying speeds, as intuitively expected. Somewhat counter-intuitively at low speeds (10 and 20 fps, first two meta-columns on the left, Figure 3) the accuracy decreases with increasing fiber sizes. We attribute this decrease to our definition of accuracy rather than to an inherent difficulty of tracing larger fibers (see discussion).

For a convenient representation, we depict in Figure 5 some accuracy values on representative fibers of our size classes.

Main effects of speed and size

We run a 2-way factorial repeated measures ANOVA (f-rmAN) for 3 size levels and 4 speed levels. The assumption of sphericity was violated (Mauchly´s test) for the main effects of the size, ($\chi2(2) = 6.5$, $p = .04$), for the speed, ($\chi2(5) = 15.1$, $p = .01$), and for the interaction speed/size, ($\chi2(20) = 66.3$, $p = .000$). The Greenhouse-Geisser estimates of corrected degrees of freedom became .76, .66 and .53 respectively.

There was a significant main effect of the size on the accuracy, ($F(1.5, 27.3) = 85.1$, $p = .000$, $\eta2 = .825$). Contrasts with small fibers revealed that the average accuracy for large fibers ($F(1,18) = 112.8$, $r = .37$, $\eta2 = .862$) and medium fibers ($F(1,18) = 21.6$, $r = .67$, $\eta2 = .545$) were larger than that of small fibers.

There was a significant main effect of the speed on the average accuracy, ($F(1.98, 35.6) = 3.49$, $p = .042$, $\eta2 = .162$). There was a significant interaction effect between the size and speed of tracing, ($F(3.2, 57.2) = 4.98$, $p = .003$, $\eta2 = .217$). The size of the fiber to be traced had therefore a different effect on tracing accuracy depending on the speed.

Interplay of speed and size

In order to characterize the effect of the speed for each different size level we run three separate 1-way repeated measures ANOVA (rmAN) with Bonferroni corrections. Figure 6 shows the accuracy values for the 12 speed/size conditions tested.

The tracing accuracy for **large fibers** (yellow bars, Figure 6) was independent of the speed and its mean was 50 ± 5 pixels ($F(3, 54) = 3358$, $P = 0.25$, $\eta2 = 0.157$), no significant difference between pairs (post hoc comparisons, $p > 0.05$). Because large fibers have a diameter larger than 65 pixels, the gaze input therefore sometimes was located outside of the fiber boundary.

The accuracy for **medium fibers** (red bars, Figure 6) depended on tracing speeds ($F(3, 54) = 53.55$, $p < 0.0005$, $\eta2 = 0.933$) and the average accuracy decreased linearly with speed from 34 ± 8 pixels for 10 fps to 48 ± 7 pixels for 40 fps, as intuitively expected. Post hoc tests (with Bonferroni correction) showed a statistically significant accuracy decrease ($p = .000$) for the speed pairs (10, 30) and (10, 40).

The accuracy for **small fibers** (blue bars, Figure 6) also decreased with increasing speeds ($F(3, 54) = 17.207$, $p < 0.0005$, $\eta2 = 0.489$) from 27 ± 15 pixels for 10 fps to 62 ± 28 pixels for 40 fps. Post hoc tests (with Bonferroni correction) showed a statistically significant accuracy decrease ($p = .000$) between the pairs (10, 30), (10, 40) and (20, 40) fps.

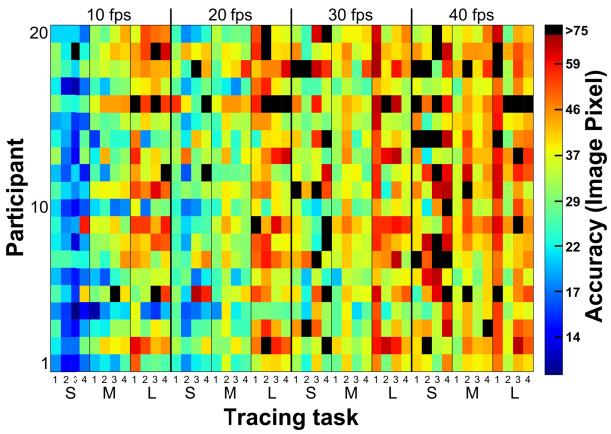

Figure 3. Heat map of the accuracy for each task from the speed/size experiment for all participants. S: small, M: medium, L: large

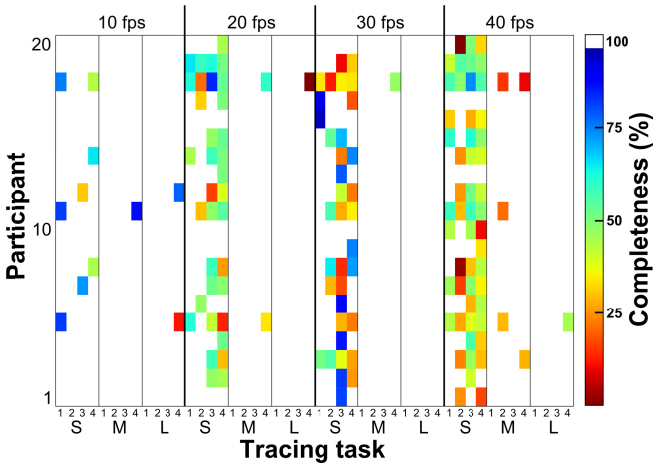

Figure 4. Heat map of the completeness for each task from the speed/size experiment for all participants. S: small, M: medium, L: large

In summary rmAN results are supplementing the general findings we obtained from f-rmAN: rmAN reveals the effect of tracing speed for each fiber size individually and f-rmAN shows that the effect of speed differs depending on size.

Collaborative traces

The accuracies of the collaborative traces for all tasks of the speed/size experiment are shown in Figure 7. In all tasks of the speed/size experiment, the collaborative trace (Figure 7) has higher accuracy than the averaged accuracies of the traces taken individually (Figure 6). This improvement in tracing accuracy is shown in detail in Figure 8 for each of the 48 tasks of the speed/size experiment.

Smoothed bias-corrected traces

The accuracies of the smoothed bias-corrected traces are shown in Figure 9. The bias and smoothing corrections show the greatest effect at low speeds.

Fiber Repetition Experiment

In the repetition experiment, a medium and a small fiber were repetitively traced consecutively 4 times at 20 fps. Some participants noticed the repetition. The average accuracy for the medium fiber was not affected by the repetition (Figure 10 left, red bars, 1-way rmAN, $F(3, 54) = 1.233$, $p = 0.307$). The same was true for the small fiber, (Figure 10 left, blue bars, 1-way rmAN, $F(3, 54) = 1.415$, $p = 0.25$).

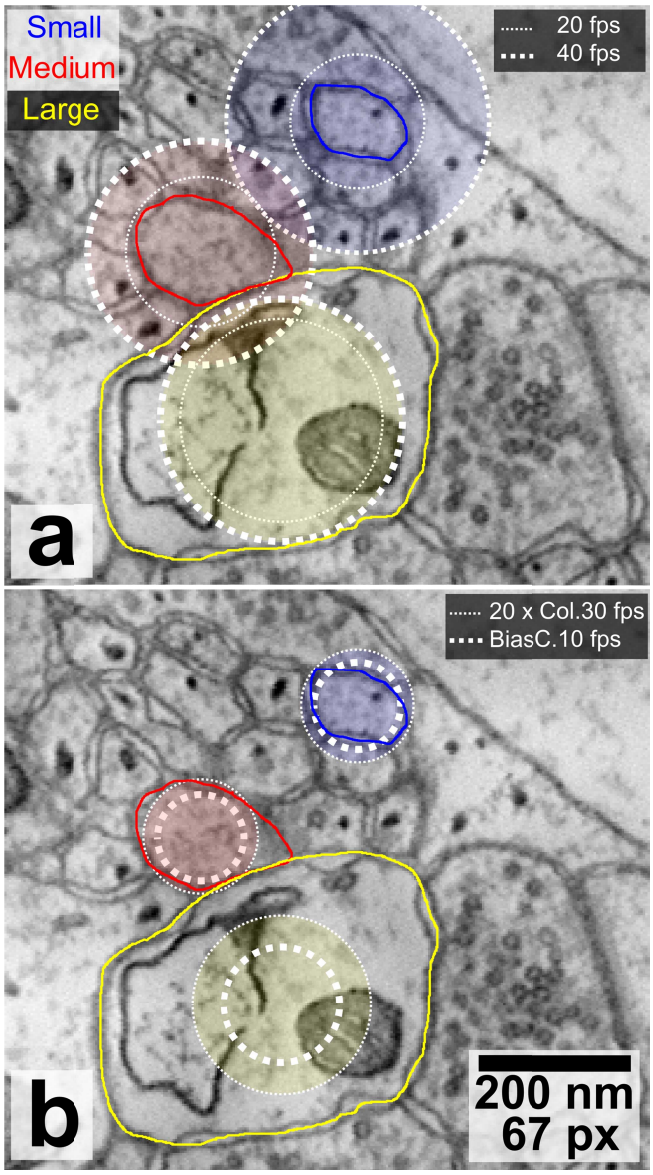

Figure 5. Accuracy of eyegaze tracing as a function of fiber size and browsing speed. Discs with a radius equal to the accuracy are centered on an example small (blue), medium (red), and large fiber (blue). Fiber boundaries are highlighted in corresponding colors. Px:image pixels (3 nm/pixel). a: fine and coarse dotted circles depict the average accuracy of all participants at 20 and 40 fps, respectively; b: fine dotted circles depict the collaborative RMSE at 30 fps. Coarse dotted circles depict the average accuracy of the smoothed bias corrected traces at 10 fps.

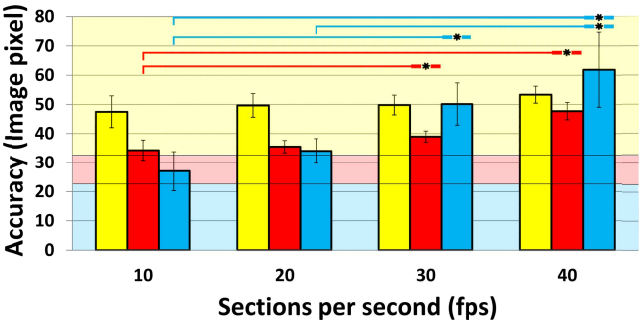

Figure 6. Accuracies for all browsing speeds (x-axis) and fiber sizes (color code as in Figure 3: Yellow: large, red: medium, blue: small.). Error bars show two standard errors of the mean. The colored background indicates the three size classes with the same color code. Stars indicate significance (* = p<0.05, post-hoc Bonferroni).

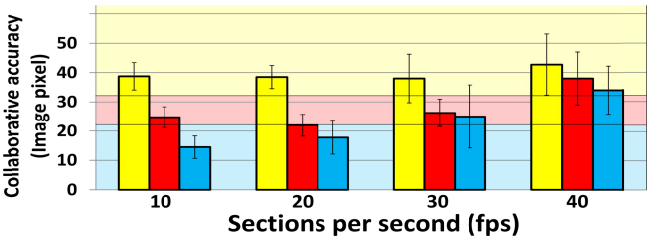

Figure 7. Accuracies of the collaborative trace for all browsing speeds (x-axis) and fiber sizes. Error bars and color codes as in Figure 6.

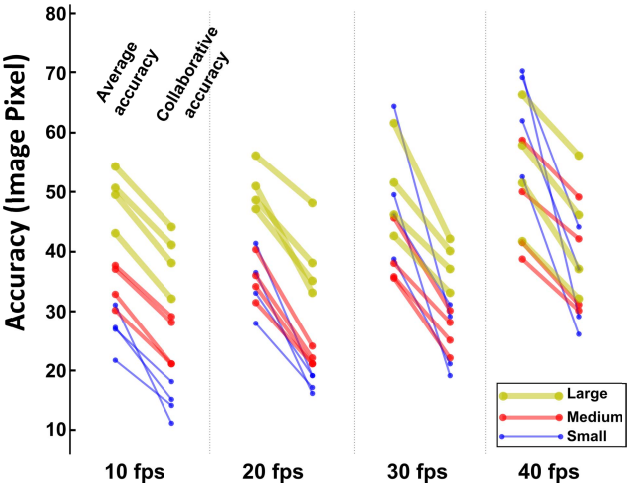

Figure 8. Collaborative tracing. Comparison of the average across all participants of the accuracies of a task with the accuracy of the corresponding collaborative trace.

Task Repetition Experiment

To assess learning of the eyegaze tracing task, participants repeated two tasks (one small, one medium fiber), with the first instance appearing within the first 10 tasks and the second instance appearing more than 40 tasks later. Figure 10 right shows the accuracy for the two repeated pairs of tasks. A pairwise t-test showed a significant increase in accuracy only for the medium fiber ($t(18) = 4.77$, $p < 0.0005$) from 40 ± 6 to 33 ± 6 pixels, and no significant difference for the small fiber ($t(18) = 1.52$, $p = 0.146$). The relatively small differences observed (though statistically significant for the medium fiber) combined with the high accuracies values show that users reach their good performance almost immediately. No participant reportedly noticed that the same fiber was being presented again after 40 tasks.

The task completeness for the repetitively traced medium fiber did not change with repetition and was on average 0.98. (1-way rmAN with Greenhouse-Geisser correction (violated sphericity), $F(1.006, 19.123) = 0.991$, $P = 0.33$). Hence fibers were already completely traced at the first repetition. For the group of small fibers, there was a slight increase in the task completeness after repetition (1st trial: 0.89 ± 0.22 and 4th trial: 0.98 ±0.04) but it was not a significant effect ($F(1.802, 34.244) = 1.264$, $P = 0.293$).

Long Fiber Experiment

The RMSE of the long medium (task 57) and long small (task 62) fibers were 23 ± 3 and 24 ± 3 pixels, respectively (2 traces were excluded as the communication with the eye tracker broke during task 62). These tracing accuracies are comparable with the ones for the short fibers (no tests performed).

Difficulty and Usability Ratings

Figure 11 shows a summary of the difficulty ratings. The subjective difficulty depended on tracing speed (non-parametric Friedman test, $\chi^2(3) = 8.647$, $p = .034$, Figure 11 left) and there was an increase in difficulty as a function of speed, as intuitively expected (though not significant).

The subjective difficulty also significantly depended on fiber size (non-parametric Friedman test , $\chi^2(2) = 24.5$, $p < 0.005$, Figure 11 middle). Small fibers were clearly perceived as the most difficult ones to trace with a statistically significant increase in perceived difficulty between large and small fibers, ($Z = -3.52$, $p < 0.005$) as well as between medium and small fibers, ($Z = -3.52$, $p < 0.005$).

Did the perceived difficulty change when a same tracing task was repeated multiple times? Figure 11, right, shows a slight decrease in difficulty after repetition, however a statistically significant reduction was only found from the first to the fourth presentations for the small fiber ($Z = -3.27$, $p = 0.001$) and no statistically significant changes were found for the repeated medium fiber.

Usability Assessment

The average SUS score of our setup was 68.1, *SD*: 13.2. Based on the literature [2] our score is in the marginal-high part (62.5 to 70 on a scale from 0 to 100) of the *Acceptability Range* and is classified as "good" (between *"ok"* and *"excellent"*) in terms of *Adjective Ratings*.

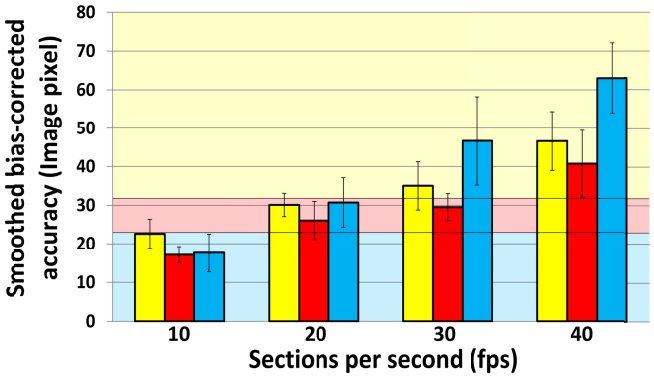

Figure 9. Accuracies of all smoothed bias-corrected traces. Error bars and color codes as in Figure 6.

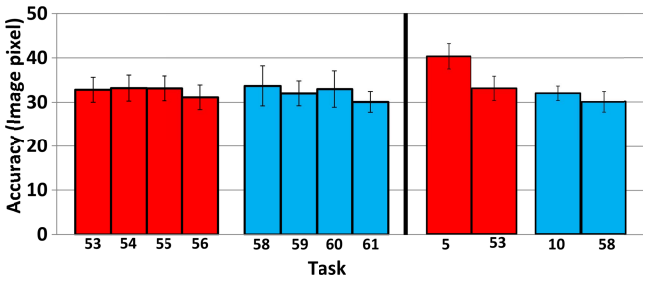

Figure 10. Learning effects with eyegaze tracing. Left: A medium (red) and a small (blue) fibers have been traced four times in a row by each participant; there are no accuracy benefits due to repetition; Right: A same task with a medium (red) and a small (blue) fiber is performed at the beginning of the experiment and more than 40 tasks later.

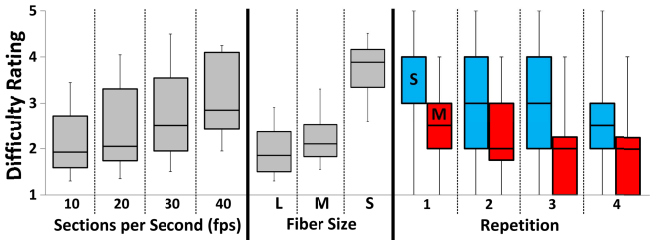

Figure 11. Subjective difficulty ratings (1: very easy, 5: very difficult) as a function of speed, of fiber size, and of repetitions in the fiber repetition experiment.

DISCUSSION

Validity of the Approach

The general impression given by the results of the participant experiment is that our eyegaze tracing approach provides acceptable skeleton traces of neuronal fibers. We found that users can follow fibers (high completeness) at high speed (10 to 40 fps) with reasonable accuracy (accuracy ~ fiber size) and that we see no severe bottleneck in performance that could arise from the technology platform chosen.

Q1. Accuracy

From Figures 3 and 6 we see that for all fiber sizes the gaze remains within the vicinity of the targeted fiber at speeds 10 and 20 fps. The study from Berning et al. [4] reports a state of the art tracing speed of 7.2h/mm, i.e., 1.3 sections/second, using accurate mouse inputs. By comparison, our system is less accurate, but allows for 10 to 40 fps browsing, which is about 15 times faster. To what extent can these numbers be compared? Clearly, the classic mouse-based approach is more accurate because users always click inside the boundary of the fiber of interest. Also, the speed comparison should be interpreted with caution because branching and termination points were not addressed here whereas these are taken into account in the speed reported for the mouse approach. In this sense it might not make sense to compare these tracing speeds.

In our approach we focus on the fact that humans are still unsurpassed in their ability to track intermingled objects and we increase the speed at the expense of the pointer accuracy. A non-automated segmentation system relying exclusively on eye gaze input would probably suffer from the lack of accuracy observed. Therefore, we believe that in future work gaze input can help automated methods to select fiber paths among diverse candidates. For example, if a fiber is erroneously traced as turning to the left by an automated method and that a user is following the fiber to the right, then the rough skeleton of the fiber would be very valuable input to correct the automated segmentation. In this sense, we hope that the achieved accuracy will be acceptable. We therefore do not see this study as a solution ready to be deployed but instead as a proof-of-principle for a scalable system that could eventually be fed into automated machine vision pipelines.

At 10 fps, smoothing and bias-correcting a trace leads to improved tracing accuracy, successfully compensating for jitter and offset produced by the eye tracker. As the ground truth and hence the bias are not known in a real application setting, querying the annotator about the exact location of his eyegaze could be a solution. For example, a salient point such as a bright item could be presented in a way to trigger the foveation of the user for a short moment on that known location, thus inferring the bias. Such a procedure could be seamlessly integrated into the workflow of a game. We note also that the quality of eye trackers is likely to improve quickly in the next few years.

As shown in Figures 3 and 5, at first glance it might be counter-intuitive that the accuracy decreases when the fiber size increases, that is, when the difficulty decreases. Our interpretation is that the gaze actually remains close to the boundaries of the fiber rather than close to the center. Instead of quantifying tracing accuracy as the simple RMSE to the approximate centers of mass, we could have added a penalty cost accounting for when the gaze is located outside of the boundary of the fiber of interest. We believe that this unexpected effect would then have vanished. However we chose to not perform the time-consuming manual contour tracing of all fibers necessary to compute such a refined accuracy.

Finally, rather specific to our neuronal reconstruction goal, it was recently demonstrated by Pallotto et al. [32] that a non-conventional brain sample preparation preserving the extracellular space between fibers aided automated machine vision algorithms. Neighboring fibers come indeed into contact much more rarely and are separated by large white gaps. We imagine that this sample preparation could compensate for the relatively lower accuracy of the eyegaze compared to a precise mouse approach.

q2. Crowd Accessibility

Scaling up the annotation task can not only be achieved by increasing the throughput of single individuals, but also by making the task accessible to a large number of individuals. Is our approach accessible to reach a large crowd? As shown in Figure 10, participants reached a high level of accuracy within a few minutes and they did not significantly improve after performing 40 tasks. Also, the heat maps in Figures 3 and 4 show qualitatively that all participants except one performed roughly equally well. From the questionnaires we learned that 14 out of the 20 participants had never manipulated such microscopy data. This therefore lets us encouragingly conclude that our approach is broadly feasible.

q3. Learning a fiber

At 20 fps, there was no significant improvement in the accuracy of participants annotating repetitively four times the same fiber, showing that the accuracy is already close to its maximum at the first attempt. This confirms also that the eyegaze approach relies on a robust mechanism of human vision to identify moving targets. A minor positive effect was observed for the completeness of these repetitively traced fibers showing that users were less likely to lose track of the fiber as they were tracing the fiber again.

q4. Long fiber segments

Our results show that users can continuously maintain attention with an appropriate foveation for at least one minute without problem (1200 sections at 20 fps). The accuracy of the long medium fiber (Task 57) was even slightly higher than the average of the short medium fibers tested in the speed/size experiment (although this long fiber might have inherently been easier to trace compared to the set of medium fibers from the speed/size experiment). We believe that this can be valuable information for the implementation of our approach for large datasets, namely to calibrate the size of the tasks presented to users. Nevertheless, such long fibers are not likely to be presented in a proofreading context as most computer errors are local and therefore users are more likely to be asked to trace short segments for local disambiguation.

Choice of the fibers

Finding a large number of fibers that were contained in a small stack from the first to the last section revealed to be a difficult task, therefore we chose to select a few (12 unique fibers for the size/speed experiment) and to apply the backward and/or the 180° rotation transformations. We were concerned that fibers could be learned, which would have biased our speed/size analysis. However we observed that the fibers displayed at such a high speed in such different settings cannot be learned. The repetition experiments tend to show that there is no learning effect even when the same fiber is repeated 4 times in a row. Also the four tasks based on a same fiber were conducted at four different speeds and therefore helped to reduce bias between different speed conditions that could have arisen from diverse difficulty levels (we assume that a fiber exhibits the same difficulty when displayed in the 4 different settings).

Another limitation maybe arose from the choice of fibers that were present from the first to the last section of the 2000x2000x300 voxels stacks which represent volumes of 6 µm x 6 µm x 9 µm. The fibers might therefore have exhibited a bias towards evolving in the direction perpendicular to the imaging plane, thus appearing more like roundish structures and maybe easing the tracing. Nevertheless, though a subjective precaution, among the candidate fibers we found, we chose on purpose some that looked tortuous to us to compensate for this possible bias. Nonetheless, our results should be considered with some degree of caution, given the limited number of fibers which have been tested.

Navigation

Magnification

In a preliminary pilot experiment, we observed that accuracy tends to increase at high magnification factors. Therefore in a different user interface version we implemented an interactive zoom to let the user adapt the display to the size of the traced fiber. However we thought that this interactive zoom would have made the task too difficult to learn as the participants were present for only about an hour.

Browsing speed

For convenience we decided to simply let the participants browse at a predefined frame rate to focus on the speed and the size of the fibers for the first characterization of our eyegaze approach. In a real setting, these speed parameters could be made easily adjustable, namely accelerating and breaking as in a racing game could also be used to navigate through the data conveniently.

Eyegaze panning

Panning laterally in the x-y plane was performed with a joystick actuated with the left thumb. It could also be done with gaze input only with appropriate treatment of the gaze signal, so that whenever the fiber deviates from the center of the display, the field of view is translated to bring the fiber back to the center of the display. Such an implementation would be desirable in mobile devices to free the hands of the user.

Complex controllers

Improving navigation probably calls for more complex control mechanisms to manipulate the data in a more efficient way, see the virtual reality system from Cali et al. [10] for example. Special handheld controllers, wearable controllers or gesture sensing devices might provide seamless navigation through such complex datasets. However a tradeoff arises between the efficiency and complexity of the human machine interaction and the accessibility of the setup to large crowds.

Collaborative Annotation

Figure 8 convincingly shows a significant increase in accuracy when averaging the trace of a fiber across the 20 participants of the study, even without removing outliers. This improvement means that if a certain level of accuracy is desired, for example as requirement from an automated pipeline, more annotators can be recruited to trace independently the same fibers. As eye tracking is about to reach mass markets, crowdsourcing our proposed eyegaze approach with the aid of online tools appears feasible.

Semi-Automated Eyegaze Tracing

Some semi-automated pipelines require that a proofreader focuses on a given fiber, follows it while the data are browsed for a couple of sections, and finally indicates the new location of the fiber. Using eyegaze information during this procedure might add some noise to the final location of the fiber provided by the annotator, however the complete approximate path would also be recorded, which could also be a valuable input to the algorithms. In a similar fashion, [4] has developed a semi-automated method that currently takes as inputs manually generated skeletons of fibers. The SOPNET framework for neuron circuit reconstruction [15–17] also interestingly makes use of candidate 2-dimensional segmentations of the fibers and could integrate our eyegaze data as input. It will be interesting in the future to assess the minimal accuracy required by these pipelines and whether our eyegaze traced fibers can be fed to them.

From the point of view of the management of the tasks given to annotators, short segments that need to be traced could be distributed among different users or players, as currently implemented in the Eyewire game and other applications [4, 20, 27]. A possible very large scale implementation of that approach could be a login procedure for new generation wearable glasses [35] during which the user has to foveate on a fiber across a few sections while his gaze is recorded. Such login procedure could constitute a new generation of recaptchas [1] with a currently unsolved complex computer vision problem that would immediately receive a great attention from the machine vision community, maybe leading to a resolution faster than without this publicity.

General Applications

The eyegaze tracing approach might be suitable for any visual data in which spatial or temporal trajectories have to be drawn: tracing of tubular objects (neurons, vasculature) in various microscopy modalities, tracking of objects over time (dividing cells, growing neurons, interacting animals, evolving particles in a gas, vehicles and humans in surveillance imagery). Automated tracking or guidance of fast moving or occluded military targets such as soldiers, vehicles or missiles could also be enhanced with gaze input.

We think that our application in itself could also be seen as a novel contribution to the field of human machine interaction as to our knowledge, it uniquely (apart from games) challenges individuals with complex tasks at an unprecedentedly high temporal rate, in some way similar to a trained pianist hitting more than 10 keys per second. Complex high throughput human computer interaction systems may not have appeared yet because the applications were missing.

Future Work

In other tasks of the experiment not analyzed in this article, participants were instructed to press a button whenever the currently traced fiber was splitting into two fibers or was merging with another one. In future work the collaborative detection of branches or objects of interest such as synaptic contacts between fibers might be achieved to create wiring diagrams of the neuroanatomical networks.

The current most promising way to scale up this approach to the analysis of large volumes of electron microscopy imagery of brain tissue would be to feed semi-automated pipelines [4, 17] with eyegaze-traced skeletons.

CONCLUSION

The analysis of increasingly large and complex data requires not only the improvement of automated methods such as machine learning but also new ways for individuals to visualize and manipulate them, making the link between the data and the automated algorithms.

In this paper we designed and implemented a novel image annotation method for the analysis of large volumetric imagery of brain tissue. By displaying dynamically the data, we enabled the readout of the decisions of the individuals directly at the earliest possible sense: the eyegaze. We performed a participant experiment to validate the approach and showed acceptable accuracy during fast visualization of the data. We also showed that our approach is scalable to be used by crowds of novice users, making our approach a good candidate for analyzing increasingly large datasets.

ACKNOWLEDGMENTS

We thank the openconnectome project, the Lichtman laboratory for making the data available and the participants. We thank Andrew Duchowski and Bart Knijnenburg for comments.

REFERENCES

1. Luis von Ahn, Benjamin Maurer, Colin McMillen, David Abraham, and Manuel Blum. 2008. reCAPTCHA: human-based character recognition via Web security measures. *Science (New York, N.Y.)* 321: 1465–1468. http://doi.org/10.1126/science.1160379

2. Aaron Bangor, Philip Kortum, and James Miller. 2009. Determining what individual SUS scores mean: Adding an adjective rating scale. *Journal of usability studies* 4, 3: 114–123.

3. Kenan Bektas, Arzu Cöltekin, Jens Krüger, and Andrew T Duchowski. 2015. A Testbed Combining Visual Perception Models for Geographic Gaze Contingent Displays. *https://diglib.eg.org/handle/10.2312/eurovisshort.20151127.067-071*.

4. Manuel Berning, Kevin M. Boergens, and Moritz Helmstaedter. 2015. SegEM: Efficient Image Analysis for High-Resolution Connectomics. *Neuron* 87, 6: 1193–1206. http://doi.org/10.1016/j.neuron.2015.09.003

5. Davi D Bock, Wei-Chung Allen Lee, Aaron M Kerlin, et al. 2011. Network anatomy and in vivo physiology of visual cortical neurons. *Nature* 471, 7337: 177–182. http://doi.org/10.1038/nature09802

6. Kevin L Briggman, Moritz Helmstaedter, and Winfried Denk. 2011. Wiring specificity in the direction-selectivity circuit of the retina. *Nature* 471, 7337: 183–188. Retrieved from http://dx.doi.org/10.1038/nature09818

7. John Brooke. 1996. SUS-A quick and dirty usability scale. *Usability evaluation in industry* 189: 194.

8. Daniel J Bumbarger, Metta Riebesell, Christian Rödelsperger, and Ralf J Sommer. 2013. System-wide rewiring underlies behavioral differences in predatory and bacterial-feeding nematodes. *Cell* 152, 1-2: 109–19. http://doi.org/10.1016/j.cell.2012.12.013

9. Randal Burns, William Gray Roncal, Dean Kleissas, et al. 2013. The Open Connectome Project Data Cluster: Scalable Analysis and Vision for High-Throughput Neuroscience. *International Conference on Scientific and Statistical Database Management*: 1–11. http://doi.org/10.1145/2484838.2484870

10. Corrado Calì, Jumana Baghabra, Daniya J Boges, et al. 2015. Three-dimensional immersive virtual reality for studying cellular compartments in 3D models from EM preparations of neural tissues. *Journal of Comparative Neurology*: n/a–n/a. http://doi.org/10.1002/cne.23852

11. K R Cave and N P Bichot. 1999. Visuospatial attention: beyond a spotlight model. *Psychonomic bulletin & review* 6, 2: 204–223.

12. Eyewire. 2014. *Reconstructing a Neuron in 3D*. Retrieved from https://www.youtube.com/watch?v=noDx7TmMr8Q

13. Ribel Fares, Shaomin Fang, and Oleg Komogortsev. 2013. Can we beat the mouse with MAGIC? *Proceedings of the SIGCHI Conference on Human Factors in Computing Systems - CHI '13*: 1387. http://doi.org/10.1145/2470654.2466183

14. P M Fitts. 1992. The information capacity of the human motor system in controlling the amplitude of movement. 1954. *Journal of experimental psychology. General* 121, 3: 262–269.

15. Jan Funke, Bjoern Andres, Fred a. Hamprecht, Albert Cardona, and Matthew Cook. 2012. Efficient automatic 3D-reconstruction of branching neurons from em data. *Proceedings of the IEEE Computer Society Conference on Computer Vision and Pattern Recognition*: 1004–1011. http://doi.org/10.1109/CVPR.2012.6247777

16. Jan Funke, Björn Andres, Fred Hamprecht, Albert Cardona, and Matthew Cook. 2011. Multi-Hypothesis CRF-Segmentation of Neural Tissue in Anisotropic EM Volumes. i: 1–8. Retrieved from http://arxiv.org/abs/1109.2449

17. Jan Funke, Julien N P Martel, Stephan Gerhard, and Bjoern Andres. 2014. Candidate Sampling for Neuron Reconstruction from Anisotropic Electron Microscopy Volumes. *MICCAI Supplement*, 1: 0–5. http://doi.org/10.1007/978-3-319-10404-1_3

18. Wilson S Geisler and Lawrence K Cormack. 2011. Models of overt attention. In *The Oxford handbook of eye movements*. 439–454. http://doi.org/10.1093/oxfordhb/9780199539789.013.0024

19. Daniel Haehn, Seymour Knowles-barley, Mike Roberts, et al. 2014. Design and Evaluation of Interactive Proofreading Tools for Connectomics. http://doi.org/10.1109/TVCG.2014.2346371

20. Moritz Helmstaedter, Kevin L Briggman, and Winfried Denk. 2011. High-accuracy neurite reconstruction for high-throughput neuroanatomy. *Nature neuroscience* 14, 8: 1081–1088. http://doi.org/10.1038/nn.2868

21. Moritz Helmstaedter, Kevin L Briggman, and Winfried Denk. 2011. High-accuracy neurite reconstruction for high-throughput neuroanatomy. *Nat Neurosci* 14, 8: 1081–1088. http://doi.org/10.1038/nn.2868

22. Moritz Helmstaedter, Kevin L Briggman, Srinivas C Turaga, Viren Jain, H Sebastian Seung, and Winfried Denk. 2013. Connectomic reconstruction of the inner plexiform layer in the mouse retina. *Nature* 500, 7461: 168–74. http://doi.org/10.1038/nature12346

23. Moritz Helmstaedter and Partha P Mitra. 2012. Computational methods and challenges for large-scale circuit mapping. *Curr Opin Neurobiol* 22, 1: 162–169. http://doi.org/10.1016/j.conb.2011.11.010

24. V Jain, J F Murray, F Roth, et al. 2007. Supervised Learning of Image Restoration with Convolutional Networks. *Computer Vision, 2007. ICCV 2007. IEEE 11th International Conference on*, 1–8. http://doi.org/10.1109/ICCV.2007.4408909

25. Viren Jain, H Sebastian Seung, and Srinivas C Turaga. 2010. Machines that learn to segment images: a crucial technology for connectomics. *Curr Opin Neurobiol* 20, 5: 653–666. http://doi.org/10.1016/j.conb.2010.07.004

26. Narayanan Kasthuri, Kenneth Jeffrey Hayworth, Daniel Raimund Berger, et al. 2015. Saturated Reconstruction of a Volume of Neocortex. *Cell* 162: 648–661. http://doi.org/10.1016/j.cell.2015.06.054

27. Jinseop S. Kim, Matthew J. Greene, Aleksandar Zlateski, et al. 2014. Space–time wiring specificity supports direction selectivity in the retina. *Nature*, 4. http://doi.org/10.1038/nature13240

28. Manu Kumar, Andreas Paepcke, and Terry Winograd. 2007. EyePoint: practical pointing and selection using gaze and keyboard. *Proceedings of the SIGCHI conference on Human factors in computing systems*, 430. http://doi.org/10.1145/1240624.1240692

29. Jeff William Lichtman. 2014. *Brain Connectomics?* Retrieved from https://www.youtube.com/watch?v=2QVy0n_rdBI

30. Julio C Mateo. 2008. Gaze Beats Mouse : Hands-free Selection by Combining Gaze and EMG. *Chi Ea*: 3039–3044. http://doi.org/10.1145/1358628.1358804

31. Atsuo Murata. 2006. Eye-Gaze Input Versus Mouse: Cursor Control as a Function of Age. *International Journal of Human-Computer Interaction* 21, 1: 1–14. http://doi.org/10.1207/s15327590ijhc2101_1

32. Marta Pallotto, Paul V Watkins, Boma Fubara, Joshua H Singer, and Kevin L Briggman. 2015. Extracellular space preservation aids the connectomic analysis of neural circuits. *eLife*. http://doi.org/10.7554/eLife.08206

33. Stephen M Plaza, Louis K Scheffer, and Dmitri B Chklovskii. 2014. Toward large-scale connectome reconstructions. *Current opinion in neurobiology* 25C: 201–210. http://doi.org/10.1016/j.conb.2014.01.019

34. M I Posner, C R Snyder, and B J Davidson. 1980. Attention and the detection of signals. *Journal of experimental psychology* 109, 2: 160–174.

35. H S Raffle, A Wong, and R Geiss. 2012. Unlocking a screen using eye tracking information.

36. Stephan Saalfeld, Albert Cardona, Volker Hartenstein, and Pavel Tomančák. 2009. CATMAID: Collaborative annotation toolkit for massive amounts of image data. *Bioinformatics* 25, 15: 1984–1986. http://doi.org/10.1093/bioinformatics/btp266

37. M. Sadeghi, G. Tien, G. Hamarneh, and Ms Atkins. 2009. Hands-free interactive image segmentation using eyegaze. *Proc. of SPIE Vol* 7260: 72601H–1. http://doi.org/10.1117/12.813452

38. Johannes Schindelin, Ignacio Arganda-Carreras, Erwin Frise, et al. 2012. Fiji: an open-source platform for biological-image analysis. *Nature Methods* 9, 7: 676–682. http://doi.org/10.1038/nmeth.2019

39. Linda E. Sibert and Robert J. K. Jacob. 2000. Evaluation of eye gaze interaction. *Proc. CHI* 2, 1: 281–288. http://doi.org/10.1145/332040.332445

40. Sophie Stellmach and Raimund Dachselt. 2012. Look & Touch : Gaze-supported Target Acquisition. 2981–2990. http://doi.org/10.1145/2207676.2208709

41. Sophie Stellmach, Sebastian Stober, Andreas Nürnberger, and Raimund Dachselt. 2011. Designing gaze-supported multimodal interactions for the exploration of large image collections. *Proceedings of the 1st Conference on Novel Gaze-Controlled Applications - NGCA '11*: 1–8. http://doi.org/10.1145/1983302.1983303

42. Shin-ya Takemura, Arjun Bharioke, Zhiyuan Lu, et al. 2013. A visual motion detection circuit suggested by Drosophila connectomics. *Nature* 500, 7461: 175–181. Retrieved from http://dx.doi.org/10.1038/nature12450

43. Shin-ya Takemura, Arjun Bharioke, Zhiyuan Lu, et al. 2013. A visual motion detection circuit suggested by Drosophila connectomics. *Nature* 500, 7461: 175–81. http://doi.org/10.1038/nature12450

44. Srinivas C Turaga, Joseph F Murray, Viren Jain, et al. 2010. Convolutional networks can learn to generate affinity graphs for image segmentation. *Neural Comput.* 22, 2: 511–538. http://doi.org/http://dx.doi.org/10.1162/neco.2009.10-08-881

45. Shumin Zhai, Carlos Morimoto, and Steven Ihde. 1999. Manual and gaze input cascaded (MAGIC) pointing. *Proceedings of the SIGCHI conference on Human factors in computing systems the CHI is the limit CHI 99*: 246–253. http://doi.org/10.1145/302979.303053

46. Eyewire A Game To Map The Brain. Retrieved from https://eyewire.org

Conclusion

Cellular-resolution connectomics aims to provide detailed neuronal wiring diagrams at synaptic resolution of small chunks of brain tissue. Such diagrams will undoubtedly contribute to our understand of brain function. Volumetric electron microscopy (EM) is currently still the only method able to reveal all neuronal wires and all chemical synaptic connections within a small chunk of tissue. Volumetric EM nevertheless suffers from the difficulty to prepare and analyze samples large enough to be biologically relevant. This thesis presents new approaches to alleviate this issue by enriching the studied small chunks with contextual information, by inventing a technology for the collection of ultrathin sections directly onto silicon wafers and suitable for automated large scale correlative light and electron microscopy, and by introducing the broad ion beam milling technology to biological electron microscopy.

In the first part of this thesis I have developed a complete pipeline for the acquisition of large data sets of correlative light and electron microscopy imagery of zebra finch brain tissue. I extended the correlative array tomography approach with additional neuroanatomical tracers and rendered it compatible with connectomics-grade tissue preparation protocols, yielding uncompromised EM imagery quality despite the necessary immunostaining treatments. A longstanding weakness of this approach has been the difficulty to reliably collect hundreds of consecutive utlrathin sections onto flat substrates suitable for correlative light and electron microscopy imaging. I solved this problem by inventing a groundbreaking section collection technology using magnetic actuation. For this I developed a composite resin containing magnetic and fluorescent particles that can be appended to blocks of resin-embedded tissue. Ultrathin sections cut from such blocks carry magnetic material that enable their remote magnetic actuation at the surface of the water bath of a diamond knife. Sections are agglomerated at high density before sinking and finally landing onto a previously immersed piece of silicon wafer.

The ability to collect ultrathin sections at high packing density onto silicon wafers offers an excellent platform for large scale automated CLEM. A small chip of wafer of less than 2 cm x 2 cm contains the 507 consecutive sections used to produce the main proof of concept for this new CLEM platform: a large volumetric CLEM data set of the zebra finch nucleus HVC showing labeled neurons from tracer injections in the nuclei Robustus of the Arcopallium, Area X, and Avalanche.

In the second part of this thesis I have introduced the technology of broad ion beam (BIB) milling to biological electron microscopy. I demonstrated that resin-embedded pieces of biological tissues can be submitted to cycles of BIB milling and EM imaging to create a serial block face imaging effect. I anticipate that BIB milling will prove in the future indispensable to volumetric high-throughput electron microscopy, because BIB milling technology allows to serially ablate samples both with extremely thin layers and over multi-centimeter-squared areas. In the context of my magnetic collection technology, BIB milling will not only enable the collection of larger data sets by increasing the thickness of the collected sections but also enable unprecedentedly high axial resolution for initially mechanically cut samples.

I foresee that my magnetic collection platform combined with BIB milling technology will enable routine large scale correlative light and isotropic multibeam electron microscopy.

Appendix

Readme of the MagC script repository available at https://github.com/templiert/MagC.

Platforms

Windows - for all steps except Linux for after LM-EM registration (for exports to render and Neuroglancer)
Linux - should work too but currently untested (probably to adjust: call to concorde linkern for reordering, maybe add some fc.cleanLinuxPath to problematic paths with trakEM)

Installation

Download Fiji - java8
Download Fiji - java6 (needed because some components currently broken in the java 8 version, e.g., elastic montage and moving least squares transforms in trakEM2)
Place the file fijiCommon.py in the 'plugins' folder of Fiji: it is a library of helpful functions.
Python 2 for everything until final data export in linux - Typically install with anaconda
Python 3 for the data export in linux
Git for windows recommended to make command line calls
The software Concorde for solving traveling salesman problems. On Windows, download linkern-cygwin and place both linkern.exe and cygwin1.dll in this locally cloned repository.

Imaging

LM Imaging

Wafer overview for section segmentation

No scripts were used for the acquisition of low magnification (5x) brightfield imagery of wafers. Using the software of my microscope (ZEN) I acquired DAPI and brightfield mosaics of the wafer. Assemble the obtained data in a folder:

```
AllImages
|ProjectName_Fluo_b0s0c0x22486-1388y7488-1040m170.tif
|... (all tiles from the Fluo DAPI channel)
|
|ProjectName_BF_b0s0c0x22486-1388y7488-1040m170.tif
|...(all tiles from the Brightfield channel)
|
|Mosaic_Metadata.xml (the mosaic metadata file written by ZEN, rename it with this exact name)
```

This part of the name "b0s0c0x22486-1388y7488-1040m170" comes from ZEN and cannot be controlled. Any 'ProjectName' is ok, but `_Fluo_` and `_BF_` must be present to indicate which channel is which.

If you are not using ZEN, then adjust the code to use your own mosaic format.

Fluorescent imaging of beads for section order retrieval

After following the section segmentation step explained later, you will have the folder 'preImaging' containing

- images showing the locations of the landmarks: these images help navigating when setting up the landmarks at the light and electron microscopes
- text files with
  - the locations of the corners of the magnetic portion of the sections
  - the locations of the corners of the tissue portion of the sections
  - the locations of the landmarks
  - the locations of the corners of the tissue and of the magnetic portion of a reference section
  - the locations of the corners of the tissue portions and of a region of interest relative to that tissue portion (optional)

Configure your microscope to be usable with Micromanager. In LM_Imaging.py, adjust the paths of the configuration at the beginning of the script. The current configuration is suited for the Nikon BC Nikon2 G-Floor of Peter's lab at ETHZ.

To use with another microscope, you will probably need to adjust names of some components (e.g., 'Objective-Turret' might have another name on another microscope, etc.)

Setup

- Load the wafer and set the 20x objective.
- In LM_Imaging.py, adjust experiment parameters such as, waferName, channels, mosaic size. These parameters are at the beginning of the script.

Calibrate landmarks

- Run LM_imaging.py with spyder. In the GUI, click on the button "loadSectionsAndLandmarksFromPipeline" and select the 'preImaging' folder containing the section coordinates.
- Click on "Live BF" to activate live brightfield imaging. Using the overview images from the 'preImaging' folder, locate the first landmark on wafer (red cross) by moving the stage. Once the landmark is centered on the central cross in the field of view, press 'Add lowres landmark'.
- Navigate to the second landmark and press again 'Add lowres landmark'. This button press has triggered the movement of the stage to the 3rd landmark: adjust it to the center and press 'Add lowres landmark' again.
- The last button press has triggered again a stage movement. The stage is now centered on the 4th landmark: adjust and press again the 'Add lowres landmark'. All four landmarks are now calibrated (message updates are given in the console). If you had defined more than 4 landmarks in the wafer segmentation pipeline, then you would need to adjust more landarks similarly. Only the first two landmarks need to be adjusted manually.

Warning: when using with another microscope, make sure that the axes are not flipped and that

there is no scaling different between the x and y axes (e.g., the confocal Visitron at ETHZ has a factor 3.x between x and y axes, and the y axis is flipped). Adjust the getXY and setXY functions accordingly (e.g., y = -y, x = x * 1/3.), etc.).

- To verify the position of the landmarks, now click "Add highres landmark": it will move to the first landmark. Adjust the landmark if needed, then press again 'Add highres landmark' and so on until the last (typically 4th) landmark is calibrated. The landmarks are now calibrated.

This "Add highres landmarks" procedure is actually useful when calibrating with 20x without oil and then calibrating with a higher-magnification oil objective (typically done for imaging immunostained sections at high resolution).

After successful calibration, a file "target_highres_landmarks.txt" has been added in the preImaging folder. Keep it for further processing in the section reordering part of the pipeline (this file helps orienting correctly the acquired images).

Calibrate hardware autofocus

To calibrate the hardware autofocus (HAF) - start live imaging with a fluorescent channel with which beads are visible (e.g. "Live Green" for 488) - locate a patch of fluorescent beads - press the button "ToggleNikonHAF" (you hear a beep from the hardware autofocus) - adjust the focus with the wheel of the HAF - press again "ToggleNikonHAF".

If there is a focus offset between different channels, then adjust the offset values at the beginning of the script. These values are already calibrated for the ETHZ Nikon microscope.

Fluorescent bead acquisition

If you had stopped the GUI, you can restart it by rerunning the script and loading the wafer file that had been automatically saved when calibrating the landmarks (button "load wafer"). The wafer file is in the saveFolder defined in the script. Press the button "Acquire mag HAF" to start the automated acquisition of the bead imagery.

Fluorescent imaging for immunostained tissue

Setup

Load the wafer (which has mounting medium and a coverslip), set the 20x objective, and ensure that the sample holder is well anchored to one corner of the sample holder slot (so that you can remove and replace the sample holder at the same position without too much offset).

Calibrate landmarks

The calibration procedure is the same as described earlier for the imaging of beads. After successful calibration of the "low resolution" landmarks (with the 20x, and with the coverslip **without** immersion oil) - remove the sample holder - add immersion oil on the coverslip above the area with sections (ensure that no oil is touching the wafer, which would be a bad contamination) -

set the 63x oil objective - place back the holder at the same location (make sure it touches well one of the corners the same way as you inserted it before adding immersion oil).

Adjust manually the focus to make sure that the objective is well immersed in the oil, then press "Add highres landmark": it will move the stage to the first landmark. Adjust it and press the same button again, and so on until all landmarks are calibrated.

Calibrate hardware autofocus

Same procedure as described earlier for the beads.

Acquisition of fluorescently stained tissue

Press "Acquire tissue HAF" to start the automated acquisition.

The ROI in each section is defined in the file "source_ROI_description" in the "preImaging" folder (created in the wafer segmentation part of the pipeline). This ROI description can also be created manually, it contains the coordinates of the four corners of a section (the tissue portion, x,y) and the four corners of the ROI (a,b) (tab-delimited).

```
x1,y1   x2,y2   x3,y3   x4,y4
a1,b1   a2,b2   a3,b3   a4,b4
```

If there is no "source_ROI_description" file, then the center of the tissue section is the center of the region acquired.

EM Imaging

The script EM_imaging.py was used with a Zeiss Merlin that controlled the microscope through the Zeiss API.

Setup

Load the wafer and adjust imaging parameters (brightness, contrast). These imaging parameters will not be changed during automated imaging and can be changed during the acquisition if needed. Adjust parameters at the bottom of the EM_imaging.py script (mosaic grid, tile size, scan speed, wafer name).

Calibrate landmarks

Run EM_Imaging.py with Spyder. Click "loadSectionsAndLandmarksFromPipeline" in the GUI and select the "preImaging" folder containing section coordinates.

Locate the first landmark and center it in the field of view. Similarly as for the LM landmark calibration, repetitively press the same button and calibrate the other landmarks (the first two landmarks are calibrated manually, the following ones are precomputed and you simply need to adjust them).

Automated acquisition

Set the correct detector and start automated acquisition with "Acquire wafer". If you want to acquired only a subset of sections, press the "Acquire sub wafer" and then enter the indices of the sections in the spyder console then press enter.

The acquisition of a wafer can be interrupted and restarted. The wafer file keeps track of which sections were already acquired.

The acquisition of a specific ROI in the tissue section is determined the same way as for the LM described earlier, that is, by the text file with the coordinates of a reference tissue section and of a the relative ROI.

Section segmentation

Organize the sections in a folder like described earlier in the LM 'Wafer overview for section segmentation' paragraph.

Adjust the root folder in the script of sectionSegmentation.py and run it with the Fiji script editor. Follow the instructions that will pop up during the processing.

The output of this script is the folder "preImaging" that contains - images showing the locations of the landmarks: these images help navigating when setting up the landmarks at the light and electron microscopes - text files with - the locations of the corners of the magnetic portion of the sections - the locations of the corners of the tissue portion of the sections - the locations of the landmarks - the locations of the corners of the tissue and of the magnetic portion of a reference section - the locations of the corners of the tissue portions and of a region of interest relative to that tissue portion (optional).

Section order retrieval with fluorescent beads

Organize the fluorescent imagery of the beads acquired with the pipeline with the following format:

```
rootFolder
|└──preImaging (comes from section segmentation part)
|└──section_0000
|   |section_0000_channel_488_tileId_00-00-mag.tif
|   |section_0000_channel_488_tileId_00-01-mag.tif
|   |...
|   |section_0000_channel_546_tileId_00-00-mag.tif
|   |...
|└──section_0001
|└──...
|└──section_n
```

In the file SOR.py (Section Order Retrieval), adjust the inputFolder path to your rootFolder.

Run the SOR.py script from the Fiji script editor. It will output the section order in the folder "calculations" with the name solution488-546.txt (using two fluorescent channels) or solution488.txt (using only one fluorescent channel). You can manually copy paste this file for the data assembly pipeline below.

The script also outputs many trakemProjects that show reordered bead imagery at different stages of the processing and with all fluorescent channels.

CLEM Data assembly

Initial folder setup with input data

If you have used a different imaging pipeline than the one described above you should arrange your data with the following format:

```
YourMagCProjectFolder
|MagCParameters.txt
|solutionxxx.txt
|sectionOrder.txt
|LMEMFactor.txt
└──EMDataRaw
|   |SomeName_EM_Metadata.txt
|   └──section_0000
|   |   |Tile_0-0.tif (Tile_x-y.tif)
|   |   |Tile_0-1.tif
|   |   |Tile_1-0.tif
|   |   |Tile_1-1.tif
|   └──section_0001
|   └──...
|   └──section_n
|
└──LMData
|   |xxx_LM_Meta_Data.txt
|   └──section_0000
|   |   |section_0000_channel_488_tileId_00-00-tissue.tif
|   |   |section_0000_channel_488_tileId_00-01-tissue.tif
|   |   |...
|   |   |section_0000_channel_546_tileId_00-01-tissue.tif
|   |   |...
|   |   |section_0000_channel_brightfield_tileId_00-01-tissue.tif
|   └──section_0001
|   └──...
|   └──section_n
```

Description of the files above: - MagCParameters.txt - if you do not put it yourself from the template in the repository, the default one will be added with default parameters. There are surely parameters that you need to adjust. - solutionxxx.txt (e.g. solution488-546.txt, solution488.txt) - the section reordering solution computed from Concorde from the reordering pipeline using fluorescent beads - sectionOrder.txt - indices of the sections in the correct order, one number per

line; If this file does not exist, then it will be automatically generated from solutionxxx.txt, or it will be generated at the beginning of the EM data assembly pipeline using EM imagery - LMEMFactor.txt - the magnification factor between LM and EM imagery (float, the file contains this single number). Typically around 7-13 for 60x magnification LM and about 10 nm EM pixel size. Typically measure the distance between 2 easily identifiable points in LM and EM and calculate the distance ratio in piixels. - xxx_EM_Metadata.txt - created by EM_Imaging.py. If you do not use this script for EM imaging, look at the Example_EM_Metadata.txt to create this file yourself - xxx_LM_Meta_Data.txt - created by LM_Imaging.py. If you do not use this script for LM imaging, look at the Example_LM_Meta_Data.txt to create this file yourself

Running the pipeline

The pipeline consists of Fiji scripts that are called one after the other externally from the orchestrator python script MagC.py. You can run it directly from where you have cloned the repository. Upon first run it will open a GUI to ask the user to input: - the location of the Fiji-java8 executable - the location of the Fiji-java6 executable - the location of YourMagCProjectFolder

It will create three corresponding text files in the repository that store the three locations. If you want to change these, edit these files or remove them to trigger the GUI (the GUI does not pop up when these files are already present).

Scripts of the pipeline

If you want to run only a part of the pipeline, comment out the steps in MagC.py

Here is a brief description of what each script does in the pipeline.

LM

- preprocess_ForPipeline - copy and reorder the LM sections. Copy EM sections.
- assembly_LM - preprocess the LM channels (local contrast enhancement, thresholding, and 8-biting). Creates the contrastedBrightfield channel used for alignmnent, stiching, and CLEM registration. Assemble the tiles of the reference brightfield channel in a trakem project according to LM metadata.
- montage_LM - use on of the montage plugins to montage the LM tiles (phase correlation from Cardona, least squares from Saalfeld, or the main Fiji stitching plugin from Preibisch)
- alignRigid_LM - align (with rigid transforms) the 3D stack (using the brightfield imagery). This alignment is not crucial. If it is faulty, set doAlignment in the parameters to 0. The alignment will anyway be redone during the CLEM registration.
- export_LMChannels - export to disk assembled sections from all channels

EM

- init_EM - read metadata and initialize folder
- EM_Reorderer - performs sections order retrieval using EM imagery. Pairwise similarities between sections are calculated at the center of each tile of the mosaic grid (e.g. 2x2), and then averaged.

- downsample_EM - downsample and preprocess all tiles with local contrast normalization
- assembly_lowEM - assemble the downsampled tiles into a trakem project according to metadata (to determine tile position) followed by montaging with translations (using Fiji's stitching plugin by Preibisch et al.)
- assembly_EM - assemble a trakem project with original resolution using the transforms computed previously on low resolution data
- montage_ElasticEM - montage all tiles with elastic transforms
- export_stitchedEMForAlignment - downscale and export to file the stitched sections
- reorder_postElasticMontage - reorder projects and exported sections with the order provided in the sectionOrder.txt file (or solutionxxx.txt file if sectionOrder.txt not present)
- alignRigid_EM - rigidly align the low resolution EM stack and propagate the transforms to the high resolution project
- alignElastic_EM' - elastically align the EM stack at full resolution
- export_alignedEMForRegistration' - export all sections to file with the downscaling LMEMFactor so that the exported EM sections have roughly the same resolution as the LM imagery

LM-EM registration

- compute_RegistrationMovingLeastSquares - compute the cross-modality moving least squares (MLS) LM-EM transforms
- export_TransformedCroppedLM - export to file affine transformed and cropped LM channels : these images can be transformed with the computed MLS transforms and upscaled to fit in the EM imagery
- assembly_LMProjects - create trakem projects containing the LM imagery transformed with the MLS transforms (not upscaled)

Export of assembled data (linux only)

Install

In a folder, e.g. 'repos', clone the following repositories: - this repo - render from Saalfeld's lab

Create a folder with the following data computed from the pipeline above:

```
projects
└──project_yourProjectName
    │ElasticaAlignedEMProject.xml (from the pipeline)
    │LMProject_488.xml (from the pipeline)
    │LMProject_546.xml (from the pipeline)
    │LMProject_brightfield.xml (from the pipeline)
    └──EMData (from the pipeline)
    └──affineCropped_488 (from the pipeline)
    └──affineCropped_546 (from the pipeline)
    └──affineCropped_brightfield (from the pipeline)
```

In trakemToNeuroglancer.py adjust the paths to the 'repo' folder and 'projects' folder.

Run

Run trakemToNeuroglancer.py. It will
- create separate render projects for the EM and for the LM channels - render to file mipmaps from the EM and the LM channels - create precomputed chunks for the EM and LM channels ready to be visualized with neuroglancer

Section collection

The script Motor.py allows control of a 2-axis manipulator (Thorlabs) using the PyAPT library from Michael Leung. Follow instructions on the github page of the repo for installation.

The script syringePump.py allows control of a syringe pump (KDScientific 200) for water infusion and withdrawal.

Thomas Templier
French
12/11/1987

Education

2011-2018 PhD, "Technologies for Cellular-Resolution Connectomics", Institute of Neuroinformatics, University of Zurich and ETH Zurich, Switzerland

2009-2011 Diploma in Electrical Engineering – Technical University Munich, Germany

2007-2011 French General Engineer Diploma – Ecole Supérieure d'Electricité (Supélec), France

2005-2007 Intensive preparation for national competitive entrance exams to leading Grandes Ecoles, specializing in mathematics, physics and informatics (MPSI-MP*), Lycée Michel Montaigne, Bordeaux, France

2005 Baccalaureate in Science, First class honors, Pau, France

Professional Experience

March-September 2011 Diploma thesis, Max Planck Institute for Neurobiology, Munich, Germany

June–Sept 2009 Research training, National Institute of Solar Energy, Chambéry, France

August 2008 Internship: builder, Nice, France

2007–2009 Private lessons for undergraduate in mathematics, physics, chemistry, Rennes, France

Miscellaneous

Fluent: French, English, German
Tennis, Jazz Manouche